University of Reading

Representation of polar lows in numerical weather prediction models

PhD in Atmosphere, Oceans and Climate

PhD by Published Works

Department of Meteorology

Marta Moreno Ibáñez

April 2026

TABLE OF CONTENTS

Declaration 2

Abstract 2

Acknowledgements 3

Dedication 5

List of initials and acronyms 6

CHAPTER 1: INTRODUCTION 9

CHAPTER 2: SCIENTIFIC CONTRIBUTION OF THE PUBLISHED WORKS 11

2.1 List of published works 11

2.2 Polar lows: What do we know? 11

2.3 Impact of horizontal resolution on the representation of polar lows 13

2.4 Insights on the development mechanisms of a polar low provided by the Canadian Regional Climate Model 16

2.4.1 The Canadian Regional Climate Model 17

2.4.2 Impact of initial conditions on the representation of a polar low 18

2.4.3 Structure and development mechanisms of a polar low 19

CHAPTER 3. CONCLUSIONS AND FUTURE RESEARCH 22

3.1 Summary and conclusions 22

3.2 Limitations and future courses of research 25

REFERENCES 28

APPENDIX: PUBLISHED WORKS 33

Declaration

I confirm that this is my own work and the use of all material from other sources has been properly and fully acknowledged.

Marta Moreno Ibáñez

Abstract

Polar lows (PLs) are relatively small and intense maritime cyclones that develop at high latitudes, typically during marine cold air outbreaks. Their representation in numerical weather prediction models is challenging due to their small size, rapid development and short lifetime, as well as the sparseness of conventional observations at high latitudes. PLs can impact the ocean circulation, so the atmospheric horizontal resolution of climate models needs to be high enough to capture them. The overarching goal of this thesis by published works is to analyse how PLs are represented in models with horizontal grid spacings ranging from coarse (50 km) to fine (2.5 km); it is composed of seven published outputs: two literature reviews, three research articles, and two datasets.

The literature reviews provide an overview of our knowledge of PLs and research gaps. The first research study uses the Weather Research and Forecasting Model to analyse how the representation of PLs varies with typical climate model resolutions. On reducing the grid spacing from 50 to 25 km, PLs become more frequent, smaller, and more intense. However, a further reduction to 12.5 km does not lead to substantial differences. In the second and third research articles, the Canadian Regional Climate Model is used at convection-permitting resolution to conduct a PL case study. The model represents the observed PL reasonably well and provides details of its structure; however, its skill strongly depends on initial conditions. Consistent with previous studies, moist baroclinic instability plays an essential role in PL development.

Key implications of this work are: Firstly, this thesis shows that increasing the atmospheric model horizontal resolution does not necessarily lead to an improvement in the representation of PLs. Secondly, the research objective (weather vs climate studies) and the quality of the initial conditions will affect the potential benefits of enhanced atmospheric model horizontal resolution.

Acknowledgements

It has been a long and challenging path to get here, so I would like to thank all the people who have supported me along the way.

First, I would like to deeply thank my supervisor Suzanne L. Gray for her excellent guidance, support and kindness. It is no overstatement to say that I would not be where I am today without her help. I would also like to deeply thank John J. Cassano for hosting me as CIRES Visiting Fellow at the University of Colorado Boulder and for his excellent guidance. Thank you also to Mark Seefeldt for providing valuable guidance with the Weather Research and Forecasting Model, and to Katja Winger for being always there to help me with the Canadian Regional Climate Model. I would also like to thank my PhD examiners, Reinhard Schiemann and Thomas Bracegirdle, for making the viva such a pleasant experience. I am also grateful to all the organizations that have funded my work, which are acknowledged in the published works that form this thesis.

A big thanks to the amazing Association of Polar Early Career Scientists family, who has been a great pleasure to work with. Working with you has helped me cope with the sheer insanity of doing a PhD, not least because many of you were going through the same insanity! Y por supuesto, mil gracias a mi familia y amig@s… Gracias a mi madre y a mi padre, que han hecho todo lo posible por dar a sus hijos la oportunidad de tener una educación de calidad, y que siempre me han apoyado en mis estudios. Aunque, lamentablemente, mi padre no haya podido ser testigo de mi reconversión profesional, estoy segura de que estaría orgulloso de mí. Mis agradecimientos van también a mi hermana y a mis dos hermanos, gracias a quienes he aprendido habilidades de colaboración (y de competencia por recursos) a lo largo de mi infancia y juventud, y que también me han apoyado moralmente en mis estudios. Merci aussi à la famille Schiffmann pour montrer toujours de l'intérêt sur l'évolution de mon doctorat et, plus particulièrement, mon beau-père pour avoir toujours cru fermement que ma recherche contribuerait à la solution de la crise climatique même si cette thèse n'a aucun rapport avec cela. Je veux remercier également Kevin Anav pour maintenir mon mari occupé pendant plusieurs années, y a Adelaida Gómez Villarraga por las agradables conversaciones que hemos mantenido, que me permitieron salir de la rutina. También quiero dar las gracias a Marta Zuloaga de Prada, con la que he compartido muchos momentos en la vida, y que ha mostrado gran curiosidad por mi investigación. Finally, I want to thank the friends I have met all around the world because they have helped me, in different ways, to be where I am today.

Et, bien évidemment, un gros merci à mon mari Matthieu Schiffmann, mon « kind of », qui m'a soutenu sans relâche tout au long de ce parcours difficile. Gracias por todo lo que has hecho por

mí, especialmente estos últimos años. Que ce soit à pied, à vélo, à ski… tu as toujours marché à côté de moi. Gracias por celebrar conmigo los buenos momentos, y por darme un hombro para llorar en los malos. C'est grâce à toi que j'ai pu récupérer la confiance en moi dans les moments difficiles. El mundo sería mucho más duro y menos emocionante sin ti, gordito. Ne range pas tes valises… de nouvelles aventures nous attendent !

Dedication

À mon époux…

Ben oui !

Pourquoi pas ?

List of initials and acronyms

ACCACIA	Aerosol–Cloud Coupling And Climate Interactions in the Arctic
AMOC	Atlantic Meridional Overturning Circulation
AMPS	Antarctic Mesoscale Prediction System
AMSU	Advanced Microwave Sounding Unit
ASCAT	Advanced Scatterometer
ASR	Arctic System Reanalysis
AVHRR	Advanced Very High Resolution Radiometer
CAESAR	Cold Air Outbreak Experiment in the Sub-Arctic Region
CALIPSO	Cloud–Aerosol lidar and Infrared Pathfinder Satellite Observations
CAPE	Convective available potential energy
CARRA	Copernicus Arctic Regional Reanalysis
CFSR	Climate Forecast System Reanalysis
CIN	Convective inhibition
CISK	Convective Instability of the Second Kind
CMIP	Coupled Model Intercomparison Project
COMBLE	Cold-air Outbreaks in the Marine Boundary Layer Experiment
CPM	Convection-permitting model
CRCM	Canadian Regional Climate Model
EAPE	Eddy available potential energy
ECMWF	European Centre for Medium-Range Weather Forecasts
EKE	Eddy kinetic energy
EPLWG	European Polar Low Working Group
ERA-I	ERA-Interim
EUMETSAT	European organisation for the exploitation of Meteorological Satellites
GCM	Global climate model
GDP	Global Drifter Program
GEM	Global Environmental Multiscale Model
GSHHG	Global Self-consistent, Hierarchical, High-resolution Geography Database
HadGEM3-GA3	Hadley Centre Global Environment Model version 3 Global Atmosphere-only version 3
HALO	High Altitude and Long Range Research Aircraft
HighResMIP	High Resolution Model Intercomparison Project
HOAPS	Hamburg Ocean Atmosphere Parameters and Fluxes from Satellite Data
IFS	Integrated Forecast System

IMILAST	Intercomparison of mid-latitude storm diagnostics
IPCC	Intergovernmental Panel on Climate Change
IPY	International Polar Year
IR	Infrared
ISBA	Interactions between Soil, Biosphere, and Atmosphere
ISDM	Integrated Science Data Management
IWC	Ice water content
JRA-55	The Japanese 55-year Reanalysis
LHF	Latent heat flux
LOFZY	Lofoten cyclone
LWC	Liquid water content
MCAO	Marine cold air outbreak
ME	Mean error
MERRA	Modern-Era Retrospective analysis for Research and Applications
MET Norway	Norwegian Meteorological Institute
MetUM	Unified Model of Met Office
MIZ	Marginal ice zone
MODIS	Moderate Resolution Imaging Spectroradiometer
MSLP	Mean sea level pressure
MYNN2	Mellor-Yamada-Nakanishi-Niino Level 2.5
NAO	North Atlantic Oscillation
NASA	National Aeronautics and Space Administration
NCEP	National Centers for Environmental Prediction
NNE	North-north-east
NOAA	National Oceanic and Atmospheric Administration
NORA3	3-km Norwegian Reanalysis
OSI SAF	Ocean and Sea Ice Satellite Application Facility
OSTIA	Operational Sea Surface Temperature and Sea Ice Analysis
P3	Predicted Particle Properties
PGI	Polar low genesis potential index
PL	Polar low
PMC	Polar mesoscale cyclone
PPP	Polar Prediction Project
PV	Potential vorticity
RCM	Regional climate model
RMSE	Root mean square error

RMSE-WVD	Root mean square wind-vector-difference error
RRTMG	Rapid radiative transfer model for general circulation models
SAR	Synthetic aperture radar
SHF	Sensible heat flux
SIC	Sea ice concentration
SIMIP	Sea Ice Model Intercomparison Project
SLP	Sea level pressure
SN	Spectral nudging
SSM/I	Special Sensor Microwave Imager
SST	Sea surface temperature
SSW	Sudden stratospheric warming
STARS	Sea Surface Temperature and Altimeter Synergy for Improved Forecasting of Polar Lows
TC	Tropical cyclone
THORPEX	Observing System Research and Predictability Experiment
UNESCO	United Nations Educational, Scientific and Cultural Organization
VIIRS	Visible Infrared Imaging Radiometer Suite
WISHE	Wind Induced Surface Heat Exchange
WMO	World Meteorological Organization
WRF	Weather Research and Forecasting model
YOPP	Year of Polar Prediction

CHAPTER 1: INTRODUCTION

Polar lows (PLs) are maritime polar mesoscale cyclones with near-surface wind speeds above 15 m s^{-1} and a horizontal scale of less than 1,000 km (Heinemann and Claud, 1997). They typically develop near the sea ice edge and the snow-covered continents when very cold air moves over the relatively warm ocean, and their lifetime ranges from 6 to 48 h (Renfrew, 2015). They have a comma-shaped or a spiraliform cloud structure (Figure 1), which can change during their lifetime (e.g., Lackner et al., 2023). PLs are associated with severe weather conditions such as strong winds, large waves, heavy snow showers, and icing. Therefore, they pose a threat to coastal communities, marine and air transportation, and marine operations such as offshore construction (Gudmestad, 2024). The accurate representation of PLs in numerical weather prediction models is essential to correctly forecast them and to understand their role in the climate system. However, correctly simulating the track and characteristics of PLs remains a challenge due to their small size, their short lifetime, and their rapid development, as well as due to the sparseness of conventional observations in the polar regions, especially over the ocean. PLs and other polar mesoscale cyclones are associated with an increase in the frequency and depth of ocean convection (Condron and Renfrew, 2013). Hence, if PLs are not correctly represented in climate models, which have a coarse atmospheric horizontal resolution, these models may not accurately represent the ocean circulation.

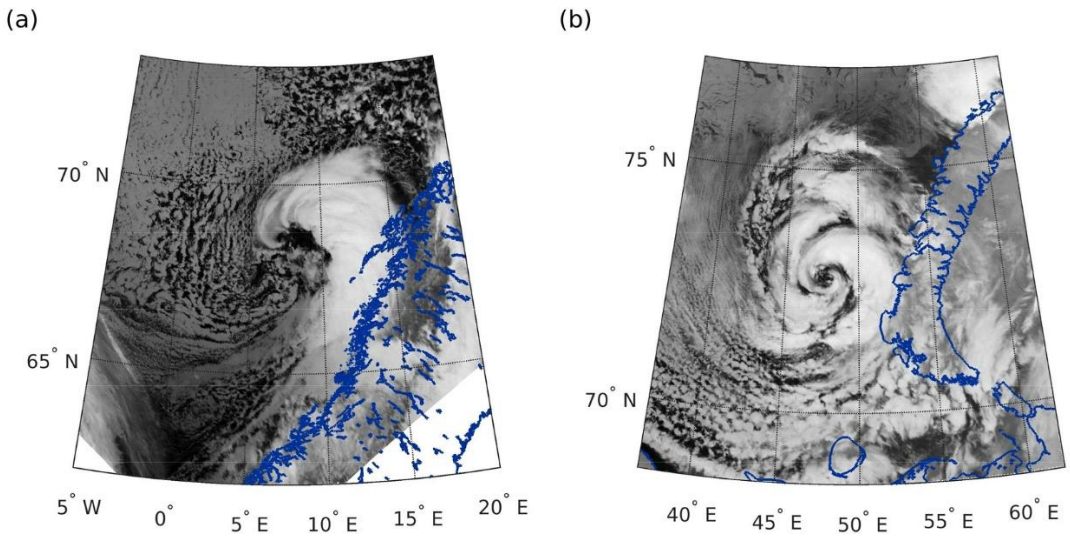

Figure 1. Infrared satellite images of (a) a comma-shaped polar low and (b) a spiraliform polar low. From Moreno-Ibáñez et al. (2021). © 2021 The Author(s). Published by Informa UK Limited, trading as Taylor & Francis Group. This is an Open Access article distributed under the terms of the Creative Commons Attribution-NonCommercial License (http://creativecommons.org/licenses/by-nc/4.0/).

The overarching goal of this thesis is to explore how PLs are represented in numerical weather prediction models with different horizontal resolutions. The models selected for this work are the Advanced Research Weather Research and Forecasting (WRF) Model Version 4.5.1 (Skamarock et al., 2019) and the convection-permitting Canadian Regional Climate Model version 6 (CRCM6), whose dynamical core was developed from the limited-area version of the Global Environmental Multiscale Model (GEM4; Côté et al., 1998; Bélair et al., 2005; Bélair et al., 2009; Girard et al., 2014). Whereas WRF has been used previously in PL studies (e.g., Kolstad and Bracegirdle, 2017), only an older version of CRCM with a 30-km grid mesh has been used to study a PL (Gachon et al., 2003). The research questions that guide this thesis are:

1. How does the representation of PLs in WRF vary with typical climate model horizontal resolutions?
2. What is the potential of CRCM6/GEM4 for the study of PLs?
    a. What is the skill of CRCM6/GEM4 at reproducing an observed PL?
    b. What is the sensitivity of a PL simulated with CRCM6/GEM4 to initial conditions?
    c. What are the development mechanisms of a PL simulated with CRCM6/GEM4?

This thesis consists of three chapters and five appendices. This first chapter indicates the broad motivation for this work. The second chapter provides a critical overview of the published works and their contribution to atmospheric science. The third chapter focuses on the conclusions of this thesis and its limitations, and suggests future courses of research. Finally, each of the manuscripts published in peer-reviewed journals is included as an appendix, followed by a page with a description of the two datasets.

CHAPTER 2: SCIENTIFIC CONTRIBUTION OF THE PUBLISHED WORKS

2.1 List of published works

The list of published works (Table 1, Table 2) includes two literature reviews (LIT1, LIT2), three original research articles (RES1, RES2, RES3), and two datasets (DAT1, DAT2). The author of this thesis is the first author of all the published works.

Table 1. Manuscripts published in peer-reviewed journals.

	Title	Journal	Year	doi	Short name
1	Recent advances in polar low research: current knowledge, challenges and future perspectives	Tellus A: Dynamic Meteorology and Oceanography	2021	10.1080/16000870.2021.1890412	LIT1
2	Polar low research: recent developments and promising courses of research	Frontiers in Earth Science	2024	10.3389/feart.2024.1368179	LIT2
3	Sensitivity of the Representation of Polar Lows to Typical Climate Model Resolutions	Atmospheric Science Letters	2025	10.1002/asl.1319	RES1
4	Assessment of simulations of a polar low with the Canadian Regional Climate Model	PLOS ONE	2023	10.1371/journal.pone.0292250	RES2
5	Analysis of the Development Mechanisms of a Polar Low over the Norwegian Sea Simulated with the Canadian Regional Climate Model	Atmosphere	2023	10.3390/atmos14060998	RES3

Table 2. Datasets.

	Title	Related publication	Year	doi	Short name
1	North Atlantic polar low tracks from September 2008 to May 2009 from WRF simulations at 50, 25 and 12.5 km grid spacings	RES1	2025	10.17864/1947.001433	DAT1
2	Polar low developed in the Norwegian Sea on 25 March 2019 – Simulations with the Canadian Regional Climate Model (CRCM6/GEM4) and manual track	RES2	2023	10.5683/SP3/6E3ITE	DAT2

2.2 Polar lows: What do we know?

In the context of the 13th PL workshop that took place in 2016, researchers emphasized the need for a new literature review about PLs (Spengler et al., 2017) because many studies had been conducted since the publication of the book about PLs edited by Rasmussen and Turner (2003). A literature review was needed to provide an updated overview of PL research and the main

challenges that needed to be tackled. The encyclopaedia article on PLs prepared by Terpstra and Watanabe (2020) provides a detailed account on the development mechanisms of PLs, but the coverage of other topics, especially the numerical representation of PLs and future research directions, is less exhaustive. The published manuscript entitled *"Recent advances in polar low research: current knowledge, challenges and future perspectives"* (LIT1; Moreno-Ibáñez et al., 2021) is a literature review that provided an up-to-date and exhaustive overview about PLs and the related research topics that deserved special attention. As this research field continued to advance during the following years, the author of this thesis realised that the research community would highly benefit from a new article focused on the most recent findings rather than having to wait several years for another comprehensive literature review on PLs to be published. Thus, the author published the manuscript entitled *"Polar low research: recent developments and promising courses of research"* (LIT2; Moreno-Ibáñez, 2024), which summarizes advances in PL research since the publication of LIT1, and highlights remaining gaps in PL research. Both LIT1 and LIT2 are timely since the preparatory phase for the 5th International Polar Year in 2032–2033 is currently underway (https://www.ipy5.info/). They constitute valuable reference documents not only for PL researchers at all career stages, but also for other researchers working on related fields (e.g., shipping risks). In addition, since PLs are not well-known outside of the research community, the author has published two articles about PLs addressed to the broader public:

1. Moreno Ibáñez, M. 2021. The Challenges of Forecasting Small, But Mighty, Polar Lows. *Eos. Science News by AGU*, *102*(10), 22–27. Available at https://eos.org/wp-content/uploads/2021/09/OCT21.pdf
    - Online version (English): https://eos.org/features/the-challenges-of-forecasting-small-but-mighty-polar-lows
    - Online version (Spanish): https://eos.org/features/the-challenges-of-forecasting-small-but-mighty-polar-lows-spanish
2. Moreno Ibáñez, M. 2021. Arctic storms: How scientists are improving forecasts of dangerous polar lows. *The Conversation*. Available at https://theconversation.com/arctic-storms-how-scientists-are-improving-forecasts-of-dangerous-polar-lows-156732
    - French version: https://theconversation.com/pourquoi-il-faut-se-mefier-des-depressions-polaires-156347

By indicating what we know and what we do not know about PLs, LIT1 and LIT2 have inspired the research questions that are addressed in the following sections. One of the main challenges identified is that atmospheric models do not always correctly represent PLs, which explains our limited knowledge about their future climatology, their impact on the ocean, and their

development mechanisms. The choice of a global or a limited-area atmospheric model to study PLs depends on the topic of interest. Global atmospheric models, which are usually coarser, are particularly useful to study the present and future climatology of PLs and their impact on the ocean. The resolution of the atmospheric model needs to be high enough to capture PLs, which can be computationally costly given their small size. Section 2.3 focuses on the topic of the horizontal resolution of the atmospheric model needed, considering typical climate model horizontal resolutions, to correctly represent PLs in climate models. Limited-area atmospheric models with very high resolution are essential to analyse the development mechanisms of PLs since they provide details of their structure and the small-scale atmospheric features. Section 2.4 focuses on a case study of a PL conducted with the limited-area, convection-permitting CRCM6/GEM4. After showing that CRCM6/GEM4 captures an observed PL reasonably well, the case study provides an insight on the development mechanisms of that PL. In addition, the case study explores the sensitivity of a PL simulated with CRCM6/GEM4 to initial conditions.

2.3 Impact of horizontal resolution on the representation of polar lows

The correct representation of PLs in atmospheric models is essential not only to analyse their climatology, but also to examine their impact on the ocean. Deep convection and dense water formation in the North Atlantic mainly occur in the Labrador Sea, the Irminger Sea, and the Nordic Seas north of Iceland (Roberts et al., 2020), which are regions where PLs develop (Stoll, 2022). Condron and Renfrew (2013) found that the occurrence of polar mesoscale cyclones—which encompass PLs—results in an increase in the frequency, depth and area of deep ocean convection. The authors used a global, eddy-permitting, coupled ocean-sea ice model to analyze the impact of polar mesoscale cyclones on the northeast Atlantic Ocean circulation during the period 1978–1998. Since the atmospheric forcing fields they used were based on ERA-40, which has a 1.125° grid spacing, they parameterized PLs into the surface wind fields. Although their study shed some light on the potential impact of PLs on the Atlantic Meridional Overturning Circulation (AMOC), this topic remains to be thoroughly researched (LIT1, LIT2).

The impact of PLs on the ocean circulation over long timescales can be investigated using global coupled climate models, but there is a lack of evidence of the minimum horizontal resolution of the atmospheric model required to obtain a representation of PLs that is sufficiently accurate for climate studies. Given that increasing the horizontal resolution entails a large computational cost, any such increase must be justified by its added value. A systematic analysis of how the representation of PLs over at least one extended winter season varies with increasing resolution of an atmospheric model, considering feasible resolutions for climate models, was long overdue. Although Shkolnik and Efimov (2013) sought to analyse the impact of horizontal resolution on

the representation of PLs in decadal simulations using a global atmospheric model with a 200-km horizontal grid mesh and with a regional atmospheric model with 50 and 25-km grid meshes, their criteria to identify PLs did not include a marine cold air outbreak (MCAO) criterion, which is essential to differentiate PLs from extratropical systems (Yanase et al., 2016). Moreover, the minimum lifetime of the detected cyclones was 12 h, thus excluding many PLs (e.g., Golubkin et al., 2021), and the maximum near-surface wind speed was 30 m s^{-1}, which excludes the strongest PLs (e.g., Smirnova et al., 2015).

The published manuscript entitled *"Sensitivity of the Representation of Polar Lows to Typical Climate Model Resolutions"* (RES1; Moreno-Ibáñez et al., 2025) explores how the number and characteristics of PLs, as well as their associated surface heat fluxes, vary with the horizontal resolution of a limited-area atmospheric model. Therefore, this study provides some evidence on the atmospheric resolution needed to represent the impact of PLs on the ocean circulation. The dataset entitled *"North Atlantic polar low tracks from September 2008 to May 2009 from WRF simulations at 50, 25 and 12.5 km grid spacings"* (DAT1; Moreno-Ibáñez, 2025) contains the model configuration files of the three simulations conducted with WRF, the PL tracks, and the statistics of the characteristics of the PL tracks and their associated fields.

In RES1, simulations with grid spacings of 50, 25 and 12.5 km were conducted with WRF (Skamarock et al., 2019). WRF is an appropriate atmospheric model for this work since it has previously been used to conduct research on PLs (e.g., Wu et al., 2011; Føre and Nordeng, 2012; Kolstad and Bracegirdle, 2017). PLs were detected and tracked in each simulation by applying the sea level pressure (SLP)-based objective tracking algorithm detailed in Crawford et al. (2021), which was adapted to PLs for this study, followed by a subjective tracking method. The track matching method of Crawford et al. (2021) was used to match PL tracks across simulations. In addition, for each simulation, the PL tracks were compared against three PL track climatologies. Overall, the temporal and spatial distribution of the PLs, as well as their average wintertime lifetime and average propagation speed, in the three simulations are consistent with previous climatologies (Moreno-Ibáñez et al., 2021). The results show that, as the resolution increases, the number of PLs represented in each simulation increases. The tracks of observed PLs are somewhat better captured as the horizontal resolution of the model increases. The PLs in the two higher-resolution simulations are smaller than those in the lower-resolution one, and this difference is statistically significant. The PL lifetime maxima of the area-maximum 10-m wind speed, the area-maximum 1-h accumulated precipitation, and the area-average surface sensible heat fluxes are also significantly larger in the two higher-resolution simulations than in the lower-resolution one. The only statistically significant difference found between the PLs in the two higher-resolution simulations is the lifetime maximum of the area-maximum 1-h accumulated precipitation, which

is larger in the 12.5-km simulation. In practice, this means that decreasing the horizontal grid spacing of an atmospheric model from 50 to 25 km will improve their representation, but further decreasing the grid spacing to 12.5 km will not lead to a notable improvement.

The main contribution of RES1 is that it is the first study that has revealed how the representation of PLs developed during one extended winter season varies as the horizontal grid spacing of an atmospheric model decreases from 50 to 12.5 km [research question 1]. The results of RES1 indicate that we can expect the PL climatologies of Bresson et al. (2022), who used an atmospheric-only global climate model with a 25-km grid spacing, and Landgren et al. (2019), who used an atmospheric-only regional climate model with a 12-km grid spacing, to capture the frequency of PLs significantly better than the PL climatologies obtained with atmospheric models with grid spacings of ~50 km or more (e.g., Zahn and von Storch, 2008). However, it is important to note that other factors such as the quality of the model also have an impact on the representation of PLs. The findings of RES1 could inform future Couple Model Intercomparison Projects (CMIPs; https://wcrp-cmip.org/), which contribute to climate assessments such as the Intergovernmental Panel on Climate Change (IPCC) reports. The Sixth Assessment Report of the IPCC reviewed results from CMIP phase 6 (CMIP6) (IPCC, 2021). The global coupled climate models participating in CMIP6, excluding those of the High Resolution Model Intercomparison Project (HighResMIP; Haarsma et al., 2016), had an atmospheric grid spacing ranging from ~50 km to ~260 km (IPCC, 2021). Therefore, RES1 provides evidence that PLs are likely to be substantially underrepresented in those simulations, or, in the case of the coarsest models, be missing altogether. The coupled models that participated in HighResMIP had an atmospheric grid spacing as low as ~25 km (Roberts et al., 2025), so the HighResMIP models with the highest atmospheric resolution likely provide a better representation of PLs, as well as their impact on the ocean, compared to the coarse models of CMIP6. Looking to the future, HighResMIP phase 2 (HighResMIP2; Roberts et al., 2025) for CMIP7 aims to conduct coupled simulations with atmospheric grid spacing of down to ~10 km. The output of these simulations has the potential to be used to investigate the long-term impact of PLs on the ocean circulation. Finally, a secondary contribution of RES1 is that it provides researchers with another tool to track PLs as this is the first time that the tracking algorithm of Crawford et al. (2021) has been used to track PLs. Since this algorithm computes the equivalent radius of cyclones, it has been possible to provide the PL size distribution corresponding to each simulation. The PL size distribution has been rarely provided in previous PL climatologies that have used an objective tracking algorithm (Pezza et al., 2016; Stoll, 2022). The algorithm of Crawford et al. (2021) can be used by any researcher since it is freely available online (https://github.com/alexcrawford0927/cyclonetracking) and is well documented.

RES1 focused on atmospheric model horizontal resolutions that are reasonable for global climate studies, which can provide an insight on the climatology of PLs and their impact on the ocean circulation. Nevertheless, models with higher resolution provide a better representation of the processes involved in PL development. Thus, limited-area atmospheric models with horizontal grid spacings of less than 10 km are commonly used to obtain PL forecasts (e.g., Hallerstig et al., 2024) and to study the structure and development mechanisms of PLs (e.g., Føre and Nordeng, 2012). The next section focuses on the case study of a PL that was conducted using such an atmospheric model.

2.4 Insights on the development mechanisms of a polar low provided by the Canadian Regional Climate Model

Limited-area atmospheric models are useful to study PLs using high resolution while keeping the computational costs reasonable. Since the development of the first mesoscale models in the 1970s, these models have been greatly improved with more sophisticated parameterizations of physical processes and very high resolution grid meshes (Dudhia, 2014), which has opened the door to the study of the details of mesoscale phenomena such as PLs (e.g., Revokatova et al., 2021). Compared to models with a coarser grid mesh, very high resolution models allow for a better representation of convective cells (e.g., Sergeev et al., 2017) and topography effects (e.g., Hallerstig et al., 2021). Therefore, these models are very useful for the study of the development mechanisms of PLs. One of such models is the Canadian Regional Climate Model, which had never been used before to study PLs at convection-permitting resolution. The published manuscripts entitled *"Assessment of simulations of a polar low with the Canadian Regional Climate Model"* (RES2; Moreno-Ibáñez et al., 2023a), and *"Analysis of the Development Mechanisms of a Polar Low over the Norwegian Sea Simulated with the Canadian Regional Climate Model"* (RES3; Moreno-Ibáñez et al., 2023b), show the potential of the very high-resolution CRCM6/GEM4 for the study of PLs by conducting a case study of a PL that developed over the Norwegian Sea on 25 March 2019. The dataset entitled *"Polar low developed in the Norwegian Sea on 25 March 2019 – Simulations with the Canadian Regional Climate Model (CRCM6/GEM4) and manual track"* (DAT2; Moreno-Ibáñez et al., 2023c) contains the simulation output and the coordinates of the track points of the simulated and observed PL. This PL had been forecast by the Norwegian Meteorological Institute, and a PL warning had been issued in BarentsWatch (https://www.barentswatch.no/polarelavtrykk/). The choice of this PL for this case study was motivated by the fact that it had been captured by ERA5 global reanalysis (Hersbach et al., 2020), which provided the initial and boundary conditions for the simulations with CRCM6/GEM4.

2.4.1 The Canadian Regional Climate Model

In RES2, several simulations of the PL were conducted, and the results were verified against observations. The simulations were conducted with CRCM6/GEM4 with a grid spacing of 0.0225° (≈ 2.5 km) and 62 vertical levels, and the model was driven by ERA5 (Hersbach et al., 2020). The model was initialised every six hours between 23 March at 0000 UTC and 24 March at 1800 UTC, thus obtaining eight simulations using different initial conditions. Satellite infrared images and conventional observations from surface stations and drifting buoys were used to verify the simulation output, and the performance of CRCM6/GEM4 was also compared with ERA5 to determine its added value. First, an object-oriented verification focused on the lifetime, track, size and intensity of the PL. Object-oriented verification is essential when analysing high-impact weather events such as PLs (Hallerstig et al., 2024). Second, the representation of several near-surface variables in the region affected by the PL was assessed. The selected variables were SLP, 2-m temperature, 2-m dewpoint temperature, 2-m relative humidity, 10-m wind speed and direction, 10-m maximum wind gusts and 1-h accumulated precipitation. These surface variables were selected for two main reasons. First, the weather conditions associated with PLs have a negative impact on coastal populations (Turner et al., 2003) and marine operations (Gudmestad, 2024), so correctly predicting them is of uttermost importance. Second, surface stations and drifting buoys provide hourly observations of these variables, which are invaluable given the rapid development of PLs. Since conventional observations are point observations, traditional verification scores were used in the study to assess the model performance. More specifically, the mean error, the root mean square error or the root mean square wind-vector-difference error, and the Spearman correlation coefficient were computed.

RES2 found that the best simulation of the observed PL represented its lifetime, track, size and associated SLP field relatively well. However, despite its lower resolution, ERA5 captured this PL better than CRCM6/GEM4. This is likely due to the fact that observations are assimilated in ERA5, and that the traditional verification methods may not capture the added value of high-resolution models compared to lower-resolution models (e.g., Stoll et al., 2020). In effect, the use of traditional verification scores to verify high-resolution forecasts is affected by the "double-penalty" problem (Jolliffe and Stephenson, 2012). Although new spatial forecast verification methods such as the method for object-based diagnostic evaluation (Davis et al., 2009) are more suitable for the verification of PL forecasts than traditional verification scores, the sparseness of surface observations in the polar regions limits the applicability of such methods to this type of observations (Casati et al., 2017). Moreover, the application of spatial verification methods to verify PL forecasts is in its infancy. Only recently, Hallerstig et al. (2024) tested features-based verification methods to verify PL forecasts.

The main contribution of RES2 is that it has shown that CRCM6/GEM4 at high resolution can capture the track and life cycle of an observed PL reasonably well, indicating that this model can be used for the study of PLs [research question 2a]. In addition, the fact that the two best simulations represent a PL deeper than the observed one and their 2-m temperature mean bias is roughly twice as high as that of ERA5 suggests that a better parameterization of the surface heat fluxes may improve the performance of CRCM6/GEM4. Another relevant contribution of RES2 is that it includes an exhaustive objective verification of the simulated PL using conventional observations, which is something that has been rarely done in PL studies. Instead, LIT1 indicated that most PL studies have only performed visual verification of PL forecasts.

2.4.2 Impact of initial conditions on the representation of a polar low

As mentioned in the previous section, RES2 conducted several experiments with different initialisation times to analyse the skill of CRCM6/GEM4 at representing an observed PL. The reason for doing this is that the representation of a PL in an atmospheric model is quite sensitive to both the quality of initial conditions and the initialisation time (Xue et al., 2021). Two relevant studies on this topic published before RES2 are those of McInnes et al. (2011) and Wagner et al. (2011), who analysed the impact of the initialisation time on the representation of a PL that developed on 3–4 March 2008 and was observed during the Norwegian International Polar Year (IPY) Observing System Research and Predictability Experiment (THORPEX) field campaign (Kristjánsson et al., 2011). McInnes et al. (2011) conducted simulations with UK Met Office Unified Model using 12-km and 4-km grid spacings, and Wagner et al. (2011) used Polar WRF with a 2-km grid spacing. Surprisingly, McInnes et al. (2011) found that the skill of the model at representing the PL notably decreased in the 4-km simulation when the model was initialised closer to the time of the PL genesis. They speculated that, when using a 4-km grid spacing, an earlier initialisation was needed to represent the dynamics during the pre-conditioning stage of the PL. In contrast, Wagner et al. (2011) found that simulations initialised closer to the time when the PL formed better captured its track and central pressure compared to the simulations that were initialised at an earlier time. In agreement with Wagner et al. (2011), the case study of a PL conducted by Xue et al. (2021) found that the best results were obtained when the simulation was initialised closer to the genesis time of the PL.

Two main limitations of these studies are the limited number of initialisation times tested and the use of visual verification as the only method to verify the output of the simulations against observations. These case studies of PLs only tested two (Xue et al., 2021) or three (McInnes et al., 2011; Wagner et al., 2011) different initialisation times. Regarding the verification of the simulations against observations, McInnes et al. (2011) performed a visual verification of the PL

simulations against infrared satellite images and dropsonde observations, and Wagner et al. (2011) performed visual verification of the PL simulations against infrared satellite images. Xue et al. (2021) conducted visual verification of the PL against infrared satellite images, 10-m wind ASCAT product, liquid and ice water content CloudSat profiles, and dropsonde observations.

Compared to these previous studies, RES2 conducted a more comprehensive analysis of the impact of initial conditions on the representation of an observed PL by conducting experiments with eight different initialisation times, covering a period of two days with a 6-h separation between initial times. Since the observed genesis time of the PL was around 0100 UTC on 25 March 2019, the initial conditions covered the period from 7 h to around two days before genesis time. In addition, RES2 applied objective verification metrics to measure the impact of the initialisation time on the representation of the PL. Consistent with previous studies, RES2 has shown that the skill of CRCM6/GEM4 at correctly representing the PL, or simply capturing its genesis, strongly depends on initial conditions. The two simulations whose initialisation time was the closest to the genesis time showed the most skill at representing the PL. One of the simulations with an earlier initialisation time also captured a PL, but it was smaller and had shorter lifetime than the observed one. RES2 went beyond simply quantifying the impact of the initialisation time on the representation of the observed PL, and analysed the simulated atmospheric fields before the genesis time of the PL to investigate why only the latest initialised simulations correctly captured the PL. Although a baroclinic environment is present before the PL genesis in all simulations, the two latest initialised simulations show stronger low-level northerly cold air advection compared to the other ones, leading to baroclinic instability. In summary, another important contribution of RES2 is that it has objectively shown that the PL simulated with CRCM6/GEM4 is very sensitive to initial conditions, and it has also provided an insight into why the PL developed or not in each simulation [research question 2b].

2.4.3 Structure and development mechanisms of a polar low

Historically, there has been a debate about the mechanisms leading to the formation and intensification of PLs, which is summarised in LIT1. While some authors argued that baroclinic instability played a main role in PL development (e.g., Harrold and Browning, 1969), others maintained that PLs were convective systems similar to tropical cyclones (e.g., Rasmussen, 1979). The resemblance of the structure of some PLs to that of hurricanes led some authors to refer to those PLs as “Arctic hurricanes” (e.g., Emanuel and Rotunno, 1989), but the possibility of a PL experiencing hurricane-like intensification has been put into question (Kolstad and Bracegirdle, 2017; Stoll et al., 2021). Several studies have found that both baroclinic instability and convection play a role in PL development (e.g., Sardie and Warner, 1985; Bracegirdle and

Gray, 2009). More recently, as LIT2 has highlighted, studies have pointed at moist baroclinic instability as the main mechanism explaining PL development (Terpstra et al., 2015; Haualand and Spengler, 2020; Stoll et al., 2021). Atmospheric models are a useful tool to explore the genesis and intensification mechanisms of PLs. Among the convection-permitting models that have been used to analyse the development mechanisms of PLs we find WRF (e.g., Kolstad and Bracegirdle, 2017), AROME-Arctic (Stoll et al., 2020), and Met Office's Unified Model (Sergeev et al., 2018). Since RES2 provided evidence that the convection-permitting CRCM6/GEM4 can represent an observed PL reasonably well, this model was used to study the mechanisms leading to the genesis and intensification of that PL.

RES3 investigated the development mechanisms of the PL that formed over the Norwegian Sea on 25 March 2019 using the atmospheric fields of the simulation conducted in RES2 that best captured it. First, the PL life cycle and the vertical wind shear environment were analysed. Then, the interaction between the different levels of the atmosphere during PL development was explored through the analysis of the horizontal wind divergence and other relevant atmospheric fields. To further analyse the mechanisms underlying the formation and intensification of the PL, RES3 developed and applied a diagnostic equation expressing the atmospheric surface pressure tendency as a function of two terms, one representing the contribution of the geopotential tendency at 500 hPa and another one representing the contribution of the atmospheric column warming. The computation of the baroclinic term was essential to show the role of the baroclinic mechanism in the development of the PL, and the calculation of the convective available potential energy in the regions with significant upward vertical motion enabled determination of the role of convection in the development of the PL. Finally, the role of latent heat release, as well as surface heat and latent heat fluxes, were also explored. The results of RES3 showed that, like most PLs, this PL developed in a forward-shear environment (Stoll, 2022). Following the occurrence of a MCAO in a baroclinic environment, the PL formed near the surface and downstream of a 500 hPa trough. The intensification of the PL was associated with southward cold air advection to the left of the PL centre and northward warm air advection to the right of the PL centre. Low-level baroclinic instability gradually extended upward up to the mid-troposphere. Latent heat release, and surface sensible and latent heat fluxes, also contributed to PL intensification.

The main contribution of RES3 is that it showed that moist baroclinic instability played an essential role in the development of this PL, and that the latent heat of condensation and the surface heat fluxes also contributed to its intensification [research question 2c]. Hence, RES3 is in agreement with recent studies that have concluded that moist baroclinic instability plays an essential role in the formation and intensification of PLs (Terpstra et al., 2015; Haualand and

Spengler, 2020; Stoll et al., 2021). In addition, RES3 has shown that CRCM6/GEM4 provides fine details of the structure of the PL and of the environment where it forms, such as strong temperature gradients, strong horizontal wind shear, upward vertical motion with small horizontal scale, as well as front waves and the resulting low-level mesoscale cyclonic vortices. Thanks to the details provided by the high resolution of the model, it has been possible to comprehend the mechanisms involved in the development of the PL.

CHAPTER 3. CONCLUSIONS AND FUTURE RESEARCH

3.1 Summary and conclusions

Coast communities and sailors have endured PLs since time immemorial, but only when polar-orbiting satellite imagery became available in the 1960s could we finally deepen our knowledge about these cyclones (Turner et al., 2003). During the last decades, research on PLs has benefited from "the quiet revolution of numerical weather prediction" (Bauer et al., 2015). Although early attempts to represent PLs in atmospheric models during the 1980s were not very successful due the coarseness of the models, there have been many advances in atmospheric modelling since then (Turner et al., 2003). Nevertheless, it is still challenging to correctly represent PLs in atmospheric models, even when using convection-permitting models, since they are small, short-lived and they undergo rapid development. Given that PLs pose a risk to coastal populations, maritime and air transportation, and economic activities, forecasting them is of utmost importance. Furthermore, a correct representation of PLs in atmospheric models is needed in order to gain deep knowledge about their impact on the ocean. The overarching goal of this thesis was to explore how PLs are represented in numerical weather prediction models with horizontal grid spacings ranging from coarse (50 km) to fine (2.5 km). Two different models were used: WRF, which has been used in the past to study PLs, and CRCM6/GEM4, which had never been used before to investigate PLs. The list of published works that form this thesis includes two literature reviews (LIT1, LIT2), three original research articles (RES1, RES2, RES3), and two datasets (DAT1, DAT2).

LIT1 and LIT2 provide an updated and comprehensive literature review of our knowledge about PLs and the remaining challenges in this research field. Hence, they are valuable resources for PL researchers and researchers in other related fields. In addition, the author has published two articles, in *Eos* and in *The Conversation*, to communicate the importance of PLs to the broader public in an effort to raise public awareness about this weather phenomenon. The publication metrics from Clarivate Web of Science indicate that, as of 7 December 2025, LIT1 and LIT2 have been cited 33 and 5 times, respectively, indicating that these manuscripts have been a useful source of information for researchers.

In RES1, simulations of one extended winter season were conducted with WRF to analyse how the representation of PLs varies with horizontal resolution. Given that the motivation for this study was to provide evidence on the atmospheric model horizontal resolution needed to correctly represent PLs in climate studies, the selected grid spacings were 50, 25 and 12.5 km. PLs were tracked using a combination of objective and subjective methods. The SLP-based objective

tracking algorithm of Crawford et al. (2021) was used to track PLs for the first time. The results show that the number of PLs increases, and their average equivalent radius decreases, as the horizontal resolution of the model increases. The PLs are significantly more intense in the two higher-resolution simulations compared to the lower-resolution one. However, only the lifetime maximum of the area-maximum 1-h accumulated precipitation was significantly higher in the 12.5-km simulation compared to the 25-km one. Therefore, while there are benefits to decreasing the grid spacing of an atmospheric model from 50 to 25 km, the benefits of further reducing the grid spacing to 12.5 km are less clear. The main contribution of RES1 is that it has shown for the first time how the representation of PLs formed during one extended winter season varies with the atmospheric model horizontal grid spacing (typical for climate models). The results of RES1 provide an indication of the limitations of studies that have obtained climatologies of PLs using the output of atmospheric models with coarse horizontal resolution. In addition, RES1 has provided evidence that PLs are likely to be underrepresented in the global coupled climate models that participated in CMIP6, excluding HighResMIP, which suggests that their impact on the ocean is not correctly captured by these models. Based on studies on the ocean response to high-frequency atmospheric forcing (Condron and Renfrew, 2013; Jung et al., 2014; Holdsworth and Myers, 2015), we could expect a decreased AMOC strength in those simulations as a result of the underrepresentation of PLs. Although the CMIP6 multimodel ensemble mean reproduces the observed AMOC mean strength reasonably well, the model spread is large (Weijer et al., 2020). Using a multimodel, multiresolution ensemble of HighResMIP experiments, Roberts et al. (2020) found that increasing the atmospheric model horizontal resolution leads to either a small weakening or a small strengthening of the AMOC depending on the model. However, the authors only used a small set of models and resolutions, which limits the representativity of the results. The results of RES1 also indicate that a thoughtful analysis of the cost-benefit of increasing the resolution of the atmospheric model should be made before conducting climate simulations to study PLs.

RES2 and RES3 present a case study of a PL that formed over the Norwegian Sea on 25 March 2019. In RES2, eight simulations of this PL were conducted with the convection-permitting CRCM6/GEM4 driven by ERA5 reanalysis. The model, which has a horizontal grid spacing of 0.0225° and 62 vertical levels, was initialised every six hours between 23 March at 0000 UTC and 24 March at 1800 UTC. The simulations were verified against infrared satellite data, observations from surface stations and observations from drifting buoys. In particular, the lifetime, track, size and intensity of the simulated PL were compared with those of the observed PL. The representation of several near-surface variables in the region affected by the PL was assessed by computing the mean error, the root mean square error or the root mean square wind-vector-difference error, and the Spearman correlation coefficient. The results show that

CRCM6/GEM4 can provide a reasonable representation of an observed PL, but the ability of the model to represent the observed PL strongly depends on initial conditions. The main contribution of RES2 is that is has shown the potential of CRCM6/GEM4 for the study of PLs. In addition, RES2 has quantified the sensitivity of the PL simulations to initial conditions. Moreover, RES2 has shown that the PL simulations are substantially sensitive to initial conditions, a finding that is supported by the results of object-oriented metrics and traditional verification scores. Only the two latest-initialised simulations captured the observed PL, and one of the simulations initialised at an earlier time represented a much smaller and short-lived PL.

In RES3, the development mechanisms of the PL were analysed with the data from the simulation that had best captured it. The development of a diagnostic equation of the atmospheric surface pressure tendency allowed to express it as a function of two contributions, one due to the geopotential height tendency and the other one due to the atmospheric column temperature tendency. The horizontal wind divergence and the baroclinic term were computed to analyse the interactions between the different levels of the atmosphere as well as the role of baroclinic instability in the development of the PL. Thanks to its high resolution, the CRCM6/GEM4 provides fine details of the structure of the PL and the environment where it formed. The results show that moist baroclinic instability plays an essential role in the formation and intensification of the PL. During PL development, the low-level baroclinic instability gradually extends upward up to the mid-troposphere. The latent heat of condensation and the surface latent and sensible heat fluxes also contribute to the intensification of the PL. The main contribution of RES3 is that it has provided evidence of the development mechanisms of the PL simulated with the CRCM6/GEM4, and these results are in line with recent studies.

Taken together, RES2 and RES3 show that, although convection-permitting models can provide fine details of the structure of PLs and their development mechanisms, their skill at forecasting PLs is strongly dependent on the initial conditions. Since forecasts errors grow faster in convection-permitting models compared to models with lower resolution (Køltzow et al., 2019), a convection-permitting model may not necessarily lead to improved representation of a PL compared to its lower-resolution counterpart if the precursors to PL development are not accurately represented in the initial conditions. As an example, in their case study of a PL that formed on 16 March 2008, McInnes et al. (2011) found that simulations with both 12-km and 4-km horizontal grid spacings, whose initialisation time was the same, failed to capture the PL. Hence, improving the initial conditions of an atmospheric model may be more relevant for PL forecasting than increasing the atmospheric model horizontal resolution, especially in the polar regions where conventional observations are sparse and not homogeneously distributed in space (Casati et al., 2017). It is important to note that the improvement in PL forecasting will be limited

by the intrinsic predictability of PLs, an area of research that has recently started to gain attention (see the case studies of Lloveras and Doyle (2025) and Boyd et al. (2025)).

3.2 Limitations and future courses of research

The three original research works that are part of this thesis share three main limitations. First, their representativeness is somewhat limited. RES1 only uses one atmospheric model to assess the impact of horizontal resolution on the representation of PLs; however, different atmospheric models might yield different results. In addition, RES1 only covers one winter season, and the PLs developing during that winter season may not be representative of PLs developing in other winter seasons. These limitations could be overcome if an accurate automated method to detect and track PLs existed since it would be unrealistically time-consuming to use a combination of objective and subjective methods, like in RES1, to track PLs in multiyear simulations with different atmospheric models. RES2 was only able to assess the performance of CRCM6/GEM4 during the mature and dissipation stages of the PL because most conventional observations were obtained from surface stations located in Norway. More *in situ* observations of PLs are needed over the ocean to be able to verify simulations of PLs during all their development stages. RES3 only investigated the development mechanisms of one PL, but the development processes of PLs that develop in other environments may be different.

The second limitation shared by the original research works is that the resolution of the ocean surface boundary conditions of the atmospheric models, which are provided by ERA5, is relatively low. As a result, the marginal ice zone (MIZ) is smoothed and mesoscale SST anomalies may not be well represented. Since near-surface atmospheric fields are less accurate over the MIZ than over the ice-free ocean when the ocean surface boundary conditions of the model have a smoothed MIZ (Renfrew et al., 2021), using such boundary conditions will have a negative impact on the simulation of observed PLs, which often form near de sea ice edge. Moreover, a straight sea ice edge is less favourable for PL development than an indented one (Albright et al., 1995; Gachon et al., 2003). Regarding mesoscale SST anomalies, using WRF with a grid spacing of 10 km, Lin et al. (2025) found that, over four winter seasons, forcing by these anomalies enhanced the intensity of PLs through increased atmospheric moisture and decreased atmospheric static stability. Therefore, it is recommended that future studies similar to the ones that form this thesis be performed using high-resolution ocean surface boundary conditions. A step further would be to couple the atmospheric model with an ocean-sea ice model, which would lead to a more realistic representation of PL development. A study with satellite-based SST products found that, of 380 PLs developed over the Nordic Seas between 1999 and 2018, warming and cooling of the ocean surface occurred, respectively, in 32% and 40% of the events (Tomita and Tanaka, 2024).

In turn, the warming ocean response led to higher surface heat fluxes, resulting in slower decay rate of PLs, and the cooling ocean response led to smaller surface heat fluxes, resulting in faster decay rate of PLs (Tomita and Tanaka, 2024). Given that PL development can result in SST warming when there is an ocean temperature inversion (Wu, 2021; Tomita and Tanaka, 2024), representing the vertical temperature profile in the upper ocean with an ocean model is essential to capture these atmosphere-ocean feedbacks. As an example, Wu (2021) found that a PL simulated with WRF coupled with the Nucleus for European Modelling of the Ocean model, both with a horizontal grid spacing of 5 km, reached lower minimum SLP than when the same PL was simulated with WRF stand-alone. The results of RES1 could be compared with a similar study using WRF coupled with an ocean-sea ice model to investigate if the interactions between the ocean and the atmosphere modulate the impact of the atmospheric model horizontal resolution on the representation of PLs. The Regional Arctic System Model (Cassano et al., 2017), a regional coupled climate model whose atmospheric component is WRF, could be used for this purpose. Similarly, it would be interesting to couple CRCM6/GEM4 with an ocean-sea ice model and compare the results with those of RES2 and RES3.

As for the third limitation, the original research works, especially RES2 and RES3, could have benefited from having initial and lateral boundary conditions from a reanalysis with higher horizontal resolution than ERA5. Regional reanalyses can be used when simulating PLs provided that they cover the region and period of interest. Two regional reanalyses that cover the Arctic and sub-arctic regions are the Arctic System Reanalysis (ASR; Bromwich et al., 2018), which has a 15-km horizontal grid spacing, 71 vertical levels, and 3-hourly outputs, and the Copernicus Arctic Regional Reanalysis (CARRA; Yang et al., 2020), which has a 2.5-km horizontal grid spacing, 65 vertical levels, and 3-hourly outputs. ASR covers the period 2000-2016 (NCAR/UCAR and PMG/BPCRC/OSU, 2017) whereas CARRA covers the period 1991 onwards (Schyberg et al., 2020). Some studies have indicated that CARRA shows better performance than ERA5 (Isaksen et al., 2022; Køltzow et al., 2022).

The literature reviews, original research articles, and associated datasets that constitute this thesis have helped us gain knowledge about how PLs are represented in atmospheric models with different horizontal grid spacings. RES1 has focused on atmospheric model horizontal grid spacings that are typical of climate models. These resolutions are coarser than the “convective grey zone”, which comprises grid spacings between 4 and 10 km and is usually avoided because deep convection schemes are not valid and deep convection is not well resolved by the models (Prein et al., 2015). Case studies of PLs with the Met Office Unified Model have found that decreasing the grid spacing from 4 to 2.2 km (Sergeev et al., 2018) and from 2.2 to 0.5 km (Sergeev et al., 2017) does not significantly improve the representation of the wind, temperature

and pressure fields, although convective cells are better represented with higher resolution. Thus, an interesting course of research would be to conduct a study similar to RES1 using grid spacings finer than the “convective grey zone”. With the increase in computing power and the advances in convection-permitting atmospheric models, new opportunities arise to conduct such studies. This thesis constitutes a small step toward the larger goal of understanding the intricacies of PL development and the role that they play in the climate system.

REFERENCES

Albright, M. D., Reed, R. J. and Ovens, D. W. 1995. Origin and structure of a numerically simulated polar low over Hudson Bay. *Tellus A* **47**, 834-848. doi: 10.1034/j.1600-0870.1995.00123.x

Bauer, P., Thorpe, A. and Brunet, G. 2015. The quiet revolution of numerical weather prediction. *Nature* **525**, 47-55. doi: 10.1038/nature14956

Bélair, S., Mailhot, J., Girard, C. and Vaillancourt, P. 2005. Boundary Layer and Shallow Cumulus Clouds in a Medium-Range Forecast of a Large-Scale Weather System. *Mon. Weather Rev.* **133**, 1938-1960. doi: 10.1175/mwr2958.1

Bélair, S., Roch, M., Leduc, A.-M., Vaillancourt, P. A., Laroche, S. and co-authors. 2009. Medium-Range Quantitative Precipitation Forecasts from Canada's New 33-km Deterministic Global Operational System. *Weather Forecast.* **24**, 690-708. doi: 10.1175/2008waf2222175.1

Boyd, K., Wang, Z. and Doyle, J. 2025. Initial Condition Sensitivity of Polar Low Intensity and Location Determined Using Ensemble Sensitivity Analysis. *Mon. Weather Rev.* **153**, 1385-1399. doi: 10.1175/MWR-D-24-0187.1

Bracegirdle, T. J. and Gray, S. L. 2009. The dynamics of a polar low assessed using potential vorticity inversion. *Q. J. Roy. Meteorol. Soc.* **135**, 880-893. doi: 10.1002/qj.411

Bresson, H., Hodges, K. I., Shaffrey, L. C., Zappa, G. and Schiemann, R. 2022. The Response of Northern Hemisphere Polar Lows to Climate Change in a 25 km High-Resolution Global Climate Model. *J. Geophys. Res. Atmos.* **127**, e2021JD035610. doi: 10.1029/2021JD035610

Bromwich, D. H., Wilson, A. B., Bai, L., Liu, Z., Barlage, M. and co-authors. 2018. The Arctic System Reanalysis, Version 2. *Bull. Am. Meteorol. Soc.* **99**, 805-828. doi: 10.1175/BAMS-D-16-0215.1

Casati, B., Haiden, T., Brown, B., Nurmi, P. and Lemieux, J.-F. 2017. Verification of Environmental Prediction in Polar Regions: Recommendations for the Year of Polar Prediction. WWRP 2017 - 1, World Meteorological Organization, Geneva, Switzerland.

Cassano, J. J., DuVivier, A., Roberts, A., Hughes, M., Seefeldt, M. and co-authors. 2017. Development of the Regional Arctic System Model (RASM): Near-Surface Atmospheric Climate Sensitivity. *J. Clim.* **30**, 5729-5753. doi: 10.1175/jcli-d-15-0775.1

Condron, A. and Renfrew, I. A. 2013. The impact of polar mesoscale storms on northeast Atlantic Ocean circulation. *Nat. Geosci.* **6**, 34. doi: 10.1038/ngeo1661

Côté, J., Gravel, S., Méthot, A., Patoine, A., Roch, M. and co-authors. 1998. The Operational CMC–MRB Global Environmental Multiscale (GEM) Model. Part I: Design Considerations and Formulation. *Mon. Weather Rev.* **126**, 1373-1395. doi: 10.1175/1520-0493(1998)126<1373:Tocmge>2.0.Co;2

Crawford, A. D., Schreiber, E. A. P., Sommer, N., Serreze, M. C., Stroeve, J. C. and co-authors. 2021. Sensitivity of Northern Hemisphere Cyclone Detection and Tracking Results to Fine Spatial and Temporal Resolution Using ERA5. *Mon. Weather Rev.* **149**, 2581-2598. doi: 10.1175/mwr-d-20-0417.1

Davis, C. A., Brown, B. G., Bullock, R. and Halley-Gotway, J. 2009. The Method for Object-Based Diagnostic Evaluation (MODE) Applied to Numerical Forecasts from the 2005 NSSL/SPC Spring Program. *Weather Forecast.* **24**, 1252-1267. doi: 10.1175/2009waf2222241.1

Dudhia, J. 2014. A history of mesoscale model development. *Asia-Pac. J. Atmos. Sci.* **50**, 121-131. doi: 10.1007/s13143-014-0031-8

Emanuel, K. A. and Rotunno, R. 1989. Polar lows as arctic hurricanes. *Tellus A* **41**, 1-17. doi: 10.1111/j.1600-0870.1989.tb00362.x

Føre, I. and Nordeng, T. E. 2012. A polar low observed over the Norwegian Sea on 3–4 March 2008: high-resolution numerical experiments. *Q. J. Roy. Meteorol. Soc.* **138**, 1983-1998. doi: 10.1002/qj.1930

Gachon, P., Laprise, R., Zwack, P. and Saucier, F. J. 2003. The effects of interactions between surface forcings in the development of a model-simulated polar low in Hudson Bay. *Tellus A* **55**, 61-87. doi: 10.3402/tellusa.v55i1.12079

Girard, C., Plante, A., Desgagné, M., McTaggart-Cowan, R., Côté, J. and co-authors. 2014. Staggered Vertical Discretization of the Canadian Environmental Multiscale (GEM) Model Using a Coordinate of the Log-Hydrostatic-Pressure Type. *Mon. Weather Rev.* **142**, 1183-1196. doi: 10.1175/mwr-d-13-00255.1

Golubkin, P., Smirnova, J. and Bobylev, L. 2021. Satellite-Derived Spatio-Temporal Distribution and Parameters of North Atlantic Polar Lows for 2015-2017. *Atmos.* **12**, 224. doi: 10.3390/atmos12020224

Gudmestad, O. T. 2024. Marine Operations in the Norwegian Sea and the Ice-Free Part of the Barents Sea with Emphasis on Polar Low Pressures. *Water* **16**, 3313. doi: 10.3390/w16223313

Haarsma, R. J., Roberts, M. J., Vidale, P. L., Senior, C. A., Bellucci, A. and co-authors. 2016. High Resolution Model Intercomparison Project (HighResMIP v1.0) for CMIP6. *Geosci. Model Dev.* **9**, 4185-4208. doi: 10.5194/gmd-9-4185-2016

Hallerstig, M., Magnusson, L., Kolstad, E. W. and Mayer, S. 2021. How grid-spacing and convection representation affected the wind speed forecasts of four polar lows. *Q. J. Roy. Meteorol. Soc.* **147**, 150-165. doi: 10.1002/qj.3911

Hallerstig, M., Køltzow, M. Ø. and Mayer, S. 2024. Developing a methodology for user-oriented verification of polar low forecasts. *Q. J. Roy. Meteorol. Soc.* **150**, 4348-4370. doi: 10.1002/qj.4819

Harrold, T. W. and Browning, K. A. 1969. The polar low as a baroclinic disturbance. *Q. J. Roy. Meteorol. Soc.* **95**, 710-723. doi: 10.1002/qj.49709540605

Haualand, K. F. and Spengler, T. 2020. Direct and Indirect Effects of Surface Fluxes on Moist Baroclinic Development in an Idealized Framework. *J. Atmos. Sci.* **77**, 3211-3225. doi: 10.1175/jas-d-19-0328.1

Heinemann, G. and Claud, C. 1997. Report of a workshop on "theoretical and observational studies of polar lows" of the European Geophysical Society Polar Lows Working Group. *Bull. Am. Meteorol. Soc.* **78**, 2643-2658. doi: 10.1175/1520-0477-78.11.2643

Hersbach, H., Bell, B., Berrisford, P., Hirahara, S., Horányi, A. and co-authors. 2020. The ERA5 global reanalysis. *Q. J. Roy. Meteorol. Soc.* **146**, 1999-2049. doi: 10.1002/qj.3803

Holdsworth, A. M. and Myers, P. G. 2015. The Influence of High-Frequency Atmospheric Forcing on the Circulation and Deep Convection of the Labrador Sea. *J. Clim.* **28**, 4980-4996. doi: 10.1175/jcli-d-14-00564.1

IPCC 2021. Annex II: Models. In: *Climate Change 2021: The Physical Science Basis. Contribution of Working Group I to the Sixth Assessment Report of the Intergovernmental Panel on Climate Change* (eds. J. M. Gutiérrez and A.-M. Tréguier). Cambridge University Press, Cambridge, United Kingdom and New York, NY, USA, pp. 2087–2138.

Isaksen, K., Nordli, Ø., Ivanov, B., Køltzow, M. A. Ø., Aaboe, S. and co-authors. 2022. Exceptional warming over the Barents area. *Scientific Reports* **12**, 9371. doi: 10.1038/s41598-022-13568-5

Jolliffe, I. T. and Stephenson, D. B. 2012. *Forecast verification a practitioner's guide in atmospheric science*. John Wiley & Sons, Hoboken.

Jung, T., Serrar, S. and Wang, Q. 2014. The oceanic response to mesoscale atmospheric forcing. *Geophys. Res. Lett.* **41**, 1255-1260. doi: 10.1002/2013GL059040

Kolstad, E. W. and Bracegirdle, T. J. 2017. Sensitivity of an apparently hurricane-like polar low to sea-surface temperature. *Q. J. Roy. Meteorol. Soc.* **143**, 966-973. doi: 10.1002/qj.2980

Køltzow, M., Casati, B., Bazile, E., Haiden, T. and Valkonen, T. 2019. An NWP Model Intercomparison of Surface Weather Parameters in the European Arctic during the Year of Polar Prediction Special Observing Period Northern Hemisphere 1. *Weather Forecast.* **34**, 959-983. doi: 10.1175/WAF-D-19-0003.1

Køltzow, M., Schyberg, H., Støylen, E. and Yang, X. 2022. Value of the Copernicus Arctic Regional Reanalysis (CARRA) in representing near-surface temperature and wind speed in the north-east European Arctic. *Polar Res.* **41**, 8002. doi: 10.33265/polar.v41.8002

Kristjánsson, J. E., Barstad, I., Aspelien, T., Føre, I., Godøy, Ø. and co-authors. 2011. The Norwegian IPY–THORPEX: Polar Lows and Arctic Fronts during the 2008 Andøya Campaign. *Bull. Am. Meteorol. Soc.* **92**, 1443-1466. doi: 10.1175/2011bams2901.1

Lackner, C. P., Geerts, B., Wang, Y., Juliano, T. W., Xue, L. and co-authors. 2023. Insights into the relation between vertical cloud structure and dynamics of three polar lows: Observations from COMBLE. *Q. J. Roy. Meteorol. Soc.*, 1-22. doi: 10.1002/qj.4543

Landgren, O. A., Batrak, Y., Haugen, J. E., Støylen, E. and Iversen, T. 2019. Polar low variability and future projections for the Nordic and Barents Seas. *Q. J. Roy. Meteorol. Soc.* **145**, 3116-3128. doi: 10.1002/qj.3608

Lin, T., Rutgersson, A. and Wu, L. 2025. Influence of mesoscale sea surface temperature anomaly on polar lows. *Environmental Research Letters* **20**, 014051. doi: 10.1088/1748-9326/ad9ec6

Lloveras, D. J. and Doyle, J. D. 2025. Exploring the intrinsic predictability of an Arctic polar low. *Q. J. Roy. Meteorol. Soc.*, e70001. doi: 10.1002/qj.70001

McInnes, H., Kristiansen, J., Kristjánsson, J. E. and Schyberg, H. 2011. The role of horizontal resolution for polar low simulations. *Q. J. Roy. Meteorol. Soc.* **137**, 1674-1687. doi: 10.1002/qj.849

Moreno-Ibáñez, M., Laprise, R. and Gachon, P. 2021. Recent advances in polar low research: current knowledge, challenges and future perspectives. *Tellus A* **73**, 1-31. doi: 10.1080/16000870.2021.1890412

Moreno-Ibáñez, M., Laprise, R. and Gachon, P. 2023a. Assessment of simulations of a polar low with the Canadian Regional Climate Model. *PLOS ONE* **18**, e0292250. doi: 10.1371/journal.pone.0292250

Moreno-Ibáñez, M., Laprise, R. and Gachon, P. 2023b. Analysis of the Development Mechanisms of a Polar Low over the Norwegian Sea Simulated with the Canadian Regional Climate Model. *Atmos.* **14**, 998. doi: 10.3390/atmos14060998

Moreno-Ibáñez, M., Laprise, R. and Gachon, P. 2023c. Polar low developed in the Norwegian Sea on 25 March 2019 – Simulations with the Canadian Regional Climate Model (CRCM6/GEM4) and manual track. Borealis.

Moreno-Ibáñez, M. 2024. Polar low research: recent developments and promising courses of research. *Frontiers in Earth Science* **12**, 1368179. doi: 10.3389/feart.2024.1368179

Moreno-Ibáñez, M. 2025. North Atlantic polar low tracks from September 2008 to May 2009 from WRF simulations at 50, 25 and 12.5 km grid spacings. University of Reading.

Moreno-Ibáñez, M., Cassano, J. J., Gray, S. L. and Seefeldt, M. 2025. Sensitivity of the Representation of Polar Lows to Typical Climate Model Resolutions. *Atmos. Sci. Lett.* **26**, e1319. doi: 10.1002/asl.1319

NCAR/UCAR and PMG/BPCRC/OSU 2017. Arctic System Reanalysis version 2, National Center for Atmospheric Research, Computational and Information Systems Laboratory.

Pezza, A., Sadler, K., Uotila, P., Vihma, T., Mesquita, M. D. S. and co-authors. 2016. Southern Hemisphere strong polar mesoscale cyclones in high-resolution datasets. *Clim. Dyn.* **47**, 1647-1660. doi: 10.1007/s00382-015-2925-2

Prein, A. F., Langhans, W., Fosser, G., Ferrone, A., Ban, N. and co-authors. 2015. A review on regional convection-permitting climate modeling: Demonstrations, prospects, and challenges. *Rev. Geophys.* **53**, 323-361. doi: 10.1002/2014RG000475

Rasmussen, E. 1979. The polar low as an extratropical CISK disturbance. *Q. J. Roy. Meteorol. Soc.* **105**, 531-549. doi: 10.1002/qj.49710544504

Rasmussen, E. A. and Turner, J. 2003. *Polar Lows: Mesoscale Weather Systems in the Polar Regions*. Cambridge University Press, Cambridge.

Renfrew, I. A. 2015. Polar Lows. In: *Encyclopedia of Atmospheric Sciences (Second Edition)* (eds. G. R. North, J. Pyle and F. Zhang). Academic Press, Oxford, pp. 379-385.

Renfrew, I. A., Barrell, C., Elvidge, A. D., Brooke, J. K., Duscha, C. and co-authors. 2021. An evaluation of surface meteorology and fluxes over the Iceland and Greenland Seas in ERA5 reanalysis: The impact of sea ice distribution. *Q. J. Roy. Meteorol. Soc.* **147**, 691-712. doi: 10.1002/qj.3941

Revokatova, A., Nikitin, M., Rivin, G., Rozinkina, I., Nikitin, A. and co-authors. 2021. High-Resolution Simulation of Polar Lows over Norwegian and Barents Seas Using the COSMO-CLM and ICON Models for the 2019–2020 Cold Season. *Atmos.* **12**, 137. doi: 10.3390/atmos12020137

Roberts, M. J., Jackson, L. C., Roberts, C. D., Meccia, V., Docquier, D. and co-authors. 2020. Sensitivity of the Atlantic Meridional Overturning Circulation to Model Resolution in CMIP6 HighResMIP Simulations and Implications for Future Changes. *J. Adv. Model. Earth Syst.* **12**, e2019MS002014. doi: 10.1029/2019MS002014

Roberts, M. J., Reed, K. A., Bao, Q., Barsugli, J. J., Camargo, S. J. and co-authors. 2025. High-Resolution Model Intercomparison Project phase 2 (HighResMIP2) towards CMIP7. *Geosci. Model Dev.* **18**, 1307-1332. doi: 10.5194/gmd-18-1307-2025

Sardie, J. M. and Warner, T. T. 1985. A numerical study of the development mechanisms of polar lows. *Tellus A* **37**, 460-477. doi: 10.3402/tellusa.v37i5.11689

Schyberg, H., Yang, X., Køltzow, M. A. Ø., Amstrup, B., Bakketun, Å. and co-authors. 2020. Arctic regional reanalysis on single levels from 1991 to present. Copernicus Climate Change Service (C3S) Climate Data Store (CDS).

Sergeev, D., Renfrew, I. A. and Spengler, T. 2018. Modification of Polar Low Development by Orography and Sea Ice. *Mon. Weather Rev.* **146**, 3325-3341. doi: 10.1175/mwr-d-18-0086.1

Sergeev, D. E., Renfrew, I. A., Spengler, T. and Dorling, S. R. 2017. Structure of a shear-line polar low. *Q. J. Roy. Meteorol. Soc.* **143**, 12-26. doi: 10.1002/qj.2911

Shkolnik, I. M. and Efimov, S. V. 2013. Cyclonic activity in high latitudes as simulated by a regional atmospheric climate model: added value and uncertainties. *Environmental Research Letters* **8**, 045007. doi: 10.1088/1748-9326/8/4/045007

Skamarock, W. C., Klemp, J. B., Dudhia, J., Gill, D. O., Liu, Z. and co-authors. 2019. A Description of the Advanced Research WRF Version 4. Tech. Note NCAR/TN-556+STR, NCAR

Smirnova, J. E., Golubkin, P. A., Bobylev, L. P., Zabolotskikh, E. V. and Chapron, B. 2015. Polar low climatology over the Nordic and Barents seas based on satellite passive microwave data. *Geophys. Res. Lett.* **42**, 5603-5609. doi: 10.1002/2015GL063865

Spengler, T., Claud, C. and Heinemann, G. 2017. Polar Low Workshop Summary. *Bull. Am. Meteorol. Soc.* **98**, ES139-ES142. doi: 10.1175/bams-d-16-0207.1

Stoll, P. J., Valkonen, T. M., Graversen, R. G. and Noer, G. 2020. A well-observed polar low analysed with a regional and a global weather-prediction model. *Q. J. Roy. Meteorol. Soc.* **146**, 1740-1767. doi: 10.1002/qj.3764

Stoll, P. J., Spengler, T., Terpstra, A. and Graversen, R. G. 2021. Polar lows – moist-baroclinic cyclones developing in four different vertical wind shear environments. *Weather and Climate Dynamics* **2**, 19-36. doi: 10.5194/wcd-2-19-2021

Stoll, P. J. 2022. A global climatology of polar lows investigated for local differences and wind-shear environments. *Weather and Climate Dynamics* **3**, 483-504. doi: 10.5194/wcd-3-483-2022

Terpstra, A., Spengler, T. and Moore, R. W. 2015. Idealised simulations of polar low development in an Arctic moist-baroclinic environment. *Q. J. Roy. Meteorol. Soc.* **141**, 1987-1996. doi: 10.1002/qj.2507

Terpstra, A. and Watanabe, S.-i. 2020. Polar Lows. In: *Oxford Research Encyclopedia of Climate Science*. Oxford University Press.

Tomita, H. and Tanaka, R. 2024. Ocean Surface Warming and Cooling Responses and Feedback Processes Associated With Polar Lows Over the Nordic Seas. *J. Geophys. Res. Atmos.* **129**, e2023JD040460. doi: 10.1029/2023JD040460

Turner, J., Rasmussen, E. A. and Carleton, A. M. 2003. Introduction. In: *Polar Lows: Mesoscale Weather Systems in the Polar Regions* (eds. E. A. Rasmussen and J. Turner). Cambridge University Press, Cambridge, pp. 1-51.

Wagner, J. S., Gohm, A., Dörnbrack, A. and Schäfler, A. 2011. The mesoscale structure of a polar low: airborne lidar measurements and simulations. *Q. J. Roy. Meteorol. Soc.* **137**, 1516-1531. doi: 10.1002/qj.857

Weijer, W., Cheng, W., Garuba, O. A., Hu, A. and Nadiga, B. T. 2020. CMIP6 Models Predict Significant 21st Century Decline of the Atlantic Meridional Overturning Circulation. *Geophys. Res. Lett.* **47**, e2019GL086075. doi: 10.1029/2019GL086075

Wu, L., Martin, J. E. and Petty, G. W. 2011. Piecewise potential vorticity diagnosis of the development of a polar low over the Sea of Japan. *Tellus A* **63**, 198-211. doi: 10.1111/j.1600-0870.2011.00511.x

Wu, L. 2021. Effect of atmosphere-wave-ocean/ice interactions on a polar low simulation over the Barents Sea. *Atmos. Res.* **248**. doi: 10.1016/j.atmosres.2020.105183

Xue, J., Bromwich, D. H., Xiao, Z. and Bai, L. 2021. Impacts of initial conditions and model configuration on simulations of polar lows near Svalbard using Polar WRF with 3DVAR. *Q. J. Roy. Meteorol. Soc.* **147**, 3806-3834. doi: 10.1002/qj.4158

Yanase, W., Niino, H., Watanabe, S. I. I., Hodges, K., Zahn, M. and co-authors. 2016. Climatology of polar lows over the sea of Japan using the JRA-55 reanalysis. *J. Clim.* **29**, 419-437. doi: 10.1175/jcli-d-15-0291.1

Yang, X., Schyberg, H., Palmason, B., Bojarova, J., Box, J. and co-authors. 2020. C3S Arctic regional reanalysis—full system documentation. Copernicus Climate Change Service, Reading, UK.

Zahn, M. and von Storch, H. 2008. Tracking Polar Lows in CLM. *Meteorologische Zeitschrift* **17**, 445-453. doi: 10.1127/0941-2948/2008/0317

APPENDIX: PUBLISHED WORKS

This appendix includes the five manuscripts published in peer-reviewed journals, each one preceded by a cover page:

	Title	Journal	Year	doi	Short name
1	Recent advances in polar low research: current knowledge, challenges and future perspectives	Tellus A: Dynamic Meteorology and Oceanography	2021	10.1080/16000870.2021.1890412	LIT1
2	Polar low research: recent developments and promising courses of research	Frontiers in Earth Science	2024	10.3389/feart.2024.1368179	LIT2
3	Sensitivity of the Representation of Polar Lows to Typical Climate Model Resolutions	Atmospheric Science Letters	2025	10.1002/asl.1319	RES1
4	Assessment of simulations of a polar low with the Canadian Regional Climate Model	PLOS ONE	2023	10.1371/journal.pone.0292250	RES2
5	Analysis of the Development Mechanisms of a Polar Low over the Norwegian Sea Simulated with the Canadian Regional Climate Model	Atmosphere	2023	10.3390/atmos14060998	RES3

The peer-reviewed manuscripts are followed by a page with a description of the two datasets:

	Title	Related publication	Year	doi	Short name
1	North Atlantic polar low tracks from September 2008 to May 2009 from WRF simulations at 50, 25 and 12.5 km grid spacings	RES1	2025	10.17864/1947.001433	DAT1
2	Polar low developed in the Norwegian Sea on 25 March 2019 – Simulations with the Canadian Regional Climate Model (CRCM6/GEM4) and manual track	RES2	2023	10.5683/SP3/6E3ITE	DAT2

Published work 1

Recent advances in polar low research: current knowledge, challenges and future perspectives

Authors:	Marta Moreno-Ibáñez, René Laprise and Philippe Gachon
Year:	2021
Journal:	*Tellus A* 73, 1-31
DOI:	10.1080/16000870.2021.1890412

Authorship statement: MMI has contributed 95% (conceptualization, literature review, visualization, writing and editing of the original draft). The coauthors reviewed the draft and made minor comments.

Tellus SERIES A DYANAMIC METEOROLOGY AND OCEANOGRAPHY
PUBLISHED BY THE INTERNATIONAL METEOROLOGICAL INSTITUTE IN STOCKHOLM

Recent advances in polar low research: current knowledge, challenges and future perspectives

By MARTA MORENO-IBÁÑEZ[1,2], RENÉ LAPRISE[1,2], and PHILIPPE GACHON[1,3], [1]*Centre for the Study and Simulation of Regional-Scale Climate (ESCER), University of Quebec in Montreal (UQAM), Montreal, QC, Canada;* [2]*Department of Earth and Atmospheric Sciences, University of Quebec in Montreal (UQAM), Montreal, QC, Canada;* [3]*Department of Geography, University of Quebec in Montreal (UQAM), Montreal, QC, Canada*

(Manuscript Received 22 December 2020; in final form 11 February 2021)

ABSTRACT

Polar lows (PLs) are high-latitude intense maritime mesoscale weather systems that develop over open water near the sea ice margin or near snow-covered continents during cold air outbreaks. PLs pose a threat to coastal and island communities, transportation and offshore drilling platforms. PLs mainly develop during the cold season and their frequency exhibits a large interannual variability. Observations from polar-orbiting satellites are the main source of observational data to study PLs since conventional observations are sparse and unevenly distributed in high latitudes. PL forecasting has long remained a challenge due to the small size and short lifetime of these systems. Nevertheless, the representation of PLs in numerical models has significantly improved with the advent of high-resolution atmospheric models. Several studies have shown that baroclinic instability and convection play an important role in the development of PLs, but a thorough understanding of the physical mechanisms involved in the formation and intensification of PLs is yet to be developed. The relevant role of surface sensible heat flux and latent heat release in PL development has often been highlighted. The diabatic fluxes from the oceanic surface and associated with PLs can cause a decrease in the sea surface temperature (SST), whereas the strong wind speeds can lead to upper-ocean mixing in regions where an ocean temperature inversion is present. It is expected that global warming associated with anthropogenic climate changes may lead to an increase in the static stability of the atmosphere, thus affecting the climatology of PLs. In the North Atlantic the regions of PL activity will shift northwards as seasonal sea-ice margins migrate towards higher latitudes areas, and the frequency of PLs will decrease. Although our knowledge about PLs has significantly increased during the last decades, the are still many unanswered questions. Among the most pressing issues in PL research are the need to determine the objective criteria that define PLs and to devise an international intercomparison project of PL detection and tracking.

Keywords: polar low, severe weather, marine cold air outbreak, Arctic, Antarctic

1. Introduction

Polar lows (PLs) are high-latitude intense maritime mesoscale weather systems with lifetime ranging from three to 36 hours (Renfrew, 2003). They mainly develop over open water near the sea-ice edge and near the snow-covered continents during marine cold air outbreaks (MCAOs). The fact that MCAOs tend to be more intense in the Northern Hemisphere than in the Southern Hemisphere (Fletcher et al., 2016) probably explains why PLs are more intense in the Northern Hemisphere (Stoll et al., 2018). PLs are associated with severe weather such as gale-force winds that can reach hurricane force ($\geq$33 m s^{-1}), and heavy snow showers or intense blizzard events. Consequently, they pose a threat to coastal and island communities, marine and air transportation, and offshore platforms in subarctic and Arctic regions. The harsh weather associated with PLs has long been endured by sailors and coastal populations living at high latitudes. Among other impacts, PLs have likely caused the loss of a large number of small vessels (Turner et al., 2003) and cases of PLs having caused the loss of human life have been documented. On 28 December 1986, following a derailment of a train on the Amarube Bridge in western Honsu, in Japan, due to strong winds associated with a PL, six persons deceased and six

*Corresponding author e-mail: marta.moreno-ibanez@outlook.com

Citation: Tellus A: 2021, **73**, 1890412, https://doi.org/10.1080/16000870.2021.1890412

others were injured (Yanase et al., 2016). On 31 October 2001, the storm Torsvåg rapidly intensified over the island Vannøya, in Norway, causing the capsize of a small boat and the subsequent death of one of the crew members (Norwegian Meteorological Institute, 2013). While PLs do not always cause such severe consequences, they often have an impact on the normal operations of the affected regions. PLs not only have important effects as high-impact meteorological phenomena, but also play a role as actors of the climate system; the strong surface sensible and latent heat fluxes from the ocean surface associated with PLs (e.g., Gachon et al., 2003) can in the long term act as forcing on the thermohaline circulation (Condron and Renfrew, 2013).

For a long time, the origin of PLs was elusive. The incipiency of polar-orbiting satellite imagery in the 1960s facilitated the advancement in the knowledge of PLs (Turner et al., 2003). Notwithstanding the large number of studies about PLs, a comprehensive and complete physical understanding of these systems is still lacking. The main challenges in the study PLs are the lack of a universally accepted definition of PLs and the fact that atmospheric models and reanalyses do not always succeed at representing observed PLs. Consequently, their spatio-temporal distribution and the physical development mechanisms involved are not well understood yet.

This review article is motivated by the need to provide an updated review of the state of knowledge of PLs since the last comprehensive review, the book 'Polar Lows: Mesoscale Weather Systems in the Polar Regions' edited by Rasmussen and Turner (2003), was published almost twenty years ago. Moreover, during the 13th Polar Low Workshop, in 2016, the scientific community agreed that a new review article on PLs was needed due to the advancement of the field since the last review (Spengler et al., 2017). The publication of this review article also fits well within the current research themes of the Polar Prediction Project (PPP, Jung et al., 2016). The PPP, which spans from 2013 to 2022, was devised in the framework of the World Weather Research Programme of the World Meteorological Organization with the aim of promoting international cooperation in the domain of weather forecasting in the polar regions. Several studies of PLs have been published in the context of the Year of Polar Prediction (YOPP), a key activity of the PPP that consisted in the organisation of an intensive period of observation, modelling, verification and other activities.

This review is organised in seven sections. The next section describes the main characteristics of PLs and their climatology. The third section provides an overview of the main observational data used in PL studies, including conventional and satellite observations. The fourth section describes the main advances and current challenges in the numerical representation of PLs. The fifth section presents the different mechanisms of formation and intensification of PLs. The sixth section describes the impact of PLs on the ocean and how climate change will affect the climatology of PLs. The last section focuses on the challenges and futures perspectives of PL research.

2. Characteristics of PLs

2.1. Definition

PLs are part of the wider family of polar mesoscale cyclones (PMCs), which are defined by the European Polar Low Working Group (EPLWG) as 'meso-α and meso-β-scale cyclonic vortices poleward of the main polar front' (Heinemann and Claud, 1997), where the meso-α and meso-β scales correspond to $200-2{,}000$ km and $20-200$ km, respectively, according to Orlanski (1975). PLs are defined by the EPLWG as maritime PMCs whose horizontal scale does not exceed 1,000 km and which are associated with near-surface wind speeds of more than 15 m s^{-1} (Heinemann and Claud, 1997). Another definition that has been widely used in the literature is that of Turner et al. (2003):

'A polar low is a small, but fairly intense maritime cyclone that forms poleward of the main baroclinic zone (the polar front or other major baroclinic zone). The horizontal scale of the polar low is approximately between 200 and 1,000 kilometres and surface winds near or above gale force.'

A few authors have suggested a classification of PLs in different types based on the synoptic environment where they form and their development mechanisms. Businger and Reed (1989) classified PLs in short-wave/jet-streak type, Arctic front type, cold-low type, and a combination of these three. The cold-low type included the meteorological systems known as 'Mediterranean hurricanes' or 'medicanes', which resemble hurricanes. Medicanes share in common with some PLs a spiraliform cloud signature and a warm core (Romero and Emanuel, 2017). PLs are now considered as distinct from medicanes, in particular because PLs forms over cold arctic and sub-artic environments, which is not the case for Mediterranean hurricanes, although they share some common characteristics with them. Both of them are relatively small-scale cyclones, and they develop in an environment with a large temperature contrast between the ocean surface and the atmosphere. Surface heat fluxes from the ocean and latent heat release play an important role in the development of both medicanes and PLs. Nevertheless, whereas the formation of medicanes requires the presence of an upper cut-off low with a cold core and large vertical extent, as well as important temperature contrast between the ocean surface and the atmosphere, the mechanisms of

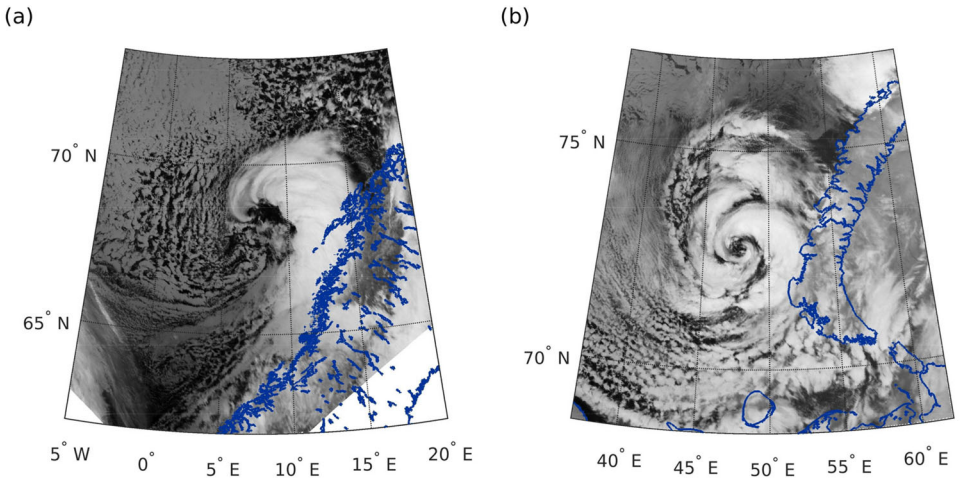

Fig. 1. IR satellite images of two PLs with different cloud signatures: (a) Comma-shaped PL over the Norwegian Sea on 25 March 2019 (image from AVHRR channel 4) and (b) Spiraliform PL over the Barents Sea on 20 December 2002 (image from MODIS spectral band 31).

PL genesis are more varied. Unlike PLs, medicanes peak season is autumn and early winter. With an average of two medicanes per year, these systems are much rarer than PLs (Romero and Emanuel, 2017). Rasmussen et al. (2003b) suggested a more detailed classification by dividing PLs into the following groups: reverse shear systems, trough systems, boundary-layer front, cold lows, comma clouds, baroclinic wave-forward shear and orographic PLs. Based on their cloud signature, PLs can be divided into spiraliform and comma-shaped (Fig. 1). However, the cloud signature of PLs can change from one type to another during their lifetime (e.g., Fu et al., 2004). Although in the past researchers thought spiraliform and comma-shaped clouds had clearly different genesis mechanisms, it has been shown that these differences are not clear-cut (Carleton and Carpenter, 1990). There are some differences between spiraliform and comma-shaped PLs though. Comma-shaped PLs have higher cloud tops than spiraliform PLs, and spiraliform PLs are characterised by much larger ice water content (IWC) and larger effective radius in the upper region of the cloud compared to comma-shaped PLs (Listowski et al., 2020).

2.2. Main characteristics

The definition of PLs by the EPLWG and by Turner et al. (2003) do not always suffice to classify a given cyclone as a PL. One of the main challenges to detect and track PLs in reanalyses and atmospheric models is to determine the objective characteristics that allow the identification of PLs. In effect, the number of detected PLs is rather sensitive to the choice of parameters (e.g., Yanase et al., 2016). The main criteria that have been used to differentiate PLs from other type of cyclones are based on their size, intensity, lifetime and trajectory, as well as the static stability of the atmospheric region where they develop. Following Turner et al. (2003), many authors consider that the diameter of PLs ranges between 200 km and 1,000 km (e.g., Stoll et al., 2018). Other authors, however, consider that PLs have no minimum size (e.g., Blechschmidt, 2008), and some consider that their maximum diameter is 500 km (e.g., Wilhelmsen, 1985). The intensity criterion is often based on the maximum near-surface wind speed or the maximum vorticity at 850 hPa. Among the thresholds used, 13.9 m s^{-1} (e.g., Chen and von Storch, 2013) and 15 m s^{-1} (e.g., Yanase et al., 2016) were used for the near-surface wind speed, and 6×10^{-5} s^{-1} (Zappa et al., 2014; Michel et al., 2018) and 10×10^{-5} s^{-1} (Yanase et al., 2016) for the maximum vorticity at 850 hPa. Although the aforementioned definitions of PLs do not include a minimum lifetime, some researchers have considered a minimum lifetime of 6 hours (Zappa et al., 2014; Yanase et al., 2016), 9 hours (Landgren et al., 2019a), 12 hours (Michel et al., 2018) and even one day (Xia et al., 2012; Pezza et al., 2016) in their PL tracking algorithm. Pezza et al. (2016) also discarded cyclones whose lifetime was longer than 40 hours. Some authors consider that PLs move southwards (e.g., Zappa et al., 2014), but this criterion is too restrictive since in the North Pacific some PLs move zonally (Chen and von Storch, 2013), and in the Nordic Seas a significative number of PLs move westwards and even northwards (Rojo et al., 2015). Finally, given that a great number of PLs form in an atmosphere with low static stability, a criterion often used is the difference between the sea surface temperature (SST) and the temperature at 500 hPa (T_{500}). Most authors require that $SST - T_{500} > 43$ K

to classify a cyclone as a PL (e.g., Xia et al., 2012); however, this threshold excludes a significant number of PLs (Stoll et al., 2018). In effect, the SST – T_{500} criterion allows distinguishing between PLs and extratropical cyclones, but the line between these two types of cyclones is not clear enough (Yanase et al., 2016). In some cases, this criterion excludes PLs that develop in environments characterised by low stability in the lower troposphere but with SST – T_{500} values that do not exceed the 43 K threshold (Radovan et al., 2019). Given the diversity of environments in which PLs develop, the suitability of the SST – T_{500} criterion has recently been questioned on the basis that this criterion could favour classifying certain types of lows, such as those associated with significant convection, as PLs (Spengler et al., 2017). For PL forecasting, the Norwegian Meteorological Institute (MET Norway) uses a threshold of 40 K for the SST – T_{500} criterion (Landgren et al., 2019a).

Many studies have investigated the structure of PLs. The vertical extension of PLs is rather variable, with some PLs being shallow and others having a large vertical extension. For example, Claud et al. (2009) analysed a PL of less than 2 km deep, whereas Føre et al. (2011) studied a PL whose circulation extended up to the tropopause. Using radar and lidar satellite cloud products, Listowski et al. (2020) analysed the clouds of 82 PLs that occurred between 2006 and 2017. They found an average cloud top altitude of 5.7 ± 1.4 km and a maximum cloud top of 9 km. The authors also found a small but statistically significant positive correlation between cloud top and diameter. As for the inner structure of PLs, a great number of case studies have noted the development of a warm core (e.g., Fu et al., 2004; Sergeev et al., 2018), which is caused by adiabatic warming in downdrafts (e.g., Yanase et al., 2004), by warm air seclusion (e.g., Føre and Nordeng, 2012) or by sensible heat fluxes and latent heat release (Gachon et al., 2003). When the warm core is due to adiabatic warming in downdrafts, a cloud-free eye is formed (e.g., Yanase et al., 2004). Regarding the cloud composition of PLs, Listowski et al. (2020) found that in the PL cloud band virtually all the condensed phase was ice, with only 0%–4% being supercooled liquid water, whereas in the eye the supercooled liquid water fraction increased from 20% at roughly 1 km below the cloud top to 60% near the bottom. They also found that the average IWC of PLs increased from $0.02\,\mathrm{g\,m^{-3}}$ at the cloud top to $0.2 - 0.5\,\mathrm{g\,m^{-3}}$ further down.

Based on the current knowledge, the following characteristic scales of PLs emerge. Their horizontal scale is $L = 100$ km and their vertical scale is $H = 1$ km. Their horizontal translation speed scale is $U = 10\,\mathrm{m\,s^{-1}}$, with most PLs between 4 and $13\,\mathrm{m\,s^{-1}}$ (Rojo et al., 2015; Smirnova et al., 2015). Thus, the advective time scale of PLs is $L/U \approx 3$ h. Based on these characteristic scales of PLs, we can determine whether the hydrostatic and geostrophic approximations are appropriate for their study. The validity of the hydrostatic approximation in the study of a meteorological phenomenon depends on the aspect ratio of the system. If $H/L \ll 1$, the acceleration of the vertical speed in pressure coordinates is negligible compared with the vertical gradient of the pressure perturbation (Markowski and Richardson, 2010). For PLs, $H/L = 10^{-2}$, so the hydrostatic approximation is valid when studying the system as a whole. The validity of the geostrophic approximation is determined by the Rossby number $Ro = U/Lf$, where f is the Coriolis parameter. At the latitudes where PLs develop $f \sim 10^{-4}$, so $Ro = 1$, and the geostrophic approximation is not valid for the study of PLs.

2.3. Impacts on oceanic waves

PLs are associated with severe weather such as gale-force winds and heavy snow showers. Despite the relatively small horizontal extent of PLs, their strong winds can lead to the development of high waves due to the effect of the moving fetch on wave growth. If the wave group velocity is similar to the translation speed of the PL, the wave will be within the moving fetch for a long time. This phenomenon is known as 'group velocity quasi-resonance' or 'extended fetch' (Orimolade et al., 2016). Based on conventional observations of 29 PLs that passed over marine stations in the Norwegian and the North Seas, Rojo et al. (2019) found that the maximum significant wave height ranged from 3.2 to 11 m and, on average, the maximum significant wave height was 6.3 m. Orimolade et al. (2016) used a one-dimensional parametric wave model to determine significant wave height associated with 155 PLs. They found that extended wave development was possible in more than 50% (90%) of the PLs if they had an average translation speed of $10\,\mathrm{m\,s^{-1}}$ ($8\,\mathrm{m\,s^{-1}}$). For PLs moving at $8\,\mathrm{m\,s^{-1}}$, the estimated maximum significant wave height was 9.13 m. There has been recorded at least one case of a rogue wave, which is an extreme storm wave, associated with a PL: the Draupner wave that occurred on 1 January 1995 in the North Sea. At the time when the rogue wave developed, the significant wave height of the sea was nearly 12 m. The Draupner wave reached 25.6 m of height (Cavaleri et al., 2016). Multiple PLs seem to generate larger maximum wind speeds and maximum significant wave heights than single PLs, although more data are needed to confirm these extreme wave features (Rojo et al., 2019).

2.4. Climatology

Owing to important differences between the Arctic and Antarctic environments, PLs that develop in the

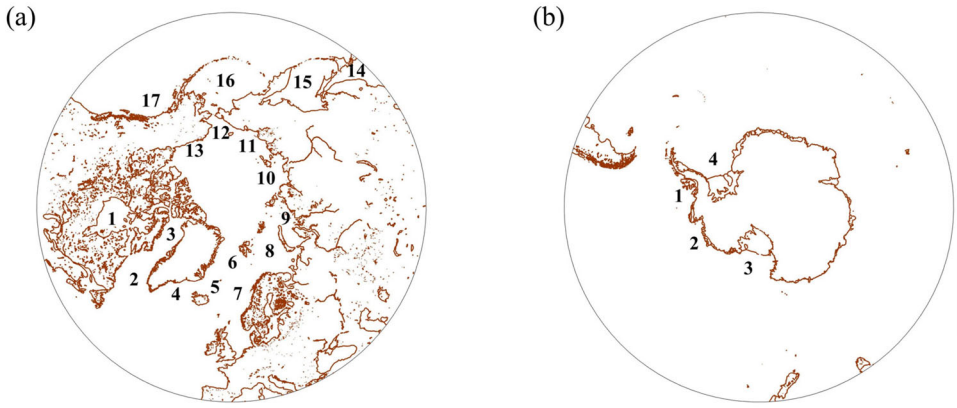

Fig. 2. Map of the marginal seas and other geographical features in the (a) Northern Hemisphere: (1) Hudson Bay, (2) Labrador Sea, (3) Baffin Bay, (4) Irminger Sea, (5) Iceland Sea, (6) Greenland Sea, (7) Norwegian Sea, (8) Barents Sea, (9) Kara Sea, (10) Laptev Sea, (11) East Siberian Sea, (12) Chukchi Sea, (13) Beaufort Sea, (14) Sea of Japan, (15) Sea of Okhotsk, (16) Bering Sea, (17) Gulf of Alaska, and (b) Southern Hemisphere: (1) Bellingshausen Sea, (2) Amundsen Sea, (3) Ross Sea, (4) Weddell Sea.

Northern Hemisphere and in the Southern Hemisphere possess distinctive characteristics, mainly due to major differences in the surface conditions and in the distribution of the continental and water masses (Fig. 2). Given that PLs develop during MCAOs, the climatology of PLs is closely related to their mean and variability features. The climatology of MCAOs has been studied using diverse indexes. The daily variability of the MCAO index depends almost uniquely on the lower troposphere air temperature, with no significant correlation between MCAOs and SST. In the northern North Atlantic and in the southern half of the Southern Hemisphere except for the Pacific Ocean, the seasonal variability of MCAOs is also primarily due to the variance of air temperature (Kolstad et al., 2009; Bracegirdle and Kolstad, 2010). In the southern Pacific Ocean, the seasonal variability of MCAOs is due to the variance of both air temperature and SST (Bracegirdle and Kolstad, 2010). MCAOs are more intense and more frequent in the Northern Hemisphere than in the Southern Hemisphere (Fletcher et al., 2016), mainly due to the presence of cold land masses in the winter months and high surface temperature gradients between the North American or Eurasian continents versus the adjacent seas during the cold season. Therefore, in the Antarctic the difference between the air temperature and the SST near the sea ice margin is smaller than in the Arctic and sub-arctic areas. Furthermore, the flow in the Antarctic is strongly zonal, even though at synoptic time scales the flow can become meridional (Rasmussen et al., 2003a). Although intense MCAOs are less frequent in the Southern Hemisphere, the most intense MCAOs in the Southern Hemisphere are as intense as their counterparts in the Northern hemisphere (Bracegirdle and Kolstad, 2010). Given that MCAOs tend to be more intense in the Arctic, it is not surprising that overall the PLs that develop in the Southern Hemisphere are less intense than Northern Hemisphere ones (Stoll et al., 2018). Southern Hemisphere PLs are also smaller than the Northern Hemisphere ones (Turner et al., 2003).

Before giving a detailed description of the state of knowledge regarding the climatology of PLs, it is appropriate to give a short overview of the climatology studies of PMCs, which include PLs. The research community has developed a large number of climatologies of PMCs in the Northern Hemisphere (e.g. Harold et al., 1999; Michel et al., 2018) and in the Southern Hemisphere (e.g., Carleton and Carpenter, 1990; Verezemskaya et al., 2017). For a long time, the research on PMCs was mainly focussed on the Arctic region since there was a lack of observational data covering a long time period in the Antarctic region (Rasmussen et al., 2003b). As a result, climatology studies of PMCs in the Southern Ocean have been developed relatively recently (Pezza et al., 2016). The identified climatologies have shown that PMCs seem to be ubiquitous phenomena in both hemispheres, whereas PLs are a small portion of PMCs. For instance, in the Southern Ocean, Verezemskaya et al. (2017) found 1,735 PMCs during the austral winter of 2004, whereas Pezza et al. (2016) found 1,127 PLs between 2009 and 2012. In the Northeast Atlantic, two climatologies covering the same time period and a similar region found an average of 2,027 PMCs per year (Harold et al., 1999) and 69 PLs per year (Zahn and von Storch, 2008b). Michel et al. (2018) found just an average of 243 PMCs per winter in the Nordic Seas, but this low number may be explained by the strict lifetime criteria ($\geq$ 12 h) applied to classify a cyclone as a PMC. Most of the PMCs in the Southern Hemisphere have a comma-

Table 1. Information about climatology studies of PLs developed using a subjective tracking method.

Author/s	Data used to identify PLs	Region	Period	Months
Wilhelmsen (1985)	Synoptic charts, conventional observations	Nordic Seas	1978–1982	All
Ese et al. (1988)	Synoptic charts	Norwegian and Barents Seas	1971–1983	All
Blechschmidt (2008)	IR imagery from AVHRR, wind speed from HOAPS	Nordic Seas	2004–2005	All
Noer et al. (2011)	MET-Norway PL list, IR imagery from AVHRR, wind speed from ASCAT and QuikSCAT, conventional observations	Nordic Seas	2000–2009	All
Rojo et al. (2015)	MET-Norway PL list, IR imagery from AVHRR	Nordic Seas	1999–2013	Oct.–Apr.
Smirnova et al. (2015)	Total water vapour and sea surface wind speed from SSM/I, IR imagery from AVHRR	Nordic Seas	1995–2009	Sep.–Apr.
Verezemskaya et al. (2017)	IR and water vapour satellite mosaics, wind speed from QuikSCAT	Southern Ocean	2004	June–Sept.

Only the data used to identify PLs is listed, even though some authors also used reanalyses to study the large-scale circulation associated with PL development.

shaped cloud signature (Carleton and Carpenter, 1990; Verezemskaya et al., 2017), which is at variance with the findings of Harold et al. (1999) that only a little over half of the PMCs in the Nordic Seas had a comma-shaped signature, the rest being spiraliform.

The climatologies of PLs provide an overview of the spatio-temporal distribution of PLs, even though there is still a lack of agreement regarding certain details such as PL frequency. These disagreements are due to a different selection of PL identification criteria, type of methodology used, and region and time period covered. Some researchers have used a subjective detection and tracking method to analyse the spatio-temporal distribution of PLs (Table 1), whereas others have used an objective method (Table 2). Bracegirdle and Gray (2008) have used a combination of a subjective and objective methods. Breakthroughs in computer science, especially in the domain of machine learning, have opened new possibilities for the detection and tracking of PLs. Recently Krinitskiy et al. (2018) have applied deep convolutional neural networks to detect the cloud signature of PMCs in the Southern Ocean, with promising results. The main challenges of using this method are the high computation cost and amount of time needed to train these neural networks and to optimise the hyperparameters.

Stoll et al. (2018) were the first to obtain a global climatology of PLs (Fig. 3). They applied a storm tracking algorithm to ERA-Interim (ERA-I, Dee et al., 2011) and the Arctic System Reanalysis (ASR, Bromwich et al., 2018), covering the periods 1979 – 2016 and 2000 – 2012, respectively, and compared their results to lists of PLs detected with a subjective method. In both hemispheres, they found that PLs mainly develop during the cold season, this season being longer in the Southern Hemisphere (from April to October) than in the Northern Hemisphere (from November to March). Given the link between MCAOs and the development of PLs, these results seem coherent with the fact that between latitudes 55°N and 75°N, MCAOs are more frequent in winter and in autumn, and almost inexistent during summer, whereas between latitudes 55°S and 75°S the annual cycle of MCAOs is somewhat weak and the MCAOs can also occur in summer (Fletcher et al., 2016). The study of Stoll et al. (2018) also found that the Northern Hemisphere shows a maximum in the occurrence of PLs in January, when the temperature of the air masses over the North American and Eurasian continents reach the coldest values of the year (Serreze and Barry, 2014). In both hemispheres, the interannual variability of the PL activity is high. As for their location, PLs develop in the Northern Hemisphere down to latitudes of 40°N and 50°N in the North Pacific and the North Atlantic, respectively, and in the Southern Hemisphere up to latitudes of 50°S – 60°S (Stoll et al., 2018). This geographical distribution is related with the main features of the seasonal sea-ice margins.

2.4.1. Northern hemisphere. PL activity is higher in the North Atlantic than in the North Pacific (Stoll et al., 2018; Fig. 3). In the North Atlantic, PLs form in the Nordic Seas[1] (e.g., Føre et al., 2011; Wu, 2021), the Denmark Strait (e.g., Kristjánsson et al., 2011b), the Labrador Sea (e.g., Moore and Vachon, 2002), the Davis

Table 2. Information about climatology studies of PLs developed using an objective tracking method applied to reanalysis data or simulated variables.

Author/s	Dataset/Model	Region	Period	Months
Zahn and von Storch (2008a)	COSMO-CLM	North Atlantic	1948–2006	All
Zahn and von Storch (2008b)	COSMO-CLM	North Atlantic	1993–1995	All
Chen and von Storch (2013)	COSMO-CLM	North Pacific	1948–2010	Oct.–Apr.
Yanase et al. (2016)	JRA-55	Sea of Japan	1979–2015	Oct.–Mar.
Pezza et al. (2016)	ERA-I	Southern Hemisphere	2009–2012	All
	AMPS			
Stoll et al. (2018)	ERA-I	Global	1979 – 2016	All
	ASRv2	Northern Hemisphere	2000–2012	
Michel et al. (2018)	ERA-I	Nordic Seas	1979–2014	Oct.–Apr.

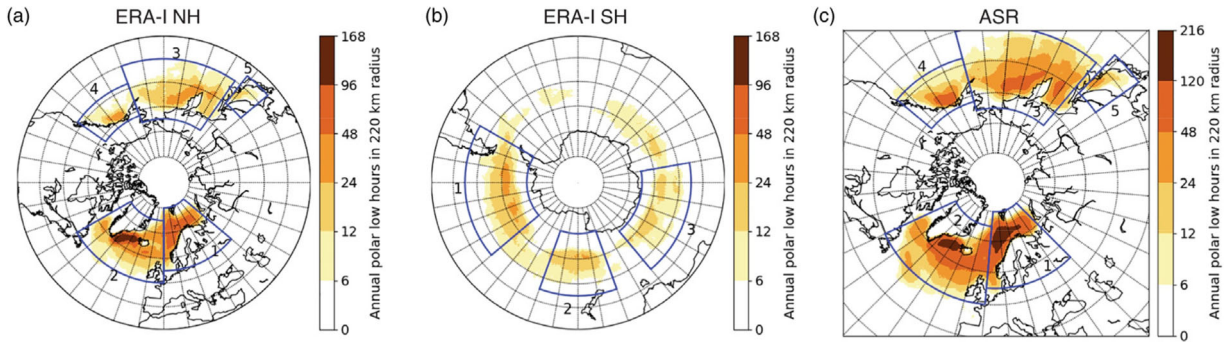

Fig. 3. Geographic distribution of PLs in the (a, c) Northern Hemisphere and (b) Southern Hemisphere, obtained applying an objective tracking algorithm to (a, b) ERA-I and (c) ASR reanalyses. The colour represents the annual average of PL duration within a radius of 220 km, which is calculated by multiplying the number of detected PL points by the temporal resolution of the reanalysis. From Stoll et al. (2018). © 2018 Royal Meteorological Society.

Strait (e.g., Roch et al., 1991) and the Hudson Bay (e.g., Gachon et al., 2003). In the North Pacific, PLs mainly form over the Sea of Okhotsk, the Sea of Japan (e.g., Fu et al., 2004), the Bering Sea and the Gulf of Alaska (e.g., Businger, 1987). PLs seldom develop over the marginal seas around the Arctic Ocean (Turner and Rasmussen, 2003); for instance, a PL has been observed in the Chukchi Sea (Inoue et al., 2010) and in the Kara Sea (Verezemskaya and Stepanenko, 2016) in the beginning of the PL season.

The best studied region is the Nordic Seas, where most PLs develop between September and May (Wilhelmsen, 1985; Ese et al., 1988; Blechschmidt, 2008; Bracegirdle and Gray, 2008; Zahn and von Storch, 2008a; Noer et al., 2011; Rojo et al., 2015). When looking at the monthly frequency of PLs, several authors have noted a minimum in February (e.g., Wilhelmsen, 1985), which seems to be associated with the presence of an anticyclone over Scandinavia (Noer et al., 2011). Nevertheless, some authors have found that the minimum of PL activity in February is not significant (e.g., Smirnova et al., 2015) or does not exist at all (Blechschmidt, 2008; Zahn and von Storch, 2008a). The annual frequency of PLs varies greatly depending on the study. For instance, applying a subjective detection method, Smirnova et al. (2015) found an average of 45 PLs per year for the period between 1995 and 2009 in the Nordic Seas, whereas Noer et al. (2011) found an average of 12 PLs per year for the period between 2000 and 2009 in the Nordic Seas. What seems clear is that PL frequency exhibits a large interannual variability (e.g., Zahn and von Storch, 2010).

Studies of PLs in the Nordic Seas show that PLs develop near the sea ice margin (e.g., Harold et al., 1999) and in regions where SST is relatively high, particularly where the Norwegian Atlantic Current is found (Noer et al., 2011; Rojo et al., 2015). The regions where this current converges with the West Spitsbergen Current and the Barents Sea are particularly favourable for the formation of PLs (Rojo et al., 2015). In effect, these regions are characterised by a high MCAO index, which means that the atmospheric static stability is low (Kolstad et al., 2009). Thus, PL genesis occurs mainly between Iceland and the Finnmark county, in Norway, and over the Barents Sea (e.g., Wilhelmsen, 1985). PLs also form between the South of Greenland and Iceland (Blechschmidt, 2008) in the Irminger sea, which is

another region with a high MCAO index (Kolstad et al., 2009) where the presence of high elevated terrain from the Greenland ice-sheet strongly affects the low-level flow (Doyle and Shapiro, 1999). Synoptic conditions favourable for PL formation are the presence of northerly winds (e.g., Businger, 1985), north-westerly winds over the Greenland sea (Mallet et al., 2013) and north-easterly winds over the Barents Sea (Ese et al., 1988; Noer et al., 2011). Most PLs move southwards (Wilhelmsen, 1985; Blechschmidt, 2008; Rojo et al., 2015), but some move eastwards, westwards at even northwards (Rojo et al., 2015). Regarding the characteristics of PLs, different studies obtain somewhat differing results. For instance, the typical diameter and lifetime of PLs are respectively 300 km and 15 h according to Blechschmidt (2008), 350 km and 6 – 30 h according to Rojo et al. (2015), and 200 – 400 km and 9 – 18 h according to Smirnova and Golubkin (2017). The diameter of most PLs does not exceed 500 km (Smirnova et al., 2015), and few among them have a lifetime exceeding two days (Blechschmidt, 2008; Rojo et al., 2015). The steering level wind, which is the wind that dictates the translation direction of PLs, is located at 850 hPa (Rojo et al., 2015). With a characteristic propagation speed ranging from 4 to 13 m s^{-1} (Rojo et al., 2015; Smirnova et al., 2015), most of them travel a distance of less than 1,000 km (Rojo et al., 2015). Regarding the weather conditions associated with PLs, Rojo et al. (2019) analysed conventional observations of 29 PLs developed over the Norwegian Sea and the North Sea between 1999 and 2013 to obtain their associated maximum wind speeds and associated maximum significant wave heights. They found that the maximum wind speed associated with the PLs ranged from 7 to 31 m s^{-1} and, on average, the maximum wind speed was 17.1 m s^{-1}. They also found that, on average, large PLs are associated with higher maximum wind speed and higher maximum significant wave height than small PLs, and that fast-moving PLs are associated with higher maximum wind speed and higher maximum significant wave height than slow-moving PLs.

Some researchers have analysed the large-scale circulation patterns that are present during PL formation and intensification, in particular during wintertime weather patterns over the North Atlantic-Europe area (e.g., Mallet et al., 2013). In general, large-scale patterns leading to MCAOs are favourable for PL development. Blechschmidt et al. (2009) analysed the large-scale patterns associated with PL development in the Northeast Atlantic. They found that the large-scale circulation pattern associated with PL development over the Barents Sea is characterised by a low mean sea level pressure (MSLP) anomaly over the Barents Sea and a high MSLP anomaly over Iceland that tilts westwards with height. As for the Norwegian, Iceland and Greenland Seas, the large-scale circulation pattern associated with PL development consists of a low MSLP anomaly over the Norwegian Sea and a ridge anomaly over Greenland and the Irminger Sea. The large-scale circulation pattern associated with the PLs that develop in the region between South Greenland and Iceland is characterised by a low MSLP anomaly east of Iceland that tilts westwards with height. These large-scale circulation patterns associated with PLs over the Nordic Seas and over the region between South Greenland and Iceland are similar, albeit somewhat shifted, to the respective patterns found during winter MCAOs in those regions (Kolstad et al., 2009).

Since PL development is related to specific large-scale circulation patterns, some studies have analysed the link between PLs and low-frequency variability patterns (Claud et al., 2007) or weather regimes (Mallet et al., 2013). The formation of PLs can be associated with North Atlantic weather regimes because the synoptic-scale anomalies that favour their development often have the same duration as those weather regimes. In the Norwegian Sea and the Barents Sea, PLs mainly develop during the Atlantic Ridge regime and the negative phase regime of the NAO (Mallet et al., 2013). This is in agreement with the small negative correlation between the annual wintertime MCAO index and the NAO index in the Barents Sea found by Kolstad et al. (2009). These authors did not find a significant correlation between the annual wintertime NAO index and the MCAO in the region comprising the Norwegian, Iceland and Greenland Seas. In the Labrador Sea, PLs primarily develop during the positive phase of the NAO and are virtually absent during its negative phase (Mallet et al., 2013), in agreement with the positive correlation between the annual wintertime MCAO index and the NAO index in the Labrador and the Irminger Seas (Kolstad et al., 2009). The positive phase of the NAO is not only associated with significantly low temperatures at 500 hPa, but also with northerly to westerly winds over the Labrador Sea and east of Canada, which are favourable for PL formation (Claud et al., 2007).

Another region that has received the attention of the scientific community is the North Pacific. Similarly to the Nordic Seas, most PLs develop during winter and their frequency is characterised by a high interannual variability (Chen and von Storch, 2013; Yanase et al., 2016). PLs are most frequent in the Western North Pacific. Specifically, they are most often found east of Japan, as well as in the Gulf of Alaska (Chen and von Storch, 2013). In the Japan Sea, PLs develop mainly west of Hokkaido, halfway between the Asian continent and Japan, and east of the North Korean coast. The PLs that develop over the Sea of Japan tend to move towards a

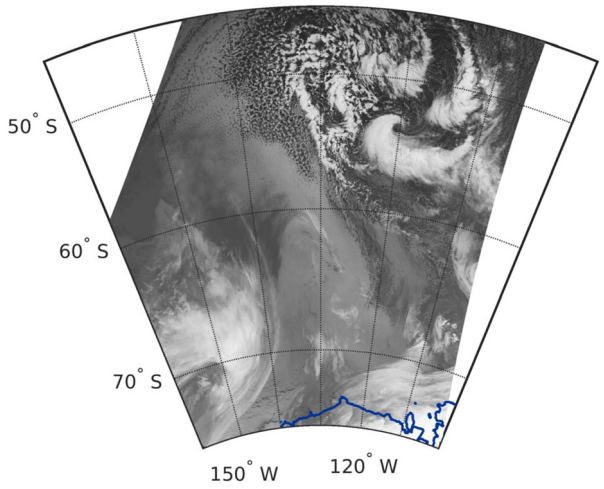

Fig. 4. AVHRR channel 4 image of a comma-shaped PL over the South Pacific Ocean on 14 July 2019.

direction somewhere in between the south and the east, and they reach their maximum intensity west of Japan. The steering level wind of the PLs that move southwards is located in the lower troposphere where north-westerly winds prevail, associated with synoptic cyclones and the winter Asian monsoon, whereas the steering level wind of eastward moving PLs is located in the mid-troposphere where mid-latitude westerly winds are present. The propagation speed of PLs that move eastwards is higher than that of the PLs that move southwards (Yanase et al., 2016). Regarding the frequency of PLs in the region, Chen and von Storch (2013) found an average of 172 PLs per cold season in the North Pacific and Yanase et al. (2016) found an average of 6.8 PLs per cold season over the Sea of Japan.

2.4.2. Southern hemisphere. In the Southern Hemisphere, PLs are more frequent during the winter season, although they are relatively frequent in autumn and spring, and a few develop in summer (Pezza et al., 2016). PLs mainly develop over the Bellingshausen Sea and along the eastern East Antarctica marginal ice zone (Verezemskaya et al., 2017; Stoll et al., 2018) as well as over the Amundsen Sea and the Southern Sea south of New Zealand (Stoll et al., 2018; Fig. 3). There is high PL occurrence along the Antarctic sea ice margin, which is likely due to the combined effect of katabatic winds and MCAOs (Verezemskaya et al., 2017). In effect, the mean MCAO index in winter has large values near the Antarctic sea ice edge (Bracegirdle and Kolstad, 2010). Although PLs are more frequent near the sea ice edge, they can also develop at lower latitudes (e.g. Fig. 4). Despite the fact that, on average, PMCs move south-eastwards, roughly 30% of PLs that develop in winter move northwards. Explosive PLs are rare, constituting less than 1% of PLs (Pezza et al., 2016).

3. Observational data used in PL studies

3.1. Conventional observations and field campaigns

In the polar regions, surface observations are sparse and unevenly distributed in space. Most stations are concentrated in the more populated land regions, and they are mainly located along the coast (Casati et al., 2017). Therefore, the number of surface observations available for the study of PLs is limited. Surface observations from land meteorological stations have been used to study PLs affecting Norway (e.g., Hallerstig et al., 2021), Iceland (Kristjánsson et al., 2011b) and Japan (Fu et al., 2004), as well as more isolated regions such as the Hudson Bay (Albright et al., 1995; Gachon et al., 2003) and Kamchatka (Businger, 1987). Although upper-air stations are particularly sparse in high latitudes and the observation frequency is much lower than that of surface stations, these type of observations have also been used to study PLs (e.g., Kristjánsson et al., 2011b). Observations from maritime stations provide not only atmospheric variables such as MSLP, wind speed and temperature, but also SST and significant wave height associated with PLs (e.g., Rojo et al., 2019).

The most valuable source of PL observations are observational fields campaigns. Unfortunately, observational campaigns for the study of PLs using airborne instruments are rare, the first such campaign taking place in 1984 during the Norwegian Polar Low Project. Observational data of PLs have also been obtained by research flights during the Alaska Storms Program in 1987 and the Coordinated Eastern Arctic Experiment in 1989. The first time that low-level flights where performed in a region where a PL developed was during the Lofoten cyclone (LOFZY) field campaign in 2005 (Kristjánsson et al., 2011a). As part of the campaign, 21 drifting buoys, a research vessel and the research aircraft Falcon were deployed. The LOFZY campaign provided observations of two PLs that developed on 7 March 2005. The aircraft took measurements down to 30 m, which enabled the computation of surface sensible heat and moisture fluxes (Brümmer et al., 2009). A few years later, as part of the Norwegian International Polar Year (IPY) Observing System Research and Predictability Experiment (THORPEX, Kristjánsson et al., 2011a), a field campaign took place from 25 February to 17 March 2008. The main observational platform was the research aircraft Falcon that was equipped with probes for the *in situ* measurement of atmospheric turbulent fluctuations, a Doppler wind lidar, a Differential Absorption Lidar and

dropsondes. This campaign provided valuable observations of two PLs that developed on 3 – 4 March and on 16 – 17 March 2008, which were observed during three flights and one flight, respectively. The short-range forecast of the first PL was good, whereas the forecast of the second one was quite poor (Kristjánsson et al., 2011a). The PL that developed in the beginning of March is probably the most studied PL in the scientific literature (Linders and Saetra, 2010; Aspelien et al., 2011; Føre et al., 2011; Irvine et al., 2011; McInnes et al., 2011; Wagner et al., 2011; Føre and Nordeng, 2012; Stoll et al., 2020). The observations from the IPY-THORPEX campaign have also been used to evaluate simulations of a low-pressure system that developed during the IPY-THORPEX campaign but, despite the conditions being favourable for PL development, did not become a PL (Adakudlu and Barstad, 2011). More recently, the Aerosol–Cloud Coupling And Climate Interactions in the Arctic (ACCACIA) field campaign in March and April 2013 provided airborne and dropsonde observations of a PL developed on 26 March 2013 over the Norwegian Sea (Sergeev et al., 2017).

3.2. Remote sensing observations

Polar-orbiting satellite observations are the main source of observational data in high latitudes, particularly over the ocean. Products derived from the observations of passive instruments have proved very useful to study PLs. One of the satellite products that have been most widely used in PL research are Infra-Red (IR) satellite images, mostly IR calibrated radiances from the Advanced Very High Resolution Radiometer (AVHRR, e.g. Figs. 1a and 4) and from the Moderate Resolution Imaging Spectroradiometer (MODIS, e.g. Fig. 1b). Since the cloud signature of PLs can be identified in IR satellite images, these images have been often used to develop climatologies of PLs using a subjective tracking method (e.g., Rojo et al., 2015), to verify simulations (e.g., Sergeev et al., 2017) or simply to show the cloud signature of observed PLs (e.g., Furevik et al., 2015). More recently, Krinitskiy et al. (2018) have used IR satellite images as input for deep convolutional neural networks to detect PMCs. Products derived from the observations of microwave imagers and sounders have also been used in PL research. Microwaves penetrate through clouds and are only sensitive to clouds constituted by large ice particles; therefore, PLs associated with convective cells can be detected using satellite passive microwave radiometers (Claud et al., 2009). The Special Sensor Microwave Imager (SSM/I) products that have been used to study PLs are integrated water vapour (e.g., Smirnova et al., 2015) and surface wind speed (e.g., Martin and Moore, 2006). The Advanced Microwave Sounding Unit - A (AMSU-A), which is a microwave temperature sounder, has been used to analyse the large-scale temperature field during PL development (Claud et al., 2009) and the warm core of a PL (Moore and Vonder Haar, 2003). The Advanced Microwave Sounding Unit - B (AMSU-B), which is a microwave humidity sounder, has been used to detect PLs whose development is mainly driven by convection since the scattering by large ice particles leads to low brightness temperature (Claud et al., 2009).

Products derived from the observations of active instruments have also been commonly used to study PLs. Scatterometers are undoubtedly one of the most valuable instruments to obtain information about the ocean surface wind field associated with PLs. Unfortunately, the current horizontal resolution of scatterometers is not high enough to capture strong wind gradients, and their temporal resolution is too low to capture the evolution of cyclones that evolve quickly (Bourassa et al., 2013). The main ocean surface wind products that have been used in PL research are those derived from the observations of SeaWinds scatterometer on board the QuikSCAT satellite (e.g., Kolstad and Bracegirdle, 2017) and the Advanced Scatterometer (ASCAT) (e.g., Furevik et al., 2015; see also Fig. 5). Ocean surface winds can also be derived from the observations of synthetic aperture radars (SARs), which have higher spatial resolution but smaller temporal resolution than scatterometer wind products. However, no SAR wind product is directly available (Furevik et al., 2015), at least at a global scale. As a result, SAR data has been used by a few researchers to obtain high-resolution data of the wind field associated with PLs (e.g., Martin and Moore, 2006) and to analyse the structure of convective cells (Hallerstig et al., 2021). The Cloud Profiling Radar, on board CloudSat, together with the Cloud-Aerosol Lidar with Orthogonal Polarisation, on board CALIPSO, have proven useful to obtain data about PL clouds such as the IWC, the liquid water content (LWC) and the cloud top height (e.g., Listowski et al., 2020). Forsythe and Haynes (2015) estimated that CloudSat/CALIPSO could capture an average of five PLs per year during the day.

Although less common, ground-based remote sensing is also a valuable source of PL observations. Ground-based weather radars provide reflectivity and reflectivity-inferred precipitation estimate data that allows the analysis of the precipitation field associated with PLs (e.g., Fu et al., 2004; see also Fig. 6). The infrasound signals detected in infrasound stations can be used to detect PLs since some of the processes associated with the development of the PL, such as convective turbulence, are among the possible sources an infrasound signal. However, for an infrasound signal to be detected, the environmental conditions need to be favourable for its propagation (Claud et al., 2017).

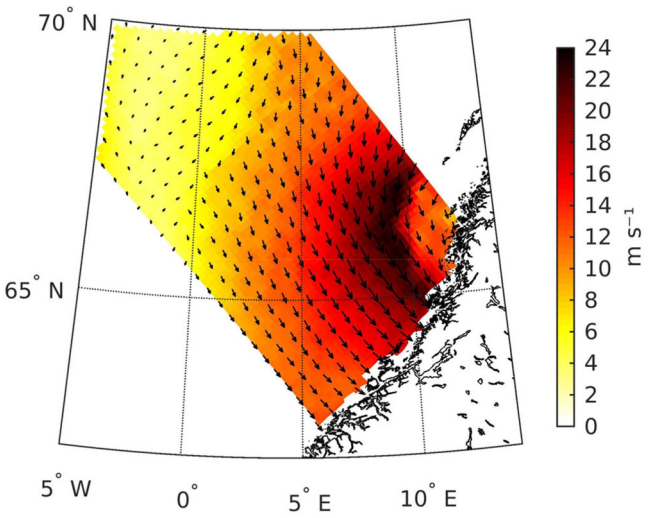

Fig. 5. Ocean surface wind speed (colour shading) and direction (arrows) derived from the observations of ASCAT on the 25 March 2019 at 18:40 UTC, when a PL (see Fig. 1a) was dissipating over the Norwegian coast.

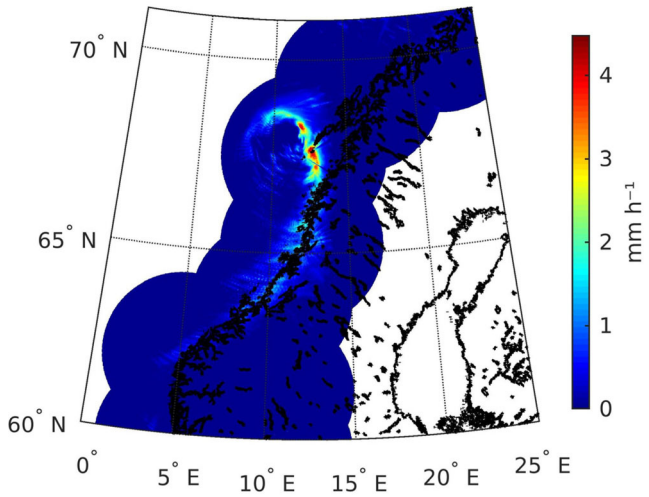

Fig. 6. Multi-radar mosaic of liquid water equivalent precipitation rate associated with a PL (see Fig. 1a) on 25 March 2019 at 15:00 UTC.

4. Numerical representation of PLs

In general, the performance of numerical weather prediction models over the polar regions is not very good due to, among other things, the lack of conventional observational data and an underperforming data assimilation. As a result, models do not correctly represent certain phenomena such as stable planetary boundary layers and thin clouds (Jung et al., 2016). For the simulation of PLs, compounding the challenge is the fact that PLs are small and short-lived systems.

The comparisons of simulation output against analyses, reanalyses and observations is a necessary step to evaluate the skill of the models at reproducing observed PLs. Given that forecast verification against analyses is not adequate in the polar regions due to the strong influence that the model exerts on the analysis (Jung et al., 2016), satellite observations have been often used to verify the simulation of PLs. Unfortunately, the lack of high-resolution and high-quality observational data makes it difficult to evaluate convection-permitting models (Prein et al., 2017), which are the main atmospheric models used to simulate PLs. The type of method that has been the most used to verify PL simulations against observations is visual verification (e.g., Sergeev et al., 2017). To the best of our knowledge, Stoll et al. (2020) have been the first authors to use a spatial verification

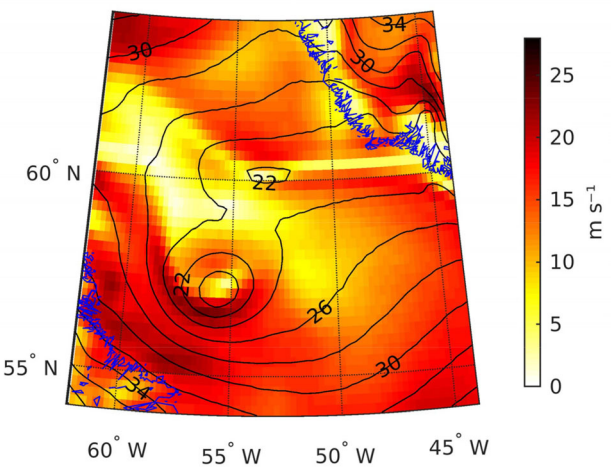

Fig. 7. Geopotential height (contour lines) and wind speed (colour shading) at 950 hPa on 8 March 2019 at 06:00 UTC from ERA5. The contour lines are drawn every 4 dam and the wind speed is in m s^{-1}. The geopotential height and wind fields show a PL over the Labrador Sea.

method to verify the simulations of an observed PL using a limited-area and a global atmospheric models. More specifically, they applied a 'fuzzy' verification method to verify their simulations against dropsonde observations. The results with the fuzzy verification technique showed that the limited-area model had better skill at simulating extreme values at small scales at the analysis time than the global model, whereas the standard verification statistics did not show this advantage of the limited-area model over the global one.

4.1. Reanalyses

The advances in global reanalyses, including the increase in resolution, has allowed a better representation of PLs. For instance, Laffineur et al. (2014) have shown that the ERA-I reanalysis with a grid mesh of 0.75° captures more PLs than the ERA-40 reanalysis (Uppala et al., 2005) with a grid mesh of 1.25°. Nevertheless, there are still some challenges in the representation of PLs in reanalyses, one of them being the correct representation of near-surface wind speeds. A large number of PLs are not captured by ERA-I since it underestimates near-surface wind speeds (Laffineur et al., 2014; Zappa et al., 2014); therefore, selecting a value of 15 m s^{-1} as threshold for the wind speed criterion, used to classify a cyclone detected in ERA-I as PL, excludes a significant number of PLs (Stoll et al., 2018). The underestimation of the near-surface wind by reanalyses seems to be a widespread issue. In their study of PMCs developed in the Southern Ocean, Verezemskaya et al. (2017) found that, compared to QuikSCAT observations, the Climate Forecast System Reanalysis (CFSR, Saha et al., 2010), the Modern-Era Retrospective analysis for Research and Applications (MERRA-2, Gelaro et al., 2017), the Japanese 55-year Reanalysis (JRA-55, Kobayashi et al., 2015) and ERA-I underestimate the maximum near-surface wind speed associated with PMCs. Whereas the underestimation by CFSR and MERRA is quite small, JRA-55 and ERA-I significantly underestimate the maximum wind speed, with differences of up to 10 m s^{-1}. A promising global reanalysis for the study of PLs is ERA5 (Hersbach et al., 2020; e.g. Fig. 7), which is the fifth-generation reanalyses of the European Centre for Medium-Range Weather Forecasts (ECMWF). ERA5 has a grid mesh of 31 km, a temporal resolution of one hour and so far covers the period starting from 1979, and recently released back to 1950.

Compared to global reanalyses, regional reanalyses seem to be more adequate to represent the phenomena characteristic of a particular region such as PLs. Moreover, since they tend to have higher resolution than global reanalyses, they are more likely to capture more small-sized PLs than global reanalyses. Smirnova and Golubkin (2017) found that the first version of the ASR, using a grid mesh of 30 km, captured more PLs than ERA-I, the reason being that in ASR the identification criteria regarding relative vorticity and surface wind speed were satisfied more often. They also found that the ability of ERA-I to capture PLs significantly increased with PL size, whereas the performance of the ASRv1 only decreased slightly for the smallest PLs. In contrast, Laffineur et al. (2014) did not find a relation between the PL size and the ability of ERA-I to capture PLs. PLs are probably better captured by the second version of ASR, which has a grid mesh of 15 km, since it is better than the

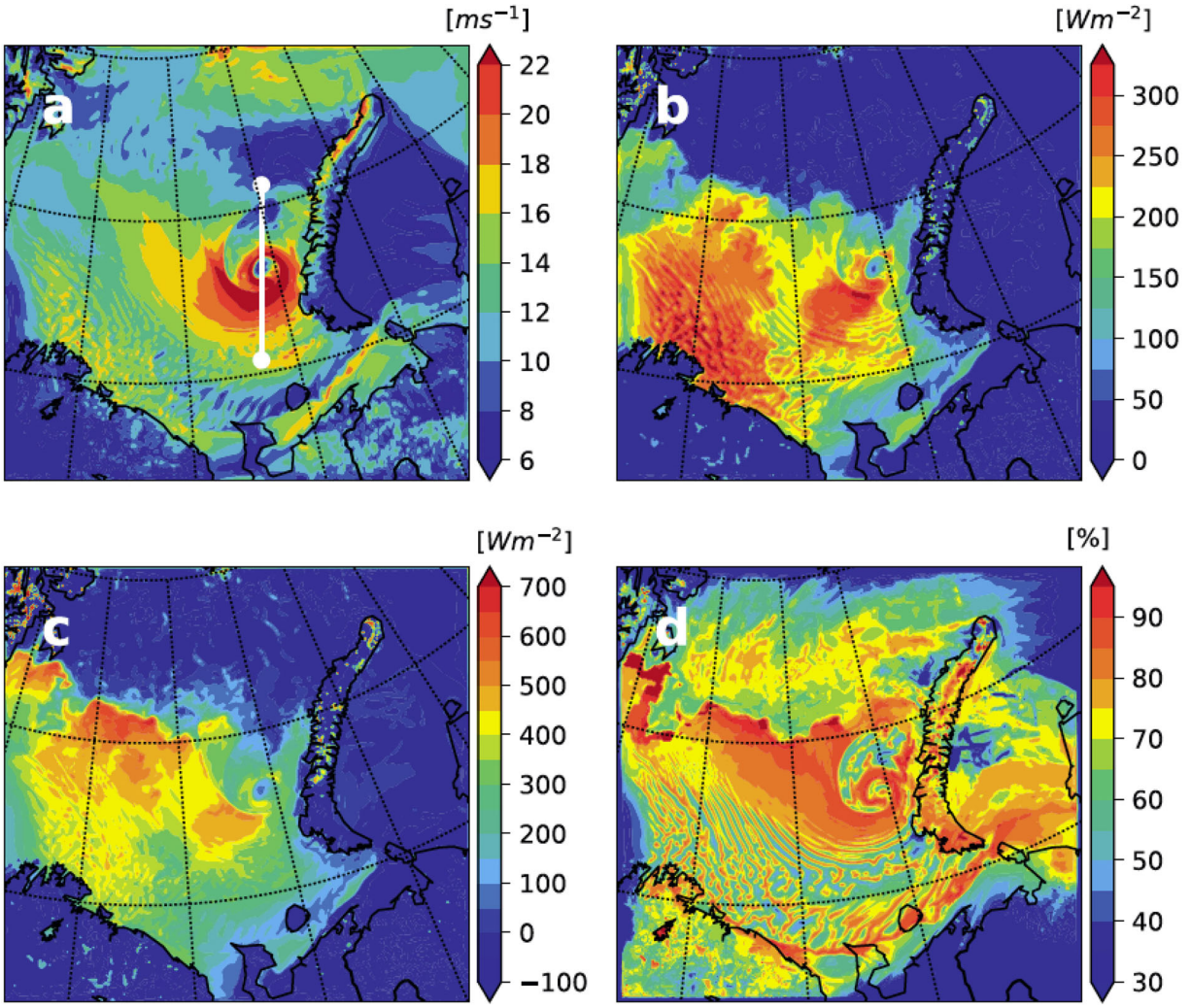

Fig. 8. PL developed over the Barents Sea (see Fig. 1b) simulated with the Weather Research and Forecasting (WRF) model: (a) mean wind speed at 10 m, (b) latent heat flux, (c) sensible heat flux and (d) relative humidity at 2 m on 19 December 2002 at 10:00 UTC (+34 h). The SST and the sea ice concentration are provided by the NEMO model and are maintained constant during the simulation

first version of ASR and ERA-I at reproducing near-surface atmospheric fields, including 10-m wind speed (Bromwich et al., 2018).

4.2. Atmospheric models

Until recently, global atmospheric models were too coarse to capture PLs and correctly represent their structure. For this reason, researchers have mainly used limited-area atmospheric models to study PLs (e.g. Fig. 8). A comparison of the performance of a global model and a limited-area model is provided by the study of Stoll et al. (2020), who simulated an observed PL with both the limited-area model AROME-Arctic, which has a grid mesh of 2.5 km, and the global model ECMWF HRES, which has a grid mesh of 25 km. They found that both models showed good skill at simulating the PL, but the small-scale features, such as cloud patterns, and processes, such as convection, were better represented by AROME-Arctic than by ECMWF HRES. Hallerstig et al. (2021) have also compared PL forecasts produced by the model ECMWF HRES with grid spacings of 5 km, 9 km and 18 km, with those produced by the AROME-Arctic. They verified the forecasts of 10 m wind speeds against *in situ* and ASCAT observations. The authors found that the AROME-Arctic model performed better than the other models only when the verification was made against *in situ* wind observations. Given that the ASCAT product

that the authors used had a grid spacing of 25 km, the worse performance of the AROME-Arctic over the ocean may have been due to the lower resolution of the observational data. Hence, the representation of PLs can be improved by performing dynamical downscaling with a high-resolution model, which can be either used operationally or initialised with reanalyses or simulation output from an atmospheric model. For instance, Laffineur et al. (2014) found that, out of 29 observed PLs, more PLs were represented by simulations with the model Meso-NH initialised with ERA-I (22) or ERA-40 (17), than by ERA-I (13) and ERA-40 (6). Similarly, Pezza et al. (2016) found that the Antarctic Mesoscale Prediction System (AMPS), which employs the Polar WRF and has a grid mesh of 0.5°, represented 46% more PLs than ERA-I.

The representation of polar lows in numerical models has significantly improved with the advent of high-resolution non-hydrostatic atmospheric models. High-resolution models allow a better representation of surface or low-level processes such as the forcing of near-surface winds by topography (Jung et al., 2016) and convection (e.g., Sergeev et al., 2017, 2018). The study of McInnes et al. (2011) illustrates this added value from the increase in horizontal resolution of atmospheric models. The authors used the Unified Model of Met Office (MetUM) with the different horizontal grid meshes – 1 km, 4 km and 12 km – to simulate two PLs observed during the fieldwork campaign IPY-THORPEX. Convection was simulated explicitly in the 1-km model, whereas it was parameterised in the 12-km model. In the 4-km model, the authors used a modified convection scheme permitting explicit simulation of large-scale clouds. For the PL that was captured by the models, the increase in resolution lead to an improved simulation of the PL due to a better representation of convective precipitation. Nevertheless, other studies that also used the MetUM to simulate PLs did not find any significant improvement on the simulation of the wind, temperature and pressure fields when decreasing the grid mesh from 4 km to 2.2 km (Sergeev et al., 2018) and from 2.2 km to 0.5 km (Sergeev et al., 2017), although they did note that convective cells were better represented at higher resolution.

Increasing the resolution of atmospheric models entails the need to adapt the parameterisations to the higher resolution. In the case of the Arctic, the models already struggle to correctly represent the processes underlying the transformation of the air masses exchanged between the Arctic and mid-latitudes (Pithan et al., 2018). One of the parameterisations that needs to be optimised is that of surface fluxes. In the polar regions, the spatiotemporal scales over which fluxes vary are smaller than elsewhere (Bourassa et al., 2013). Given the relevant role played by surface sensible and latent heat fluxes in PL development, the correct parameterisation of these fluxes is essential to model PLs. The main sources of error of the bulk flux algorithms are the systematic errors in the transfer coefficient, which is a function of the wind speed and surface layer static stability, and the precision of the measurements. The occurrence of strong winds or large differences between the SST and the overlying air temperature lead to disagreements between the different bulk parameterizations (Bourassa et al., 2013). Since PLs develop during MCAOs and are associated with strong winds, the use of different bulk parameterizations to simulate PLs could lead to different results.

A better representation of PLs requires not only improving atmospheric models, but also the use of quality input data. Many authors have noted the significant impact that initial conditions have on the representation of PLs (e.g., McInnes et al., 2011; Wagner et al., 2011). In the case of small-scale weather systems, initial conditions uncertainties are associated with convective and mesoscale instabilities (Zhang et al., 2019). In particular, the initial conditions of moisture at the mesoscale are critical for PL prediction (Spengler et al., 2016). The resolution of the model used may also have an impact on the forecast error growth. Stoll et al. (2020) found that the forecast error growth was higher for AROME-Arctic than for ECMWF HRES, and the authors argued that it was probably due to perturbations originating from convective processes. In the case of limited-area models, it is also important to use good-quality boundary conditions and to make sure that the synoptic conditions are well represented since the synoptic conditions preceding PL formation are crucial for their development (e.g., McInnes et al., 2011). Given that upper-level anomalies often play an important role in PL development, the use of the large-scale spectral nudging (SN) technique to enforce the synoptic-scale conditions with a regional climate model (RCM) allows a better representation of PL development (Zahn et al., 2008). For simulations in forecast mode, Zahn et al. (2008) showed that the SN technique improved the representation of PLs when the lead time was two weeks. For simulations in climate mode, Akperov et al. (2018) found that the climatology of cyclones in the Arctic was better represented by the RCM that used SN of the wind as opposed to those RCM that did not use it. The results could be further improved by using SN of temperature in addition to wind.

Since PLs can have an important impact on coastal populations, it is essential to improve the forecasts of PLs. Given the uncertainties in atmospheric models originated from diabatic processes, it is more adequate to use ensemble forecasts for severe weather forecasting in high latitudes (Spengler et al., 2016). One way to improve

forecasts in data-sparse regions is to use targeted observations, which can help reduce the initial condition errors (Aspelien et al., 2011; Irvine et al., 2011). However, it has been shown that targeted observations do not necessarily improve PL forecasts. For instance, when the additional observations provided by the IPY-THORPEX campaign were used in the data assimilation cycle, deterministic and probabilistic forecasts of the PL developed in the beginning of March were improved (Aspelien et al., 2011; Irvine et al., 2011), whereas this was not the case for the PL developed mid-March (Aspelien et al., 2011). Moreover, the improvement in the forecast may be modest compared to the spread between operational ensemble forecast members (Irvine et al., 2011).

It has been recently recognised that forecasting skill in the polar and sub-polar regions could be improved by using a coupled atmosphere-ocean-sea ice model (Jung et al., 2016; Spengler et al., 2016), in particular over the southern limit of seasonal sea ice margin in western Atlantic, i.e. the Gulf of St-Lawrence area (Pellerin et al., 2004; Smith et al., 2013). To the best of our knowledge, the only study that has used a coupled model to simulate a PL is that of Wu (2021). It showed that the simulation of the interactions between the atmosphere, ocean/ice and wave components allows a better representation of the surface heat fluxes, thus improving the representation of PLs during the stage of their development when the surface heat fluxes play a major role. Moreover, as might be expected, the high frequency interaction between these components determines the sea ice fraction and its dynamic (i.e. moving and growth at the sub-daily scale), which is another important variable involved in PL development.

5. Mechanisms of formation and intensification of PLs

5.1. Approaches for the study of PL development

The main hydrodynamic instability types of interest for the study of PLs are the baroclinic, barotropic and convective instabilities. As its name indicates, baroclinic instability develops in an environment where the air density depends on pressure and temperature. This type of instability is associated with the vertical shear of the average flow, which, as expressed by the thermal wind equation, is a function of the temperature horizontal gradient. Thus, baroclinic instability develops in regions characterised by strong horizontal temperature gradients and vertical shear of the horizontal wind, which is a common feature along the sea ice margin over polar and sub-polar areas in winter (Tansley and James, 1999). Barotropic instability develops in an environment where air density only depends on pressure, which implies that isobaric surfaces are also isopycnic and isothermal. This type of instability is associated with the horizontal shear of the horizontal wind. Convective instability occurs in an atmosphere where entropy decreases with altitude, which corresponds to a statically unstable atmosphere.

For the study of the types of hydrodynamic instability that explain PL development, the approaches used are those typical of instability analysis, mainly the normal modes method and the initial value approach (van Delden et al., 2003). In addition, a large number of case studies of PLs, among them sensitivity studies, have been conducted with high-resolution atmospheric models to analyse the role of different atmospheric processes in PL development. The traditional sensitivity experiments consist of deactivating a specific process or processes throughout the whole simulation. Nevertheless, Yanase et al. (2004) have showed that deactivating a process throughout the whole simulation does not only have a direct impact on the development of the PL, but also has an indirect impact on the environment. Therefore, they have recommended that sensitivity experiments consist of deactivating a specific process during a short period of time at a particular moment during the simulation, thus ensuring that the environment will not be largely affected by the lack of that process. Following Yanase et al. (2004), Føre and Nordeng (2012) conducted sensitivity studies where they removed the physical process once the PL had developed with the aim of ensuring that the deactivation of the physical process would only have a direct impact on PL development. In contrast with the traditional approach of conducting sensitivity experiments on an observed PL, Adakudlu and Barstad (2011) conducted sensitivity experiments on a surface low that, despite developing in an environment favourable for PL development, did not become a PL. The aim of their study was to analyse whether they could trigger PL development by modifying the sea ice margin and the SST.

A useful approach to analyse the development mechanisms of PLs is the analysis of their energy budget. A few studies have been made on PL energetics, and the majority have used simplified atmospheric models and/or idealised initial and boundary conditions. For instance, Duncan (1977) conducted an energetics study of three PL cases with a two-dimensional linear atmospheric model. The author computed the eddy kinetic energy (EKE) and eddy available potential energy (EAPE) tendencies as well as the rate of conversion between different types of energy contributing to those tendencies. Other authors have used more complex atmospheric models, which are three-dimensional and non-hydrostatic, but with idealised atmospheric conditions such as cyclic boundary conditions (Yanase and Niino, 2007; Sergeev and Stepanenko,

2014; Terpstra et al., 2015). Given that PLs develop in a wide range of environments, the use of idealised conditions limits the representativeness of the results. Instead of using simulation output, Shimada et al. (2014) used operational analysis data from the Japan Meteorological Agency, whose grid mesh was approximately 11 km, to compute the EAPE and the EKE budgets of three PL with the aim of analysing the contribution of baroclinic and diabatic processes to PL development.

5.2. Polar low spectrum

The fact that PLs develop in different environments explains why different mechanisms can contribute to PL development. Baroclinic instability is a possible mechanism of PL development as PLs often develop in a shallow baroclinic atmospheric layer, mainly near the sea ice edge, and they can also develop in a deep baroclinic atmosphere (Terpstra et al., 2016). Barotropic instability is also a possible mechanism since some PLs form in an equivalent barotropic atmosphere (Businger, 1985). Convection can also contribute to PL development because the static stability of the atmosphere significantly decreases during MCAOs. A common synoptic situation leading to PL development in the Nordic Seas (Blechschmidt et al., 2009) and in the Sea of Japan (Yanase et al., 2016) is the presence of northerly winds on the west side of mid-latitude synoptic-scale cyclones, which produce MCAOs. Upper-level anomalies can also play an important role in PL development as shown by the fact that a cold trough or cold low at 500 hPa is often located over the region where PLs form in the Nordic Seas (Blechschmidt et al., 2009) and in the Sea of Japan (Yanase et al., 2016). In the Sea of Japan mature PLs moving southwards are located below an upper-level cold trough, thus favouring convection, whereas mature PLs moving eastwards are located in the east side of a upper-level cold trough, thus favouring baroclinic development (Yanase et al., 2016). Some researchers have tried to determine the large-scale environment associated with PL development in different regions. Such is the case of the studies conducted by Blechschmidt et al. (2009) and Bracegirdle and Gray (2008) who analysed the environments characteristic of PL development in the Nordic Seas, but reached partly contradicting conclusions. For PLs developing over the Barents Sea, Blechschmidt et al. (2009) found that the atmosphere was on average weakly baroclinic, whereas Bracegirdle and Gray (2008) found that the atmosphere was strongly baroclinic. These results emphasise the difficulty of trying to determine the characteristics of the environment leading to PL genesis in a particular region.

Between the end of 1970 and the beginning of the 1980s, there was an important discussion about the nature of PLs (van Delden et al., 2003). Whereas several authors affirmed that PLs were generated through baroclinic instability (e.g., Harrold and Browning, 1969), other stated that PLs were convective systems similar to tropical cyclones (e.g., Rasmussen, 1979). Several authors also suggested that baroclinic instability and convection can act together in the development of PLs (e.g., Sardie and Warner, 1985). Recent studies have confirmed that PL development is more complex that initially thought. Thanks to the valuable observations provided by the THORPEX campaign, it has been possible to study the PL that developed on 3 – 4 March 2008 in detail. Stoll et al. (2020) concluded that the development of this PL was divided into an initial baroclinic and a mature convective stage. Sensible heat fluxes and latent heat release played an important role in both stages: they contributed to the intensification of baroclinicity during the baroclinic stage, and they lead to a decrease in atmospheric stability during the convective stage.

As of today, there is still no widespread agreement on the importance of these different mechanisms in PL formation. Two conceptual models that have occasionally been used to explain PL development are the model developed by Montgomery and Farrell (1992), which was invoked by Grønås and Kvamstø (1995) to explain the development of two simulated PLs, and the Diabatic Rossby Vortex model, which has been invoked by Terpstra et al. (2015) to explain PL development in an ideal simulation with an Arctic moist-baroclinic environment and by Stoll et al. (2020) to explain how latent heat release affected the translation speed of an observed PL.

Given that several dynamic and thermodynamic factors play a certain role in PL development, and that the relevance of each factor varies depending on the case, it is convenient to refer to a PL spectrum in which PLs would be found with only a baroclinic or a convective origin, but also PLs formed as a result of the combined action of different forcing mechanisms (Rasmussen et al., 2003b). The idealised experience conducted by Yanase and Niino (2007) with a high-resolution non-hydrostatic model supports the idea of a continuum of PL formation mechanisms. The authors used simplified atmospheric conditions and imposed an axisymmetric vortex in gradient wind equilibrium as initial conditions. By applying different levels of baroclinicity for each experience, they noted that the structure and the dynamics of PLs varied gradually with the increase in the environment baroclinicity. In a barotropic environment, the development mechanisms of the vortex as well as its structure were similar to those of tropical cyclones. In an environment with strong baroclinicity, the meso-α-scale structure was similar to

that characteristic of a dry baroclinic instability wave. Moreover, the warming caused by condensation produced meso-β-scale structures showing a warm core near the PL centre.

5.3. Baroclinic and barotropic instability

Baroclinic instability mechanisms leading to PL formation appear in different forms. Several researchers have used the normal modes method to analyse the growth rate of perturbations of different wavelengths with the aim of finding the growth rate and wavelength corresponding to the PLs that develop fastest. Among the studies that have used the normal modes method, we find dry baroclinic models (e.g., Duncan, 1977; Reed and Duncan, 1987) and moist baroclinic models (e.g., Yanase and Niino, 2004). Duncan (1977) used a bidimensional quasi-geostrophic model to compute the normal modes of the unstable perturbations corresponding to three observed PLs. Among other approximations, this author neglected friction and the diabatic warming term. The results showed that the wavelengths of the unstable modes decreased as the static stability and the depth of the perturbation decreased. The model developed by Duncan (1977) was used by Reed and Duncan (1987) to analyse the serial development of four PLs. Noting that the intensification of the perturbations was due to a baroclinic mechanism, Duncan (1977) and Reed and Duncan (1987) concluded that the PLs that they had studied could be considered as shallow baroclinic waves. However, the model used was not capable of correctly reproducing all the characteristics of the observed PLs. The authors admitted that the quasi-geostrophic model, which neglects the horizontal variation of the static stability, was not adequate to analyse the development of PLs in the presence of important variations of the static stability. Reed and Duncan (1987) suggested that, after the initial baroclinic stage of PL development, deep convection likely played an important role in the development of the PLs. Using a non-geostrophic and non-hydrostatic model of a baroclinic flow, Yanase and Niino (2004) analysed the effect of convective warming on baroclinic instability. The authors concluded that the amount and spatial distribution of convective warming have a significative impact on the energy converted through the baroclinic mechanism.

All these studies have undoubtedly helped shape our understanding of PL development. Notwithstanding this, several models used were too simplified to enable a deep understanding of the development mechanisms of PLs. In general, the perturbations from which weather systems develop are complex and, subsequently, cannot be described as perturbations of only one normal mode (Holton and Hakim, 2013). Idealised simulations can provide additional information on PL development. For instance, Terpstra et al. (2015) conducted idealised simulations in a moist baroclinic atmosphere, and they showed that, in the absence of an upper-level anomaly, friction, surface fluxes or radiation, a surface cyclonic warm-core perturbation can amplify in a moist baroclinic environment, with latent heat release being essential for the initial amplification of the perturbation. Simulations with three-dimensional atmospheric models are most suited for the analysis of the development mechanisms of PLs since all relevant processes are represented.

The baroclinic development of PLs can be triggered by forcing by shortwave upper-tropospheric troughs. A large number of case studies show that upper-level forcing by negative anomalies of geopotential height contribute to the development of PLs (e.g., Grønås and Kvamstø, 1995; Gachon et al., 2003). In some environments, upper-level forcing can be the main mechanism of PL formation. Mallet et al. (2013) concluded that during the weather regime known as 'Scandinavian Blocking', which is not associated with a significant anomaly of $SST - T_{500}$, an upper-level potential vorticity (PV) anomaly must be present to trigger PL development.

The PV approach has been often invoked to explain the development of PLs in situations where a upper-tropospheric PV anomaly is located over a low-level baroclinic zone (e.g., Føre et al., 2011; Shimada et al., 2014) or a near-surface PV anomaly (e.g., Moore et al., 1996; Verezemskaya and Stepanenko, 2016), or both (Moore and Vachon, 2002; Martin and Moore, 2006). According to the PV framework, the vertical extension of the influence exerted by a PV anomaly is expressed by the Rossby depth, defined as $H_R = (fL)/N$, where f is the Coriolis parameter, L is the horizontal scale of the perturbation, and N is the Brunt-Väisälä frequency which represents static stability and is defined as $N^2 = g(dln\theta_0/dz)$, where g is the gravity acceleration and θ_0 is the potential temperature of the environment (Holton and Hakim, 2013). Accordingly, the vertical scale of a perturbation increases as the static stability decreases and as the horizontal scale of the anomaly increases. Therefore, for an upper air perturbation of a relatively small scale to produce baroclinic instability near the surface, static stability must significantly decrease and/or the vertical distance between the perturbation and the baroclinic zone must be relatively small (e.g., Shimada et al., 2014).

The PV approach can be used to explain the development of certain PLs. For instance, Moore et al. (1996) applied this approach to analyse a PL formed within a cloud band over the Labrador Sea. They explained that the generation of this PL was the result of an interaction between a high-level positive PV anomaly and a low-level

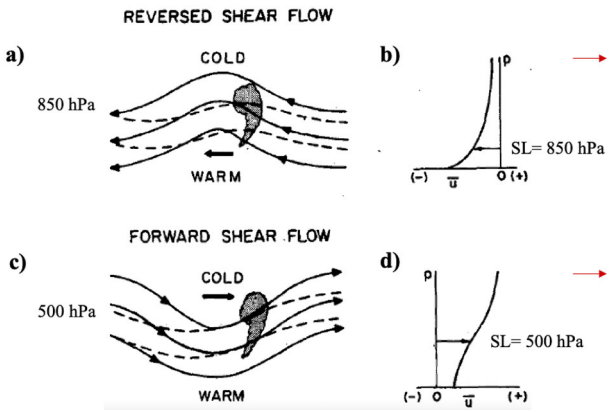

Fig. 9. Perturbation structure at the steering level in a (a) reverse-shear and (c) forward-shear flow. The solid lines represent the streamlines, and the dashed lines represent the isotherms. The thick black arrows represent the phase propagation vector and the steering level wind. The shaded grey region shows a comma-shaped cloud associated with the perturbation. The zonal component of the wind (u) at different pressure levels (p) is shown for the (b) reverse-shear and (d) forward-shear flow. The steering level wind is represented by the black arrows, and the direction of the thermal wind is schematically represented by the red arrows. Adapted from Businger and Reed (1989). © American Meteorological Society. Used with permission.

positive PV anomaly. Taking into account the fact that the horizontal scale of the high-level PV anomaly was roughly 500 km, and that the static stability over the Labrador Sea was very weak, the authors obtained a Rossby depth of around 8 km, which was sufficient to allow the interaction between both PV anomalies. The PV inversion method allows the quantification of the contribution of a certain PV anomaly to the temperature and wind fields. A particularly suitable method for the analysis of PL development is a piecewise PV inversion method, which consists of dividing the total PV anomaly field into three atmospheric layers to examine the contribution of discrete PV anomalies located in the upper troposphere, the lower troposphere and in a layer near the surface (Bracegirdle and Gray, 2009; Wu et al., 2011). The PV anomaly field can also be analysed at different scales to better understand the role that different scales of PV anomalies play in PL development (Shimada et al., 2014).

A type of PL that has attracted the attention of researchers is the reverse-shear PL (Fig. 9). This type of PL develops in regions where the steering level wind, which is normally located at the lower levels in the case of these type of PLs, is antiparallel to the thermal wind. In contrast to a typical baroclinic development, associated with a forward-shear flow, the perturbation tilts forward with height (forward meaning in the direction of motion of the PL). In such systems, the warm air advection and the upwards movement take place upstream of the perturbation, and the cold air advection and the downwards movement take place downstream. Favourable conditions for the development of reverse shear PLs are found mainly in the Norwegian Sea, followed by the region south of the Denmark Strait, the Bering Sea and the Sea of Okhotsk (Kolstad, 2006). Accordingly, reverse-shear PLs have been commonly observed in the Nordic Seas (e.g., Blechschmidt, 2008), and they are much more frequent in the Norwegian Sea than in the Barents Sea (Terpstra et al., 2016). These PLs often develop over the maritime regions located west and north of Norway (Businger and Reed, 1989). In particular, one of the situations where these PLs are found is near the coast of Finnmark, where there are strong temperature gradients, when the wind blows from the north-east (Noer et al., 2011). In the Nordic Seas and in the Sea of Japan, reverse-shear PLs move southwards and forward-shear PLs move eastwards (Terpstra et al., 2016; Yanase et al., 2016). In the Nordic Seas, reverse-shear PLs move in a direction perpendicular to the SST isolines, towards regions of higher SST, whereas forward-shear PLs move following the SST isolines (Terpstra et al., 2016).

Contrary to baroclinic instability, the role of barotropic instability in PL development has received less attention. Only high-resolution models, with a grid mesh of a few kilometres, can correctly represent barotropic instability because the horizontal wind shear zone can be narrow (Leutwyler and Schär, 2019). Nagata (1993) showed that barotropic instability can significantly contribute to the formation of vortices at the meso-β scale. Even though barotropic instability has been observed in some PL case studies (e.g., Sergeev et al., 2017), it seems to play a secondary role (Businger and Reed, 1989).

5.4. Convection

The similarity between the structure of certain PLs and tropical cyclones (TCs) has led several authors to apply to PLs the theories developed to explain the intensification of TCs. The two main theories in the study of TCs are Convective Instability of the Second Kind (CISK) of Charney and Eliassen (1964), and Wind Induced Surface Heat Exchange (WISHE) of Emanuel (1986). The CISK and WISHE theories have several points in common, among them, the assumption of gradient wind balance and the use of an axisymmetric model. The two theories state that there is a positive feedback between the intensity of a cyclone and the convective warming by either the sensible and latent surface heat fluxes, according to WISHE, or the convergence due to friction in the

planetary boundary layer, according to CISK (Craig and Gray, 1996).

In order to develop the CISK theory, Charney and Eliassen (1964) assumed that the atmosphere is stable against large-scale convection, therefore in hydrostatic equilibrium, despite being unstable against small-scale convection. A hurricane is considered as a forced circulation that results from the latent heat released by the organised convection of the cumulus clouds. Taking into account these assumptions, the authors developed a quasi-hydrostatic two-level model in gradient wind balance and represented the flow as an axisymmetric vortex. The authors concluded that the amplification of an infinitesimal perturbation is the result of the combined effect of the convection associated with the cumuli and the TC. On the one hand, the TC provides humidity to the cumuli by means of the humidity convergence induced by the surface friction. On the other hand, by releasing latent heat associated with precipitation, the cumuli provide the TC with energy. This model has been applied to the study of PLs by, among others, Rasmussen (1979). Using a two-layer quasi-geostrophic and hydrostatic atmospheric model, the author found that the most unstable wavelengths computed with the model were in agreement with the size of the observed PLs, and that the intensification of the PLs was proportional to the contribution from the latent heat sources.

The CISK theory was criticised by Emanuel (1986) who highlighted that the tropical atmosphere is almost neutral to deep moist convection. In effect, the heat transport by convection quickly drains the convective available potential energy (CAPE) created, so that the CAPE could not play an important role in the maintenance of the cyclone. As in the case of the tropical regions, some authors affirm that the CAPE present in the polar atmosphere is constantly being drained due to the convection triggered by the strong sensible and latent heat fluxes from the ocean surface (Emanuel and Rotunno, 1989; Linders and Saetra, 2010). Accordingly, some authors have found low values of CAPE (Bracegirdle and Gray, 2009; Adakudlu and Barstad, 2011; Laffineur et al., 2014) and even no CAPE (Verezemskaya and Stepanenko, 2016) during the development of observed PLs. Van Delden et al. (2003) have argued that significant values of CAPE can occasionally be produced in polar regions as a result of the combined action of the surface fluxes and cold air advection in the higher layers of the atmosphere, and that CAPE does not disappear as fast as it is generated.

Emanuel (1986) developed an alternative theory to explain the intensification of TCs, which has been named WISHE. This author used a hydrostatic and axisymmetric model in gradient wind balance and imposed an initial perturbation of finite amplitude. The author concluded that the maintenance of a TC in a stationary state is due to a positive feedback between the cyclone circulation and the sensible and latent heat fluxes from the ocean surface. By noting that certain environmental conditions favourable for the development of hurricanes are similar to those observed in the development of PLs, Emanuel and Rotunno (1989) decided to apply the WISHE model to the study of PLs. The results of their study showed a good agreement between the central pressure of the PL computed with the model and that observed in reality. Moreover, they noted that the PL structure as determined by the model was quite similar to that of the hurricanes, the main differences being that the PL showed a shallower circulation and more warming at the surface associated with the sensible heat fluxes from the ocean. In view of these results, they concluded that certain PLs can be considered as 'Arctic hurricanes', and that this type of PLs require a pre-existing perturbation whose amplitude must be equal to or larger than a critical amplitude.

To try to settle the debate regarding the importance of the CISK and WISHE mechanisms, Craig and Gray (1996) conducted several experiments with a non-hydrostatic and axisymmetric model with the aim of analysing separately the effect of modifying the moist and heat transfer coefficients, and the effect of modifying the quantity of momentum transfer coefficient. Their results showed that the intensification rate of PLs increased with the increase in the moist and heat transfer coefficients, whereas the modification of the momentum transfer coefficient had a small impact on the intensification rate, except when then modification of this latter coefficient was very large. Thus, the authors concluded that the WISHE mechanism explains PL intensification. Nevertheless, the CISK *versus* WISHE debate is not settled yet. In effect, some PL case studies have pointed at CISK as a possible mechanism involved in PL development (Sardie and Warner, 1985; Yanase et al., 2004), whilst others have pointed at WISHE (Albright et al., 1995; Bracegirdle and Gray, 2009; Føre et al., 2012).

The consideration of certain PLs as 'Arctic hurricanes' remains controversial. The intensity of PLs does increase with increasing SST (Kolstad and Bracegirdle, 2017; Stoll et al., 2020). Stoll et al. (2020) estimated that the maximum near-surface wind speed associated with an observed PL increased by 1 to 2 m s^{-1} per K of increase in SST, and that this correlation seemed to be nonlinear for the highest SST. Nonetheless, sensitivity studies have shown that hurricane-like PLs can become as intense as hurricanes only when the SST is increased 6 K (Kolstad and Bracegirdle, 2017) and 8 K (Albright et al., 1995), which is unrealistic.

5.5. The role of surface heat fluxes and latent heat release

Sensible and latent surface heat fluxes can become very important during MCAOs, thus contributing to the development of PLs (e.g. Figs. 8b and 8c). For example, Føre and Nordeng (2012) found sensible and latent surface heat fluxes of 1,200 W m^{-2} and 400 W m^{-2}, respectively, in the region of the eyewall of a simulated PL that reached a minimum pressure of 961 hPa. Many case studies have highlighted the importance of surface heat fluxes for PL intensification (e.g., Wagner et al., 2011), whereas a few case studies have found that surface heat fluxes played a negligible role in PL development (Sardie and Warner, 1985; Verezemskaya and Stepanenko, 2016). Some case studies have highlighted that sensible heat fluxes played a more important role than latent heat fluxes in the intensification of a PL (e.g., Føre et al., 2012). Given that, according to the Clausius-Clapeyron equation, the saturation vapour pressure increases exponentially with temperature, it can be expected that the higher the latitude where PLs develop, the more important the role of sensible heat fluxes should be compared to latent heat fluxes and vice versa. This is confirmed by the study of PLs in the Sea of Japan conducted by Yanase et al. (2016). Regarding condensational heating, many case studies have found that latent heat release played an important role in the development of a PL (e.g., McInnes et al., 2011; Stoll et al., 2020).

Surface heat fluxes and latent heat release can not only directly contribute to PL development, but also indirectly by modifying, for example, the distribution of thermal and vorticity advection terms at low levels as well as the baroclinic structure along the sea ice margin during the mature stage of the PL (Gachon et al., 2003). In effect, several case studies have indicated that surface heat fluxes and latent heat release can contribute to the maintenance of the baroclinic environment necessary for PL development. Sensitivity studies conducted by Føre and Nordeng (2012) showed that condensational heating was crucial in supporting the initial baroclinic environment, whereas surface latent heat fluxes and, although less importantly, sensible heat fluxes contributed to the maintenance of the baroclinic environment during the mature stage of the PL. Surface sensible fluxes (Yanase et al., 2004; Stoll et al., 2020), latent heat fluxes (Yanase et al., 2004) and latent heat release (Wu et al., 2011) contribute to maintain the environment favourable for PL development by rendering the atmosphere less stable. As will be explained below, the surface heat fluxes also have an indirect impact on PL intensification through the modification of the SST (Wu, 2021).

5.6. The role of topography and sea ice

Topography is a factor that can facilitate the formation of PLs near, among other places, the Antarctic, Svalbard and Greenland. In the Antarctic, the katabatic winds play an important role in the generation of PMCs (Turner et al., 2003). In the case of Svalbard, Sergeev et al. (2018) found that the topography of the archipelago did not play a crucial role in the development of two observed PLs, although it provided a secondary source of positive vorticity on the lower level of the atmosphere that contributed to their intensification.

The role of Greenland's topography in the development of PLs has been noted since a long time (e.g., Businger, 1985; Sardie and Warner, 1985). The elevated terrain of the south of Greenland can alter the propagation of a synoptic cyclone, thus inducing a secondary circulation over the Labrador Sea that can contribute to PL development (Moore and Vachon, 2002; Martin and Moore, 2006). Another phenomenon that results from the topography of Greenland are katabatic winds, whose vertical extension does not normally exceed 300 m (Klein and Heinemann, 2002). The downhill direction of the katabatic winds is influenced by the Coriolis effect in regions where the topography does not impose too many restrictions to the flow. In the case of Greenland's coasts, the influence of the Coriolis effect is limited since the flow is canalised by the fjords and valleys (Serreze and Barry, 2014). This double effect of topography – the generation of katabatic winds and the imposition of restrictions to their flow – is evident in the study of Kristjánsson et al. (2011b), who conducted sensitivity experiments to study the impact of Greenland's topography on the development of a PL observed over the Denmark Strait. The PL did not form in the simulation where the whole Greenland surface was located at sea level, and therefore in absence of katabatic winds. In the simulation where only the high-level terrain of Greenland's east coast was removed, in addition to being weaker, the simulated PL developed more southerly than the observed PL, which could be explained by the influence of the Coriolis effect on the katabatic winds in the absence of restrictions to the flow.

In the case of Greenland's east coast, the intensification of the katabatic winds by a synoptic forcing can cause katabatic storms. Klein and Heinemann (2002) showed that these storms can play an important role in the formation of mesoscale cyclones. In a normal situation, the katabatic winds create favourable conditions for the formation of mesoscale cyclones. The flow convergence in the valleys causes the vertical stretching of vorticity, and the transport of very cold air towards the ocean contributes to the intensification of baroclinicity in the

lower layers of the atmosphere. The katabatic winds can be intensified by the forcing by a synoptic low positioned between Greenland and Iceland, resulting in katabatic storms. In effect, the winds associated with such a low cause an increase in the vertical extension of the katabatic winds, thus contributing to the vertical stretching of vorticity. Furthermore, there can be a positive feedback between the intensity of the katabatic winds and that of a mesoscale cyclone through the intensification of the pressure gradient between Greenland and the cyclone.

A factor that must be considered when analysing the effect of topography on the development of PLs is the adiabatic warming of cold air associated with katabatic winds. Whilst Klein and Heinemann (2002) have noted that the katabatic winds transport cold air towards the ocean, increasing low-level baroclinicity, Kristjánsson et al. (2011b) highlighted that, due to adiabatic warming of the cold air associated with katabatic winds, the temperature of this air becomes higher than the air temperature of the environment, thus contributing to the decrease in surface pressure.

Another factor that influences PL development is the sea ice cover. Sergeev et al. (2018) conducted a study to investigate the sensitivity of simulations of two PLs to the sea ice cover. They concluded that the sea ice cover near Svalbard exerts an influence on the intensification of PLs, but it is not a determinant factor of PL development. Similarly, Adakudlu and Barstad (2011) found that the modification of the sea ice edge around Svalbard did not trigger PL development of a low-pressure system that developed in the Barents Sea, despite the environmental conditions being favourable for PL development. The problem with these two experiments is that, given that the authors changed several features of the sea ice cover at the same time, it is not possible to attribute any changes in cyclone intensification to the sea ice extent, the orientation of the sea ice edge or its shape. In these experiments the modified sea ice edge was oriented zonally (Sergeev et al., 2018) or almost zonally (Adakudlu and Barstad, 2011), and was smoothed. Moreover, in both studies the SST was modified so that all the new ice-free ocean was assigned a SST of around 271 K, which was not realistic since the strong SST gradients remained in the original region instead of near the new sea ice edge. Some case studies indicate that the shape of the sea ice edge has an impact on PL development. An indented sea ice edge is more favourable for cyclogenesis than a straight sea ice edge (Albright et al., 1995; Gachon et al., 2003), because an indented sea ice margin generates a discontinuity in the sources or sinks of surface heat fluxes, resulting in a local Laplacian of diabatic and thermal forcing involved in low level trough or vorticity formation (Gachon et al., 2003).

6. PLs and climate change

6.1. Impact of PLs on the ocean

As atmospheric phenomena, PLs interact with the other components of the climate system. The impact of PLs on the ocean has long intrigued researchers. The surface heat fluxes associated with PL development directly cause a cooling of the ocean surface. The Greenland/Norwegian Seas and the Labrador Sea, which are regions of deep water formation, are frequently affected by PLs (Rasmussen et al., 2003a). By cooling the water of the ocean surface in these regions, PLs could modify the formation rate of the ocean deep water. For instance, intense storms in the Labrador Sea can cause major events of deep convection (Garcia-Quintana et al., 2019). Moore et al. (1996) were probably the first to highlight the possible existence of a coupling between PLs, whose time scale is short, and the thermohaline circulation, whose time scale is long. After computing the surface fluxes associated with a PL developed over the Labrador Sea, they concluded that the resulting water cooling was sufficient to trigger the sinking of water masses, thus contributing to deep water formation. Nevertheless, Isachsen et al. (2013) argued that the impact of PLs on the ocean circulation is rather weak. The authors computed the effective forcing period by PLs, defined as T_f = radius/speed of movement, and their results indicated that in the Nordic Seas the forcing of more than 50% of PLs over a portion of the ocean lasts less than six hours.

In spite of the small forcing exerted by individual PLs on the ocean, the whole forcing exerted by PLs and other PMCs that develop every year can have an important impact on the thermohaline circulation. Condron and Renfrew (2013) analysed the impact of PMCs on the thermohaline circulation of the Northeast Atlantic with a global, eddy-permitting, coupled ocean-sea ice model. They conducted two simulations covering the period 1978 – 1998, one with parameterised PMCs and the other without them. Their results indicated that the increase in the surface heat fluxes associated with PMCs, with an associated decrease in the ocean surface temperature, caused the destabilisation of the water column. Consequently, the presence of PMCs caused an increase in the frequency and depth of ocean convection, as well as an increase in the area affected by convection. The authors concluded that the presence of PMCs induces an increase in the oceanic heat transport towards the Nordic Seas and a transport of deep water southwards through the Denmark Strait. A limitation of this study is that the authors used a coupled ocean-sea ice model, so the interactions between the ocean and the atmosphere were not represented. The recent study of Hirschi et al. (2020) has demonstrated that the atmosphere-ocean interactions

need to be resolved at high resolution in a coupled model as the Atlantic Meridional Overturning Circulation (AMOC) is quite sensitive to the model horizontal resolution. High resolution processes and models are needed to incorporate both ocean mesoscale eddies and atmospheric regional features, including PMCs and PLs, especially when high-frequency interactions between ocean/sea ice and atmosphere are key factors for the deep water formation as in the case of the AMOC (Garcia-Quintana et al., 2019).

The importance of the SST cooling caused by surface heat fluxes has been questioned by Saetra et al. (2008) who argued that the vertical mixing associated with strong winds may actually lead to an increase in SST. The authors showed that when strong ocean surface winds occur on a time scale of hours to a few days, the subsequent vertical mixing leads to a warming of the ocean surface in regions where the ocean surface water is colder than the water at depth. They highlighted that, although surface heat fluxes contribute to some cooling of the SST, their effect is weaker than that of vertical mixing. Nonetheless, their study has some limitations since they used a one-dimensional ocean model forced with constant values of surface wind speed, air temperature and relative humidity. Using a coupled atmosphere-wave-ocean/ice model to simulate a PL, Wu (2021) showed that PL development is indeed associated with both an increase and a decrease in SST. The surface heat fluxes that result from both the strong winds associated with the PL and the large difference between the SST and the overlying air temperature lead to a decrease in the SST. At the same time, in regions where there is an ocean temperature inversion (i.e., cold water near the surface and warm water in a deeper layer), such as near the ice edge, the upper-ocean mixing induced by the strong winds leads to the transport of warm water from a deeper layer to the sea surface.

6.2. Impact of climate change on the climatology of PLs

It is well known since a long time that the surface temperature shows higher variability, sensitivity and tendency in the Arctic region than at a global level. This phenomenon, known as 'Arctic Amplification', implies that global warming will be particularly intense and rapid in the Arctic (Serreze and Barry, 2011). Global warming will affect the sea ice and the snow cover as well as the mean and variability features of MCAOs. Since PLs form near the sea ice edge and near the snow-covered continents during MCAOs, we can expect that the spatio-temporal distribution and intensity of PLs will be affected by climate change.

6.2.1. Recent climate change. Over the last two decades, the Arctic surface air temperature has increased by more than twice the global average. Global warming has caused a decline in the Arctic sea ice extent for all months of the year, whereas the evolution of the Antarctic sea ice extent overall has not shown any statistically significant trend. The snow cover has also declined over continents bordering the Arctic (IPCC, 2019). Despite these changes, recent climate change seems to have had a relatively small impact on PL climatology. Michel et al. (2018) did not find any significant long-term trend in the frequency of PMCs in the Nordic Seas over the period 1979 – 2014. Similarly, Stoll et al. (2018) did not find any significant long-term trend in PL activity, neither in the Northern Hemisphere nor in the Southern Hemisphere, over the period 1979 – 2016. Nonetheless, they found a significant decrease in the activity of the most intense PLs in the Northern Hemisphere, which the authors attributed to a decrease in the intensity of MCAOs. There has been a small positive trend in PL occurrence in the North Pacific over the period 1948 – 2010 (Chen and von Storch, 2013). Given the few studies conducted on the impact of recent climate change on the climatology of PLs, it is not possible to draw any definite conclusion.

6.2.2. Future climate change. The reduction in the Arctic sea ice extent is projected to continue over the first half of the 21st century as a result of global warming (IPCC, 2019). According to most Coupled Model Intercomparison Project phase 6 (CMIP6) climate projections, the Arctic will become virtually sea-ice-free in summer before 2050 for the emission scenarios SSP1-1.9, SSP1-2.6, SSP2-4.5 and SSP5-8.5 (Notz and SIMIP Community, 2020). As for the Southern Hemisphere, there is low confidence in climate projections regarding the evolution of the Antarctic sea ice. Global warming will also continue to cause a decrease of snow on land in the Arctic (IPCC, 2019).

Global warming will lead to an increase in the static stability of the atmosphere in the North Atlantic (Zahn and von Storch, 2010; Mallet et al., 2017; Landgren et al., 2019b) and in the North Pacific, although the increase will be smaller in the latter (Landgren et al., 2019b). In the North Atlantic, the SST – T_{500} will decrease almost everywhere where PLs develop, and situations of high vertical instability will become less frequent (Mallet et al., 2017). Moreover, the loss of sea ice will lead to a change on the spatial distribution of atmospheric static stability. In effect, the static stability will decrease in some ocean regions that are presently ice-covered during winter and will become ice-free in the future (Mallet et al., 2017; Landgren et al., 2019b). According

Table 3. Information about the studies on the future climatology of PLs developed using dynamical downscaling and an objective tracking method.

Author/s	Driving data	Nested model	Region	**Historical period**	Future period	Scenarios
Zahn and von Storch (2010)	ECHAM5/ MPI-OM	COSMO-CLM	North Atlantic	1960–1989	2070–2099	B1, A1B, A2
Landgren et al. (2019a)	CESM Large Ensemble	HCLIM-ALARO	Nordic Seas	1990–2005	2026–2035 2071–2080	RCP8.5

to Landgren et al. (2019b), in the Nordic Seas, excluding the Barents Seas, the decrease in the MCAO index will be stronger in December and January than in February and March, so the maximum MCAO index is projected to shift from January to February. In the Barents Sea, the opposite is projected to occur. In a future scenario with high greenhouse gas emissions, weather regimes in the North Atlantic are projected to have less influence on the local static stability of the atmosphere, represented by SST – T_{500}. Thus, the observed link between weather regimes and PL development may disappear in the future (Mallet et al., 2017).

The impact of global warming on the frequency and spatial distribution of PLs in the North Atlantic has been studied using dynamical downscaling (Zahn and von Storch, 2010; Landgren et al., 2019a) and statistical downscaling (Romero and Emanuel, 2017). Table 3 summarises the relevant information from the two studies of the future climatology of PLs developed using dynamical downscaling. Zahn and von Storch (2010) used a model with a grid mesh of 50 km, whereas Landgren et al. (2019a) used a model with a grid mesh of 12 km. Romero and Emanuel (2017; Fig. 10) used a complex statistical–deterministic method to analyse the evolution of the PL frequency between the periods 1986 – 2005 and 2081 – 2100 using the IPCC scenario RCP8.5 (for an overview of the representative concentration pathways, see van Vuuren et al., 2011). They generated a large number of synthetic PL tracks compatible with the historic and future climates simulated by CMIP5 models. All these studies found that in the North Atlantic the regions of PL activity will shift northwards as the sea ice extent decreases (Zahn and von Storch, 2010; Romero and Emanuel, 2017; Landgren et al., 2019a). The frequency of PLs will decrease by the end of the 21st century (Zahn and von Storch, 2010; Romero and Emanuel, 2017), and this decrease is observed for all months of the cold season, although there is high uncertainty since some climate projections show an increase in PL frequency (Romero and Emanuel, 2017). According to the best climate projections, the number of PLs will decrease by 15% on average (Romero and Emanuel, 2017). The decline in PL frequency will be due to the increase in the static stability of the atmosphere (Zahn and von Storch, 2010). In the Nordic Seas, excluding the Barents Sea, PL frequency will decline in October, November, December and January, and will increase in March. There will be a reduction in the lifetime of PLs in December in the Barents Sea, and in November, December and January in the Nordic Seas (Landgren et al., 2019a). Regarding the future intensity of PLs, the studies do not seem to agree. Romero and Emanuel (2017) found that the probability of intense PLs will decrease (increase) in the west (east) region of the North Atlantic, whereas Landgren et al. (2019a) found a decrease in PL intensity for three winter months in the Nordic Seas.

Condron and Renfrew (2013) hypothesised that the decrease in the frequency of PLs and their northward movement due to climate change would be followed by a decrease in deep convection in the Nordic Seas as well as a decrease in the formation rate of the deep water of the Greenland Sea and the reduction of the volume of the Denmark Strait Overflow Water (freshwater) that flows towards the North Atlantic. This would result in a weakening of the AMOC. In fact, the recent study of Garcia-Quintana et al. (2019) points out the fact that a decrease in the storms crossing the Labrador Sea with a consequent reduction in the winter heat loss might be a bigger threat to deep convection and Labrador sea water formation in the future, than the expected increases in the freshwater input from the Arctic area.

7. Challenges and future perspectives

7.1. Detecting and tracking PLs

Although our knowledge about PLs has significantly increased during the last few decades, the are still many unanswered questions. During the last Polar Low Workshops organised by the EPLWG, the scientific community highlighted the need to determine the objective criteria that define PLs (Spengler et al., 2017; Heinemann et al., 2019). These objective criteria could be then used in detection and tracking algorithms to study the climatology of PLs. In this regard, during the 13th Polar Low Workshop the scientific community expressed the need to

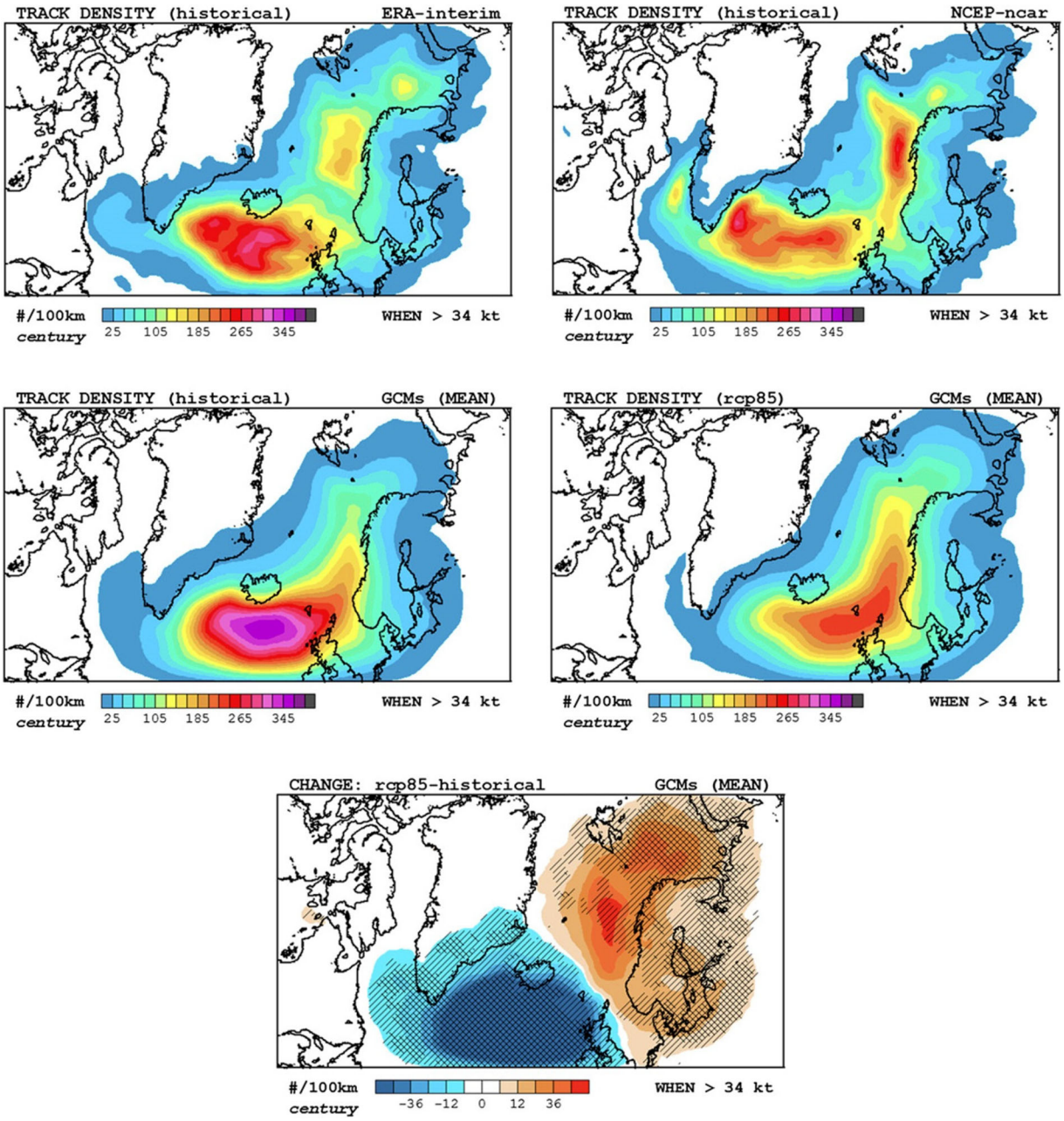

Fig. 10. PL track density obtained by applying a statistical downscaling method to (top left) ERA-I and (top right) NCEP-NCAR reanalyses, and to the multimodel mean of 20 Global Climate Models for the (middle row, left) historical and (middle row, right) future RCP8.5 scenarios. (Bottom) Change in PL track density between the historical and the future periods. Model agreement at 66% and 80% levels is indicated by the hatched and cross-hatched areas, respectively. The PL track density is the number of storms per century within a radius of 100 km. From Romero and Emanuel (2017). © American Meteorological Society. Used with permission.

create an international intercomparison project of PL detection and tracking (Spengler et al., 2017). PL research would enormously benefit from a project similar to the 'Intercomparison of mid-latitude storm diagnostics' (IMILAST) project, which is an intercomparison project of extratropical cyclone detection and tracking. Among other achievements, the research conducted within this project has provided information about the characteristics of mid-latitude cyclones that are consistent across different tracking methods (Neu et al., 2013). Since some of the challenges for identifying and tracking mid-latitude storms, such as their different shapes and sizes, are

similar for PLs, a project similar to IMILAST applied to PLs could help unveil the characteristics of PLs that are consistent across different tracking methods. In the framework of the IMILAST project, Simmonds and Rudeva (2014) conducted an intercomparison of tracking methods applied to extreme Arctic cyclones, showing the potential of such an approach to analyse the characteristics of cyclones developed in high latitudes. In particular, there is a need to analyse the climatology of PLs in the Southern Hemisphere, which has received scarce attention so far.

7.2. Observing and modelling PLs

For a PL detection and tracking algorithm to successfully identify PLs, the data used as input needs to correctly capture PLs. Hence, the correct representation of PLs in analyses, reanalyses and in the output of atmospheric models constitutes another key challenge for PL research. In order to obtain a better representation of PLs, more observations and better models are needed. Given the sparseness of the conventional observations in the polar regions, improving the quantity and quality of observations cannot be achieved in the short term. However, observational campaigns focussed on PLs could provide data against which simulation output could be verified, which is a necessary step to improve high-resolution atmospheric models. In particular, more airborne campaigns to observe the three-dimensional structure of PLs are needed. Dropsondes observations can provide valuable data for the analysis of the development mechanisms of PLs (e.g., Føre et al., 2011) and for the verification of PL simulations (e.g., Stoll et al., 2020). Unfortunately, given the small size and short lifetime of PLs, the success of such observational campaigns strongly depends on the skill of the models at forecasting them. The need to improve PL forecasting is indeed another challenge highlighted during the last Polar Low Workshops organised by the EPLWG (Spengler et al., 2017; Heinemann et al., 2019). For weather in mid-latitudes, the lead time of a skilful deterministic forecast is roughly ten days. This practical atmospheric predictability limit could be improved by reducing the uncertainty on the initial conditions. A decrease in the uncertainty of an order of magnitude would result in an increase of up to five days in the lead time. Nevertheless, for small-scale weather systems the room for improvement is much smaller given that many initial conditions uncertainties are associated with convective and mesoscale instabilities (Zhang et al., 2019). Moreover, in contrast to forecasting in tropical regions and mid-latitudes, the sources of perturbation growth are not well known yet for the polar regions (Jung et al., 2016). Thus, an interesting course of research would be to analyse the sources of perturbation growth in order to determine the atmospheric predictability limit for PLs. As far as atmospheric models are concerned, PL forecasting has benefitted from the development of high-resolution atmospheric models, although an increased resolution entails the need to adapt the parameterisations accordingly. In this regard, one of the current issues in operational forecasting is that the current size of the grid mesh of operational models, which is of a few kilometres, corresponds to the 'grey zone' of convection (Heinemann et al., 2019).

The use of high-resolution, limited-area coupled atmosphere-ocean-ice models to simulate PLs is a promising area for future research. The recent study by Wu (2021) has shown that a coupled atmosphere-wave-ocean-ice model provides an improved the representation of PLs by accounting for the coupling processes that directly and indirectly affect PL development. Further, coupled models provide a more comprehensive picture of the impact of PLs on the ocean. In addition, coupled atmosphere-ocean-wave models are required to correctly represent how surface winds are modulated by ocean waves (Gutowski et al., 2020).

The upgrading of numerical models needs to be accompanied by appropriate methods to verify the simulation results against observations. In PL research, it has been customary to perform visual verification of PL simulations. Nevertheless, objective verification methods should be applied since they allow the quantification of model performance. Among the objective verification methods available, spatial verification methods are preferred over traditional verification statistics because they are more suitable for the verification of spatial forecasts. Feature-based verification methods are particularly suitable for the verification of PL simulations since they provide information on the structure, location and intensity errors of identified features (Jolliffe and Stephenson, 2012).

7.3. Understanding the development mechanisms of PLs

Despite the large number of case studies conducted, a comprehensive understanding of the mechanisms involved in the formation and intensification of PLs is yet to be obtained. The analysis of the energy budget of PLs is a valuable approach to acquire knowledge about the energy sources, sinks and conversions involved in PL development. Although some work has already been done in that direction, there is still room for improvement. The energy budget equations should ideally be applied to the output from high-resolution coupled ocean-atmosphere models as they represent the energy fluxes between the ocean and

the atmosphere, thus capturing the atmosphere-ocean feedbacks involved in PL intensification. The energy budget of a PL could be analysed using local energy cycle equations such as those developed by Nikiéma and Laprise (2013), which have been successfully applied by Clément et al. (2017) to analyse the role of different mechanisms in the development of an extratropical cyclone.

7.4. Analysing the impact of climate change on the climatology of PLs

Finally, the impact of climate change on the spatio-temporal distribution of PLs is an area of research that has received attention in recent times. With the advent of high-resolution RCMs, it has become possible to analyse the future climatology of PLs. The use of coupled atmosphere-ocean RCMs to analyse the impact of climate change on PLs is a promising area of research, although it has been limited so far by the high computational cost. Global climate models (GCMs), which have long been excluded from the study of PLs due to their mesh coarseness, could prove to be a valuable tool to analyse the climatology of PLs. In effect, with the development of variable-resolution GCMs, it may be computationally feasible to study the climatology of PLs in a particular region using such GCMs. These advances in climate modelling will likely lead to prolific research on the impacts of recent and future climate change on the climatology of PLs, and its potential characteristics in terms of occurrence, intensity, lifetime, track and frequency.

Note

1. The Nordic Seas include the Norwegian Sea, the Greenland Sea, the Iceland Sea and the Barents Sea.

Acknowledgements

The authors are grateful for the availability of valuable observational and reanalyses datasets which have captured PLs, with specific acknowledgements addressed to ECMWF, EUMETSAT, NASA, and MET Norway. The IR imagery used are AVHRR channel 4 observations provided by EUMETSAT (https://navigator.eumetsat.int/product/EO:EUM:DAT:METOP:AVHRRL1) and MODIS spectral band 31 observations available at the Level-1 and Atmosphere Archive & Distribution System Distributed Active Archive Center (http://dx.doi.org/10.5067/MODIS/MYD021KM.061). The ocean surface wind vectors product derived from the observations of ASCAT is provided by EUMETSAT (https://navigator.eumetsat.int/product/EO:EUM:DAT:METOP:OSI-104), and the multi-radar mosaic has been downloaded using MET Norway Thredds Service (https://thredds.met.no/thredds/catalog/remotesensing/reflectivity-nordic/catalog.html). ERA5 reanalysis from ECMWF is available at https://www.ecmwf.int/en/forecasts/datasets/reanalysis-datasets/era5. The authors are also grateful for the Global Self-consistent, Hierarchical, High-resolution Geography Database (GSHHG), developed and maintained by Dr. Paul Wessel, SOEST, University of Hawai'i, and Dr. Walter H. F. Smith, NOAA Laboratory for Satellite Altimetry. The GSHHG is available at https://www.ngdc.noaa.gov/mgg/shorelines/. The GSHHG has been used to represent the coastlines of the Northern and Southern Hemispheres. The authors would like to also thank Georges Huard and Frédérik Toupin for maintaining an efficient and user-friendly local computing facility, and Katja Winger for downloading and preparing available ERA5 reanalyses at the ESCER centre.

Disclosure statement

No potential conflict of interest was reported by the authors.

Funding

This work was supported by the Natural Sciences and Engineering Research Council of Canada (NSERC) under Grant 707337, by the project "Marine Environmental Observation, Prediction and Response"(MEOPAR; http://meopar.ca) of the Networks of Centres of Excellence (NCE; http://www.nce-rce.gc.ca) of Canada, by the UQAM under the scholarship for the exemption of additional tuition fees for foreign students, and by the UQAM's Faculty of Sciences under the programme "faculty financial support".

References

Adakudlu, M. and Barstad, I. 2011. Impacts of the ice-cover and sea-surface temperature on a polar low over the Nordic seas: a numerical case study. *Q. J. R. Meteorol. Soc.* **137**, 1716–1730. doi:10.1002/qj.856

Akperov, M., Rinke, A., Mokhov, I. I., Matthes, H., Semenov, V. A. and co-authors. 2018. Cyclone activity in the Arctic from an ensemble of regional climate models (Arctic CORDEX). *J. Geophys. Res. Atmos.* **123**, 2537–2554. doi:10.1002/2017JD027703

Albright, M. D., Reed, R. J. and Ovens, D. W. 1995. Origin and structure of a numerically simulated polar low over Hudson Bay. *Tellus A* **47**, 834–848. doi:10.3402/tellusa.v47i5.11578

Aspelien, T., Iversen, T., Bremnes, J. B. and Frogner, I.-L. 2011. Short-range probabilistic forecasts from the Norwegian limited-area EPS: long-term validation and a polar low study. *Tellus A* **63**, 564–584. doi:10.1111/j.1600-0870.2010.00502.x

Blechschmidt, A. M. 2008. A 2-year climatology of polar low events over the Nordic Seas from satellite remote sensing. *Geophys. Res. Lett.* **35**. doi:10.1029/2008GL033706

Blechschmidt, A.-M., Bakan, S. and Graßl, H. 2009. Large-scale atmospheric circulation patterns during polar low events over the Nordic seas. *J. Geophys. Res.* **114**.doi:10.1029/2008JD010865

Bourassa, M. A., Gille, S. T., Bitz, C., Carlson, D. and Cerovecki, I. 2013. High-latitude ocean and sea ice surface fluxes: challenges for climate research. *Bull. Am. Meteorol. Soc.* **94**, 403–423. doi:10.1175/BAMS-D11-00244.1

Bracegirdle, T. J. and Gray, S. L. 2008. An objective climatology of the dynamical forcing of polar lows in the Nordic seas. *Int. J. Climatol.* **28**, 1903–1919. doi:10.1002/joc.1686

Bracegirdle, T. J. and Gray, S. L. 2009. The dynamics of a polar low assessed using potential vorticity inversion. *Q. J. R. Meteorol. Soc.* **135**, 880–893. doi:10.1002/qj.411

Bracegirdle, T. J. and Kolstad, E. W. 2010. Climatology and variability of Southern Hemisphere marine cold-air outbreaks. *Tellus A* **62**, 202–208. doi:10.1111/j.1600-0870.2009.00431.x

Bromwich, D. H., Wilson, A. B., Bai, L., Liu, Z., Barlage, M. and co-authors. 2018. The Arctic system reanalysis, Version 2. *Bull. Am. Meteorol. Soc.* **99**, 805–828. doi:10.1175/BAMS-D-16-0215.1

Brümmer, B., Müller, G. and Noer, G. 2009. A polar low pair over the Norwegian Sea. *Mon. Weather Rev.* **137**, 2559–2575. doi:10.1175/2009MWR2864.1

Businger, S. 1985. The synoptic climatology of polar low outbreaks. *Tellus A* **37**, 419–432. doi:10.3402/tellusa.v37i5.11686

Businger, S. 1987. The synoptic climatology of polar-low outbreaks over the Gulf of Alaska and the Bering Sea. *Tellus A* **39**, 307–325. doi:10.3402/tellusa.v39i4.11762

Businger, S. and Reed, R. J. 1989. Cyclogenesis in cold air masses. *Wea. Forecasting* **4**, 133–156. doi:10.1175/1520-0434(1989)004<0133:CICAM>2.0.CO;2

Carleton, A. M. and Carpenter, D. A. 1990. Satellite climatology of 'polar lows' and broadscale climatic associations for the Southern Hemisphere. *Int. J. Climatol.* **10**, 219–246. doi:10.1002/joc.3370100302

Casati, B., Haiden, T., Brown, B., Nurmi, P. and Lemieux, J.-F. 2017. *Verification of Environmental Prediction in Polar Regions: Recommendations for the Year of Polar Prediction. WWRP 2017 - 1*, World Meteorological Organization, Geneva, Switzerland.

Cavaleri, L., Barbariol, F., Benetazzo, A., Bertotti, L., Bidlot, J.-R. and co-authors. 2016. The Draupner wave: a fresh look and the emerging view. *J. Geophys. Res. Oceans* **121**, 6061–6075. doi:10.1002/2016JC011649

Charney, J. G. and Eliassen, A. 1964. On the growth of the hurricane depression. *J. Atmos. Sci.* **21**, 68–75. doi:10.1175/1520-0469(1964)021<0068:OTGOTH>2.0.CO;2

Chen, F. and von Storch, H. 2013. Trends and variability of North Pacific Polar Lows. *Adv. Meteorol.* **2013**, 1–11. doi:10.1155/2013/170387

Claud, C., Dalaudier, F., Kero, J., Le Pichon, A., Hauchecorne, A. and co-authors. 2017. Exploring the signature of polar lows in infrasound: the 19–20 November 2008 cases. *Tellus A* **69**, 1338885. doi:10.1080/16000870.2017.1338885

Claud, C., Duchiron, B. and Terray, P. 2007. Associations between large-scale atmospheric circulation and polar low developments over the North Atlantic during winter. *J. Geophys. Res.* **112**.doi:10.1029/2006JD008251

Claud, C., Funatsu, B. M., Noer, G. and Chaboureau, J. P. 2009. Observation of polar lows by the advanced microwave sounding unit: potential and limitations. *Tellus A* **61**, 264–277. doi:10.1111/j.1600-0870.2008.00384.x

Clément, M., Nikiéma, O. and Laprise, R. 2017. Limited-area atmospheric energetics: illustration on a simulation of the CRCM5 over eastern North America for December 2004. *Clim. Dyn.* **48**, 2797–2818. doi:10.1007/s00382-016-3198-0

Condron, A. and Renfrew, I. A. 2013. The impact of polar mesoscale storms on northeast Atlantic Ocean circulation. *Nature Geosci.* **6**, 34–37. doi:10.1038/ngeo1661

Craig, G. C. and Gray, S. L. 1996. CISK or WISHE as the mechanism for tropical cyclone intensification. *J. Atmos. Sci.* **53**, 3528–3540. doi:10.1175/1520-0469(1996)053<3528:COWATM>2.0.CO;2

Dee, D. P., Uppala, S. M., Simmons, A. J., Berrisford, P., Poli, P. and co-authors. 2011. The ERA-Interim reanalysis: configuration and performance of the data assimilation system. *Q. J. R. Meteorol. Soc.* **137**, 553–597. doi:10.1002/qj.828

Doyle, J. D. and Shapiro, M. A. 1999. Flow response to large-scale topography: the Greenland tip jet. *Tellus A* **51**, 728–748. doi:10.3402/tellusa.v51i5.14471

Duncan, C. N. 1977. A numerical investigation of polar lows. *Q. J. R. Meteorol. Soc.* **103**, 255–267. doi:10.1002/qj.49710343604

Emanuel, K. A. 1986. An air-sea interaction theory for tropical cyclones. Part I: steady-state maintenance. *J. Atmos. Sci.* **43**, 585–604. doi:10.1175/1520-0469(1986)043<0585:AASITF>2.0.CO;2

Emanuel, K. A. and Rotunno, R. 1989. Polar lows as arctic hurricanes. *Tellus A* **41**, 1–17. doi:10.3402/tellusa.v41i1.11817

Ese, T., Kanestrø, I. and Pedersen, K. 1988. Climatology of polar lows over the Norwegian and Barents Seas. *Tellus A* **40**, 248–255. doi:10.3402/tellusa.v40i3.11798

Fletcher, J., Mason, S. and Jakob, C. 2016. The climatology, meteorology, and boundary layer structure of marine cold air outbreaks in both hemispheres. *J. Clim.* **29**, 1999–2014. doi:10.1175/JCLI-D-15-0268.1

Føre, I., Kristjánsson, J. E., Kolstad, E. W., Bracegirdle, T. J., Saetra, Ø. and co-authors. 2012. A 'hurricane-like' polar low fuelled by sensible heat flux: high-resolution numerical simulations. *Q. J. R. Meteorol. Soc.* **138**, 1308–1324. doi:10.1002/qj.1876

Føre, I., Kristjánsson, J. E., Saetra, Ø., Breivik, Ø., Røsting, B. and co-authors. 2011. The full life cycle of a polar low over the Norwegian Sea observed by three research aircraft flights. *Q. J. R. Meteorol. Soc.* **137**, 1659–1673. doi:10.1002/qj.825

Føre, I. and Nordeng, T. E. 2012. A polar low observed over the Norwegian Sea on 3–4 March 2008: high-resolution

numerical experiments. *Q. J. R. Meteorol. Soc.* **138**, 1983–1998. doi:10.1002/qj.1930

Forsythe, J. M. and Haynes, J. M. 2015. CloudSat observes a Labrador Sea Polar Low. *Bull. Am. Meteorol. Soc.* **96**, 1229–1231. doi:10.1175/BAMS-D-14-00058.1

Fu, G., Niino, H., Kimura, R. and Kato, T. 2004. A Polar Low over the Japan Sea on 21 January 1997. *Mon. Wea. Rev.* **132**, 1537–1551. doi:10.1175/1520-0493(2004)132<1537:APLOTJ>2.0.CO;2

Furevik, B. R., Schyberg, H., Noer, G., Tveter, F. and Röhrs, J. 2015. ASAR and ASCAT in Polar Low situations. *J. Atmos. Ocean. Technol.* **32**, 783–792. doi:10.1175/JTECH-D-14-00154.1

Gachon, P., Laprise, R., Zwack, P. and Saucier, F. J. 2003. The effects of interactions between surface forcings in the development of a model-simulated polar low in Hudson Bay. *Tellus A* **55**, 61–87. doi:10.3402/tellusa.v55i1.12079

Garcia-Quintana, Y., Courtois, P., Hu, X., Pennelly, C., Kieke, D. and co-authors. 2019. Sensitivity of Labrador Sea water formation to changes in model resolution, atmospheric forcing, and freshwater input. *J. Geophys. Res. Oceans* **124**, 2126–2152. doi:10.1029/2018JC014459

Gelaro, R., McCarty, W., Suárez, M. J., Todling, R. and Molod, A. 2017. The modern-era retrospective analysis for research and applications, Version 2 (MERRA-2). *J. Clim.* **30**, 5419–5454. doi:10.1175/JCLI-D-16-0758.1

Grønås, S. and Kvamstø, N. G. 1995. Numerical simulations of the synoptic conditions and development of Arctic outbreak polar lows. *Tellus A* **47**, 797–814. doi:10.3402/tellusa.v47i5.11576

Gutowski, W. J., Ullrich, P. A., Hall, A., Leung, L. R., O'Brien, T. A. and co-authors. 2020. The ongoing need for high-resolution regional climate models: process understanding and stakeholder information. *Bull. Am. Meteorol. Soc.* **101**, E664–E683. doi:10.1175/BAMS-D-19-0113.1

Hallerstig, M., Magnusson, L., Kolstad, E. W. and Mayer, S. 2021. How grid-spacing and convection representation affected the wind speed forecasts of four polar lows. *Q. J. R. Meteorol. Soc.* **147**, 150–165. doi:10.1002/qj.3911

Harold, J. M., Bigg, G. R. and Turner, J. 1999. Mesocyclone activity over the North-East Atlantic. Part 1: vortex distribution and variability. *Int. J. Climatol.* **19**, 1187–1204. doi:10.1002/(SICI)1097-0088(199909)19:11<1187::AID-JOC419>3.0.CO;2-Q

Harrold, T. W. and Browning, K. A. 1969. The polar low as a baroclinic disturbance. *Q. J. R. Meteorol. Soc.* **95**, 710–723. doi:10.1002/qj.49709540605

Heinemann, G. and Claud, C. 1997. Report of a workshop on "theoretical and observational studies of polar lows" of the European Geophysical Society Polar Lows Working Group. *Bull. Am. Meteorol. Soc.* **78**, 2643–2658. doi:10.1175/1520-0477-78.11.2643

Heinemann, G., Claud, C. and Spengler, T. 2019. Polar Low workshop. *Bull. Am. Meteorol. Soc.* **100**, ES89–ES92. doi:10.1175/BAMS-D-18-0103.1

Hersbach, H., Bell, B., Berrisford, P., Hirahara, S., Horányi, A. and co-authors. 2020. The ERA5 global reanalysis. *Q. J. R. Meteorol. Soc.* **146**, 1999–2049. doi:10.1002/qj.3803

Hirschi, J. J.-M., Barnier, B., Böning, C., Biastoch, A., Blaker, A. T. and co-authors. 2020. The Atlantic Meridional overturning circulation in high-resolution models. *J. Geophys. Res. Oceans* **125**. doi:10.1029/2019JC015522

Holton, J. R. and Hakim, G. J. 2013. *An Introduction to Dynamic Meteorology*. Elsevier Inc., San Diego.

Inoue, J., Hori, M. E., Tachibana, Y. and Kikuchi, T. 2010. A polar low embedded in a blocking high over the Pacific Arctic. *Geophys. Res. Lett.* **37**.doi:10.1029/2010GL043946

IPCC. 2019. Technical Summary. In: *IPCC Special Report on the Ocean and Cryosphere in a Changing Climate* (eds. H.-O. Pörtner, D. C. Roberts, V. Masson-Delmotte, P. Zhai and E. Poloczanska).

Irvine, E. A., Gray, S. L. and Methven, J. 2011. Targeted observations of a polar low in the Norwegian Sea. *Q. J. R. Meteorol. Soc.* **137**, 1688–1699. doi:10.1002/qj.914

Isachsen, P. E., Drivdal, M., Eastwood, S., Gusdal, Y., Noer, G. and co-authors. 2013. Observations of the ocean response to cold air outbreaks and polar lows over the Nordic Seas. *Geophys. Res. Lett.* **40**, 3667–3671. doi:10.1002/grl.50705

Jolliffe, I. T. and Stephenson, D. B. 2012. *Forecast Verification a Practitioner's Guide in Atmospheric Science*. John Wiley & Sons, Hoboken.

Jung, T., Gordon, N. D., Bauer, P., Bromwich, D. H., Chevallier, M. and co-authors. 2016. Advancing Polar prediction capabilities on daily to seasonal time scales. *Bull. Am. Meteorol. Soc.* **97**, 1631–1647. doi:10.1175/BAMS-D-14-00246.1

Klein, T. and Heinemann, G. 2002. Interaction of katabatic winds and mesocyclones near the eastern coast of Greenland. *Meteorol. Appl.* **9**, 407–422. doi:10.1017/S1350482702004036

Kobayashi, S., Ota, Y., Harada, Y., Ebita, A., Moriya, M. and co-authors. 2015. The JRA-55 reanalysis: general specifications and basic characteristics. *J. Meteorol. Soc. Jpn.* **93**, 5–48. doi:10.2151/jmsj.2015-001

Kolstad, E. W. 2006. A new climatology of favourable conditions for reverse-shear polar lows. *Tellus A* **58**, 344–354. doi:10.1111/j.1600-0870.2006.00171.x

Kolstad, E. W. and Bracegirdle, T. J. 2017. Sensitivity of an apparently hurricane-like polar low to sea-surface temperature. *Q. J. R. Meteorol. Soc.* **143**, 966–973. doi:10.1002/qj.2980

Kolstad, E. W., Bracegirdle, T. J. and Seierstad, I. A. 2009. Marine cold-air outbreaks in the North Atlantic: temporal distribution and associations with large-scale atmospheric circulation. *Clim. Dyn.* **33**, 187–197. doi:10.1007/s00382-008-0431-5

Krinitskiy, M., Verezemskaya, P., Grashchenkov, K., Tilinina, N., Gulev, S. and co-authors. 2018. Deep convolutional neural networks capabilities for binary classification of polar mesocyclones in satellite mosaics. *Atmosphere* **9**, 426. doi:10.3390/atmos9110426

Kristjánsson, J. E., Barstad, I., Aspelien, T., Føre, I., Godøy, Ø. and co-authors. 2011a. The Norwegian IPY–THORPEX: polar lows and Arctic fronts during the 2008 Andøya Campaign. *Bull. Am. Meteorol. Soc.* **92**, 1443–1466. doi:10.1175/2011BAMS2901.1

Kristjánsson, J. E., Thorsteinsson, S., Kolstad, E. W. and Blechschmidt, A. M. 2011b. Orographic influence of east Greenland on a polar low over the Denmark Strait. *Q. J. R. Meteorol. Soc.* **137**, 1773–1789. doi:10.1002/qj.831

Laffineur, T., Claud, C., Chaboureau, J.-P. and Noer, G. 2014. Polar lows over the Nordic Seas: improved representation in ERA-Interim compared to ERA-40 and the impact on downscaled simulations. *Mon. Weather Rev.* **142**, 2271–2289. doi:10.1175/MWR-D-13-00171.1

Landgren, O. A., Batrak, Y., Haugen, J. E., Støylen, E. and Iversen, T. 2019a. Polar low variability and future projections for the Nordic and Barents Seas. *Q. J. R. Meteorol. Soc.* **145**, 3116–3128. doi:10.1002/qj.3608

Landgren, O. A., Seierstad, I. A. and Iversen, T. 2019b. Projected future changes in Marine Cold-Air Outbreaks associated with polar lows in the Northern North-Atlantic Ocean. *Clim. Dyn.* **53**, 2573–2585. doi:10.1007/s00382-019-04642-2

Leutwyler, D. and Schär, C. 2019. Barotropic instability of a Cyclone Core at kilometer-scale resolution. *J. Adv. Model. Earth Syst.* **11**, 3390–3402. doi:10.1029/2019MS001847

Linders, T. and Saetra, Ø. 2010. Can CAPE maintain polar lows? *J. Atmos. Sci.* **67**, 2559–2571. doi:10.1175/2010JAS3131.1

Listowski, C., Rojo, M., Claud, C., Delanoë, J., Rysman, J.-F. and co-authors. 2020. New insights into the vertical structure of clouds in Polar Lows, using Radar-Lidar satellite observations. *Geophys. Res. Lett.* **47**.doi:10.1029/2020GL088785

Mallet, P.-E., Claud, C., Cassou, C., Noer, G. and Kodera, K. 2013. Polar lows over the Nordic and Labrador Seas: synoptic circulation patterns and associations with North Atlantic-Europe wintertime weather regimes. *J. Geophys. Res. Atmos.* **118**, 2455–2472. doi:10.1002/jgrd.50246

Mallet, P.-E., Claud, C. and Vicomte, M. 2017. North Atlantic polar lows and weather regimes: do current links persist in a warmer climate? *Atmos. Sci. Lett.* **18**, 349–355. doi:10.1002/asl.763

Markowski, P. and Richardson, Y. 2010. *Mesoscale Meteorology in Midlatitudes*. John Wiley & Sons, Ltd, Chichester, UK.

Martin, R. and Moore, G. W. K. 2006. Transition of a synoptic system to a polar low via interaction with the orography of Greenland. *Tellus A* **58**, 236–253. doi:10.1111/j.1600-0870.2005.00169.x

McInnes, H., Kristiansen, J., Kristjánsson, J. E. and Schyberg, H. 2011. The role of horizontal resolution for polar low simulations. *Q. J. R. Meteorol. Soc.* **137**, 1674–1687. doi:10.1002/qj.849

Michel, C., Terpstra, A. and Spengler, T. 2018. Polar mesoscale cyclone climatology for the Nordic Seas based on ERA-interim. *J. Clim.* **31**, 2511–2532. doi:10.1175/JCLI-D-16-0890.1

Montgomery, M. T. and Farrell, B. F. 1992. Polar low dynamics. *J. Atmos. Sci.* **49**, 2484–2505. doi:10.1175/1520-0469(1992)049<2484:PLD>2.0.CO;2

Moore, G. W. K., Reader, M. C., York, J. and Sathiyamoorthy, S. 1996. Polar lows in the Labrador Sea. *Tellus A* **48**, 17–40. doi:10.3402/tellusa.v48i1.11630

Moore, G. W. K. and Vachon, P. W. 2002. A polar low over The Labrador Sea: interactions with topography and an upper-level potential vorticity anomaly, and an observation by RADARSAT-1 SAR. *Geophys. Res. Lett.* **29**, 20–1–20-4.

Moore, R. W. and Vonder Haar, T. H. 2003. Diagnosis of a polar low warm core utilizing the advanced microwave sounding unit. *Wea. Forecasting* **18**, 700–711. doi:10.1175/1520-0434(2003)018<0700:DOAPLW>2.0.CO;2

Nagata, M. 1993. Meso-β-scale vortices developing along the Japan-Sea polar-airmass convergence zone (JPCZ) cloud band: numerical simulation. *J. Meteorol. Soc. Jpn.* **71**, 43–57. doi:10.2151/jmsj1965.71.1_43

Neu, U., Akperov, M. G., Bellenbaum, N., Benestad, R., Blender, R. and co-authors. 2013. Imilast: a community effort to intercompare extratropical cyclone detection and tracking algorithms. *Bull. Am. Meteorol. Soc.* **94**, 529–547. doi:10.1175/BAMS-D-11-00154.1

Nikiéma, O. and Laprise, R. 2013. An approximate energy cycle for inter-member variability in ensemble simulations of a regional climate model. *Clim. Dyn.* **41**, 831–852. doi:10.1007/s00382-012-1575-x

Noer, G., Saetra, Ø., Lien, T. and Gusdal, Y. 2011. A climatological study of polar lows in the Nordic Seas. *Q. J. R. Meteorol. Soc.* **137**, 1762–1772. doi:10.1002/qj.846

Norwegian Meteorological Institute. 2013. The Torsvåg storm. http://polarlow.met.no/polar_lows/torsvaag/

Notz, D. and SIMIP Community. 2020. Arctic Sea Ice in CMIP6. *Geophys. Res. Lett.* **47**.doi:10.1029/2019GL086749

Orimolade, A. P., Furevik, B. R., Noer, G., Gudmestad, O. T. and Samelson, R. M. 2016. Waves in polar lows. *J. Geophys. Res. Oceans* **121**, 6470–6481. doi:10.1002/2016JC012086

Orlanski, I. 1975. A rational subdivision of scales for atmospheric processes. *Bull. Am. Meteorol. Soc.* **56**, 527–530.

Pellerin, P., Ritchie, H., Saucier, F. J., Roy, F., Desjardins, S. and co-authors. 2004. Impact of a two-way coupling between an atmospheric and an ocean-ice model over the Gulf of St. *Mon. Wea. Rev.* **132**, 1379–1398. doi:10.1175/1520-0493(2004)132<1379:IOATCB>2.0.CO;2

Pezza, A., Sadler, K., Uotila, P., Vihma, T., Mesquita, M. D. S. and co-authors. 2016. Southern Hemisphere strong polar mesoscale cyclones in high-resolution datasets. *Clim. Dyn.* **47**, 1647–1660. doi:10.1007/s00382-015-2925-2

Pithan, F., Svensson, G., Caballero, R., Chechin, D., Cronin, T. W. and co-authors. 2018. Role of air-mass transformations in exchange between the Arctic and mid-latitudes. *Nat. Geosci.* **11**, 805–812. doi:10.1038/s41561-018-0234-1

Prein, A. F., Rasmussen, R. and Stephens, G. 2017. Challenges and advances in convection-permitting climate modeling. *Bull. Am. Meteorol. Soc.* **98**, 1027–1030. doi:10.1175/BAMS-D-16-0263.1

Radovan, A., Crewell, S., Moster Knudsen, E. and Rinke, A. 2019. Environmental conditions for polar low formation and development over the Nordic Seas: study of January cases based on the Arctic System Reanalysis. *Tellus A* **71**, 1618131. doi:10.1080/16000870.2019.1618131

Rasmussen, E. 1979. The polar low as an extratropical CISK disturbance. *Q. J. R. Meteorol. Soc.* **105**, 531–549. doi:10.1002/qj.49710544504

Rasmussen, E. A., Ninomiya, K. and Carleton, A. M. 2003a. Climatology. In: *Polar Lows: Mesoscale Weather Systems in the Polar Regions* (eds. E. A. Rasmussen and J. Turner). Cambridge University Press, Cambridge, pp. 52–149.

Rasmussen, E. A. and Turner, J. 2003. *Polar Lows: Mesoscale Weather Systems in the Polar Regions*. Cambridge University Press, Cambridge.

Rasmussen, E. A., Turner, J., Ninomiya, K. and Renfrew, I. A. 2003b. Observational studies. In: *Polar Lows: Mesoscale Weather Systems in the Polar Regions* (eds. E. A. Rasmussen and J. Turner). Cambridge University Press, Cambridge, pp. 150–285.

Reed, R. J. and Duncan, C. N. 1987. Baroclinic instability as a mechanism for the serial development of polar lows: a case study. *Tellus A* **39A**, 376–384. doi:10.1111/j.1600-0870.1987.tb00314.x

Renfrew, I. A. 2003. Polar lows. In: *Encyclopedia of Atmospheric Sciences* (eds. J. R. Holton, J. A. Curry and J. A. Pyle). Academic Press, Amsterdam, pp. 1761–1768.

Roch, M., Benoit, R. and Parker, N. 1991. Sensitivity experiments for polar low forecasting with the CMC mesoscale finite-element model. *Atmos. Ocean* **29**, 381–419. doi:10.1080/07055900.1991.9649410

Rojo, M., Claud, C., Mallet, P.-E., Noer, G., Carleton, A. M. and co-authors. 2015. Polar low tracks over the Nordic Seas: a 14-winter climatic analysis. *Tellus A* **67**, 24660. doi:10.3402/tellusa.v67.24660

Rojo, M., Claud, C., Noer, G. and Carleton, A. M. 2019. In situ measurements of surface winds, waves, and sea state in polar lows over the North Atlantic. *J. Geophys. Res. Atmos.* **124**, 700–718. doi:10.1029/2017JD028079

Romero, R. and Emanuel, K. 2017. Climate change and hurricane-like extratropical cyclones: projections for North Atlantic polar lows and medicanes based on CMIP5 models. *J. Clim.* **30**, 279–299. doi:10.1175/JCLI-D-16-0255.1

Saetra, Ø., Linders, T. and Debernard, J. B. 2008. Can polar lows lead to a warming of the ocean surface? *Tellus A* **60**, 141–153. doi:10.1111/j.1600-0870.2007.00279.x

Saha, S., Moorthi, S., Pan, H.-L., Wu, X., Wang, J. and co-authors. 2010. The NCEP climate forecast system reanalysis. *Bull. Amer. Meteorol. Soc.* **91**, 1015–1058. doi:10.1175/2010BAMS3001.1

Sardie, J. M. and Warner, T. T. 1985. A numerical study of the development mechanisms of polar lows. *Tellus A* **37**, 460–477. doi:10.3402/tellusa.v37i5.11689

Sergeev, D., Renfrew, I. A. and Spengler, T. 2018. Modification of polar low development by orography and sea ice. *Mon. Weather Rev.* **146**, 3325–3341. doi:10.1175/MWR-D-18-0086.1

Sergeev, D. and Stepanenko, V. 2014. *Idealized Numerical Modeling of Polar Mesocyclones Dynamics Diagnosed by Energy Budget*. EGU General Assembly, Vienna.

Sergeev, D. E., Renfrew, I. A., Spengler, T. and Dorling, S. R. 2017. Structure of a shear-line polar low. *Q. J. R. Meteorol. Soc.* **143**, 12–26. doi:10.1002/qj.2911

Serreze, M. C. and Barry, R. G. 2011. Processes and impacts of Arctic amplification: a research synthesis. *Global Planet. Change* **77**, 85–96.

Serreze, M. C. and Barry, R. G. 2014. *The Arctic Climate System*. Cambridge University Press, New York.

Shimada, U., Wada, A., Yamazaki, K. and Kitabatake, N. 2014. Roles of an upper-level cold vortex and low-level baroclinicity in the development of polar lows over the Sea of Japan. *Tellus A* **66**, 24694. doi:10.3402/tellusa.v66.24694

Simmonds, I. and Rudeva, I. 2014. A comparison of tracking methods for extreme cyclones in the Arctic basin. *Tellus A* **66**, 25252. doi:10.3402/tellusa.v66.25252

Smirnova, J. and Golubkin, P. 2017. Comparing polar lows in atmospheric reanalyses: arctic system reanalysis versus ERA-Interim. *Mon. Weather Rev.* **145**, 2375–2383. doi:10.1175/MWR-D-16-0333.1

Smirnova, J. E., Golubkin, P. A., Bobylev, L. P., Zabolotskikh, E. V. and Chapron, B. 2015. Polar low climatology over the Nordic and Barents seas based on satellite passive microwave data. *Geophys. Res. Lett.* **42**, 5603–5609. doi:10.1002/2015GL063865

Smith, G. C., Roy, F. and Brasnett, B. 2013. Evaluation of an operational ice–ocean analysis and forecasting system for the Gulf of St Lawrence. *Q. J. R. Meteorol. Soc.* **139**, 419–433. doi:10.1002/qj.1982

Spengler, T., Claud, C. and Heinemann, G. 2017. Polar low workshop summary. *Bull. Am. Meteorol. Soc.* **98**, ES139–ES142. doi:10.1175/BAMS-D-16-0207.1

Spengler, T., Renfrew, I. A., Terpstra, A., Tjernström, M., Screen, J. and co-authors. 2016. High-latitude dynamics of atmosphere–ice–ocean interactions. *Bull. Am. Meteorol. Soc.* **97**, ES179–ES182. doi:10.1175/BAMS-D-15-00302.1

Stoll, P. J., Graversen, R. G., Noer, G. and Hodges, K. 2018. An objective global climatology of polar lows based on reanalysis data. *Q. J. R Meteorol. Soc.* **144**, 2099–2117. doi:10.1002/qj.3309

Stoll, P. J., Valkonen, T. M., Graversen, R. G. and Noer, G. 2020. A well-observed polar low analysed with a regional and a global weather-prediction model. *Q. J. R. Meteorol. Soc.* **146**, 1740–1767. doi:10.1002/qj.3764

Tansley, C. E. and James, I. N. 1999. Feedbacks between sea ice and baroclinic waves using a linear quasi-geostrophic model. *Q. J. R. Meteorol. Soc.* **125**, 2517–2534. doi:10.1002/qj.49712555909

Terpstra, A., Spengler, T. and Moore, R. W. 2015. Idealised simulations of polar low development in an Arctic moist-baroclinic environment. *Q. J. R. Meteorol. Soc.* **141**, 1987–1996. doi:10.1002/qj.2507

Terpstra, A., Michel, C. and Spengler, T. 2016. Forward and reverse shear environments during polar low genesis over the Northeast Atlantic. *Mon. Weather Rev.* **144**, 1341–1354. doi:10.1175/MWR-D-15-0314.1

Turner, J. and Rasmussen, E. A. 2003. Conclusions and future research needs. In: *Polar Lows: Mesoscale Weather Systems in the Polar Regions* (eds. E. A. Rasmussen and J. Turner). Cambridge University Press, Cambridge, pp. 575–579.

Turner, J., Rasmussen, E. A. and Carleton, A. M. 2003. Introduction. In: *Polar Lows: Mesoscale Weather Systems in the Polar Regions* (eds. E. A. Rasmussen and J. Turner). Cambridge University Press, Cambridge, pp. 1–51.

Uppala, S. M., KÅllberg, P. W., Simmons, A. J., Andrae, U., Bechtold, V. D. C. and co-authors. 2005. The ERA-40 re-analysis. *Q. J. R. Meteorol. Soc.* **131**, 2961–3012. doi:10.1256/qj.04.176

van Delden, A., Rasmussen, E. A., Turner, J. and Røsting, B. 2003. Theoretical investigations. In: *Polar Lows: Mesoscale Weather Systems in the Polar Regions* (eds. E. A. Rasmussen and J. Turner). Cambridge University Press, Cambridge, pp. 286–404.

van Vuuren, D. P., Edmonds, J., Kainuma, M., Riahi, K., Thomson, A. and co-authors. 2011. The representative concentration pathways: an overview. *Clim. Change* **109**, 5–31., doi:10.1007/s10584-011-0148-z

Verezemskaya, P., Tilinina, N., Gulev, S., Renfrew, I. A. and Lazzara, M. 2017. Southern Ocean mesocyclones and polar lows from manually tracked satellite mosaics. *Geophys. Res. Lett.* **44**, 7985–7993. doi:10.1002/2017GL074053

Verezemskaya, P. S. and Stepanenko, V. M. 2016. Numerical simulation of the structure and evolution of a polar mesocyclone over the Kara Sea. Part 1. Model validation and estimation of instability mechanisms. *Russ. Meteorol. Hydrol.* **41**, 425–434. doi:10.3103/S1068373916060078

Wagner, J. S., Gohm, A., Dörnbrack, A. and Schäfler, A. 2011. The mesoscale structure of a polar low: airborne lidar measurements and simulations. *Q. J. R. Meteorol. Soc.* **137**, 1516–1531. doi:10.1002/qj.857

Wilhelmsen, K. 1985. Climatological study of gale-producing polar lows near Norway. *Tellus A* **37**, 451–459. doi:10.3402/tellusa.v37i5.11688

Wu, L. 2021. Effect of atmosphere-wave-ocean/ice interactions on a polar low simulation over the Barents Sea. *Atmos. Res.* **248**, 105183. doi:10.1016/j.atmosres.2020.105183

Wu, L., Martin, J. E. and Petty, G. W. 2011. Piecewise potential vorticity diagnosis of the development of a polar low over the Sea of Japan. *Tellus A* **63**, 198–211. doi:10.1111/j.1600-0870.2011.00511.x

Xia, L., Zahn, M., Hodges, K., Feser, F. and Storch, H. 2012. A comparison of two identification and tracking methods for polar lows. *Tellus A* **64**, 17196. doi:10.3402/tellusa.v64i0.17196

Yanase, W., Fu, G., Niino, H. and Kato, T. 2004. A polar low over the Japan Sea on 21 January 1997. Part II: a numerical study. *Mon. Weather Rev* **132**, 1552–1574. doi:10.1175/1520-0493(2004)132<1552:APLOTJ>2.0.CO;2

Yanase, W. and Niino, H. 2004. Structure and energetics of non-geostrophic non-hydrostatic baroclinic instability wave with and without convective heating. *JMSJ.* **82**, 1261–1279. doi:10.2151/jmsj.2004.1261

Yanase, W. and Niino, H. 2007. Dependence of polar low development on baroclinicity and physical processes: an idealized high-resolution numerical experiment. *J. Atmos. Sci.* **64**, 3044–3067. doi:10.1175/JAS4001.1

Yanase, W., Niino, H., Watanabe, S. I. I., Hodges, K., Zahn, M. and co-authors. 2016. Climatology of polar lows over the Sea of Japan using the JRA-55 reanalysis. *J. Clim.* **29**, 419–437. doi:10.1175/JCLI-D-15-0291.1

Zahn, M., Storch, H. V. and Bakan, S. 2008. Climate mode simulation of North Atlantic polar lows in a limited area model. *Tellus A* **60**, 620–631. doi:10.1111/j.1600-0870.2008.00330.x

Zahn, M. and von Storch, H. 2008a. A long-term climatology of North Atlantic polar lows. *Geophys. Res. Lett.* **35**.doi:10.1029/2008GL035769

Zahn, M. and von Storch, H. 2008b. Tracking polar lows in CLM. *Metz.* **17**, 445–453. doi:10.1127/0941-2948/2008/0317

Zahn, M. and von Storch, H. 2010. Decreased frequency of North Atlantic polar lows associated with future climate warming. *Nature* **467**, 309–312. doi:10.1038/nature09388

Zappa, G., Shaffrey, L. and Hodges, K. 2014. Can polar lows be objectively identified and tracked in the ECMWF operational analysis and the ERA-Interim reanalysis? *Mon. Weather Rev.* **142**, 2596–2608. doi:10.1175/MWR-D-14-00064.1

Zhang, F., Sun, Y. Q., Magnusson, L., Buizza, R., Lin, S.-J. and co-authors. 2019. What is the predictability limit of midlatitude weather? *J. Atmos. Sci.* **76**, 1077–1091. doi:10.1175/jas-d-18-0269.1

Published work 2

Polar low research: recent developments and promising courses of research

Author:	Marta Moreno-Ibáñez
Year:	2024
Journal:	*Frontiers in Earth Science* 12, 1368179
DOI:	10.3389/feart.2024.1368179

Authorship statement: Sole authorship.

frontiers | Frontiers in Earth Science

TYPE Mini Review
PUBLISHED 06 March 2024
DOI 10.3389/feart.2024.1368179

OPEN ACCESS

EDITED BY
Bin Yu,
Environment and Climate Change Canada (ECCC), Canada

REVIEWED BY
Thomas Ballinger,
University of Alaska Fairbanks, United States

*CORRESPONDENCE
Marta Moreno-Ibáñez,
marta.morenoibanez@colorado.edu

RECEIVED 10 January 2024
ACCEPTED 20 February 2024
PUBLISHED 06 March 2024

CITATION
Moreno-Ibáñez M (2024), Polar low research: recent developments and promising courses of research.
Front. Earth Sci. 12:1368179.
doi: 10.3389/feart.2024.1368179

Polar low research: recent developments and promising courses of research

Marta Moreno-Ibáñez[1,2]*

[1]Cooperative Institute for Research in Environmental Sciences, University of Colorado Boulder, Boulder, CO, United States, [2]National Snow and Ice Data Center, University of Colorado Boulder, Boulder, CO, United States

Polar lows (PLs) are intense maritime mesoscale weather systems that develop during marine cold air outbreaks at high latitudes. The objective of this review is to describe the advances in polar low research since the last literature review—published 3 years ago—, indicate the knowledge gaps that remain, and suggest promising courses of research. Among the breakthroughs identified here are the first climatology of PLs obtained with a global atmospheric model, and increased evidence showing that baroclinic instability is the main mechanism leading to PL development. Despite these advances, many challenges persist such as the lack of conventional observations of PLs and the need to better understand coupled atmosphere-ocean processes involved in PL development. With the rapid advances in deep learning, this method has the potential to be used for PL forecasting.

KEYWORDS

polar low, mesoscale cyclone, cold air outbreak, Arctic, Antarctic, severe weather, baroclinic instability

1 Introduction

Polar lows (PLs) are strong mesoscale maritime cyclones that form near the snow-covered continents or sea ice edge during marine cold air outbreaks (MCAOs) at high latitudes. PLs have a horizontal scale ranging from 200 to 1,000 km, and their associated near-surface winds are near or above gale force (Turner et al., 2003). Their typical lifetime ranges from 12 to 32 h (Stoll, 2022). The cloud signature of PLs is comma-shaped (e.g., Moreno-Ibáñez et al., 2023b) or spiraliform (e.g., Ganeshan et al., 2022; Figure 1), and can change during their lifetime (e.g., Lackner et al., 2023). The last comprehensive literature review on PL research was published 3 years ago by Moreno-Ibáñez et al. (2021). PL research has greatly advanced since then; for instance, a climatology of PLs has been obtained using a global atmospheric model for the first time (Bresson et al., 2022).

The objective of this review is to summarize the recent advances in polar low research since the review conducted by Moreno-Ibáñez et al. (2021) in order to highlight the knowledge gaps that still need to be addressed as well as promising directions of research. This review is relevant and timely given that a preparatory planning phase is currently undergoing for the 5th International Polar Year (IPY) 2032–2033[1]. This manuscript is structured in five main sections: observations and numerical representation of PLs, present

1 The initial concept note of the IPY 2032–2033 is available at https://iasc.info/images/IPY/Initial_IPY_Concept_Note_-_Version_October_2023.pdf (accessed on 5 January 2024).

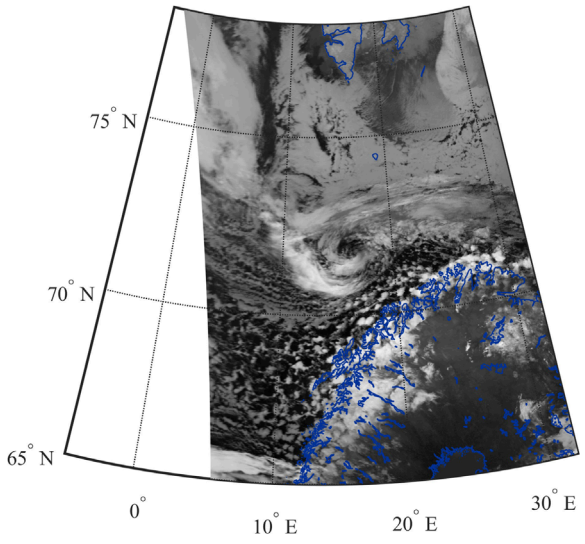

FIGURE 1
Polar low developed on 1 March 2021 captured by the Advanced Very High Resolution Radiometer (AVHRR) channel 4. The blue outlining represents the shoreline.

and future climatology of PLs, development mechanisms of PLs, other advances in PL research, and discussion.

2 Observations and numerical representation of PLs

2.1 Observations

Despite the wide variety of observations at the mesoscale (Bluestein et al., 2022), conventional observations over the ocean at high latitudes are scarce. The recent observations of PLs during the Cold-air Outbreaks in the Marine Boundary Layer Experiment (COMBLE, Geerts et al., 2022) have allowed the analysis of their vertical structure (Lackner et al., 2023). In 2022, the HALO-(AC)^3 airborne field campaign, whose objective was to provide observations of air mass transformation during meridional transport to and from the Arctic, captured several MCAOs and a PL (Ehrlich et al., 2023). This year, the Cold Air Outbreak Experiment in the Sub-Arctic Region (CAESAR)[2] will provide observations of clouds that form during MCAOs, and has therefore the potential to capture PLs. Regarding satellite observations, Synthetic Aperture Radar (SAR) observations provide details of the structure of PLs thanks to their high resolution (Tollinger et al., 2021). Atmospheric fronts and cyclonic centers are key features in SAR images that allow the identification of polar mesoscale cyclones using a deep learning algorithm (Grahn and Bianchi, 2022). However, SAR observations have rarely been used to study PLs (e.g., Hallerstig et al., 2021), probably because the current wind retrieval techniques perform poorly with highly variable wind (Tollinger et al., 2021).

2.2 Reanalyses

ERA5 (Hersbach et al., 2020; Bell et al., 2021), the fifth–generation reanalysis of the European Centre for Medium–Range Weather Forecasts, is a valuable global reanalysis for the study of PLs given its relatively high horizontal resolution and hourly output. It has a 31-km grid mesh and 137 vertical levels that extend to 0.01 hPa (Hersbach et al., 2020). Since its release, ERA5 has been used to develop climatologies of PLs (e.g., Stoll, 2022), to analyze their structure (e.g., Meyer et al., 2021) and the large–scale conditions associated with their development (e.g., Boyd et al., 2022), and as initial and boundary conditions for limited-area atmospheric models (e.g., Wu, 2021). ERA5 captures more PLs than its predecessor, ERA-Interim (Stoll et al., 2021). Nevertheless, ERA5 underestimates near–surface wind speed associated with PLs (Haakenstad et al., 2021; Gurvich et al., 2022; Køltzow et al., 2022). The Copernicus Arctic Regional Reanalysis (CARRA, Yang et al., 2020), which uses ERA5 as lateral boundary conditions, has a 2.5–km grid mesh and 65 vertical levels, and provides 3-hourly output. CARRA shows better performance than ERA5 (Isaksen et al., 2022; Køltzow et al., 2022). In particular, CARRA provides a better representation of the 10–m wind and 2–m temperature during the dissipation of PLs over land (Køltzow et al., 2022). The 3-km Norwegian Reanalysis (NORA3, Haakenstad et al., 2021) shows more skill than ERA5 at representing the 10–m wind speed, especially over the mountains and the coast.

2.3 Atmospheric models

With an increasing horizontal resolution, global atmospheric models will become a useful tool to study PLs. For example, Bresson et al. (2022) have provided the first climatology of PLs with a global atmospheric model. High-resolution atmospheric models are commonly used to study PLs because they provide details of their structure, which is essential to explain their genesis and intensification mechanisms (e.g., Moreno-Ibáñez et al., 2023a). The resolution of the model determines how certain processes associated with PL development are represented. For example, the higher the atmospheric resolution, the higher the maximum surface sensible and latent heat fluxes associated with MCAOs are (Spensberger and Spengler, 2021). Xue et al. (2021) recommend using a grid mesh of less than 3 km to simulate PLs. The representation of PLs by atmospheric models strongly depends on the initial conditions and on the initialization time (Revokatova et al., 2021; Xue et al., 2021; Moreno-Ibáñez et al., 2023b). High-resolution initial conditions are important to correctly simulate PLs (Xue et al., 2021). Moreover, high-resolution boundary conditions at the ocean surface, especially near the sea ice edge, are also likely to be important to correctly represent the atmospheric temperature gradients that contribute to PL genesis. For instance, Renfrew et al. (2021) have found that the gradients of the surface fluxes and near-surface atmospheric fields over the marginal ice zone simulated by Met Office's Unified Model

2 Information about CAESAR is available at https://www.eol.ucar.edu/field_projects/caesar (accessed on 17 February 2024).

(MetUM, Bush et al., 2020), which has a 2.2-km grid mesh, were not as sharp as observed during the Iceland-Greenland Seas Project (Renfrew et al., 2019) since the sea ice field in the surface boundary conditions was too smooth. When simulating PLs, the use of data assimilation provides better results compared to a "cold start" (i.e., using analyses and reanalyses) (Kim et al., 2019; Xue et al., 2021), and the assimilation of satellite radiances is recommended (Xue et al., 2021). Assimilating adaptively thinned cloud-cleared hyperspectral infrared radiances from the Atmospheric Infrared Sounder instrument on board the NASA Aqua satellite can have a positive impact on the representation of PLs (Ganeshan et al., 2022).

2.4 Wave models

Kudryavtsev et al. (2022) suggest applying extended duration laws to provide first-guess wave parameters that can be used with a two-dimensional parametric wave model to simulate waves associated with PLs, and this method has been applied by Yurovskaya et al. (2023) to estimate the wavelength and significant wave height of waves associated with PLs.

3 Present and future climatology of PLs

MCAO indexes have been often used in climatology studies as indicator of favorable conditions for PL genesis (e.g., Landgren et al., 2019). In general, the indexes used to identify MCAOs are computed by subtracting the potential temperature at a certain pressure level from the sea surface potential temperature (e.g., Fletcher et al., 2016). Consequently, these indexes are very sensitive to the selected pressure level (Meyer et al., 2021). To tackle this limitation, Terpstra et al. (2021) and Meyer et al. (2021) have developed new MCAO indexes that take into account the vertical structure of the air masses. By using the PL list STARS-DAT (Noer et al., 2011; Eastwood et al., 2012), Meyer et al. (2021) have shown that their MCAO index has more skill at indicating the location and time of PL formation than the traditional MCAO indexes. Nevertheless, although MCAO is an essential condition for PL genesis, it is not sufficient (Terpstra et al., 2021; Boyd et al., 2022). A more adequate proxy for PLs is the PL genesis potential index (PGI) developed by Boyd et al. (2022), which is composed of an environmental baroclinicity index in addition to a MCAO index, and captures the observed climatology of PLs reasonably well.

Recently, a few subjective and objective climatologies of PLs have been produced. Using a subjective method, Golubkin et al. (2021) have obtained a PL list in the North Atlantic for 2015–2017. In contrast to previous studies (Moreno-Ibáñez et al., 2021), the authors have not found a high PL activity over the Irminger Sea, and they have found that the PL season is somewhat shorter than previously reported. Objective global (Stoll, 2022), Northern Hemisphere (Bresson et al., 2022), and Southern Ocean (Farjami and Kazemi, 2024) climatologies of PLs have also been developed. Stoll (2022) has obtained a global climatology of PLs with ERA5 reanalysis (Hersbach et al., 2020) for 1979–2020. Bresson et al. (2022) have obtained recent (1985–2010) and future (2085–2110) climatologies of PLs in the Northern Hemisphere for the cold season with the Hadley Centre Global Environment Model version 3 Global Atmosphere-only version 3 (HadGEM3-GA3, Walters et al., 2011; Williams et al., 2015) with a 25-km grid mesh and 85 vertical levels. Farjami and Kazemi (2024) have obtained a climatology of PLs in the Southern Ocean between 60°S and 85°S for 2000–2020 using ERA5 reanalysis (Hersbach et al., 2020) and other datasets. Regarding the recent climatology of PLs, the spatial distribution and seasonal cycle obtained by Stoll (2022), Bresson et al. (2022) and Farjami and Kazemi (2024) are qualitatively similar to those reported in the literature (Moreno-Ibáñez et al., 2021). In the Northern Hemisphere, most PLs develop at latitudes poleward of 50°N in the North Atlantic and 40°N in the North Pacific (Stoll, 2022; Figure 2A). Although rare, some PLs develop in the marginal seas of the Arctic Ocean (e.g., Gurvich et al., 2022). In the Southern Hemisphere, most PLs develop near the sea ice edge, between 50°S and 65°S (Stoll, 2022; Figure 2B). They are most frequent over the Amundsen, Bellingshausen, and Ross Seas (Stoll, 2022; Farjami and Kazemi, 2024).

The impact of climate change on the frequency of PLs in the recent climate remains uncertain. In the Northen Hemisphere, Bresson et al. (2022) have not found a significant tendency in PL frequency, in agreement with previous studies (Moreno-Ibáñez et al., 2021). Nevertheless, Stoll (2022) has found a statistically significant increase in PL activity in the Northern Hemisphere for 1979–2020, and Chen and von Storch (2013) have found a slight increase in PL frequency in the North Pacific for 1948–2010. In the Southern Hemisphere, the PL frequency has not notably changed (Stoll et al., 2018; Stoll, 2022).

In the future, global warming is projected to lead to increased atmospheric stability (Landgren et al., 2019) and decreased Arctic sea ice extent (IPCC, 2021), which will affect the distribution of ocean surface heat fluxes (Moore et al., 2022). Like previous studies (Moreno-Ibáñez et al., 2021), Bresson et al. (2022) have found that there will be new areas of PL development where the sea ice retreats, and that the frequency of PLs will decrease in the Northern Hemisphere. The authors have also found a decrease in the intensity of PLs in the Northern Hemisphere, but the impact of global warming on the intensity of PLs remains uncertain. There is low confidence in the projected decline of Antarctic sea ice (IPCC, 2021), although the fact that there have been three record low summer sea ice extent in the last 7 years may indicate that the Antarctic sera ice has transitioned to a low-extent state (Purich and Doddridge, 2023). To the author's best knowledge, no study has examined how climate change will affect the spatiotemporal distribution of PLs in the Antarctic. Given the low confidence in Antarctic sea ice projections, this area of research is best left for future research when models represent the Antarctic sea ice evolution more accurately.

4 Development mechanisms of PLs

In the last decades of the past century, there was a controversy regarding the mechanisms of PL development, with some authors arguing that PLs formed by baroclinic instability (e.g., Mansfield, 1974), and others affirming that PLs were convective systems

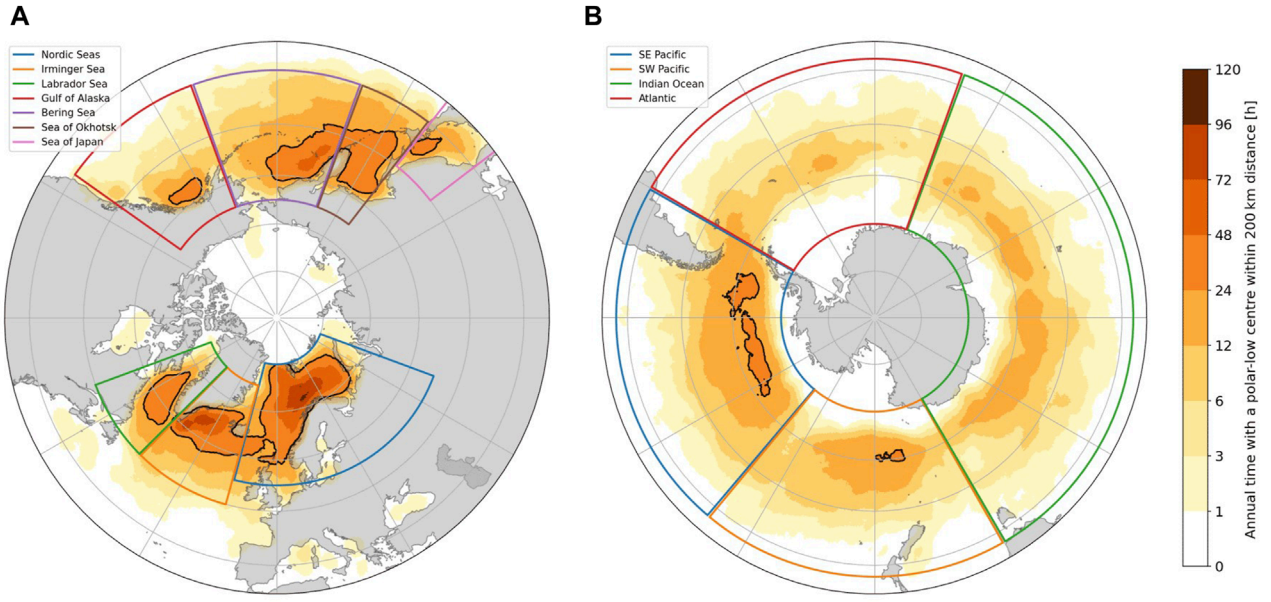

FIGURE 2
Annual mean density of polar low activity, defined as the number of polar low time steps within 200 km, for the **(A)** Northern Hemisphere and **(B)** Southern Hemisphere. The scale of the colorbar is logarithmic. Regions with polar low activity larger than 24 h yr^{-1} are delimited by a black contour.

(e.g., Rasmussen, 1979). Other studies pointed at the joint action of baroclinic instability and convection in PL development (e.g., Businger, 1985). In recent years, studies have provided evidence that moist baroclinic instability plays an important role in PL development (Terpstra et al., 2015; Haualand and Spengler, 2020; Stoll et al., 2021), and recent cases studies of PLs provide detailed examples of this mechanism (Moreno-Ibáñez et al., 2023a; Lackner et al., 2023). Moreover, the evidence does not support the existence of hurricane-like PLs (Kolstad and Bracegirdle, 2017; Stoll et al., 2021). Indeed, the spiraliform cloud signature of some PLs could be due to a warm seclusion process (Stoll et al., 2021; Lackner et al., 2023). Thus, strong baroclinicity in addition to low static stability are key ingredients for PL development (Boyd et al., 2022; Wang et al., 2023). There are other factors that contribute to PL development, such as the generation of convergence zones when MCAOs occur downstream of a sea ice edge with a certain shape (Watanabe et al., 2022), and the occurrence of weather events that can trigger PL formation, such as katabatic storms (e.g., Gutjahr et al., 2022). Although baroclinic eddies are the main responsible for poleward energy transport in mid-latitudes (Holton and Hakim, 2013), Stoll et al. (2023) have found that the meridional energy transport by mesoscale eddies—such as PLs—is negligible on annual and seasonal timescales.

Consistent with baroclinic instability as the main mechanism for PL development, PLs mainly form and intensify in environments with strong wind shear—forward-shear, reverse-shear, right-shear and left-shear—and dissipate in weak-shear environments (Stoll et al., 2021). Most often, PLs develop in forward-shear environments (Stoll, 2022). The type of environments where PLs form is closely related to their translation direction. PLs with north-eastward (southward) motion tend to develop in forward-shear (reverse-shear) environments, PLs with eastward motion are common in left-shear environments, and PLs with slow motion without a dominating direction occur in environments with any type of shear (Yan et al., 2023).

Despite coupled atmosphere–ocean-sea ice interactions being involved in PL development, this area of research has been largely neglected. Since PLs form in MCAO, the coupled processes that take place during those events are relevant for their development. A case study of an observed MCAO in the western Nordic Seas has showed that the ocean mixed layer warmed in the boundary current region, whereas it cooled in the interior region of the Iceland Sea (Renfrew et al., 2023). Consistent with this finding, Wu (2021) has found that the large surface heat fluxes associated with PLs cause sea surface temperature (SST) cooling, but, in regions with an ocean temperature inversion—such as near the sea ice edge—the strong winds associated with PLs lead to SST warming through upper-ocean mixing. In turn, this SST warming or cooling influences PL development through surface heat fluxes (Wu, 2021).

5 Other advances in PL research

Subseasonal prediction of PL activity is an area of research that has gained increased attention. The Madden-Julian Oscillation has significant impacts on PL frequency in the Northern Hemisphere (Wang et al., 2023). In the Norwegian and Barents Seas, PLs are most frequent during the Atlantic Ridge regime and the negative phase of the North Atlantic Oscillation (NAO-) regime, and are less frequent during the Scandinavian blocking regime (Mallet et al.,

2013; Yan et al., 2023; Boyd and Wang, 2024). In the Irminger Sea, PLs are more frequent during the positive phase of the NAO (NAO+) regime, and less frequent during the NAO- regime and the Scandinavian blocking regime (Boyd and Wang, 2024). In the Labrador Sea, PL activity is strongly decreased during the NAO- regime (Mallet et al., 2013; Chang et al., 2022; Yan et al., 2023; Boyd and Wang, 2024). Sudden stratospheric warmings (SSWs) are associated with a notable decrease in PL activity over the Labrador Sea during the following 3 weeks (Chang et al., 2022), which is consistent with the fact that SSWs are associated with a decreased frequency of MCAOs over this area (Afargan-Gerstman et al., 2020). In the Bering Sea, Sea of Okhotsk, and Gulf of Alaska, PL activity increases during the Arctic low regime, and decreases during the Pacific wave train regime (Boyd and Wang, 2024). A promising method to produce subseasonal forecasts of PL activity is the PGI (Boyd et al., 2023; Boyd and Wang, 2024), but its forecasting skill depends on the region, with predictability being highest over the Nordic, Irminger, Labrador, and Bering Seas (Boyd et al., 2023).

Machine learning, which has many applications in meteorology (Chase et al., 2022; Chase et al., 2023) has been used to study PLs. For instance, self-organizing maps have been used to identify typical environments where PLs develop by mapping PL-centered temperature anomaly fields to 3 × 3 nodes (Stoll et al., 2021) and deep learning has been used to detect maritime polar mesoscale cyclones in satellite images (Krinitskiy et al., 2018; Grahn and Bianchi, 2022).

6 Discussion

This review has shown that there have been important advances in PL research that address some of the challenges identified by Moreno-Ibáñez et al. (2021), such as the first climatology of PLs obtained with a global atmospheric model (Bresson et al., 2022), efforts to improve the representation of PLs in atmospheric models (e.g., Ganeshan et al., 2022), and a better understanding of PL development mechanisms (e.g., Stoll et al., 2021). Notwithstanding this, many challenges remain. The main advances in PL research and remaining challenges can be summarized as follows:

- *Observations and numerical representation of PLs*: PL research using ERA5 global reanalysis has been fruitful, but the potential of CARRA and NORA3 regional reanalyses for the study of PLs has not been explored yet. Despite efforts to improve the representation of PLs in high-resolution atmospheric models, it is unclear which variables in the initial conditions have the most important impact on PL forecasting. More conventional observations of PLs are needed to adequately assess the performance of high-resolution models.
- *Present and future climatology of PLs*: The first climatology of PLs with a global atmospheric model has opened new perspectives in the study of the impact of climate change on the spatio-temporal distribution of PLs, an area of research where many uncertainties remain. Although the need to conceive an intercomparison project of PL detection and tracking to determine the common characteristics of PLs obtained with different tracking methods and datasets has been highlighted in previous Polar Low Workshops (e.g., Spengler et al., 2017), such endeavor has not been undertaken yet.
- *Development mechanisms of PLs*: Recent research points at baroclinic instability having a major role in PL development. Knowledge about coupled atmosphere-ocean interactions involved in PL development is lacking.
- *Other advances*: The PGI is a new tool that can be used for subseasonal forecasting of PL activity. Despite its potential for the study PLs, machine learning has not been widely used in PL studies yet.

In what follows, the main key challenges in PL research and promising courses of research are discussed in more detail.

Conventional observations with high spatial and temporal resolution are needed to verify simulations of PLs with high-resolution atmospheric models. Therefore, planning for IPY 2032–2033 should ensure that targeted observations of PLs are made in regions where conventional observations are scarce. In addition, the investigation of the coupled atmosphere-ocean processes undoubtedly deserves more attention. The effect of atmosphere-ocean interactions in PL development remains to be elucidated. In the case of tropical cyclones, studies have shown that coupled atmosphere-ocean simulations lead to a decrease in their intensity compared to atmosphere-only simulations (e.g., Smith et al., 2018). Therefore, it is recommended to conduct such studies with PLs to see if the same results are obtained. The effect of atmosphere-ocean interactions on the ocean during PL development should also be investigated, with especial emphasis on the impact of PLs on the ocean circulation (e.g., Condron and Renfrew, 2013). Given that conducting high-resolution simulations with global coupled climate models is computationally expensive, a first step would be to conduct such a simulation for a short period of time. For instance, Gutjahr et al. (2022) have conducted a global coupled climate model simulation with a 5-km grid mesh covering 2 years, and they have found that katabatic storms lead to dense water formation in the western boundary current of the Irminger Sea.

Deep learning could become a useful tool for PL forecasting. The use of recurrent neural networks to forecast PL track and intensity, a method that has already been applied in tropical cyclone studies (e.g., Kapoor et al., 2023), is a promising area of research. Nevertheless, the application of deep learning to weather forecasting is in its beginnings (Schultz et al., 2021).

In summary, there have been important advances in PL research during the last 3 years, but many questions remain regarding, e.g., their impact on the ocean circulation. High-resolution coupled atmosphere-ocean-sea ice models, together with high-resolution conventional observations, are key to answering these questions.

Data availability statement

AVHRR channel 4 observations are available from EUMETSAT (2011) at https://navigator.eumetsat.int/product/EO:EUM:DAT:METOP:AVHRRL1. The dataset used to plot the shorelines is the Global Self-consistent, Hierarchical, High-resolution Geography Database (GSHHG; Wessel and Smith, 1996), available at https://www.ngdc.noaa.gov/mgg/shorelines/.

Author contributions

MM-I: Conceptualization, Investigation, Methodology, Visualization, Writing–original draft, Writing–review and editing.

Funding

The author(s) declare financial support was received for the research, authorship, and/or publication of this article. MM-I was supported by the CIRES Visiting Fellows Program, funded by NOAA Cooperative Agreement NA22OAR4320151. The statements, findings, conclusion, and recommendations are those of the author and do not necessarily reflect the views of NOAA or the U.S. Department of Commerce.

Conflict of interest

The author declares that the research was conducted in the absence of any commercial or financial relationships that could be construed as a potential conflict of interest.

Publisher's note

References

Afargan-Gerstman, H., Polkova, I., Papritz, L., Ruggieri, P., King, M. P., Athanasiadis, P. J., et al. (2020). Stratospheric influence on North Atlantic marine cold air outbreaks following sudden stratospheric warming events. *Weather Clim. Dyn.* 1 (2), 541–553. doi:10.5194/wcd-1-541-2020

Bell, B., Hersbach, H., Simmons, A., Berrisford, P., Dahlgren, P., Horányi, A., et al. (2021). The ERA5 global reanalysis: preliminary extension to 1950. *Q. J. R. Meteorological Soc.* 147 (741), 4186–4227. doi:10.1002/qj.4174

Bluestein, H. B., Carr, F. H., and Goodman, S. J. (2022). Atmospheric observations of weather and climate. *Atmosphere-Ocean* 60 (3-4), 149–187. doi:10.1080/07055900.2022.2082369

Boyd, K., and Wang, Z. (2024). Revisiting the relationship between polar lows and weather regimes. *J. Clim.* 37 (5), 1523–1538. doi:10.1175/JCLI-D-23-0309.1

Boyd, K., Wang, Z., Walsh, J., and Stoll, P. (2023). Subseasonal predictions of polar low activity using a hybrid statistical-dynamical approach. *Geophys. Res. Lett.* 50 (12), e2022GL102145. doi:10.1029/2022GL102145

Boyd, K., Wang, Z., and Walsh, J. E. (2022). A genesis potential index for polar lows. *J. Clim.* 35 (24), 7891–7902. doi:10.1175/JCLI-D-22-0100.1

Bresson, H., Hodges, K. I., Shaffrey, L. C., Zappa, G., and Schiemann, R. (2022). The response of northern Hemisphere polar lows to climate change in a 25 km high-resolution global climate model. *J. Geophys. Res. Atmos.* 127 (4), e2021JD035610. doi:10.1029/2021JD035610

Bush, M., Allen, T., Bain, C., Boutle, I., Edwards, J., Finnenkoetter, A., et al. (2020). The first Met Office unified model–JULES regional atmosphere and land configuration, RAL1. *Geosci. Model Dev.* 13 (4), 1999–2029. doi:10.5194/gmd-13-1999-2020

Businger, S. (1985). The synoptic climatology of polar low outbreaks. *Tellus A Dyn. Meteorology Oceanogr.* 37 (5), 419–432. doi:10.3402/tellusa.v37i5.11686

Chang, C.-C., Wang, Z., Walsh, J., and Stoll, P. J. (2022). Modulation of North Atlantic polar low activity and associated flow patterns by sudden stratospheric warmings. *J. Clim.* 35 (13), 4013–4026. doi:10.1175/jcli-d-21-0905.1

Chase, R. J., Harrison, D. R., Burke, A., Lackmann, G. M., and McGovern, A. (2022). A machine learning tutorial for operational meteorology. Part I: traditional machine learning. *Weather Forecast.* 37 (8), 1509–1529. doi:10.1175/WAF-D-22-0070.1

Chase, R. J., Harrison, D. R., Lackmann, G. M., and McGovern, A. (2023). A machine learning tutorial for operational meteorology. Part II: neural networks and deep learning. *Weather Forecast.* 38 (8), 1271–1293. doi:10.1175/WAF-D-22-0187.1

Chen, F., and von Storch, H. (2013). Trends and variability of North Pacific polar lows. *Adv. Meteorology* 2013, 1–11. doi:10.1155/2013/170387

Condron, A., and Renfrew, I. A. (2013). The impact of polar mesoscale storms on northeast Atlantic Ocean circulation. *Nat. Geosci.* 6 (1), 34–37. doi:10.1038/ngeo1661

Eastwood, S., Gusdal, Y., Drivdal, M., Furevik, B., Schyberg, H., and Tveter, F. T. (2012). *STARS-DAT v3 user manual*. Oslo, Bergen and Tromsø: Norwegian Meteorological Institute. Version 3.1.

Ehrlich, A., Wendisch, M., Klingebiel, M., Mech, M., Crewell, S., Herber, A., et al. (2023). *HALO-(AC)3: airborne observations of arctic clouds in airmass transformations*. Vienna, Austria: EGU General Assembly.

EUMETSAT (2011). *AVHRR Level 1b Product Guide*. Darmstadt, Germany: EUMETSAT.

Farjami, H., and Kazemi, A. F. (2024). Spatiotemporal patterns of polar low activity over the Southern Ocean. *J. Geophys. Res. Atmos.* 129 (4), e2023JD039832. doi:10.1029/2023JD039832

Fletcher, J., Mason, S., and Jakob, C. (2016). The climatology, meteorology, and boundary layer structure of marine cold air outbreaks in both hemispheres. *J. Clim.* 29 (6), 1999–2014. doi:10.1175/jcli-d-15-0268.1

Ganeshan, M., Reale, O., McGrath-Spangler, E., and Boukachaba, N. (2022). Impact of assimilating adaptively thinned AIRS cloud-cleared radiances on the analysis of polar lows and mediterranean sea tropical-like cyclone in a global modeling and data assimilation framework. *Weather Forecast.* 37 (7), 1117–1134. doi:10.1175/WAF-D-21-0068.1

Geerts, B., Giangrande, S. E., McFarquhar, G. M., Xue, L., Abel, S. J., Comstock, J. M., et al. (2022). The COMBLE campaign: a study of marine boundary layer clouds in arctic cold-air outbreaks. *Bull. Am. Meteorological Soc.* 103 (5), E1371–E1389. doi:10.1175/BAMS-D-21-0044.1

Golubkin, P., Smirnova, J., and Bobylev, L. (2021). Satellite-derived spatio-temporal distribution and parameters of North Atlantic polar lows for 2015-2017. *Atmosphere* 12 (2), 224. doi:10.3390/atmos12020224

Grahn, J., and Bianchi, F. M. (2022). Recognition of polar lows in Sentinel-1 SAR images with deep learning. *IEEE Trans. Geoscience Remote Sens.* 60, 1–12. doi:10.1109/TGRS.2022.3204886

Gurvich, I., Pichugin, M., and Baranyuk, A. (2022). Satellite multi-sensor data analysis of unusually strong polar lows over the Chukchi and Beaufort Seas in October 2017. *Remote Sens.* 15 (1), 120. doi:10.3390/rs15010120

Gutjahr, O., Jungclaus, J. H., Brüggemann, N., Haak, H., and Marotzke, J. (2022). Air-Sea interactions and water mass transformation during a katabatic storm in the Irminger Sea. *J. Geophys. Res. Oceans* 127 (5), e2021JC018075. doi:10.1029/2021JC018075

Haakenstad, H., Breivik, Ø., Furevik, B. R., Reistad, M., Bohlinger, P., and Aarnes, O. J. (2021). NORA3: a nonhydrostatic high-resolution hindcast of the North Sea, the Norwegian Sea, and the Barents Sea. *J. Appl. Meteorology Climatol.* 60 (10), 1443–1464. doi:10.1175/JAMC-D-21-0029.1

Hallerstig, M., Magnusson, L., Kolstad, E. W., and Mayer, S. (2021). How grid-spacing and convection representation affected the wind speed forecasts of four polar lows. *Q. J. R. Meteorological Soc.* 147 (734), 150–165. doi:10.1002/qj.3911

Haualand, K. F., and Spengler, T. (2020). Direct and indirect effects of surface fluxes on moist baroclinic development in an idealized framework. *J. Atmos. Sci.* 77 (9), 3211–3225. doi:10.1175/jas-d-19-0328.1

Hersbach, H., Bell, B., Berrisford, P., Hirahara, S., Horányi, A., Muñoz-Sabater, J., et al. (2020). The ERA5 global reanalysis. *Q. J. R. Meteorological Soc.* 146 (730), 1999–2049. doi:10.1002/qj.3803

Holton, J. R., and Hakim, G. J. (2013). *An introduction to dynamic meteorology*. San Diego, USA: Elsevier Inc.

IPCC (2021). "Summary for policymakers," in *Climate change 2021: the physical science basis. Contribution of Working Group I to the Sixth Assessment Report of the Intergovernmental Panel on Climate Change*. Editors Masson-Delmotte, V, Zhai, P, Pirani, A, Connors, SL, Péan, C, and Berger, S.

Isaksen, K., Nordli, Ø., Ivanov, B., Køltzow, M. A. Ø., Aaboe, S., Gjelten, H. M., et al. (2022). Exceptional warming over the Barents area. *Sci. Rep.* 12 (1), 9371. doi:10.1038/s41598-022-13568-5

Kapoor, A., Negi, A., Marshall, L., and Chandra, R. (2023). Cyclone trajectory and intensity prediction with uncertainty quantification using variational recurrent neural networks. *Environ. Model. Softw.* 162, 105654. doi:10.1016/j.envsoft.2023.105654

Kim, D.-H., Kim, H. M., and Hong, J. (2019). Evaluation of wind forecasts over Svalbard using the high-resolution Polar WRF with 3DVAR. *Arct. Antarct. Alp. Res.* 51 (1), 471–489. doi:10.1080/15230430.2019.1676939

Kolstad, E. W., and Bracegirdle, T. J. (2017). Sensitivity of an apparently hurricane-like polar low to sea-surface temperature. *Q. J. R. Meteorological Soc.* 143 (703), 966–973. doi:10.1002/qj.2980

Køltzow, M., Schyberg, H., Støylen, E., and Yang, X. (2022). Value of the Copernicus Arctic Regional Reanalysis (CARRA) in representing near-surface temperature and wind speed in the north-east European Arctic. *Polar Res.* 41, 8002. doi:10.33265/polar.v41.8002

Krinitskiy, M., Verezemskaya, P., Grashchenkov, K., Tilinina, N., Gulev, S., and Lazzara, M. (2018). Deep convolutional neural networks capabilities for binary classification of polar mesocyclones in satellite mosaics. *Atmosphere* 9 (11), 426. doi:10.3390/atmos9110426

Kudryavtsev, V., Cheshm Siyahi, V., Yurovskaya, M., and Chapron, B. (2022). On surface waves in Arctic Seas. *Boundary-Layer Meteorol.* 187 (1-2), 267–294. doi:10.1007/s10546-022-00768-9

Lackner, C. P., Geerts, B., Wang, Y., Juliano, T. W., Xue, L., Kosović, B., et al. (2023). Insights into the relation between vertical cloud structure and dynamics of three polar lows: observations from COMBLE. *Q. J. R. Meteorological Soc.* 149, 2992–3013. doi:10.1002/qj.4543

Landgren, O. A., Seierstad, I. A., and Iversen, T. (2019). Projected future changes in marine cold-air outbreaks associated with polar lows in the northern North-Atlantic Ocean. *Clim. Dyn.* 53 (5), 2573–2585. doi:10.1007/s00382-019-04642-2

Mallet, P.-E., Claud, C., Cassou, C., Noer, G., and Kodera, K. (2013). Polar lows over the Nordic and Labrador Seas: synoptic circulation patterns and associations with North Atlantic-Europe wintertime weather regimes. *J. Geophys. Res. Atmos.* 118 (6), 2455–2472. doi:10.1002/jgrd.50246

Mansfield, D. A. (1974). Polar lows: the development of baroclinic disturbances in cold air outbreaks. *Q. J. R. Meteorological Soc.* 100 (426), 541–554. doi:10.1002/qj.49710042604

Meyer, M., Polkova, I., Modali, K. R., Schaffer, L., Baehr, J., Olbrich, S., et al. (2021). Interactive 3-D visual analysis of ERA5 data: improving diagnostic indices for marine cold air outbreaks and polar lows. *Weather Clim. Dyn.* 2 (3), 867–891. doi:10.5194/wcd-2-867-2021

Moore, G. W. K., Våge, K., Renfrew, I. A., and Pickart, R. S. (2022). Sea-ice retreat suggests re-organization of water mass transformation in the Nordic and Barents Seas. *Nat. Commun.* 13 (1), 67. doi:10.1038/s41467-021-27641-6

Moreno-Ibáñez, M., Laprise, R., and Gachon, P. (2021). Recent advances in polar low research: current knowledge, challenges and future perspectives. *Tellus A Dyn. Meteorology Oceanogr.* 73 (1), 1890412–1890431. doi:10.1080/16000870.2021.1890412

Moreno-Ibáñez, M., Laprise, R., and Gachon, P. (2023a). Analysis of the development mechanisms of a polar low over the Norwegian Sea simulated with the Canadian Regional Climate Model. *Atmosphere* 14 (6), 998. doi:10.3390/atmos14060998

Moreno-Ibáñez, M., Laprise, R., and Gachon, P. (2023b). Assessment of simulations of a polar low with the Canadian Regional Climate Model. *PLOS ONE* 18 (10), e0292250. doi:10.1371/journal.pone.0292250

Noer, G., Saetra, Ø., Lien, T., and Gusdal, Y. (2011). A climatological study of polar lows in the Nordic Seas. *Q. J. R. Meteorological Soc.* 137 (660), 1762–1772. doi:10.1002/qj.846

Purich, A., and Doddridge, E. W. (2023). Record low Antarctic sea ice coverage indicates a new sea ice state. *Commun. Earth Environ.* 4 (1), 314. doi:10.1038/s43247-023-00961-9

Rasmussen, E. (1979). The polar low as an extratropical CISK disturbance. *Q. J. R. Meteorological Soc.* 105 (445), 531–549. doi:10.1002/qj.49710544504

Renfrew, I. A., Barrell, C., Elvidge, A. D., Brooke, J. K., Duscha, C., King, J. C., et al. (2021). An evaluation of surface meteorology and fluxes over the Iceland and Greenland Seas in ERA5 reanalysis: the impact of sea ice distribution. *Q. J. R. Meteorological Soc.* 147 (734), 691–712. doi:10.1002/qj.3941

Renfrew, I. A., Huang, J., Semper, S., Barrell, C., Terpstra, A., Pickart, R. S., et al. (2023). Coupled atmosphere–ocean observations of a cold-air outbreak and its impact on the Iceland Sea. *Q. J. R. Meteorological Soc.* 149 (751), 472–493. doi:10.1002/qj.4418

Renfrew, I. A., Pickart, R. S., Våge, K., Moore, G. W. K., Bracegirdle, T. J., Elvidge, A. D., et al. (2019). The Iceland Greenland seas project. *Bull. Am. Meteorological Soc.* 100 (9), 1795–1817. doi:10.1175/bams-d-18-0217.1

Revokatova, A., Nikitin, M., Rivin, G., Rozinkina, I., Nikitin, A., and Tatarinovich, E. (2021). High-resolution simulation of polar lows over Norwegian and Barents Seas using the COSMO-CLM and ICON models for the 2019–2020 cold season. *Atmosphere* 12 (2), 137. doi:10.3390/atmos12020137

Schultz, M. G., Betancourt, C., Gong, B., Kleinert, F., Langguth, M., Leufen, L. H., et al. (2021). Can deep learning beat numerical weather prediction? *Philosophical Trans. R. Soc. A Math. Phys. Eng. Sci.* 379 (2194), 20200097. doi:10.1098/rsta.2020.0097

Smith, G. C., Bélanger, J.-M., Roy, F., Pellerin, P., Ritchie, H., Onu, K., et al. (2018). Impact of coupling with an ice–ocean model on global medium-range NWP forecast skill. *Mon. Weather Rev.* 146 (4), 1157–1180. doi:10.1175/MWR-D-17-0157.1

Spengler, T., Claud, C., and Heinemann, G. (2017). Polar low workshop summary. *Bull. Am. Meteorological Soc.* 98 (6), ES139–ES142. doi:10.1175/bams-d-16-0207.1

Spensberger, C., and Spengler, T. (2021). Sensitivity of air-sea heat exchange in cold-air outbreaks to model resolution and sea-ice distribution. *J. Geophys. Res. Atmos.* 126 (5), e2020JD033610. doi:10.1029/2020JD033610

Stoll, P. J. (2022). A global climatology of polar lows investigated for local differences and wind-shear environments. *Weather Clim. Dyn.* 3 (2), 483–504. doi:10.5194/wcd-3-483-2022

Stoll, P. J., Graversen, R. G., and Messori, G. (2023). The global atmospheric energy transport analysed by a wavelength-based scale separation. *Weather Clim. Dyn.* 4 (1), 1–17. doi:10.5194/wcd-4-1-2023

Stoll, P. J., Graversen, R. G., Noer, G., and Hodges, K. (2018). An objective global climatology of polar lows based on reanalysis data. *Q. J. R. Meteorological Soc.* 144 (716), 2099–2117. doi:10.1002/qj.3309

Stoll, P. J., Spengler, T., Terpstra, A., and Graversen, R. G. (2021). Polar lows – moist-baroclinic cyclones developing in four different vertical wind shear environments. *Weather Clim. Dyn.* 2 (1), 19–36. doi:10.5194/wcd-2-19-2021

Terpstra, A., Renfrew, I. A., and Sergeev, D. E. (2021). Characteristics of cold-air outbreak events and associated polar mesoscale cyclogenesis over the North Atlantic region. *J. Clim.* 34 (11), 1–52. doi:10.1175/jcli-d-20-0595.1

Terpstra, A., Spengler, T., and Moore, R. W. (2015). Idealised simulations of polar low development in an Arctic moist-baroclinic environment. *Q. J. R. Meteorological Soc.* 141 (691), 1987–1996. doi:10.1002/qj.2507

Tollinger, M., Graversen, R., and Johnsen, H. (2021). High-resolution polar low winds obtained from unsupervised SAR wind retrieval. *Remote Sens.* 13 (22), 4655. doi:10.3390/rs13224655

Turner, J., Rasmussen, E. A., and Carleton, A. M. (2003). "Introduction," in *Polar lows: mesoscale weather systems in the polar regions*. Editors E. A. Rasmussen, and J. Turner (Cambridge: Cambridge University Press), 1–51.

Walters, D. N., Best, M. J., Bushell, A. C., Copsey, D., Edwards, J. M., Falloon, P. D., et al. (2011). The Met Office unified model global atmosphere 3.0/3.1 and JULES global land 3.0/3.1 configurations. *Geosci. Model Dev.* 4 (4), 919–941. doi:10.5194/gmd-4-919-2011

Wang, Z., Boyd, K., and Walsh, J. E. (2023). Modulation of polar low activity by the Madden-Julian Oscillation. *Geophys. Res. Lett.* 50 (12), e2023GL103719. doi:10.1029/2023GL103719

Watanabe, S.-i.I., Niino, H., and Spengler, T. (2022). Formation of maritime convergence zones within cold air outbreaks due to the shape of the coastline or sea ice edge. *Q. J. R. Meteorological Soc.* 148 (746), 2546–2562. doi:10.1002/qj.4324

Wessel, P., and Smith, W. H. F. (1996). A global, self-consistent, hierarchical, high-resolution shoreline database. *J. Geophys. Res. Solid Earth* 101 (B4), 8741–8743. doi:10.1029/96JB00104

Williams, K. D., Harris, C. M., Bodas-Salcedo, A., Camp, J., Comer, R. E., Copsey, D., et al. (2015). The Met Office global coupled model 2.0 (GC2) configuration. *Geosci. Model Dev.* 8 (5), 1509–1524. doi:10.5194/gmd-8-1509-2015

Wu, L. (2021). Effect of atmosphere-wave-ocean/ice interactions on a polar low simulation over the Barents Sea. *Atmos. Res.* 248, 105183. doi:10.1016/j.atmosres.2020.105183

Xue, J., Bromwich, D. H., Xiao, Z., and Bai, L. (2021). Impacts of initial conditions and model configuration on simulations of polar lows near Svalbard using Polar WRF with 3DVAR. *Q. J. R. Meteorological Soc.* 147 (740), 3806–3834. doi:10.1002/qj.4158

Yan, Z., Wang, Z., Peng, M., and Ge, X. (2023). Polar low motion and track characteristics over the North Atlantic. *J. Clim.* 36 (13), 4559–4569. doi:10.1175/JCLI-D-22-0547.1

Yang, X., Schyberg, H., Palmason, B., Bojarova, J., Box, J., Pagh Nielsen, K., et al. (2020). *C3S Arctic regional reanalysis—full system documentation*. Reading, UK: Copernicus Climate Change Service.

Yurovskaya, M., Kudryavtsev, V., and Chapron, B. (2023). Spatial probability characteristics of waves generated by polar lows in Nordic and Barents Seas. *Remote Sens.* 15 (11), 2729. doi:10.3390/rs15112729

Published work 3

Sensitivity of the Representation of Polar Lows to Typical Climate Model Resolutions

Authors:	Marta Moreno-Ibáñez, John J. Cassano, Suzanne L. Gray and Mark Seefeldt
Year:	2025
Journal:	*Atmospheric Science Letters* 26, e1319
DOI:	10.1002/asl.1319
Note:	This manuscript includes supplementary material

Authorship statement: MMI has contributed 75% (conceptualization, formal analysis, investigation, data curation, methodology, software, visualization, writing and editing of the original draft). MMI did the conceptualization, formal analysis, methodology and software with input from the coauthors, who also reviewed the draft.

Atmospheric Science Letters

RMetS Royal Meteorological Society

RESEARCH ARTICLE OPEN ACCESS

Sensitivity of the Representation of Polar Lows to Typical Climate Model Resolutions

Marta Moreno-Ibáñez[1,2,3] | John J. Cassano[2,3,4] | Suzanne L. Gray[1] | Mark Seefeldt[2,3]

[1]Department of Meteorology, University of Reading, Reading, UK | [2]Cooperative Institute for Research in Environmental Sciences, University of Colorado Boulder, Boulder, Colorado, USA | [3]National Snow and Ice Data Center, University of Colorado Boulder, Boulder, Colorado, USA | [4]Department of Atmospheric and Oceanic Sciences, University of Colorado Boulder, Boulder, Colorado, USA

Correspondence: Marta Moreno-Ibáñez (m.morenoibanez@pgr.reading.ac.uk)

Received: 12 May 2025 | **Revised:** 18 July 2025 | **Accepted:** 22 August 2025

Funding: Marta Moreno-Ibáñez was supported by the CIRES Visiting Fellows Program, funded by NOAA NA22OAR4320151. John J. Cassano and Mark Seefeldt are supported by the Regional and Global Model Analysis (RGMA) component of the Earth and Environmental System Modeling (EESM) program of the US Department of Energy's Office of Science, as a contribution to the HiLAT-RASM project. This work utilised the Alpine high performance computing resource at the University of Colorado Boulder. Alpine is jointly funded by the University of Colorado Boulder, the University of Colorado Anschutz, Colorado State University and the National Science Foundation (award 2201538). Data storage was supported by the University of Colorado Boulder 'PetaLibrary'. Publication of this article was funded by the University of Reading through an institutional agreement with *Atmospheric Science Letters*. The statements, findings, conclusion and recommendations are those of the authors and do not necessarily reflect the views of NOAA or the US Department of Commerce.

ABSTRACT

Polar lows (PLs) are intense maritime mesoscale cyclones that often form during marine cold air outbreaks. The objective of this study is to determine the atmospheric model horizontal resolution needed to correctly represent PLs for climate modelling. Three simulations have been conducted with the Weather Research and Forecasting (WRF) model using grid spacings of 50, 25 and 12.5 km. PLs have been tracked using a combination of objective and subjective tracking methods. The number of PLs detected in each simulation increases, and their average equivalent radius decreases, as the model resolution increases. A comparison against three PL track climatologies shows that the hit rate increases with increasing resolution of the atmospheric model. The lifetime maxima of the area-maximum 10-m wind speed and area-average surface sensible heat fluxes associated with PLs are on average 12% and 20% larger, respectively, in the higher-resolution simulations than in the lower-resolution one. The lifetime maximum of the area-maximum 1-h accumulated precipitation is 67% and 133% larger in the 25- and 12.5-km simulations, respectively, than in the lower-resolution one. We conclude that a better representation of PLs can be obtained by increasing the resolution of atmospheric models from 50 to 25 km, but further increasing the resolution to 12.5 km will not result in a substantial improvement.

1 | Introduction

Polar lows (PLs) are intense maritime mesoscale cyclones that form poleward of the main polar front (Renfrew 2015). Their diameter ranges from 200 to 1000 km (Turner et al. 2003), and they are associated with near-surface wind speeds exceeding 15 m s^{-1} (Heinemann and Claud 1997). Although their lifetime is usually 3–36 h (Renfrew 2015), some of them have a lifetime exceeding 48 h (Blechschmidt 2008; Rojo et al. 2015). Small-scale, high-frequency atmospheric phenomena such as PLs have an important impact on ocean circulation (Condron et al. 2008). Removing high-frequency atmospheric forcing in simulations with ocean-sea ice models leads to a decrease in the strength of the Atlantic Meridional Overturning Circulation (Jung et al. 2014; Holdsworth and Myers 2015). Condron and Renfrew (2013) found that parameterizing polar mesoscale cyclones, which include PLs,

in a global coupled ocean-sea ice model led to increased depth and frequency of ocean convection. However, the impact of PLs on the ocean is not well understood (Moreno-Ibáñez et al. 2021; Moreno-Ibáñez 2024). Whereas the strong surface heat fluxes associated with PLs lead to sea surface temperature (SST) cooling, upper-ocean mixing processes induced by strong winds lead to SST warming or cooling depending on the temperature profile of the water (Wu 2021). Therefore, some PLs are associated with SST warming (Saetra et al. 2008; Gutjahr and Mehlmann 2024; Tomita and Tanaka 2024), while others are associated with SST cooling (Tomita and Tanaka 2024).

A few studies have analysed how climate change will affect the frequency and spatial distribution of PLs using dynamical downscaling (Zahn and von Storch 2010; Landgren et al. 2019), statistical downscaling (Romero and Emanuel 2017) and a global atmospheric model (Bresson et al. 2022). Long-term studies with global coupled climate models that correctly represent PLs are needed to analyse how PLs are affecting and will affect the ocean circulation under climate change. The potential benefits of using high-resolution coupled climate models to investigate climate change have gained attention in recent years, as shown by the development of the High Resolution Model Intercomparison Project (HighResMIP; Haarsma et al. 2016; Roberts et al. 2025). Case studies have shown that the increase in the horizontal resolution of atmospheric models improves the representation of PLs (e.g., McInnes et al. 2011). Considering multi-event studies, Shkolnik and Efimov (2013) compared the representation of polar mesoscale cyclones in decadal simulations using a global model with a 200-km grid spacing and a regional climate model with 50 and 25 km grid spacings. However, their criteria to identify PLs did not include a marine cold air outbreak (MCAO) criterion and excluded short-lived and very strong PLs. Thus, to the authors' best knowledge, no study has conducted a systematic analysis of the impact of atmospheric model horizontal resolution (typical for climate models) on the representation of PLs developed during a winter season. This study aims at filling in this gap by addressing the following research questions:

1. How does the number and characteristics of PLs represented with a limited-area atmospheric model vary with horizontal resolution?
2. How do the ocean surface heat fluxes associated with PLs vary with horizontal resolution?

2 | Data and Methodology

2.1 | Simulations

Three simulations were conducted with the Advanced Research Weather Research and Forecasting (WRF) Model Version 4.5.1 (Skamarock et al. 2019). WRF is suitable for this study because it has been extensively used to conduct research in mesoscale meteorology (Powers et al. 2017), including research on PLs (e.g., Wu et al. 2011). The vertical grid consists of 40 levels, with the model top at 50 hPa and the domain covers the North Atlantic (Figure 1). The simulations only differ in their grid spacing (50, 25 and 12.5 km), number of horizontal grid points (110 × 90, 220 × 180 and 440 × 360) and time step (4, 2 and 1 min). In what follows, we will refer to the 50, 25 and 12.5-km simulations as W50, W25 and W12.5, respectively.

The same physics schemes were selected for the three simulations (Table 1). This selection was based on previously published studies in applying WRF to the Arctic (Cassano et al. 2011, 2017; Seefeldt et al. 2024). These and other studies (e.g., Hines et al. 2015; Bromwich et al. 2022) have found the greatest sensitivity to the selection of the microphysics, boundary layer and cumulus parameterizations. The other parameterizations have been relatively uniformly applied across WRF simulations of the Arctic. For this study, preliminary simulations were focused on studying the sensitivity of atmospheric simulations to the cumulus parameterization scheme (e.g., Field et al. 2017). Three preliminary one-month simulations of February 2009 with a 50-km grid spacing were conducted using Kain–Fritsch (Kain 2004), Grell-Freitas (Grell and Freitas 2014) and new Tiedtke (Zhang and Wang 2017) cumulus schemes. The simulation output was verified against ERA5 reanalysis (Hersbach et al. 2020) and the Clouds and the Earth's Radiant Energy System Energy Balanced and Filled Level 3b data product (Kato et al. 2018; Loeb et al. 2018). The simulation with the Grell-Freitas cumulus scheme produced too many clouds, and there were not substantial differences between the other two cumulus schemes. Therefore, the Kain–Fritsch scheme was selected. One-month simulations conducted with the 25- and 12.5-km grids showed that the selected physics schemes are also adequate for these resolutions.

The initial conditions and the hourly lateral and ocean surface conditions were provided by ERA5 reanalysis (Hersbach et al. 2020), which has a regular 0.25° latitude-longitude grid with hourly temporal resolution. Spectral nudging of temperature and wind was applied above ~541 hPa. Each simulation was initialised on 1 September 2008 at 0000 UTC and ended on 1 June 2009 at 0000 UTC, and the output frequency was 1 hour. The extended winter season 2008–2009 was selected because of the relatively high number of PLs that developed over the Nordic Seas according to previous climatologies (Noer et al. 2011; Rojo et al. 2015; Smirnova et al. 2015).

2.2 | Detection and Tracking of PLs

PLs were tracked using a combination of objective and subjective tracking methods as described briefly here (details in Appendix S1). First, the sea level pressure (SLP)-based tracking algorithm presented in Crawford et al. (2021) was applied to the hourly SLP field after being adapted to PLs. Second, some PL criteria were applied to determine the tracks that corresponded to potential PLs. Third, the potential PL tracks were manually analysed to determine if they corresponded to PLs. The PL criteria applied are the following:

1. Lifetime $\geq$ 3 h.
2. Equivalent radius $\geq$ 100 km at least once, and never exceeds 500 km.
3. Maximum 10-m wind speed $>$ 15 m s^{-1} at least once.
4. SST-T_{500} $>$ 43 K at least once.

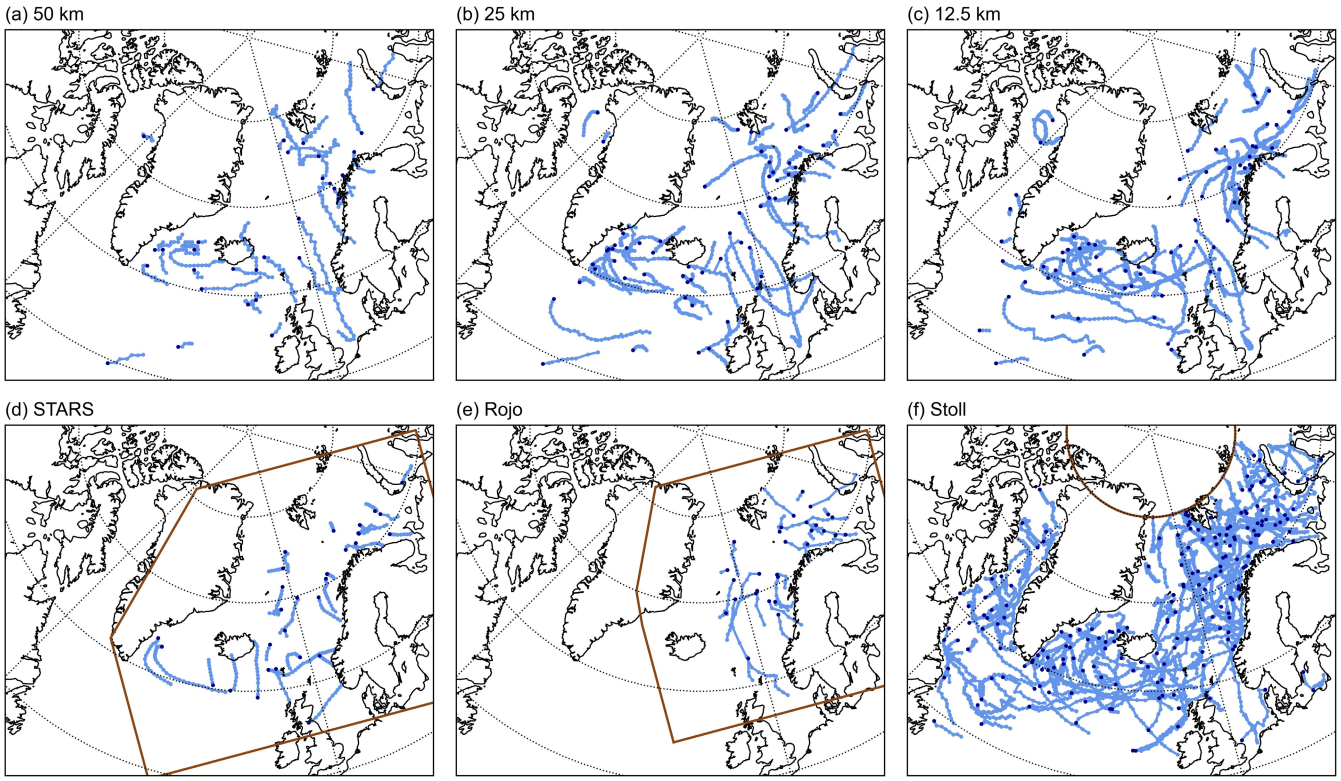

FIGURE 1 | Spatial distribution of PLs in the extended winter season 2008–2009 for the WRF simulations with (a) 50, (b) 25 and (c) 12.5 km resolutions, and for the PL track climatologies of (d) STARS (Noer et al. 2011), (e) Rojo et al. (2015, 2019) and (f) Stoll (2022). Each blue dot represents a track point, and the dark blue dot represents the first track point of each track. The temporal resolution of the track points is 1 h, except for (e), which has a temporal resolution of 3 h since the track points were linearly interpolated to obtain 3-hourly data. The climatologies cover the same period as the WRF simulations. The approximate domains of the STARS and Rojo climatologies, and the domain of the Stoll climatology (between 30° and 80°), are delimited by a brown box.

TABLE 1 | Physics schemes used in the WRF simulations.

Type of scheme	Scheme	References
Radiation—longwave and shortwave	Rapid radiative transfer model for general circulation models (RRTMG)	Iacono et al. (2008)
Planetary boundary layer	Mellor-Yamada-Nakanishi-Niino Level 2.5 (MYNN2)	Nakanishi and Niino (2006) and Nakanishi and Niino (2009)
Microphysics	Morrison two-moment	Morrison et al. (2009)
Deep and shallow convection	Kain–Fritsch scheme	Kain (2004)
Land surface	Unified Noah	Chen and Dudhia (2001) and Tewari et al. (2004)

5. Ocean fraction ≥ 0.75 and sea ice concentration < 0.15 on the first time step of the track.

The values in 4 and 5 are averages within a 100-km radius from the cyclone centre.

2.3 | Analysis of the Characteristics of PLs

Tracking yielded a set of PL tracks with hourly track points for each simulation. The characteristics of each PL track include its lifetime, average equivalent radius, average propagation speed, total distance travelled, and minimum SLP at the PL centre. The average equivalent radius was only computed for PLs that had been assigned a correct (based on visual inspection) equivalent radius by the tracking algorithm more than 50% of their lifetime, which was the case for 90%, 78% and 86% of the PLs in W50, W25 and W12.5, respectively. To compute the average equivalent radius of each PL, track points with an incorrect radius were excluded. In addition, the statistics of certain fields within 200 km from the PL centre were computed: area-maximum 10-m wind speed ($WS10_{max}$), area-maximum 1-h accumulated precipitation ($APCP_{max}$), area-average surface sensible heat fluxes (SHF_{avg}) and area-average surface latent heat fluxes (LHF_{avg}).

TABLE 2 | Number of PLs detected per month and in total for each WRF simulation. Each PL has been assigned to the month when it forms.

Model resolution	Oct 2008	Nov 2008	Dec 2008	Jan 2009	Feb 2009	Mar 2009	Apr 2009	Winter 2008–2009
50 km	7	3	7	8	3	2	0	30
25 km	13	7	9	12	7	8	2	58
12.5 km	10	9	12	17	10	7	1	66

TABLE 3 | Winter 2008–2009 averages of the characteristics of the PLs tracked in the WRF simulations.

	50 km	25 km	12.5 km
Lifetime (h)	24.6	21.8	26.8
Average equivalent radius (km)	197.5	161.4	148.6
Average propagation speed ($m\,s^{-1}$)	8.5	8.1	7.8
Distance travelled (km)	635.0	603.6	731.2
Lifetime minimum sea level pressure at the PL centre (hPa)	982.2	982.1	982.4
Lifetime maximum of the maximum 10-m wind speed within 200 km of the PL centre ($m\,s^{-1}$)	19.7	21.8	22.0
Lifetime maximum of the maximum 1-h accumulated precipitation within 200 km of the PL centre (mm)	2.4	4.0	5.6
Lifetime maximum of the average surface sensible heat fluxes within 200 km of the PL centre ($W\,m^{-2}$)	96.7	116.5	115.6
Lifetime maximum of the average surface latent heat fluxes within 200 km of the PL centre ($W\,m^{-2}$)	131.8	147.7	143.3

The radius selected for the computation of the statistics is similar to or larger than the winter average of the average equivalent radius of the PLs in the WRF simulations (Section 3.1). To compare the characteristics of the PL tracks between each pair of simulations, statistical significance testing using two-tailed permutation tests was performed to test for the differences between the winter averages. The track matching method developed by Crawford et al. (2021) was applied to pairs of datasets of PL tracks using thresholds adjusted for PLs. To be a potential match, two tracks had to be present in at least 50% of their combined observation times, and the average distance between the tracks at the times they overlapped had to not exceed 250 km. From all tracks in the second simulation that fulfilled these two criteria, the one with the smallest average distance was selected as the match for the track in the first simulation. Finally, the PL tracks in each simulation were compared against three PL track climatologies that cover the period and the domain of interest (Figure 1): the Sea Surface Temperature and Altimeter Synergy for Improved Forecasting of Polar Lows (STARS) dataset (Noer et al. 2011), the Rojo dataset (Rojo et al. 2015, 2019) and the dataset of Stoll (2022). Given that the WRF domain is larger than the region covered by the STARS and Rojo datasets, only the tracks whose first track point is within the domain of the relevant climatology are considered for track matching. After experimentation, it was decided to loosen the track matching criteria slightly to increase the number of matches. We selected 40% for the time overlap criterion and 300 km for the distance criterion. In cases where more than one track of the climatology had the same WRF track as a potential match, only one match was counted.

3 | Results

3.1 | Characteristics of PL Tracks in the Simulations

Table 2 shows the temporal distribution of PLs in each simulation. The most PLs during the winter season 2008–2009 are found in W12.5 (66) and W25 (58), whereas the number of PLs in W50 (30) is much lower. Therefore, the number of PLs identified increases as the model resolution increases. PLs occur from October to April, and no PLs were found in any simulation in September and May. This seasonality agrees with climatologies of PLs in the Nordic Seas, which have found that PLs mainly develop from October to April and that it is rare for PLs to develop in September and May (Noer et al. 2011; Rojo et al. 2015). January is the month with the most PLs in W50 and W12.5, and with the second highest number of PLs in W25, consistent with January usually being a month with high PL activity in the Nordic Seas (e.g., Bracegirdle and Gray 2008). The spatial distribution of PLs during the winter season 2008–2009 is shown in Figure 1a–c. In W50, PLs predominantly develop over the Irminger Sea and the Norwegian Sea. In W25 and W12.5, PLs mainly form in the Irminger Sea, the Norwegian Sea and the Barents Sea, in agreement with the high density of PLs found in these regions in PL climatologies (e.g., Stoll 2022). Whereas some PLs form in the Labrador Sea in W12.5, no PLs form over that region in the other simulations. The lack of PLs over the Labrador Sea may be explained by some potential PLs being discarded because their SLP field was affected by the high orography of Greenland (Appendix S1).

The winter averages of the characteristics of PLs are shown in Table 3 (monthly averages are shown in Table S1), and the *p* values are shown in Table S2. Distributions are shown for a subset of these characteristics in Figure 2. Average wintertime PL lifetimes range from 21.8 to 26.8 h. In contrast, subjective climatologies have found an average PL lifetime of 15 h in the Nordic Seas (Smirnova et al. 2015) and 20 h in the North Atlantic (Golubkin

et al. 2021). The longer lifetimes in the simulations are likely explained by the fact that Smirnova et al. (2015) and Golubkin et al. (2021) used satellite observations, which have limited temporal resolution. Most PLs in W50 (63%) and W25 (66%) have a lifetime shorter than 24 h (Figure 2a), consistent with the subjective climatology of Rojo et al. (2015), who found that 67% of PLs lasted less than 24 h. The maximum lifetimes in W50, W25 and W12.5, are 102, 65 and 93 h, respectively; these values are within the range of observed PL lifetimes (e.g., Golubkin et al. 2021). The winter-average of the average equivalent radius decreases as the resolution of the model increases, and the differences are statistically significant at the 1% level when comparing W12.5 and W50, and at the 10% level when comparing W25 and W50. The winter-average of the average equivalent radius in W12.5 is ~149 km, which is the average PL radius estimated by Smirnova et al. (2015). Whereas 80% and 84% of PLs in W25 and W12.5, respectively, have a radius that does not exceed 200 km, the corresponding percentage is 44% in W50 (Figure 2b). The winter-average of the PL average propagation speed ranges from 7.8 to 8.5 $m\,s^{-1}$, consistent with PL climatologies in the North Atlantic (Golubkin et al. 2021) and in the Nordic Seas (Rojo et al. 2015; Smirnova et al. 2015) that found a PL average propagation speed ranging from 8.1 to 8.9 $m\,s^{-1}$. The average distances travelled range from 603.6 to 731.2 km, whereas PL climatologies have found an average of 284 km (Smirnova et al. 2015) and 587 km (Golubkin et al. 2021). None of the differences between the winter means of lifetime, average propagation speed and distance travelled between any pair of simulations is statistically significant.

The winter-average of the minimum SLP at the PL centre is remarkably similar in all simulations. The differences between PLs across simulations are unveiled when analysing their intensity in terms of wind speed and precipitation. The winter-average of the lifetime maximum of $WS10_{max}$ is ~22 $m\,s^{-1}$ in W25 and W12.5, which is ~2 $m\,s^{-1}$ higher than that in W50. These differences are statistically significant at the 1% level. As a comparison, PL climatologies have found an average lifetime maximum of $WS10_{max}$ of ~20 $m\,s^{-1}$ (Smirnova et al. 2015; Golubkin et al. 2021). Only 30% of PLs in W50 show a lifetime maximum of $WS10_{max}$ of at least 21 $m\,s^{-1}$, whereas in W25 and W12.5 the corresponding percentage is 53% and 55%, respectively (Figure 2c). The winter-average of the lifetime maximum of $APCP_{max}$ increases as the resolution increases, and the differences are statistically significant at the 1% level. Whereas 93% of PLs in W50 are associated with a lifetime maximum of $APCP_{max}$ below 4 mm, 79% of PLs in W12.5 are associated with a lifetime maximum of $APCP_{max}$ over 4 mm (Figure 2d). These results show that PL hazard, in terms of high wind speeds and heavy precipitation, is higher in the higher-resolution simulations.

Given that surface heat fluxes depend on near-surface wind speeds, SHF and LHF associated with PLs are expected to be smaller in W50 compared to W25 and W12.5. Indeed, the winter-average of the lifetime maximum of SHF_{avg} is ~19 $W\,m^{-2}$ higher in W25 and W12.5 compared to W50, and these differences are statistically significant at the 10% level. Only 10% of PLs in W50 are associated with a lifetime maximum of SHF_{avg} of at least 150 $W\,m^{-2}$, whereas in W25 and W12.5 the corresponding

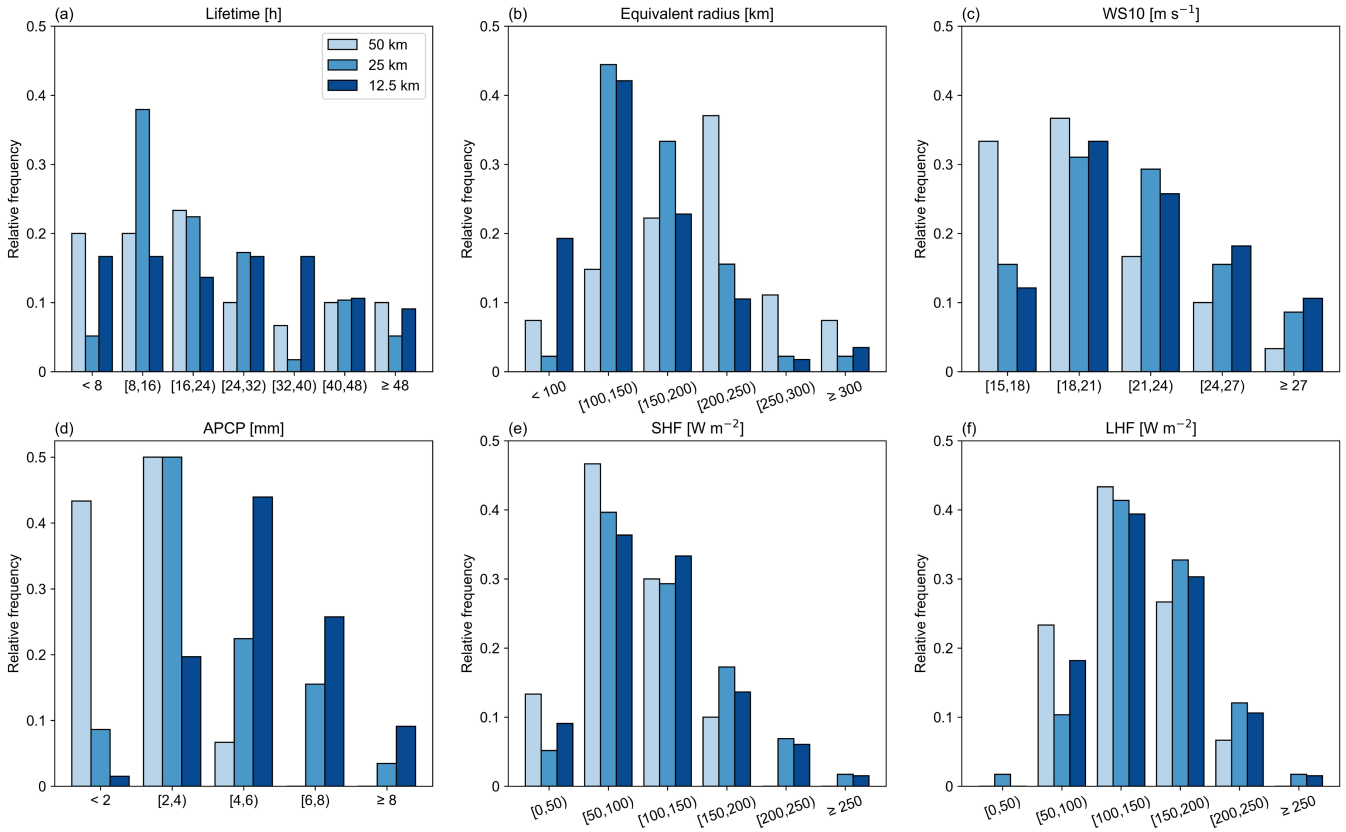

FIGURE 2 | Characteristics of the PLs represented in each simulation: (a) lifetime, (b) average equivalent radius and lifetime maxima of (c) maximum 10-m wind speed, (d) maximum 1-h accumulated precipitation, (e) average surface sensible heat flux and (f) average latent sensible heat flux, all within 200 km of the PL centre.

percentage is 26% and 21%, respectively (Figure 2e). The winter-average of the lifetime maximum of LHF_{avg} is higher in W25 and W12.5 compared to W50 (Figure 2f), but these differences are not statistically significant.

3.2 | Characteristics of PL Tracks Matched Across Simulations

Despite W50 having the fewest PLs, the fraction of PLs that are matched with PLs in the other simulations does not exceed two thirds of those present in W50. In fact, only 10 PLs are matched across all three simulations. When comparing each pair of simulations, we expect that the percentage of PLs in a simulation that have a match in another simulation will increase with the number of PLs present in the latter. This is the case for W25 and W12.5. The percentage of PLs in W25 that match a PL in W50 and W12.5 is, respectively, 33% and 62%. The percentage of PLs in W12.5 that match a PL in W50 and W25 is, respectively, 23% and 55%. However, the percentage of PLs in W50 that match a PL in W25 and W12.5 is, respectively, 63% and 50%.

For each pair of simulations, the lifetimes of some of the matched PLs differ widely, but the average lifetime of the PLs in W50 is similar to that of their counterparts in W25 and W12.5 (Figure S1a,d,g). The average equivalent radius of the PLs in W25 and W12.5 are notably similar, the slope of the least-squares fit to the data being 1 (Figure S1b,e,h). The average equivalent radius of the PLs in W50 are either similar to or larger than those in W25, and W50 can correctly represent some of the smallest PLs. Except for a few cases, the propagation speeds of the matched PLs are rather similar, and the average propagation speeds of the PLs in each simulation are similar to those of their counterparts in the other simulations (Figure S1c,f,i). There is a linear relationship between values in each pair of simulations for $APCP_{max}$, $WS10_{max}$, LHF_{max} and SHF_{max} (Figure 3), which supports that the matched PLs are likely synoptically related to one another. The PLs in the higher-resolution simulations show larger values of the lifetime maximum of $APCP_{max}$ compared to their lower-resolution counterparts. It is particularly noticeable that the values of the lifetime maximum of $APCP_{max}$ are much lower in W50 than in W12.5, the slope of the least-squares fit to the data being 2.6. The lifetime maxima of $WS10_{max}$, SHF_{avg} and LHF_{avg} of the PLs in W25 and W12.5 are larger than those of their respective counterparts in W50. However, the lifetime maxima of $WS10_{max}$, SHF_{avg} and LHF_{avg} of the PLs matched in W25 and W12.5 are similar.

3.3 | Comparison Between Simulated PL Tracks and PL Track Climatologies

Caution must be taken when comparing PL climatologies since the PL tracks obtained depend on the input data, the detection and tracking methodology, the choice of PL criteria and the area and time period covered by the study (Moreno-Ibáñez et al. 2021). The PL tracks of the STARS and Rojo datasets have been obtained using observations—whose temporal resolution and spatial coverage is not high enough to detect all PLs—and the development process has been considered when determining whether a cyclone is a PL. In contrast, the Stoll dataset (Stoll 2022) is based on ERA5—which provides atmospheric fields in a regular grid with high temporal resolution—and the cyclone tracks are not manually analysed to confirm that the PLs are indeed PLs. Therefore, it is reasonable to assume that the STARS and Rojo datasets do not include all occurring PLs, and that the Stoll dataset includes several cyclones that are not really PLs. Accordingly, for the period September 2008 to June 2009, the density of PL tracks in the STARS and Rojo datasets is notably lower than in the Stoll dataset (Figure 1d–f). The number of PL tracks in the STARS and Rojo datasets is, respectively, 30 and 29, and the number of PL tracks in the Stoll dataset is 197. Although some of the PL tracks of the STARS and Rojo datasets are similar, others are only present in one of the two datasets.

For a given dataset, the number of hits increases with the resolution of WRF, and the number of false positives is the lowest for W50, and similar for W25 and W12.5 (Table 4). The hit rate increases with increasing resolution, but the false alarm ratios are rather consistent across resolutions. Therefore, the observed PLs are somewhat better captured as the resolution of the model increases, although the increase in the number of PLs with increasing resolution also leads to a higher number of false positives. In general, the hit rates are low and the false alarm ratios are high for all the simulations. Since the simulations are driven by ERA5 reanalysis, and spectral nudging has been applied, the synoptic-scale patterns represented in the simulation are expected to be similar to the observed ones (Prein et al. 2015). However, the domain of the simulations is large, and mesoscale phenomena may be represented somewhat differently in each simulation.

4 | Conclusion

The objective of this study is to understand the impact of the horizontal resolutions typical of atmospheric climate models on the representation of PLs. Simulations with grid meshes of 50, 25 and 12.5 km were conducted using WRF, and PLs were tracked using a combination of objective and subjective tracking methods. The number of simulated PLs during the winter season 2008–2009 increases as the resolution increases. However, whereas there are twice as many PLs in W25 compared to W50, the increase in the number of PLs is more modest when increasing the resolution from 25 to 12.5 km spacing. A comparison of the simulated PL tracks against three PL climatologies indicates that the skill of the model at capturing observed PLs increases as the resolution increases. The differences in lifetime, propagation speed, distance travelled, minimum SLP and lifetime maximum of LHF_{avg} between each pair of simulations are not statistically significant. However, the PLs in W50 are significantly larger than those in W25 and W12.5, and the lifetime maxima of $WS10_{max}$, $APCP_{max}$ and SHF_{avg} are significantly larger in W25 and W12.5 compared to W50. When comparing W25 and W12.5, the only statistically significant difference found is in the lifetime maximum of $APCP_{max}$, which is larger in the latter. The differences in the characteristics of PLs found when comparing pairs of matched PLs are in line with the differences found when comparing all PL tracks. In summary, a WRF simulation with a grid spacing of 25 km, compared to 50 km, yields smaller, more frequent and more intense PLs, and further increasing the resolution to 12.5 km spacing only leads to an enhancement of

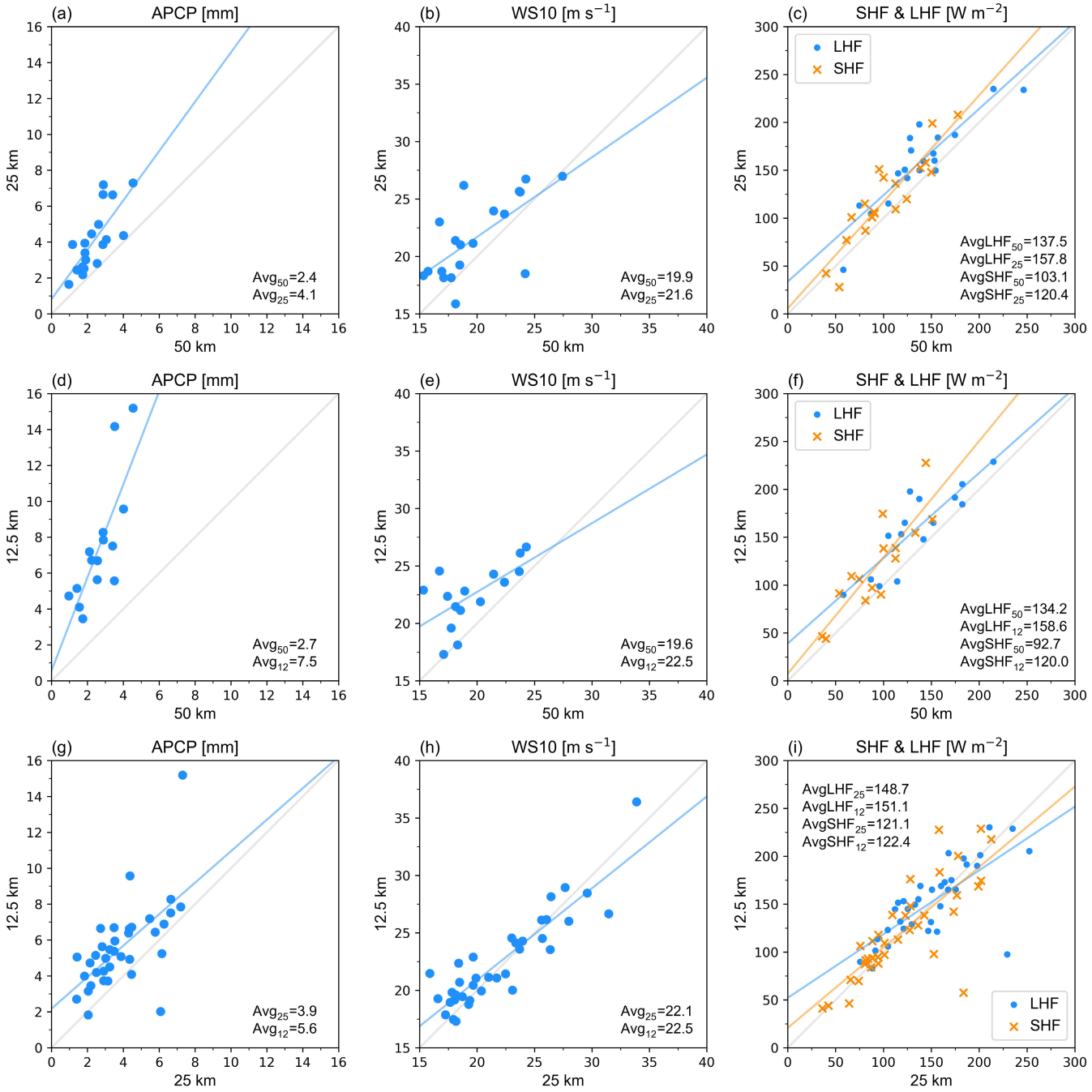

FIGURE 3 | Scatterplots displaying the relationship between the characteristics of the PLs that have been matched across (a–c) W50 and W25, (d–f) W50 and W12.5 and (g–i) W25 and W12.5. For each pair of simulations, the following characteristics of PLs are displayed: Lifetime maxima of the (a, d, g) maximum 1-h accumulated precipitation, (b, e, h) maximum 10-m wind speed and (c, f, i) average surface sensible heat flux and average surface latent heat flux, all within 200 km of the PL centre. The average values of the variables in each simulation are shown. The blue and orange lines represent the least-squares fit to the data, and the grey line is the identity line.

$APCP_{max}$. We conclude that increasing the resolution of atmospheric models from 50 to 25 km will lead to a better representation of PLs and their impact on the ocean in global climate models, but further increasing the resolution to 12.5 km will not lead to a substantial improvement.

This study constitutes a first step in examining how the resolution of an atmospheric model might affect how PLs interact with the ocean. A limitation of this work is the relatively short time period covered, which limits the representativeness in terms of PL characteristics. In addition, given that the accumulated impact of mesoscale SST anomalies over long timescales leads to more intense PLs (Lin et al. 2025), the PLs in the high-resolution simulations may have been more intense if high-resolution ocean surface conditions had been used. Further studies should be done using multiyear simulations with high-resolution coupled atmosphere–ocean–sea ice models. The data needed for such studies could come from the HighResMIP phase 2 (Roberts et al. 2025), which aims to produce global coupled simulations with an atmospheric horizontal grid spacing as high as 10 km.

TABLE 4 | Verification of PL tracks in the WRF simulations against PL climatologies.

	Hit (Miss)			Hit rate		
	50 km	**25 km**	**12.5 km**	**50 km**	**25 km**	**12.5 km**
STARS	4 (26)	8 (22)	10 (20)	0.13	0.27	0.33
Rojo	4 (25)	5 (24)	7 (22)	0.14	0.17	0.24
Stoll	12 (185)	24 (173)	34 (163)	0.06	0.12	0.17
	False positive			**False alarm ratio**		
	50 km	**25 km**	**12.5 km**	**50 km**	**25 km**	**12.5 km**
STARS	24	46	47	0.86	0.85	0.82
Rojo	15	31	29	0.79	0.86	0.81
Stoll	17	32	29	0.59	0.57	0.46

One of the main challenges is to find a suitable automated method to track PLs that can be applied to multiyear simulations since applying a combination of objective and subjective tracking methods, as was done in this study, would not be feasible for such large datasets.

Author Contributions

Marta Moreno-Ibáñez: conceptualization, data curation, formal analysis, funding acquisition, investigation, methodology, software, visualization, writing – review and editing, writing – original draft. **John J. Cassano:** conceptualization, formal analysis, funding acquisition, project administration, methodology, writing – review and editing, supervision. **Suzanne L. Gray:** formal analysis, methodology, supervision, writing – review and editing. **Mark Seefeldt:** software, methodology, writing – review and editing.

Acknowledgements

The authors are grateful to Alex Crawford and Elizabeth Cassano for providing help on how to run the cyclone tracking algorithm. The authors would also like to thank two anonymous reviewers for their constructive comments.

Conflicts of Interest

The authors declare no conflicts of interest.

Data Availability Statement

Data supporting the results reported in this paper are openly available from the University of Reading Research Data Archive at https://doi.org/10.17864/1947.001433 (Moreno-Ibáñez 2025). WRF is available at https://doi.org/10.5065/D6MK6B4K. ERA5 reanalysis, produced by the European Centre for Medium-Range Weather Forecasts, is available through the National Center for Atmospheric Research, Research Data Archive (https://rda.ucar.edu/datasets/ds633.0/) and through Copernicus Climate Change Service Climate Data Store (https://doi.org/10.24381/cds.adbb2d47). The Clouds and the Earth's Radiant Energy System Energy Balanced and Filled TOA and surface monthly means dataset is provided by NASA/LARC/SD/ASDC (2019) (https://doi.org/10.5067/TERRA-AQUA/CERES/EBAF_L3B.004.1). The Equal-Area Scalable Earth 2 grid is provided by the National Snow and Ice Data Center at https://nsidc.org/data/nsidc-0772/versions/1. The STARS dataset is available at https://projects.met.no/stars/data/v3/, the doi of the Rojo dataset is 10.1594/PANGAEA.903058 and the doi of the Stoll dataset is 10.18710/TVZDBF. The doi of the cyclone tracking algorithm (Crawford et al. 2021) code is 10.5281/zenodo.4356161.

References

Blechschmidt, A. M. 2008. "A 2-Year Climatology of Polar Low Events Over the Nordic Seas From Satellite Remote Sensing." *Geophysical Research Letters* 35: L09815. https://doi.org/10.1029/2008GL033706.

Bracegirdle, T. J., and S. L. Gray. 2008. "An Objective Climatology of the Dynamical Forcing of Polar Lows in the Nordic Seas." *International Journal of Climatology* 28: 1903–1919. https://doi.org/10.1002/joc.1686.

Bresson, H., K. I. Hodges, L. C. Shaffrey, G. Zappa, and R. Schiemann. 2022. "The Response of Northern Hemisphere Polar Lows to Climate Change in a 25 Km High-Resolution Global Climate Model." *Journal of Geophysical Research: Atmospheres* 127: e2021JD035610. https://doi.org/10.1029/2021JD035610.

Bromwich, D. H., J. G. Powers, K. W. Manning, and X. Zou. 2022. "Antarctic Data Impact Experiments With Polar WRF During the YOPP-SH Summer Special Observing Period." *Quarterly Journal of the Royal Meteorological Society* 148: 2194–2218. https://doi.org/10.1002/qj.4298.

Cassano, J. J., A. DuVivier, A. Roberts, et al. 2017. "Development of the Regional Arctic System Model (RASM): Near-Surface Atmospheric Climate Sensitivity." *Journal of Climate* 30: 5729–5753. https://doi.org/10.1175/jcli-d-15-0775.1.

Cassano, J. J., M. E. Higgins, and M. W. Seefeldt. 2011. "Performance of the Weather Research and Forecasting Model for Month-Long Pan-Arctic Simulations." *Monthly Weather Review* 139: 3469–3488. https://doi.org/10.1175/MWR-D-10-05065.1.

Chen, F., and J. Dudhia. 2001. "Coupling an Advanced Land Surface–Hydrology Model With the Penn State–NCAR MM5 Modeling System. Part I: Model Implementation and Sensitivity." *Monthly Weather Review* 129: 569–585. https://doi.org/10.1175/1520-0493(2001)129%3C0569:CAALSH%3E2.0.CO;2.

Condron, A., G. R. Bigg, and I. A. Renfrew. 2008. "Modeling the Impact of Polar Mesocyclones on Ocean Circulation." *Journal of Geophysical Research: Oceans* 113: 2007JC004599. https://doi.org/10.1029/2007JC004599.

Condron, A., and I. A. Renfrew. 2013. "The Impact of Polar Mesoscale Storms on Northeast Atlantic Ocean Circulation." *Nature Geoscience* 6: 34–37. https://doi.org/10.1038/ngeo1661.

Crawford, A. D., E. A. P. Schreiber, N. Sommer, et al. 2021. "Sensitivity of Northern Hemisphere Cyclone Detection and Tracking Results to

Fine Spatial and Temporal Resolution Using ERA5." *Monthly Weather Review* 149: 2581–2598. https://doi.org/10.1175/mwr-d-20-0417.1.

Field, P. R., R. Brož ková, M. Chen, et al. 2017. "Exploring the Convective Grey Zone With Regional Simulations of a Cold Air Outbreak." *Quarterly Journal of the Royal Meteorological Society* 143: 2537–2555. https://doi.org/10.1002/qj.3105.

Golubkin, P., J. Smirnova, and L. Bobylev. 2021. "Satellite-Derived Spatio-Temporal Distribution and Parameters of North Atlantic Polar Lows for 2015-2017." *Atmosphere* 12: 224. https://doi.org/10.3390/atmos12020224.

Grell, G. A., and S. R. Freitas. 2014. "A Scale and Aerosol Aware Stochastic Convective Parameterization for Weather and Air Quality Modeling." *Atmospheric Chemistry and Physics* 14: 5233–5250. https://doi.org/10.5194/acp-14-5233-2014.

Gutjahr, O., and C. Mehlmann. 2024. "Polar Lows and Their Effects on Sea Ice and the Upper Ocean in the Iceland, Greenland, and Labrador Seas." *Journal of Geophysical Research: Oceans* 129: e2023JC020258. https://doi.org/10.1029/2023JC020258.

Haarsma, R. J., M. J. Roberts, P. L. Vidale, et al. 2016. "High Resolution Model Intercomparison Project (HighResMIP v1.0) for CMIP6." *Geoscientific Model Development* 9: 4185–4208. https://doi.org/10.5194/gmd-9-4185-2016.

Heinemann, G., and C. Claud. 1997. "Report of a Workshop on "Theoretical and Observational Studies of Polar Lows" of the European Geophysical Society Polar Lows Working Group." *Bulletin of the American Meteorological Society* 78: 2643–2658. https://doi.org/10.1175/1520-0477-78.11.2643.

Hersbach, H., B. Bell, P. Berrisford, et al. 2020. "The ERA5 Global Reanalysis." *Quarterly Journal of the Royal Meteorological Society* 146: 1999–2049. https://doi.org/10.1002/qj.3803.

Hines, K. M., D. H. Bromwich, L. Bai, C. M. Bitz, J. G. Powers, and K. W. Manning. 2015. "Sea Ice Enhancements to Polar WRF." *Monthly Weather Review* 143: 2363–2385. https://doi.org/10.1175/MWR-D-14-00344.1.

Holdsworth, A. M., and P. G. Myers. 2015. "The Influence of High-Frequency Atmospheric Forcing on the Circulation and Deep Convection of the Labrador Sea." *Journal of Climate* 28: 4980–4996. https://doi.org/10.1175/jcli-d-14-00564.1.

Iacono, M. J., J. S. Delamere, E. J. Mlawer, M. W. Shephard, S. A. Clough, and W. D. Collins. 2008. "Radiative Forcing by Long-Lived Greenhouse Gases: Calculations With the AER Radiative Transfer Models." *Journal of Geophysical Research: Atmospheres* 113: 2008JD009944. https://doi.org/10.1029/2008JD009944.

Jung, T., S. Serrar, and Q. Wang. 2014. "The Oceanic Response to Mesoscale Atmospheric Forcing." *Geophysical Research Letters* 41: 1255–1260. https://doi.org/10.1002/2013GL059040.

Kain, J. S. 2004. "The Kain–Fritsch Convective Parameterization: An Update." *Journal of Applied Meteorology* 43: 170–181. https://doi.org/10.1175/1520-0450(2004)043%3C0170:TKCPAU%3E2.0.CO;2.

Kato, S., F. G. Rose, D. A. Rutan, et al. 2018. "Surface Irradiances of Edition 4.0 Clouds and the Earth's Radiant Energy System (CERES) Energy Balanced and Filled (EBAF) Data Product." *Journal of Climate* 31: 4501–4527. https://doi.org/10.1175/JCLI-D-17-0523.1.

Landgren, O. A., Y. Batrak, J. E. Haugen, E. Støylen, and T. Iversen. 2019. "Polar Low Variability and Future Projections for the Nordic and Barents Seas." *Quarterly Journal of the Royal Meteorological Society* 145: 3116–3128. https://doi.org/10.1002/qj.3608.

Lin, T., A. Rutgersson, and L. Wu. 2025. "Influence of Mesoscale Sea Surface Temperature Anomaly on Polar Lows." *Environmental Research Letters* 20: 014051. https://doi.org/10.1088/1748-9326/ad9ec6.

Loeb, N. G., D. R. Doelling, H. Wang, et al. 2018. "Clouds and the Earth's Radiant Energy System (CERES) Energy Balanced and Filled (EBAF) Top-of-Atmosphere (TOA) Edition-4.0 Data Product." *Journal of Climate* 31: 895–918. https://doi.org/10.1175/JCLI-D-17-0208.1.

McInnes, H., J. Kristiansen, J. E. Kristjánsson, and H. Schyberg. 2011. "The Role of Horizontal Resolution for Polar Low Simulations." *Quarterly Journal of the Royal Meteorological Society* 137: 1674–1687. https://doi.org/10.1002/qj.849.

Moreno-Ibáñez, M. 2024. "Polar Low Research: Recent Developments and Promising Courses of Research." *Frontiers in Earth Science* 12: 1368179. https://doi.org/10.3389/feart.2024.1368179.

Moreno-Ibáñez, M. 2025. *North Atlantic Polar Low Tracks From September 2008 to May 2009 From WRF Simulations at 50, 25 and 12.5 km Grid Spacings*. University of Reading. https://doi.org/10.17864/1947.001433.

Moreno-Ibáñez, M., R. Laprise, and P. Gachon. 2021. "Recent Advances in Polar Low Research: Current Knowledge, Challenges and Future Perspectives." *Tellus A* 73: 1–31. https://doi.org/10.1080/16000870.2021.1890412.

Morrison, H., G. Thompson, and V. Tatarskii. 2009. "Impact of Cloud Microphysics on the Development of Trailing Stratiform Precipitation in a Simulated Squall Line: Comparison of One- and Two-Moment Schemes." *Monthly Weather Review* 137: 991–1007. https://doi.org/10.1175/2008MWR2556.1.

Nakanishi, M., and H. Niino. 2006. "An Improved Mellor–Yamada Level-3 Model: Its Numerical Stability and Application to a Regional Prediction of Advection Fog." *Boundary-Layer Meteorology* 119: 397–407. https://doi.org/10.1007/s10546-005-9030-8.

Nakanishi, M., and H. Niino. 2009. "Development of an Improved Turbulence Closure Model for the Atmospheric Boundary Layer." *Journal of the Meteorological Society of Japan. Ser. II* 87: 895–912. https://doi.org/10.2151/jmsj.87.895.

NASA/LARC/SD/ASDC. 2019. *CERES Energy Balanced and Filled (EBAF) TOA and Surface Monthly Means Data in netCDF Edition 4.1*. NASA/LARC/SD/ASDC. https://doi.org/10.5067/TERRA-AQUA/CERES/EBAF_L3B.004.1.

Noer, G., Ø. Saetra, T. Lien, and Y. Gusdal. 2011. "A Climatological Study of Polar Lows in the Nordic Seas." *Quarterly Journal of the Royal Meteorological Society* 137: 1762–1772. https://doi.org/10.1002/qj.846.

Powers, J. G., J. B. Klemp, W. C. Skamarock, et al. 2017. "The Weather Research and Forecasting Model: Overview, System Efforts, and Future Directions." *Bulletin of the American Meteorological Society* 98: 1717–1738. https://doi.org/10.1175/BAMS-D-15-00308.1.

Prein, A. F., W. Langhans, G. Fosser, et al. 2015. "A Review on Regional Convection-Permitting Climate Modeling: Demonstrations, Prospects, and Challenges." *Reviews of Geophysics* 53: 323–361. https://doi.org/10.1002/2014RG000475.

Renfrew, I. A. 2015. "Polar Lows." In *Encyclopedia of Atmospheric Sciences*, edited by G. R. North, J. Pyle, and F. Zhang, 2nd ed., 379–385. Academic Press.

Roberts, M. J., K. A. Reed, Q. Bao, et al. 2025. "High-Resolution Model Intercomparison Project Phase 2 (HighResMIP2) Towards CMIP7." *Geoscientific Model Development* 18: 1307–1332. https://doi.org/10.5194/gmd-18-1307-2025.

Rojo, M., C. Claud, P.-E. Mallet, G. Noer, A. M. Carleton, and M. Vicomte. 2015. "Polar Low Tracks Over the Nordic Seas: A 14-Winter Climatic Analysis." *Tellus A: Dynamic Meteorology and Oceanography* 67: 24660. https://doi.org/10.3402/tellusa.v67.24660.

Rojo, M., C. Claud, G. Noer, and A. M. Carleton. 2019. "In Situ Measurements of Surface Winds, Waves, and Sea State in Polar Lows Over the North Atlantic." *Journal of Geophysical Research – Atmospheres* 124: 700–718. https://doi.org/10.1029/2017JD028079.

Romero, R., and K. Emanuel. 2017. "Climate Change and Hurricane-Like Extratropical Cyclones: Projections for North Atlantic Polar Lows

and Medicanes Based on CMIP5 Models." *Journal of Climate* 30: 279–299. https://doi.org/10.1175/jcli-d-16-0255.1.

Saetra, Ø., T. Linders, and J. B. Debernard. 2008. "Can Polar Lows Lead to a Warming of the Ocean Surface?" *Tellus A* 60: 141–153. https://doi.org/10.1111/j.1600-0870.2007.00279.x.

Seefeldt, M. W., J. J. Cassano, Y. J. Lee, W. Maslowski, A. P. Craig, and R. Osinski. 2024. "Evaluation of Dynamical Downscaling in a Fully Coupled Regional Earth System Model." *Frontiers in Earth Science* 12: 1392031. https://doi.org/10.3389/feart.2024.1392031.

Shkolnik, I. M., and S. V. Efimov. 2013. "Cyclonic Activity in High Latitudes as Simulated by a Regional Atmospheric Climate Model: Added Value and Uncertainties." *Environmental Research Letters* 8: 045007. https://doi.org/10.1088/1748-9326/8/4/045007.

Skamarock, W. C., J. B. Klemp, J. Dudhia, et al. 2019. "A Description of the Advanced Research WRF Version 4." Technical Note NCAR/TN-556+STR, NCAR.

Smirnova, J. E., P. A. Golubkin, L. P. Bobylev, E. V. Zabolotskikh, and B. Chapron. 2015. "Polar Low Climatology Over the Nordic and Barents Seas Based on Satellite Passive Microwave Data." *Geophysical Research Letters* 42: 5603–5609. https://doi.org/10.1002/2015GL063865.

Stoll, P. J. 2022. "A Global Climatology of Polar Lows Investigated for Local Differences and Wind-Shear Environments." *Weather and Climate Dynamics* 3: 483–504. https://doi.org/10.5194/wcd-3-483-2022.

Tewari, M., F. Chen, W. Wang, et al. 2004. "Implementation and Verification of the Unified Noah Land Surface Model in the WRF Model." In *20th Conference on Weather Analysis and Forecasting/16th Conference on Numerical Weather Prediction*. American Meteorological Society.

Tomita, H., and R. Tanaka. 2024. "Ocean Surface Warming and Cooling Responses and Feedback Processes Associated With Polar Lows Over the Nordic Seas." *Journal of Geophysical Research: Atmospheres* 129: e2023JD040460. https://doi.org/10.1029/2023JD040460.

Turner, J., E. A. Rasmussen, and A. M. Carleton. 2003. "Introduction." In *Polar Lows: Mesoscale Weather Systems in the Polar Regions*, edited by E. A. Rasmussen and J. Turner, 1–51. Cambridge University Press.

Wu, L. 2021. "Effect of Atmosphere-Wave-Ocean/Ice Interactions on a Polar Low Simulation Over the Barents Sea." *Atmospheric Research* 248: 105183. https://doi.org/10.1016/j.atmosres.2020.105183.

Wu, L., J. E. Martin, and G. W. Petty. 2011. "Piecewise Potential Vorticity Diagnosis of the Development of a Polar Low Over the Sea of Japan." *Tellus A* 63: 198–211. https://doi.org/10.1111/j.1600-0870.2011.00511.x.

Zahn, M., and H. von Storch. 2010. "Decreased Frequency of North Atlantic Polar Lows Associated With Future Climate Warming." *Nature* 467: 309–312. https://doi.org/10.1038/nature09388.

Zhang, C., and Y. Wang. 2017. "Projected Future Changes of Tropical Cyclone Activity Over the Western North and South Pacific in a 20-Km-Mesh Regional Climate Model." *Journal of Climate* 30: 5923–5941. https://doi.org/10.1175/JCLI-D-16-0597.1.

Supporting Information

Additional supporting information can be found online in the Supporting Information section. **Data S1:** Supporting Information.

SUPPLEMENTARY MATERIAL

Appendix S1: Detection and tracking of PLs

S1.1 Justification of choice of tracking methodology

A combination of objective and subjective tracking methods was used to take advantage of the benefits of each method and counteract their limitations (Neu et al., 2013). The objective algorithms that have been used to detect and track PLs are based on the detection of local sea level pressure (SLP) minima (e.g., Zahn and von Storch, 2008), local relative vorticity maxima or minima (e.g., Stoll et al., 2018), or local maxima of the Laplacian of the SLP (Michel et al., 2018). Whereas many PL studies have used 6-hourly (e.g., Bresson et al., 2022) and 3-hourly input fields (e.g., Landgren et al., 2019), studies with 1-hourly input fields are rare (Stoll et al., 2021). In this study, we used a SLP-based tracking algorithm with 1-hourly SLP fields. Since the output of the cyclone tracking algorithm is a large number of cyclone tracks, most of which are not PLs, PL criteria were applied to distinguish PLs from other systems. In what follows, the literature supporting our choice of PL criteria, which is detailed in S1.2, is provided.

Although PLs are maritime cyclones, many of them dissipate over land (Rojo et al., 2015), and some move across land during their lifetime (Yanase et al., 2016). Therefore, applying a maritime criterion at genesis time (e.g., Michel et al., 2018) is reasonable. PLs have horizontal scales from 200 to 1000 km (Turner et al., 2003), and, accordingly, some authors have applied a maximum radius criterion (e.g., Pezza et al., 2016). Given that PLs are associated with near-surface wind speeds of over 15 m s^{-1} (Heinemann and Claud, 1997), many studies have selected a threshold of 15 m s^{-1} for the near-surface wind speed criterion (e.g., Zappa et al., 2014). The lifetime of PLs is usually 3–36 hours (Renfrew, 2003), but some of them have a lifetime exceeding two days (Blechschmidt, 2008; Rojo et al., 2015). Although several studies have applied a minimum lifetime criterion (e.g., Zappa et al., 2014), it is rare to set a maximum lifetime criterion (Pezza et al., 2016). Finally, the criterion of a difference between the sea surface temperature (SST) and the temperature at 500 hPa (T500) exceeding 43 K has been often applied to track PLs (e.g., Bresson et al., 2022).

S1.2 Description of the PL detection and tracking methodology

Different configurations of the cyclone tracking algorithm and of the PL criteria were tested on the one-month simulations of February 2009 at all three resolutions, and they were compared to manually tracked PLs. The results informed the choice of parameters and PL criteria. After bilinearly interpolating the atmospheric fields to the Equal-Area Scalable Earth 2 grid with a 12.5-km grid spacing (Brodzik et al., 2012), the detection and tracking of PLs was done as follows:

1) Application of a cyclone detection and tracking algorithm: The SLP-based tracking algorithm presented in Crawford et al. (2021), which has been used to track synoptic-scale cyclones (Crawford and Serreze, 2016; Crawford et al., 2021), was adapted to PLs. The selected parameters for the algorithm are the same for the three simulations. The algorithm identifies local SLP minima in the hourly SLP field using a search

distance of 200 km. A SLP minimum is classified as a cyclone centre if the average SLP difference between it and the SLP of the grid points located at 200-km distance is at least 1 hPa. The contour interval used to search for the last closed contour around a cyclone centre is 1 hPa. A maximum propagation speed of 200 km h^{-1} was selected to avoid unrealistic track splitting (Crawford et al., 2021). Grid cells with high elevation were not masked since a manual analysis of the tracks was performed at a later stage. The option to the detect multicentre cyclones was turned off to avoid the algorithm miscalculating the PL area when it developed from a synoptic-scale cyclone.

2) Application of PL criteria: The following criteria were applied to determine the tracks that corresponded to potential PLs:

- Lifetime: The cyclone lifetime must be at least 3 h.
- Size: The cyclone shows an equivalent radius of 100 km or more at least once.
- MCAO: SST-T_{500}, averaged within a 100-km radius from the cyclone centre, must be larger than 43 K at least once.
- Intensity: The maximum 10-m wind speed within the cyclone area is larger than 15 m s^{-1} at least once.

The resulting number of potential PLs was 108, 148, and 171 for the 50, 25, and 12.5km simulations, respectively.

3) Manual analysis of the shortlisted potential PLs: The potential PL tracks were manually analysed to determine if they corresponded to PLs. The genesis of the cyclone (first track point) was considered to occur at the start time of the period when its centre showed at least three closed 1-hPa interval contours for at least three consecutive hours; its lysis (last track point) occurs right before the period when it showed fewer than three closed 1-hPa interval contours for at least three consecutive hours. If the cyclone track obtained by the tracking algorithm ended before the lysis condition occurred, the last time step of the cyclone track was the one determined by that algorithm. In the case of a potential PL developing from the centre of a synoptic-scale cyclone, its genesis time was taken as the time when it became clearly differentiated from the latter. After determining the genesis and lysis times of the potential PLs, the criteria applied in step 2 were applied again, in addition to these criteria:

- Maritime cyclone: On the first time step of the track, the average ocean fraction and the average sea ice concentration within a 100-km radius from the cyclone centre is, respectively, at least 0.75, and less than 0.15.
- Maximum radius: The equivalent radius of the cyclone never exceeds 500 km.

When the radius criterion could not be applied because a visual inspection detected that the area of the cyclone was not correct, the radius was estimated by dividing by two the average of the longest and shortest diameters. The cyclones that spent some of their lifetime partly or completely outside the simulation domain were discarded since the PL criteria could not be fully tested, and their tracks were incomplete. Similarly, the cyclones whose SLP field was notably affected by orography were discarded since the PL criteria could not be fully tested and/or their genesis and dissipation times could not be correctly estimated. Finally, four cyclones were discarded because determining their area and/or their genesis and dissipation dates was particularly challenging. Whenever a cyclone was discarded, the corresponding cyclone in the other simulations (if applicable) was also discarded.

Table S1

Monthly and winter 2008-2009 averages of the characteristics of the PLs tracked in the WRF simulations.

Model resolution	Oct 08	Nov 08	Dec 08	Jan 09	Feb 09	Mar 09	Apr 09	Winter 2008-09
Lifetime [h]								
50 km	20.1	21.0	27.4	18.0	31.0	52.5	n/a	24.6
25 km	21.1	18.1	29.8	16.3	30.4	19.3	17.0	21.8
12.5 km	27.5	25.7	21.7	25.7	36.3	26.1	18.0	26.8
Average equivalent radius [km]								
50 km	210.9	163.7	211.9	151.9	240.1	206.2	n/a	197.5
25 km	186.1	136.2	173.2	135.7	172.0	167.8	n/a	161.4
12.5 km	155.6	164.5	167.8	136.6	154.1	108.1	n/a	148.6
Average propagation speed [m s^{-1}]								
50 km	8.3	5.3	9.7	9.5	7.7	6.6	n/a	8.5
25 km	9.6	7.3	7.9	9.3	6.4	5.9	10.7	8.1
12.5 km	9.2	6.9	8.0	7.4	7.0	8.3	8.2	7.8
Distance travelled [km]								
50 km	458.1	389.9	891.1	522.3	757.0	992.2	n/a	635.0
25 km	705.9	488.2	757.7	500.5	761.5	377.5	619.1	603.6
12.5 km	804.1	621.4	678.6	710.8	858.5	754.8	530.9	731.2
Lifetime minimum sea level pressure at the PL centre [hPa]								
50 km	989.5	978.5	973.6	978.2	992.6	992.2	n/a	982.2
25 km	984.4	990.6	970.6	978.3	993.6	978.8	985.6	982.1
12.5 km	985.4	989.7	976.7	973.7	995.7	980.0	983.5	982.4
Lifetime maximum of the maximum 10-m wind speed within 200 km of the PL centre [m s^{-1}]								
50 km	19.1	19.4	21.6	18.8	19.3	19.3	n/a	19.7
25 km	22.8	20.5	24.4	20.3	20.5	21.3	24.6	21.8
12.5 km	23.5	20.8	23.6	21.2	20.8	21.3	26.2	22.0
Lifetime maximum of the maximum 1-h accumulated precipitation within 200 km of the PL centre [mm]								
50 km	2.4	1.9	2.4	2.5	2.5	1.8	n/a	2.4
25 km	4.7	4.5	3.3	4.2	2.7	3.7	5.5	4.0
12.5 km	6.9	5.1	6.5	5.2	5.1	4.8	4.9	5.6
Lifetime maximum of the average surface sensible heat fluxes within 200 km of the PL centre [W m^{-2}]								
50 km	73.9	119.6	95.8	107.2	116.9	72.7	n/a	96.7
25 km	95.8	114.9	112.2	137.4	129.7	107.6	141.1	116.5
12.5 km	109.8	93.1	125.3	115.5	120.7	125.9	142.2	115.6
Lifetime maximum of the average surface latent heat fluxes within 200 km of the PL centre [W m^{-2}]								
50 km	131.6	112.0	155.3	123.7	142.5	96.3	n/a	131.8
25 km	154.7	150.5	157.7	152.1	132.8	133.1	131.0	147.7
12.5 km	163.6	115.3	170.5	136.9	122.1	151.6	131.3	143.3

Table S2

P-values obtained from two-tailed permutation tests that were conducted to compare the following winter 2008-2009 average characteristics of the PL tracks: lifetime, average equivalent radius, average propagation speed, distance travelled, lifetime minimum SLP at the PL centre, and lifetime maxima of the maximum 10-m wind speed, maximum 1-h accumulated precipitation, average surface sensible heat fluxes, and average latent heat fluxes, all within 200 km of the PL centre. *P*-values that are statistically significant at the 1% level are in bold, and *p*-values that are statistically significant at the 10% level are in italics.

Simulations	lifetime	radius	speed	distance	SLP	$WS10_{max}$	$APCP_{max}$	SHF_{avg}	LHF_{avg}
W25 - W50	0.478	*0.011*	0.717	0.766	0.986	**0.009**	**<0.001**	*0.073*	0.115
W12.5 - W50	0.637	**0.001**	0.359	0.475	0.957	**0.004**	**<0.001**	*0.070*	0.242
W12.5 - W25	0.103	0.224	0.549	0.205	0.930	0.871	**<0.001**	0.920	0.587

Figure S1

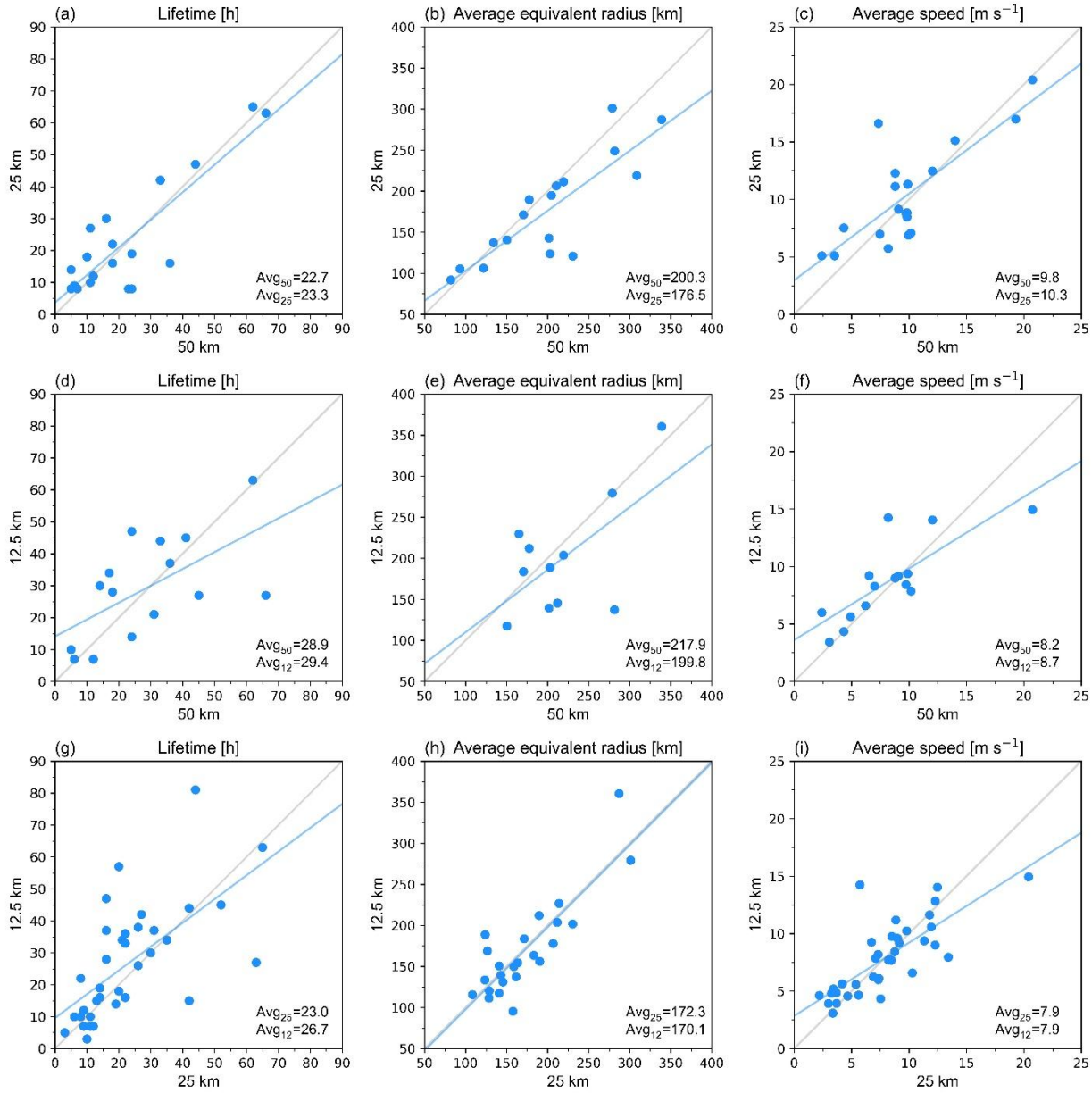

Figure S1. Scatterplots displaying the relationship between the characteristics of the PLs that have been matched across (a, b, c) W50 and W25, (d, e, f) W50 and W12.5, and (g, h, i) W25 and W12.5. For each pair of simulations, the following characteristics of PLs are displayed: (a, d, g) lifetime, (b, e, h) average equivalent radius, and (c, f, i) average propagation speed. The average values of the variables in each simulation are shown. The blue lines represent the least-squares fit to the data, and the grey line is the identity line. The equivalent radii of the matched PLs that include at least one PL for which the radius has not been computed have been excluded from the analysis.

References

Blechschmidt, A. M. 2008. A 2-year climatology of polar low events over the Nordic Seas from satellite remote sensing. *Geophys. Res. Lett.* **35**, L09815. doi: 10.1029/2008GL033706

Bresson, H., Hodges, K. I., Shaffrey, L. C., Zappa, G. and Schiemann, R. 2022. The Response of Northern Hemisphere Polar Lows to Climate Change in a 25 km High-Resolution Global Climate Model. *J. Geophys. Res. Atmos.* **127**, e2021JD035610. doi: 10.1029/2021JD035610

Brodzik, M. J., Billingsley, B., Haran, T., Raup, B. and Savoie, M. H. 2012. EASE-Grid 2.0: Incremental but Significant Improvements for Earth-Gridded Data Sets. *ISPRS International Journal of Geo-Information* **1**, 32-45. doi: 10.3390/ijgi1010032

Crawford, A. D. and Serreze, M. C. 2016. Does the Summer Arctic Frontal Zone Influence Arctic Ocean Cyclone Activity? *J. Clim.* **29**, 4977-4993. doi: 10.1175/jcli-d-15-0755.1

Crawford, A. D., Schreiber, E. A. P., Sommer, N., Serreze, M. C., Stroeve, J. C. and co-authors. 2021. Sensitivity of Northern Hemisphere Cyclone Detection and Tracking Results to Fine Spatial and Temporal Resolution Using ERA5. *Mon. Weather Rev.* **149**, 2581-2598. doi: 10.1175/mwr-d-20-0417.1

Heinemann, G. and Claud, C. 1997. Report of a workshop on "theoretical and observational studies of polar lows" of the European Geophysical Society Polar Lows Working Group. *Bull. Am. Meteorol. Soc.* **78**, 2643-2658. doi: 10.1175/1520-0477-78.11.2643

Landgren, O. A., Batrak, Y., Haugen, J. E., Støylen, E. and Iversen, T. 2019. Polar low variability and future projections for the Nordic and Barents Seas. *Q. J. Roy. Meteorol. Soc.* **145**, 3116-3128. doi: 10.1002/qj.3608

Michel, C., Terpstra, A. and Spengler, T. 2018. Polar Mesoscale Cyclone Climatology for the Nordic Seas Based on ERA-Interim. *J. Clim.* **31**, 2511-2532. doi: 10.1175/jcli-d-16-0890.1

Neu, U., Akperov, M. G., Bellenbaum, N., Benestad, R., Blender, R. and co-authors. 2013. IMILAST: A community effort to intercompare extratropical cyclone detection and tracking algorithms. *Bull. Am. Meteorol. Soc.* **94**, 529-547. doi: 10.1175/BAMS-D-11-00154.1

Pezza, A., Sadler, K., Uotila, P., Vihma, T., Mesquita, M. D. S. and co-authors. 2016. Southern Hemisphere strong polar mesoscale cyclones in high-resolution datasets. *Clim. Dyn.* **47**, 1647-1660. doi: 10.1007/s00382-015-2925-2

Renfrew, I. A. 2003. Polar Lows. In: *Encyclopedia of atmospheric sciences* (eds. J. R. Holton, J. A. Curry and J. A. Pyle). Academic Press, Amsterdam, pp. 1761-1768.

Rojo, M., Claud, C., Mallet, P.-E., Noer, G., Carleton, A. M. and co-authors. 2015. Polar low tracks over the Nordic Seas: a 14-winter climatic analysis. *Tellus A* **67**, 24660. doi: 10.3402/tellusa.v67.24660

Stoll, P. J., Graversen, R. G., Noer, G. and Hodges, K. 2018. An objective global climatology of polar lows based on reanalysis data. *Q. J. Roy. Meteorol. Soc.* **144**, 2099-2117. doi: 10.1002/qj.3309

Stoll, P. J., Spengler, T., Terpstra, A. and Graversen, R. G. 2021. Polar lows – moist-baroclinic cyclones developing in four different vertical wind shear environments. *Weather and Climate Dynamics* **2**, 19-36. doi: 10.5194/wcd-2-19-2021

Turner, J., Rasmussen, E. A. and Carleton, A. M. 2003. Introduction. In: *Polar Lows: Mesoscale Weather Systems in the Polar Regions* (eds. E. A. Rasmussen and J. Turner). Cambridge University Press, Cambridge, pp. 1-51.

Yanase, W., Niino, H., Watanabe, S. I. I., Hodges, K., Zahn, M. and co-authors. 2016. Climatology of polar lows over the sea of Japan using the JRA-55 reanalysis. *J. Clim.* **29**, 419-437. doi: 10.1175/jcli-d-15-0291.1

Zahn, M. and von Storch, H. 2008. A long-term climatology of North Atlantic polar lows. *Geophys. Res. Lett.* **35**, L22702. doi: 10.1029/2008GL035769

155 Zappa, G., Shaffrey, L. and Hodges, K. 2014. Can polar lows be objectively identified and tracked in the
156 ECMWF operational analysis and the ERA-Interim reanalysis? *Mon. Weather Rev.* **142**, 2596-
157 2608. doi: 10.1175/MWR-D-14-00064.1
158

Published work 4

Assessment of simulations of a polar low with the Canadian Regional Climate Model

Authors:	Marta Moreno-Ibáñez, René Laprise and Philippe Gachon
Year:	2023
Journal:	*PLOS ONE* 18, e0292250
DOI:	10.1371/journal.pone.0292250

Authorship statement: MMI has contributed 80% (conceptualization, formal analysis, investigation, data curation, methodology, software, visualization, writing and editing of the original draft). MMI did the conceptualization, formal analysis and methodology with input from the coauthors, who also reviewed the draft.

PLOS ONE

RESEARCH ARTICLE

Assessment of simulations of a polar low with the Canadian Regional Climate Model

Marta Moreno-Ibáñez[1,2]*, **René Laprise**[1,2], **Philippe Gachon**[1,3]

1 Centre for the Study and Simulation of Regional-Scale Climate (ESCER), University of Quebec in Montreal (UQAM), Montreal, Canada, **2** Department of Earth and Atmospheric Sciences, University of Quebec in Montreal (UQAM), Montreal, Canada, **3** Department of Geography, University of Quebec in Montreal (UQAM), Montreal, Canada

* marta.moreno-ibanez@outlook.com

Citation: Moreno-Ibáñez M, Laprise R, Gachon P (2023) Assessment of simulations of a polar low with the Canadian Regional Climate Model. PLoS ONE 18(10): e0292250. https://doi.org/10.1371/journal.pone.0292250

Editor: Delei Li, Institute of Oceanology Chinese Academy of Sciences, CHINA

Received: October 31, 2022

Accepted: September 15, 2023

Published: October 5, 2023

Peer Review History: PLOS recognizes the benefits of transparency in the peer review process; therefore, we enable the publication of all of the content of peer review and author responses alongside final, published articles. The editorial history of this article is available here: https://doi.org/10.1371/journal.pone.0292250

Data Availability Statement: AVHRR channel 4 observations are available from EUMETSAT (https://navigator.eumetsat.int/product/EO:EUM:DAT:METOP:AVHRRL1), and MODIS channel 31 observations and VIIRS channel M15 observations

Abstract

Polar lows (PLs), which are intense maritime polar mesoscale cyclones, are associated with severe weather conditions. Due to their small size and rapid development, PL forecasting remains a challenge. Convection-permitting models are adequate to forecast PLs since, compared to coarser models, they provide a better representation of convection as well as surface and near-surface processes. A PL that formed over the Norwegian Sea on 25 March 2019 was simulated using the convection-permitting Canadian Regional Climate Model version 6 (CRCM6/GEM4, using a grid mesh of 2.5 km) driven by the reanalysis ERA5. The objectives of this study were to quantify the impact of the initial conditions on the simulation of the PL, and to assess the skill of the CRCM6/GEM4 at reproducing the PL. The results show that the skill of the CRCM6/GEM4 at reproducing the PL strongly depends on the initial conditions. Although in all simulations the synoptic environment is favourable for PL development, with a strong low-level temperature gradient and an upper-level through, only the low-level atmospheric fields of three of the simulations lead to PL development through baroclinic instability. The two simulations that best captured the PL represent a PL deeper than the observed one, and they show higher temperature mean bias compared to the other simulations, indicating that the ocean surface fluxes may be too strong. In general, ERA5 has more skill than the simulations at reproducing the observed PL, but the CRCM6/GEM4 simulation with initialisation time closer to the genesis time of the PL reproduces quite well small scale features as low-level baroclinic instability during the PL development phase.

1. Introduction

The polar regions experience a variety of climate-related extreme events and high-impact weather conditions such as katabatic winds, blizzards, and polar lows (PLs) [1]. PLs are intense mesoscale maritime cyclones that develop between the poles and the main baroclinic zone, mainly during the cold season. Their diameter varies between 200 and 1,000 km, and their associated near-surface wind speed is over 15 m s^{-1} [2]. PLs are short-lived phenomena, with

are available from NASA (https://ladsweb.modaps.eosdis.nasa.gov/). The observations from surface stations can been downloaded using MET Norway Frost API (https://frost.met.no/index.html), and the observation from drifting buoys can be requested to Canada's ISDM centre (https://www.dfo-mpo.gc.ca/science/data-donnees/drib-bder/index-eng.html). The ERA5 global reanalysis from ECMWF is available at https://www.ecmwf.int/en/forecasts/datasets/reanalysis-datasets/era5. The Global Self-consistent, Hierarchical, High-resolution Geography Database (GSHHG), available at https://www.ngdc.noaa.gov/mgg/shorelines/, has been used to represent the coastlines. The divergent colourmap used in Fig 2 is provided by the Texas Advanced Computing Center at https://sciviscolor.org/. The simulation output and the coordinates of the manually obtained tracks are available at Borealis, the Canadian Dataverse Repository (doi: 10.5683/SP3/6E3ITE).

Funding: This work was supported by the Discovery Grant program of the Natural Sciences and Engineering Research Council of Canada (NSERC) under Grant 707337, by the project "Marine Environmental Observation, Prediction and Response" (MEOPAR) of the Networks of Centres of Excellence (NCE) of Canada, by the UQAM's Faculty of Sciences under the programme "faculty financial support", and by the excellence scholarship of the Trottier Family Foundation. The operation of the supercomputer Beluga is funded by the Canada Foundation for Innovation (CFI), Ministère de l'Économie et de l'Innovation du Québec (MEI) and les Fonds de recherche du Québec (FRQ). The funders had no role in study design, data collection and analysis, decision to publish, or preparation of the manuscript. There was no additional external funding received for this study.

Competing interests: The authors have declared that no competing interests exist.

lifetimes ranging from three to 36 hours [3]. They develop over the open water near the snow-covered landmasses or the sea-ice edge during marine cold air outbreaks (MCAOs). PLs are associated with severe weather conditions, including gale-force winds and heavy snowfall. These conditions can lead to large waves [e.g., 4], low visibility, snow avalanches, and icing on infrastructures. Therefore, PLs pose a threat to coastal populations, infrastructures, transport, and economic activities, and in some cases they have led to casualties [e.g., 5]. Producing accurate weather forecasts of PLs is thus critical to provide communities with enough time to prepare.

Weather forecasting in the polar regions remains a challenge since conventional observations are sparse, with weather stations being mainly concentrated along the coast [6], and data assimilation often fails to optimally use the available observational datasets [7]. The small temporal and spatial scales–horizontal and vertical scales of 100 km and 1 km, respectively –of PLs makes them particularly hard to forecast and to reanalyse [8]. Global reanalyses have low resolution ($>$ 30 km of grid mesh), so they often fail to capture observed PLs. For instance, the reanalysis of the European Centre for Medium-Range Weather Forecasts (ECMWF) known as ERA-Interim [ERA-I, 9], which has a grid mesh of 0.75˚, fails to capture many PLs [10, 11]. The fifth-generation ECMWF reanalyses ERA5 [12], which has a grid mesh of 31 km and hourly outputs, captures more PLs than its predecessor [13]. Regional reanalyses such as the Arctic System Reanalysis [ASR, 14] are likely to be more adequate to represent PLs than global reanalyses given their higher resolution, and the fact that they are adapted to a particular region. For example, the first version of the ASR, which has a grid mesh of 30 km, captures more PLs than ERA-I [15]. Limited-area high-resolution atmospheric models are also a useful tool to study PLs since they can represent more PLs compared to the coarser reanalysis used as initial and boundary conditions [e.g., 10].

PL forecasting has been improved recently thanks to the development of high-resolution, non-hydrostatic atmospheric models. Compared to large-scale models, convection-permitting models (CPMs) provide a better representation of convection as well as surface and near-surface processes [16], which play an important role in the development of PLs. Indeed, Stoll et al. [17] found that, compared to the ECMWF global model HRES based on the Integrated Forecast System (IFS) cycle 32r3 [18], which has a grid mesh of 25 km, the regional model ARO-ME-Arctic [19], which has a grid mesh of 2.5 km, represented better the small-scale features associated with a PL such as individual convective clouds.

The emergence of high-resolution atmospheric models comes with its challenges. The increased resolution of the models requires that the model parameterisations be adapted to the resolution of the CPMs [16, 20]. In the polar regions, the parameterisation of surface fluxes needs to be optimised [21]. Furthermore, to make correct forecasts, atmospheric models need to be initialised with good observed conditions. Initial conditions uncertainties affecting the prediction of small-scale weather systems are mainly associated with convective and mesoscale instabilities [22]. The initial conditions of moisture at the mesoscale are especially significant for PL forecasting [23]. The initialisation time also seems to have an impact on the representation of PLs, as shown by case studies of the PL developed on 3 March 2008 [24, 25]. McInnes et al. [24] found that the simulations with the MetUM using a grid mesh of 4 km showed better performance when the simulations were initialised at around 42 hours before the PL formed compared to the simulations initialised 24 hours later. The authors argued that this could indicate that initialising the simulations at an earlier stage may be necessary to reproduce the synoptic-scale atmospheric conditions leading to the PL development. Nevertheless, Wagner et al. [25] obtained opposite results using the Polar Weather Research and Forecasting (WRF) model with a grid mesh of 2 km. In effect, the authors found that the simulations that performed better were those whose initialisation time was closer to the genesis time of the PL.

In this work we conducted a case study of a PL that developed over the Norwegian Sea on 25 March 2019 with two main objectives:

1. To quantify the impact of the initial conditions on the simulation of the PL;
2. To assess the skill of the developmental version of the convection-permitting Canadian Regional Climate Model version 6 (CRCM6/GEM4) at reproducing the observed PL.

The main verification method used in case studies of PLs is visual verification, but this type of verification does not quantify the skill of the model [8]. Therefore, we have applied an objective method to verify the simulations of the PL against conventional observations. Since the PL made landfall in Norway, we have been able to use near-surface observations of a wide range of atmospheric variables. Given that more work is needed on the verification of near-surface fields in the polar regions [7], this study will partly contribute to fill in this research gap.

The article is organised in four sections. Section 2 provides information about the CRCM6/GEM4 and the datasets used for the verification of the simulations, as well as a description of the methods used to prepare the datasets and to verify the simulation output. Section 3 provides a description of the life cycle of the PL and includes the analysis of the results. Section 4 summarizes the main conclusions of this study.

2. Data and methods

2.1 Datasets

2.1.1 Simulations. The PL that developed over the Norwegian Sea on 25 March 2019 has been simulated with the developmental version of the convection-permitting CRCM6/GEM4. The dynamical core of the CRCM6/GEM4 has been developed from the limited-area version of the Global Environmental Multiscale Model [GEM; 26–28]. The CRCM6/GEM4 uses the dynamical core of the version 4 of the GEM model (GEM4), whose detailed description is given by Girard et al. [29]. GEM uses an implicit semi-Lagrangian method for spatiotemporal integration [26, 29]. The model uses a rotated longitude-latitude grid in the horizontal [30]. The vertical coordinate is a hybrid log-hydrostatic pressure coordinate, based on the formulation of hydrostatic pressure developed by Laprise [31]. For the spatial discretization, the model uses three-dimensional staggered grids, the Arakawa C grid in the horizontal and the Charney-Phillips grid in the vertical. For the lateral driving, GEM employs the nesting technique suggested by Davies [32], which consists of applying a sponge zone around the domain with a relaxation coefficient decreasing from the outside to the inside.

For the simulations reported here, the model uses a grid spacing of 0.0225˚ (≈ 2.5 km), a vertical grid with 62 levels, and a time step of one minute. The size of the domain is 1024 x 1024 grid points (Fig 1), including the ten grid point sponge zone around the perimeter of the domain, and the model top is at 2 hPa. The output of the simulations, excluding the sponge zone, therefore covers an area of approximately 2510 x 2510 km^2. Such domain is sufficient to capture not only the mesoscale phenomena, but also synoptic-scale features affecting polar low development.

The following subgrid parameterisation schemes have been used for the simulation: the correlated-k radiation scheme [34], the planetary boundary layer scheme MoisTKE that unifies turbulence and cloudiness [27, 35], the non-convective condensation scheme Predicted Particle Properties [P3; 36], and the land-surface scheme Interactions between Soil, Biosphere and Atmosphere [ISBA; 37]. Since convection is partially resolved, the deep convection scheme is turned off and only the shallow convection scheme Kuo-transient [27] is used. The orographic gravity wave drag and blocking, and non-orographic gravity wave drag schemes are also turned off.

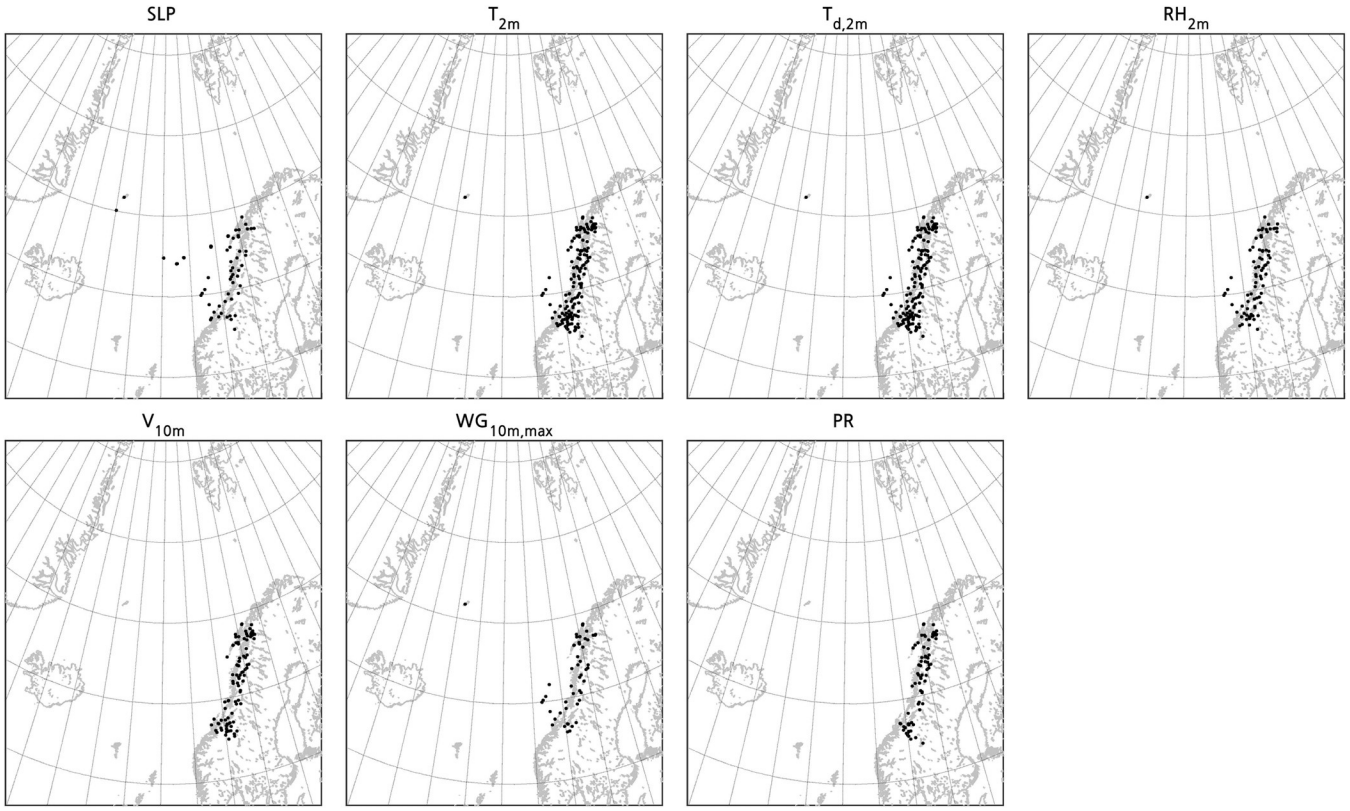

Fig 1. Location of the drifting buoys and surface stations whose data has been used for the verification of the simulations of the PL. The observations used are sea level pressure (SLP), 2-m temperature (T_{2m}), 2-m dewpoint temperature ($T_{d,2m}$), 2-m relative humidity (RH_{2m}), 10-m wind (V_{10m}), 10-m maximum wind gusts ($WG_{10m,max}$), and 1-h accumulated precipitation (PR). The region showed is the domain of the simulation excluding the sponge zone. The dataset used to plot the geographic contours has been obtained from the Global Self-consistent, Hierarchical, High-resolution Geography Database (GSHHG; [33]) under a CC BY license, with permission from Dr. Paul Wessel.

https://doi.org/10.1371/journal.pone.0292250.g001

The atmospheric and ocean surface initial and boundary conditions have been obtained from the ERA5 global reanalysis, which has a horizontal grid of 0.25˚ [12]. From September 2007 onwards, ERA5 uses the Operational Sea Surface Temperature and Sea Ice Analysis (OSTIA) product for the sea surface temperature (SST), and the Ocean and Sea Ice Satellite Application Facilities (OSI SAF) product for the sea ice concentration (SIC). The CRCM6/GEM4 is hourly (daily) driven by the atmospheric (ocean surface) fields of ERA5. The ocean surface condition is temporally interpolated. The land surface initial conditions have been obtained from the Canadian Meteorological Centre analyses. Eight simulations were conducted by initialising the model every 6 hours from 23 March at 0000 UTC to 24 March at 1800 UTC. All simulations ended on 26 March at 0600 UTC. In what follows, we will refer to each simulation by its initialisation date; for instance, the simulation initialised on 24 March at 1200 UTC will be referred to as 24d12h.

Several variables at screen level have been output to compare them with conventional observations. It is important to note that the model computes the wind gusts using the wind gust estimate method developed by Brasseur [38]. This approach assumes that turbulent eddies lead to the downward deflection of air parcels located at higher levels in the boundary layer, producing surface wind gusts. Therefore, the mean wind and the turbulent structure of the atmosphere are included in the computation of wind gusts. This method provides a wind gust estimate as well as a bounding interval around this estimate. For this study, we use the instantaneous wind gust estimate that is output every hour.

2.1.2 Conventional observations. The simulations have been evaluated against hourly observations from weather stations provided by the Norwegian Meteorological Institute (MET Norway), and from drifting buoys provided by Canada's Integrated Science Data Management (ISDM) centre. Drifting buoys have been deployed by different international programs, the largest being the Global Drifter Program (GDP), which is the result of an international collaboration under the World Meteorological Organization (WMO) and the United Nations Educational, Scientific and Cultural Organization (UNESCO) umbrella. The GDP has been deploying surface Velocity Program Lagrangian drifters equipped with barometers that measure mean sea level pressure (SLP) every hour [39]. The main advantages of using conventional observations as "truth data" are that they directly measure meteorological variables and they have high temporal resolution, which is essential to capture PL development.

The observations from weather stations used to verify the simulations are SLP, 2-m temperature, 2-m dewpoint temperature, 2-m relative humidity, 10-m wind speed and direction, 10-m maximum wind gusts, and 1-h accumulated precipitation. The registered wind speed and direction are averaged over the last ten minutes before the observation time, and the maximum wind gust is the maximum wind registered during the ten minutes before the observation time. For drifting buoys, only SLP is available. Care should be taken when comparing the observed 10-m maximum wind gusts with the simulation and ERA5 wind gusts since the latter two are instantaneous wind gusts that are output every hour.

2.1.3 ERA5. The reanalysis ERA5 is produced by the EMCWF using a 4D-Var data assimilation scheme and the IFS Cy41r2 [12]. ERA5 has a grid spacing of 31 km and 137 levels to 0.01 hPa, and it provides hourly data. It covers the period from 1978 to the present, and there is a preliminary version from 1950 to 1978 [40]. Among other data, ERA5 assimilates conventional observations from surface stations and drifting buoys [see Fig 4 of 12]. Some studies have found that ERA5 shows a good performance in the Arctic [41, 42]. For example, Graham et al. [41] found that, compared to other reanalyses, including ERA-I, ERA5 had the smallest biases and root mean square errors (RMSEs), and the highest correlation coefficients at capturing the temperature, wind speed and specific humidity in the Fram Strait. Nevertheless, some studies have found limitations of ERA5 over Arctic sea ice. Since ERA5 does not represent a snow layer on top of the sea ice, the conductive heat flux from the ocean to the atmosphere is overestimated. As a result, like other reanalyses, ERA5 sea-ice surface temperature shows a warm bias during clear-sky conditions in winter [43]. This is consistent with the large warm bias of ERA5 2-m temperature over Arctic sea ice during the cold season compared to observations from drifting buoys [44].

2.2 Data preparation

We have prepared all the data from surface stations and drifting buoys available in the domain of the simulations in order to have complete time series of the variables whenever possible. Regarding surface stations, only data with acceptable quality has been selected, and outliers have been discarded. Therefore, some of the time series were incomplete either because there was already missing data or because some observations were discarded due to their low quality. In the case of noisy variables (10-m wind, 10-m wind gusts, and 1-h accumulated precipitation), the time series with one or more missing data have been completely discarded. In the case of smooth or continuous variables (SLP, 2-m temperature, 2-m relative humidity and 2-m dewpoint temperature), the time series with more than three missing values have been discarded. For the time series with three or less missing values, these values have been computed doing a linear temporal interpolation using the closest previous and following available observations, including sub-hourly observations. When the time between the previous or following observation and the missing observation was longer than one hour, the time series was discarded. Finally, since both wind speed and

direction are needed to verify the simulations, only the data of stations that provide both wind speed and direction have been retained for the verification of the wind field. In the case of drifting buoys, no time interpolation of the missing data has been done.

The simulated and ERA5 atmospheric fields have been spatially interpolated from the model grid to the observation points using either bilinear–for noisy variables–or bicubic interpolation–for smooth variables. A simple height correction has been applied to the simulated and the ERA5 temperature and dew point temperature to account for the difference in height between the real topography and the topography of the model. The lapse rate of the simulations and ERA5 at the lowest levels of the atmosphere has been used for the height correction of their respective temperature fields.

2.3 Verification

First, the track, size and intensity of the PL captured by the simulations and ERA5 have been compared to that of the observed PL. The track of the observed PL has been manually obtained using IR radiance satellite images from the Moderate Resolution Imaging Spectroradiometer (MODIS), the Advanced Very High Resolution Radiometer (AVHRR/3) and the Visible Infrared Imaging Radiometer Suite (VIIRS). The coordinates of the centre of the observed PL have been estimated at each hour from the genesis until the dissipation of the PL. The track that has been initially obtained using the satellite images has been improved by ensuring that the track is consistent with the conventional observations of SLP and 10-m wind. The tracks of the PL in the simulations and ERA5 have been manually obtained using the SLP field. The criteria to identify the beginning of the PL is the presence of at least three SLP closed contours in a map showing the SLP isobars every 1 hPa. The size of the PL has been estimated in all the datasets by measuring the diameter of the cloud signature during the mature stage of the PL. The intensity of the PL in the simulations and ERA5 is given by the SLP minimum at its centre. In the case of observations, the SLP minimum corresponds to the SLP observation from the surface station that is the closest to the centre of the PL. Since some stations are too far from the centre of the PL, only the observations from stations within a distance of 25 km from its centre have been considered.

Second, all the simulations and ERA5 have been verified against observations from surface stations and drifting buoys affected by the PL. Therefore, we have only used observations obtained within a distance of 300 km– which approximately corresponds to the radius of the cloud signature of the PL at its mature stage –from the centre of the observed PL. The total number of observations used are 352 for SLP, 860 for 2-m temperature, 820 for 2-m dewpoint temperature, 483 for 2-m relative humidity, 534 for 10-m wind, 318 for 10-m wind gusts, and 448 for 1-h accumulated precipitation. From the genesis of the PL until 25 March at 11:00 UTC or 12:00 UTC, depending on the variable, the number of observations is no more than 10, or there are no observations at all. The number of observations notably increases when the PL gets closer to the Norwegian coast (Fig 1). Therefore, the results are mainly representative of the mature and dissipation stages of the PL. The statistics computed to measure the performance of the simulations are the mean error (ME), the root mean square error (RMSE), and the Spearman correlation coefficient (r) [45]. Since the wind is a vector, the root mean square wind-vector-difference error has been computed [RMSE-WVD; e.g., 46]. The correlation coefficient has only been computed when at least three observations were available.

3. Results and discussion

3.1 Description of the life cycle of the PL

Northerly winds on the cold side of a synoptic-scale low located over the Barents Sea caused a MCAO in Fram Strait at the end of March 2019 (Fig 2A). Cold northerly winds to the west of

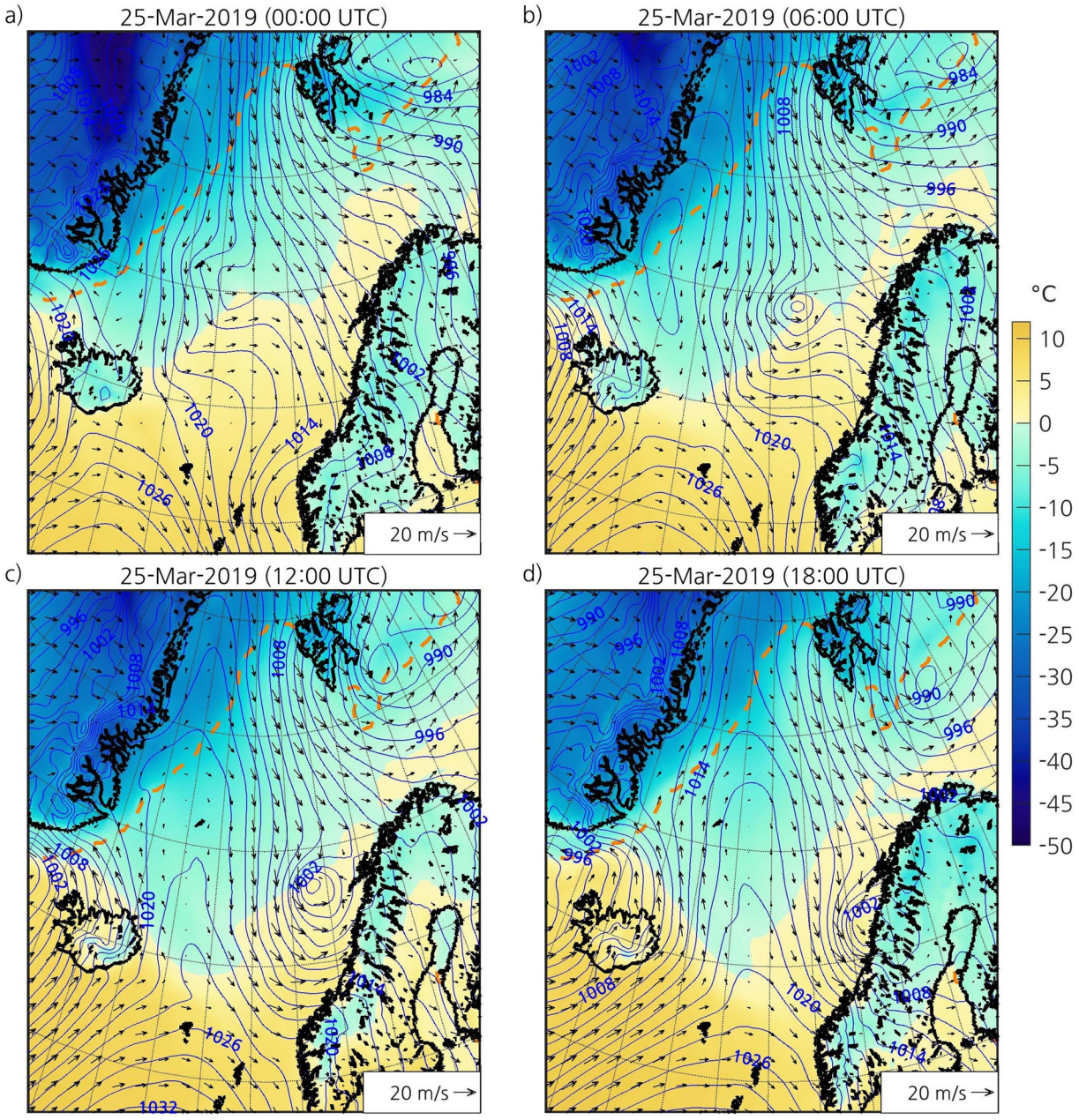

Fig 2. ERA5 atmospheric fields showing the development of the PL on 25 March 2019 at (a) 0000 UTC, (b) 0600 UTC, (c) 1200 UTC, and (d) 1800 UTC. The blue isolines represent the SLP (contours every 2 hPa), the colourmap represents the 2-m temperature (˚C), and the arrows represent the 10-m wind direction and speed, with longer arrows representing higher wind speeds. The orange dashed line represents the sea ice edge, which is defined as the 0.15 contour of the SIC corresponding to 25 March 2019 at 1200 UTC. The black outlining represents the coastline. ERA5 fields have been interpolated to the grid of the simulation using bicubic interpolation for the SLP and temperature and bilinear interpolation for the wind. The dataset used to plot the geographic contours has been obtained from the GSHHG [33] under a CC BY license, with permission from Dr. Paul Wessel.

https://doi.org/10.1371/journal.pone.0292250.g002

synoptic-scale lows is a common favourable environment for PL development in the Nordic Seas [47]. The PL developed early on 25 March near the sea ice edge east of Greenland, in a region with a strong temperature gradient (Fig 2B). The cloud streets and open cells associated with the MCAO are visible on IR satellite images from the AVHRR channel 4 (Fig 3). The PL

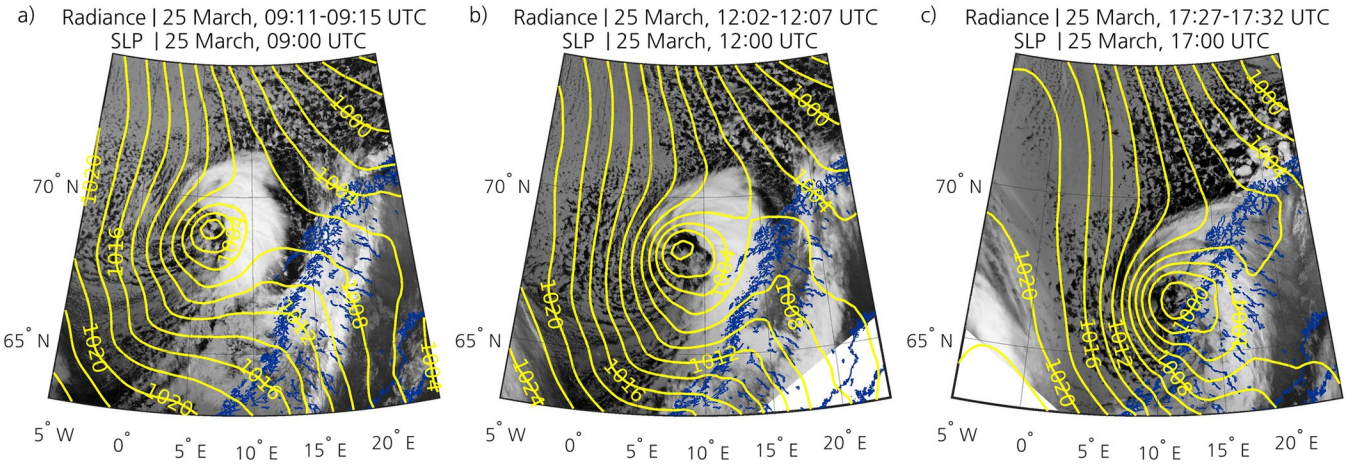

Fig 3. AVHRR channel 4 images showing the PL on 25 March (a) before it hits land, (b) when it is over a great part of the Norwegian coast, and (c) when it starts to dissipate. The yellow isolines represent the ERA5 SLP field (contours every 2 hPa). The blue outlining represents the coastline. The dataset used to plot the geographic contours has been obtained from the GSHHG [33] under a CC BY license, with permission from Dr. Paul Wessel.

https://doi.org/10.1371/journal.pone.0292250.g003

started to form over open water at the leading edge of this MCAO, and a comma-shaped cloud signature was clearly identifiable in IR images by 25 March at 0200 UTC (not shown). Like many PLs in the Nordic Seas [e.g., 48], it moved southeastward as it deepened (Fig 2B and 2C). The PL hit land in Nordland county of Norway after 0900 UTC (Fig 3A). By 1200 UTC, it had reached a large part of the Norwegian coast (Figs 2C and 3B). The winds associated with the PL reached an observed maximum speed of 24.8 m s^{-1}. The PL started to dissipate at around 1800 UTC (Figs 2D and 3C). The lifetime of this PL was 20 hours (Table 1), in agreement with climatologies of PLs in the Nordic Seas [e.g., 15]. The estimated size of the PL at its mature stage was 586 km in diameter, which is larger than the typical diameter of PLs [e.g., 48]. With an average speed of 15 m s^{-1}, the PL travelled 1,070 km. Both the average speed and distance travelled are larger than those of most PLs [48].

3.2 Verification of the track, size and intensity of the simulated PL

Fig 4 shows the SLP isobars of the eight simulations and ERA5 on 25 March 2019 at 1500 UTC, when the mature PL was affecting the Norwegian coast. The large-scale features of the SLP field are similar for all simulations, whereas the simulations notably differ from each other at the mesoscale, in particular near the location of the PL. Overall, these spaghetti plots show that most simulations fail to represent the PL. Only 23d12h and the latest initialised simulations 24d12h and 24d18h represent a PL.

The PL in the the simulations and ERA5 forms and dissipates on 25 March. The simulations 24d12h and 24d18h represent well the size and lifetime of the observed PL, as well as the the

Table 1. Lifetime, translation speed and distance travelled by the PL.

Dataset	Start hour [UTC]	End hour [UTC]	Size [km]	Average speed [m s^{-1}]	Distance [km]
Observations	0100	2100	586	15	1,070
23d12h	1200	2000	402	14	395
24d12h	0000	2000	585	12	892
24d18h	0000	2100	561	15	1,113
ERA5	0500	1900	561	13	636

https://doi.org/10.1371/journal.pone.0292250.t001

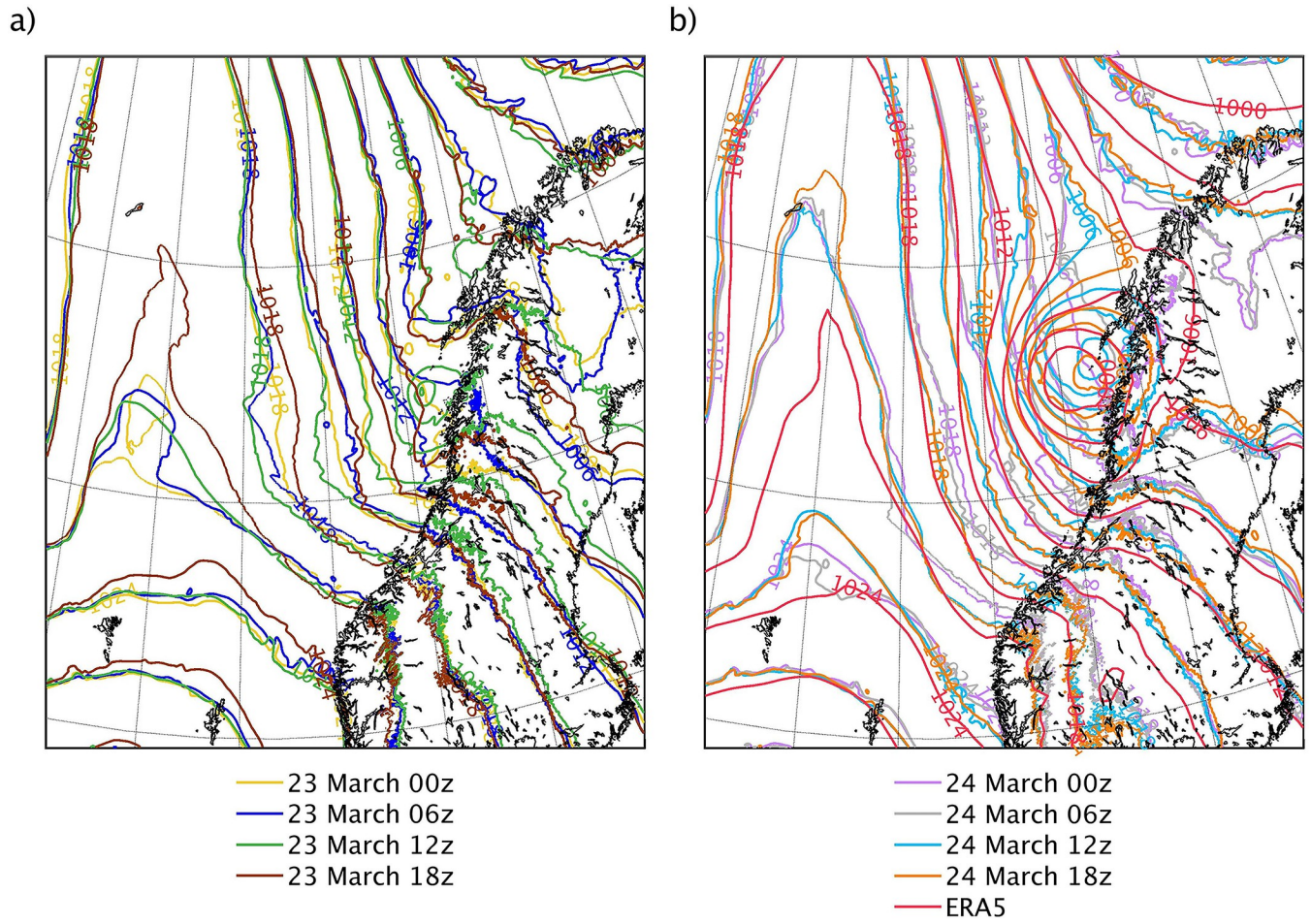

Fig 4. Spaghetti plots showing the SLP isobars (contours every 3 hPa) of the simulations and ERA5 on 25 March 2019 at 1500 UTC, when the mature PL was affecting the Norwegian coast. The contour lines correspond to the SLP field of (a) the simulations initialised on 23 March at 0000, 0600, 1200 and 1800 UTC, and (b) the simulations initialised on 24 March at 0000, 0600, 1200 and 1800 UTC, and ERA5. The black outlining represents the coastline. The dataset used to plot the geographic contours has been obtained from the GSHHG [33] under a CC BY license, with permission from Dr. Paul Wessel.

https://doi.org/10.1371/journal.pone.0292250.g004

timing of its genesis and dissipation (Table 1). The average speed of the PL in 24d18h is the same as that of the observed one, and the total distance travelled is similar. The average speed of the PL and the distance travelled are lower in 24d12h, but they are fairly close to the observed ones. The PL represented in 23d12h is much smaller than the observed PL, and its lifetime is less than half the lifetime of the observed PL. However, its average speed is similar to the observed one. The PL in this simulation forms eleven hours latter than the observed one, but it dissipates at a similar time. Therefore, the distance travelled by the PL in this simulation is significantly lower than the observed one. The PL in ERA5 has shorter lifetime and somewhat lower average speed than the observed one, but similar size.

The tracks of the PL in the simulations and in ERA5 are reasonably close to that of the observed PL (Figs 5 and 6A). The distance between the simulated and the observed tracks notably increases at the end of the lifetime of the PL, which may be partly due to the high uncertainty when determining the centre of the PL at its dissipation stage. The tracks in 24d12h and 24d18h remain within 100 km from the observed track most of the time, whereas the track in ERA5 remains within 50 km from the observed one. The observed SLP minimum attained near the centre of the PL is 999.1 hPa at 1500 UTC (Fig 6B). However, since the

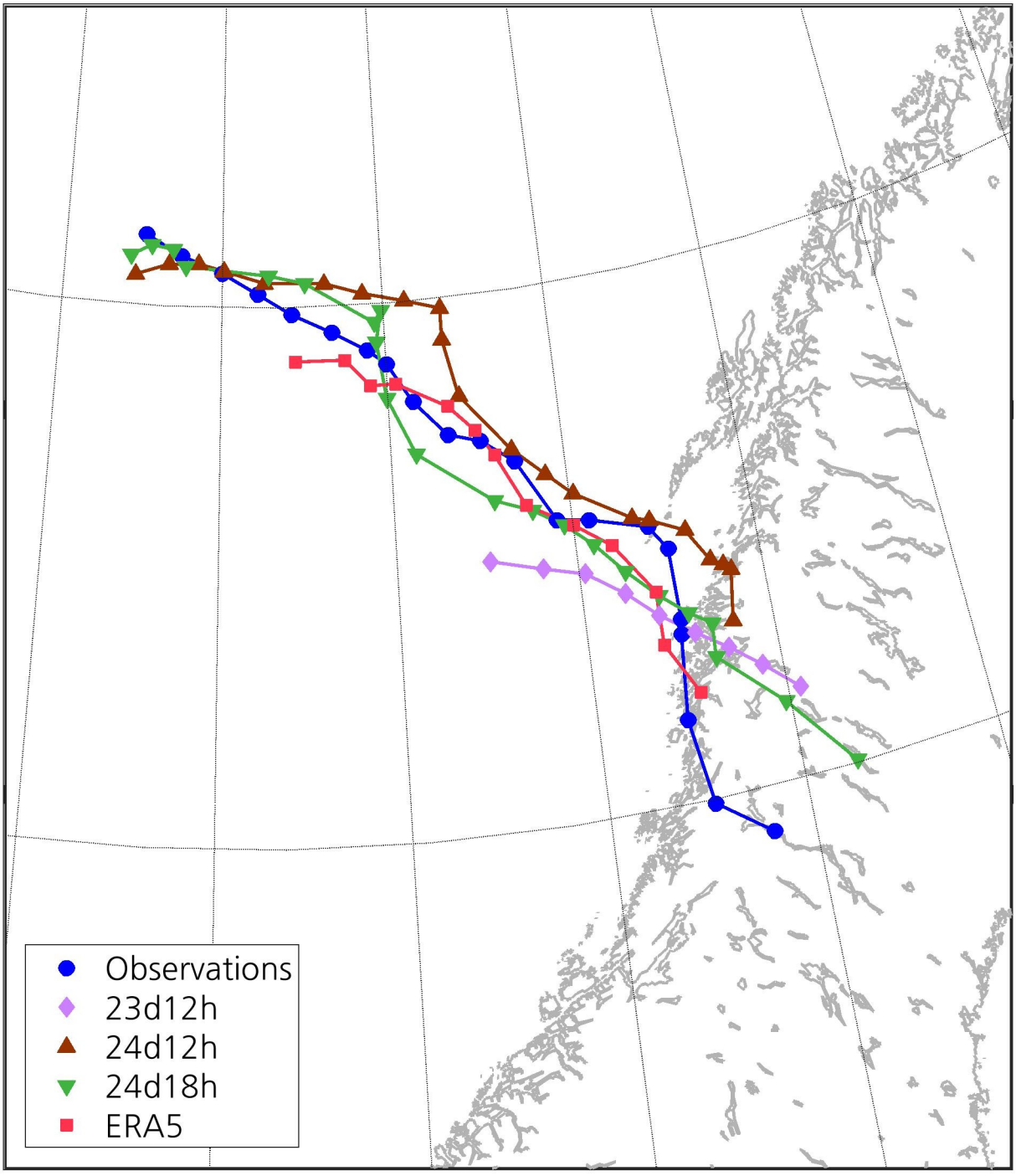

Fig 5. Track of the observed PL and of the PL in the simulations and ERA5. The markers represent the position of the PL at each hour. Information about the genesis and dissipation times of these PLs can be found in Table 1. The dataset used to plot the geographic contours has been obtained from the GSHHG [33] under a CC BY license, with permission from Dr. Paul Wessel.

https://doi.org/10.1371/journal.pone.0292250.g005

surface station providing this observation is located 8.82 km from the centre, the real SLP minimum may be lower. The SLP minimum of the PL in 24d12h and 24d18h is 995.6 and 995.7 hPa, respectively, also at 1500 UTC. The PL in 23d12h shows a steeper decrease in SLP and, as

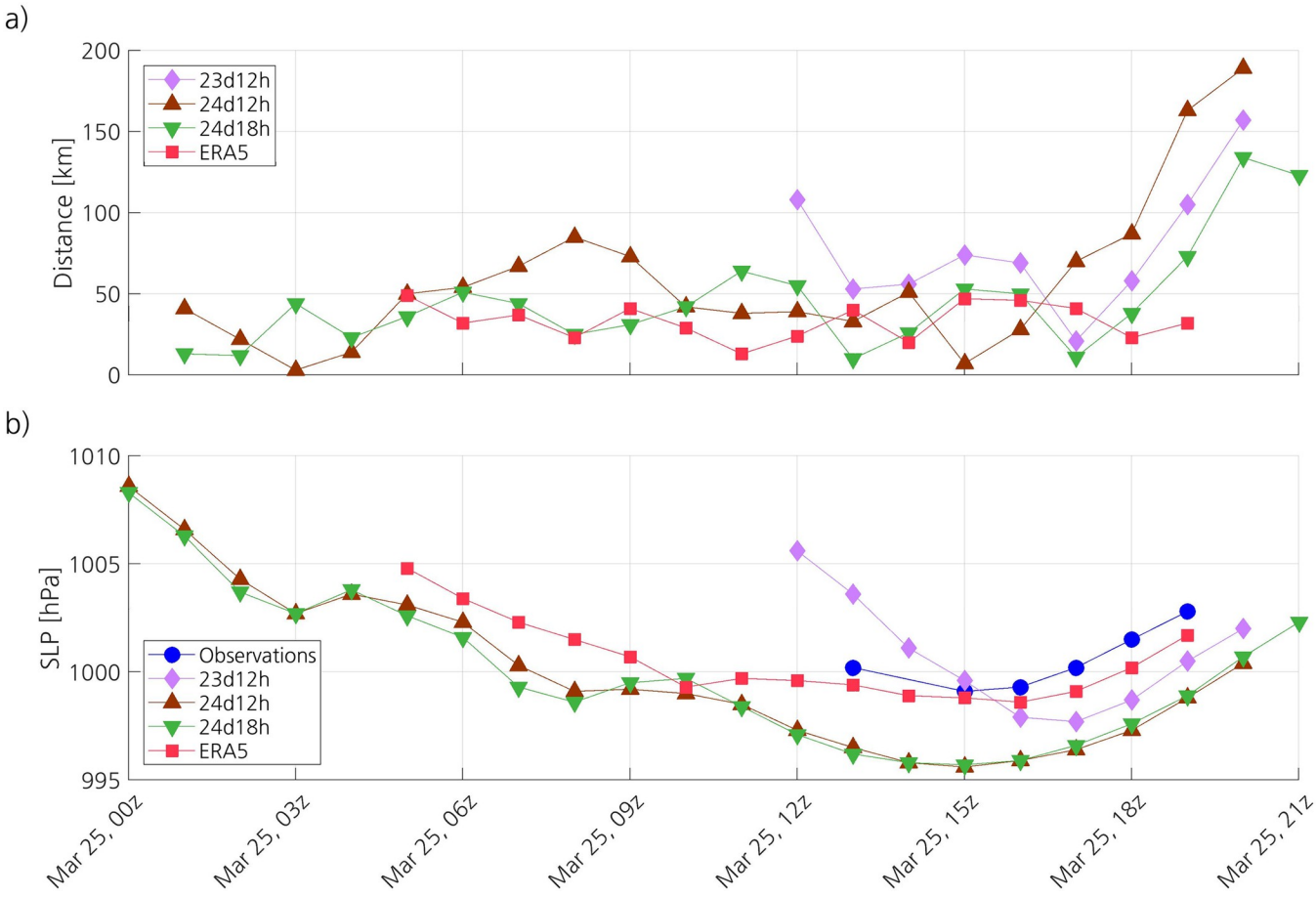

Fig 6. Time series of (a) the distance between the centre of the observed PL and the centre of the PL in the simulations and ERA5, and (b) the SLP at the centre of the PL in the simulations and ERA5, and the SLP observed at the surface station the closest to the centre of the observed PL.

https://doi.org/10.1371/journal.pone.0292250.g006

a result, the SLP minimum is reached just two hours later than in the other simulations. With a shorter lifetime than the other simulated PLs, the PL in 23d12h deepens slightly less than the others and, therefore, its associated SLP minimum is closer to the observed one. Compared to the simulations, the PL in ERA5 deepens less, corresponding better to the observations. The evolution of the SLP at the centre of the PL in ERA5 follows closely the observations, and the SLP in ERA5 attains a minimum of 998.6 hPa at 1600 UTC.

3.3 Verification of the simulated PL against observations affected by the PL

3.3.1 Sea level pressure. As expected, all simulations except for 24d12h and 24d18h notably overestimate SLP, particularly the lowest observed SLP values (Fig 7). In contrast, 24d12h and 24d18h underestimate many SLP values between 1000 and 1010 hPa. The aggregate statistics show that 24d12h and 24d18h have lower absolute mean bias, higher accuracy and higher correlation coefficient than the other simulations (Table 2). Whereas both 24d12h and 24d18h have a ME of -0.2 hPa, the ME of the other simulations ranges from 2.1 to 3.5 hPa. The RMSE of 24d12h and 24d18h (2 hPa and 1.4 hPa, respectively) is considerably lower than that of the other simulations (between 3.2 hPa and 4.5 hPa). The Spearman correlation coefficient of 24d12h and 24d18h shows that they have, respectively, a strong and a very strong positive correlation with the observations. Except for 23d12h and 23d18h, which show a quite strong correlation with the observations, the other simulations show either weak or modest correlation.

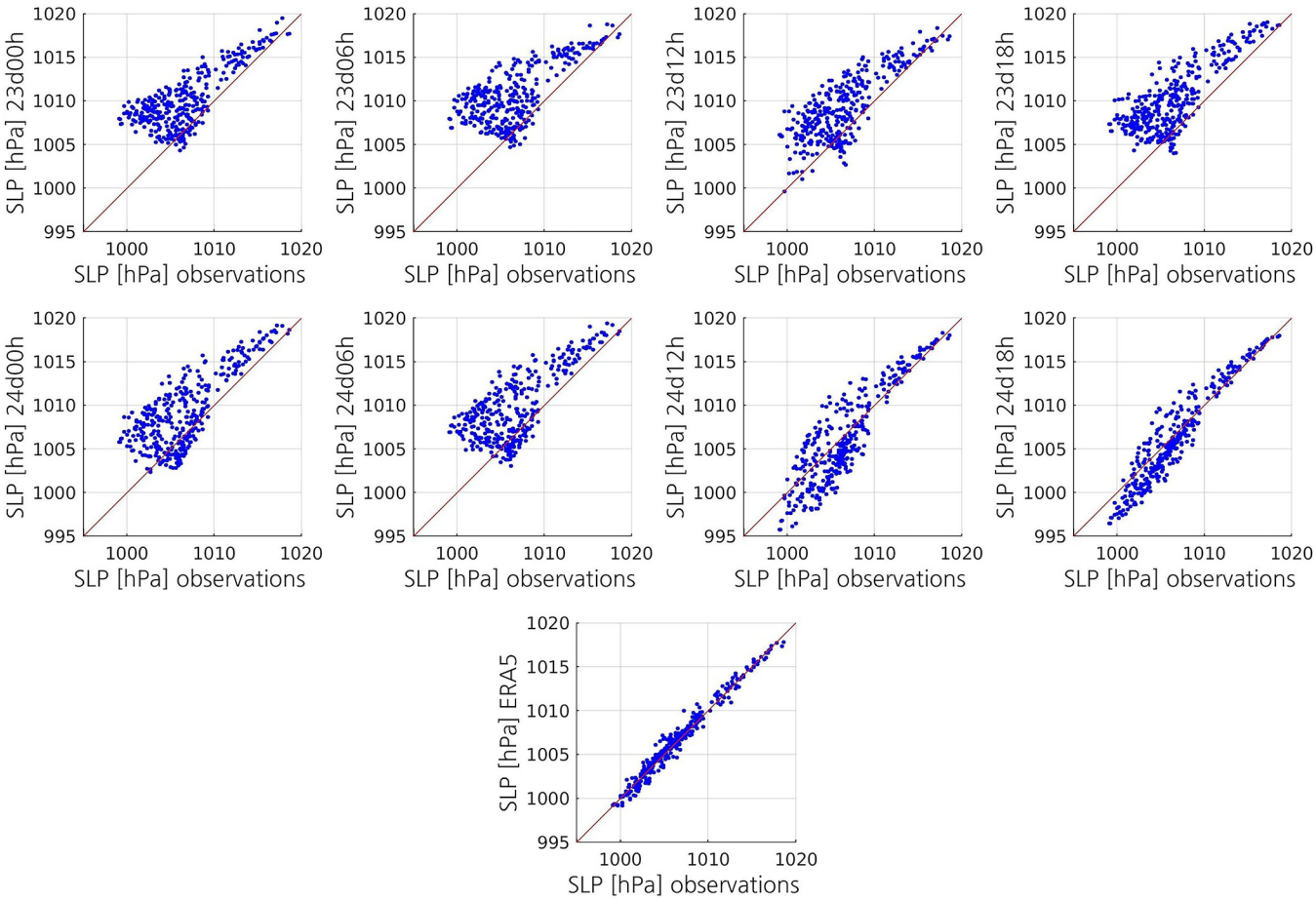

Fig 7. Scatterplots displaying, for each simulation, the relationship between the simulated SLP and the SLP measured at surface stations and drifting buoys. The scatterplot on the bottom displays the relationship between the ERA5 SLP and the observed SLP. The red line represents the regression line that would correspond to a perfect match between the values.

https://doi.org/10.1371/journal.pone.0292250.g007

The simulations 24d12h and 24d18h have a small negative ME during the mature and dissipation stages of the PL, whereas the other simulations show a positive ME during the whole lifetime of the PL (Fig 8A). The ME of the latter steadily increases from around 1100 UTC until around 1600 UTC, which is likely due not only to the deepening of the PL, but also to the fact that its centre is getting closer to the surface stations. The time series of the RMSE of these simulations shows a similar pattern to that of the ME (Fig 8B). The main difference is that 24d12h and 24d18h also show an increase in the RMSE during the deepening of the PL, although it remains much lower than that of the other simulations. This decrease in accuracy, together with the negative mean bias, confirms the previous finding that the simulated PL in both simulations is deeper than the observed one. All simulations except for 24d12h and 24d18h show a significant decrease in the Spearman correlation coefficient from 1300 UTC until 1500 UTC, when it reaches a minimum, which corresponds to the time when the SLP minimum is observed (Fig 8C). Then, the correlation coefficient increases until the PL has dissipated. The simulation 24d12h shows a similar pattern, but the decrease in the correlation coefficient is much less pronounced. In contrast, 24d18h shows a small decrease in the correlation coefficient.

ERA5 shows better skill at representing SLP than the simulations, even than 24d18h. Although the absolute ME of ERA5 and 24d18h are both small (Table 2, Fig 8A), the

Table 2. Aggregate statistics computed to verify the simulated and ERA5 SLP against the observations from surface stations and drifting buoys.

	ME [hPa]	RMSE [hPa]	*r*
23d00h	3	3.8	0.54
23d06h	3.5	4.5	0.48
23d12h	2.8	3.6	0.71
23d18h	3.2	3.9	0.67
24d00h	2.1	3.2	0.59
24d06h	2.5	3.6	0.53
24d12h	-0.2	2	0.81
24d18h	-0.2	1.4	0.92
ERA5	0.1	0.6	0.98

https://doi.org/10.1371/journal.pone.0292250.t002

scatterplot shows that ERA5 has better skill (Fig 7). The higher accuracy of ERA5 is confirmed by its aggregate RMSE (0.6 hPa), which is less than half of that of 24d18h (Table 2). The RMSE of ERA5 remains relatively constant and less than one during the whole lifetime of the PL (Fig 8B). Like 24d18h, ERA5 shows a very strong positive correlation with the observations, but its correlation coefficient is slightly higher than that of 24d18h (Table 2, Fig 8C).

3.3.2 Temperature at 2 m. All the datasets have a positive temperature bias (Fig 9). The aggregate statistics indicate that 24d12h and 24d18h have higher mean bias and lower accuracy, but higher correlation coefficient, than the other simulations (Table 3). These two simulations have a higher ME (2˚C) and a slightly higher RMSE (2.4˚C) compared to the simulations that did not simulate the PL (ME between 0.8 and 1.3˚C, and RMSE between 1.9 and 2.1˚C). The simulation that captured a small and short-lived low, 23d12h, has a ME (1.7˚C) and a RMSE (2.3˚C) lower than those of 24d12h and 24d18h, but higher than those of the other simulations. All simulations show a quite strong correlation with the observations. Although 24d12h and 24d18h show the highest Spearman correlation coefficient (0.78), the difference between the simulations is very small.

In the initial stage of the PL, all simulations show a high positive ME, with 24d12h and 24d18h showing the highest bias (Fig 10A). This could indicate that the MCAO is not well simulated. However, there are only two observations available at 0100 and one at 0200 UTC, so the results should be interpreted with care. From 1000 UTC until the dissipation of the PL, the ME of 24d12h and 24d18h remains notably higher than that of the simulations that have not captured the PL. The ME of 23d12h remains lower than that of 24d12h and 24d18h, but higher than that of the other simulations virtually all the time. The important surface heat transfer from the ocean to the atmosphere that takes place in the simulations that have captured the PL (not shown) likely explains why these simulations have higher ME. The RMSE of 23d12h, 24d12h and 24d18h remains higher than that of the other simulations most of the time (not shown). The correlation coefficients of all simulations notably increase from around 1100 UTC until around 1500 UTC, and then the simulations show a strong or a quite strong correlation with the observations (not shown).

Surprisingly, the aggregate ME of ERA5 (0.9˚C) is closer to that of the simulations that have not captured the PL than to that of the simulations that have captured it (Table 3). The ME of ERA5 remains significantly lower than that of 24d12h and 24d18h, and closer to that of the simulations that have not captured the PL, during the whole observed lifetime of the PL (Fig 10A). With an aggregate RMSE of 1.5˚C, ERA5 has slightly higher accuracy than all the simulations (Table 3). The RMSE of ERA5 remains lower than that of the simulations during virtually the whole observed lifetime of the PL, and the difference in accuracy between ERA5

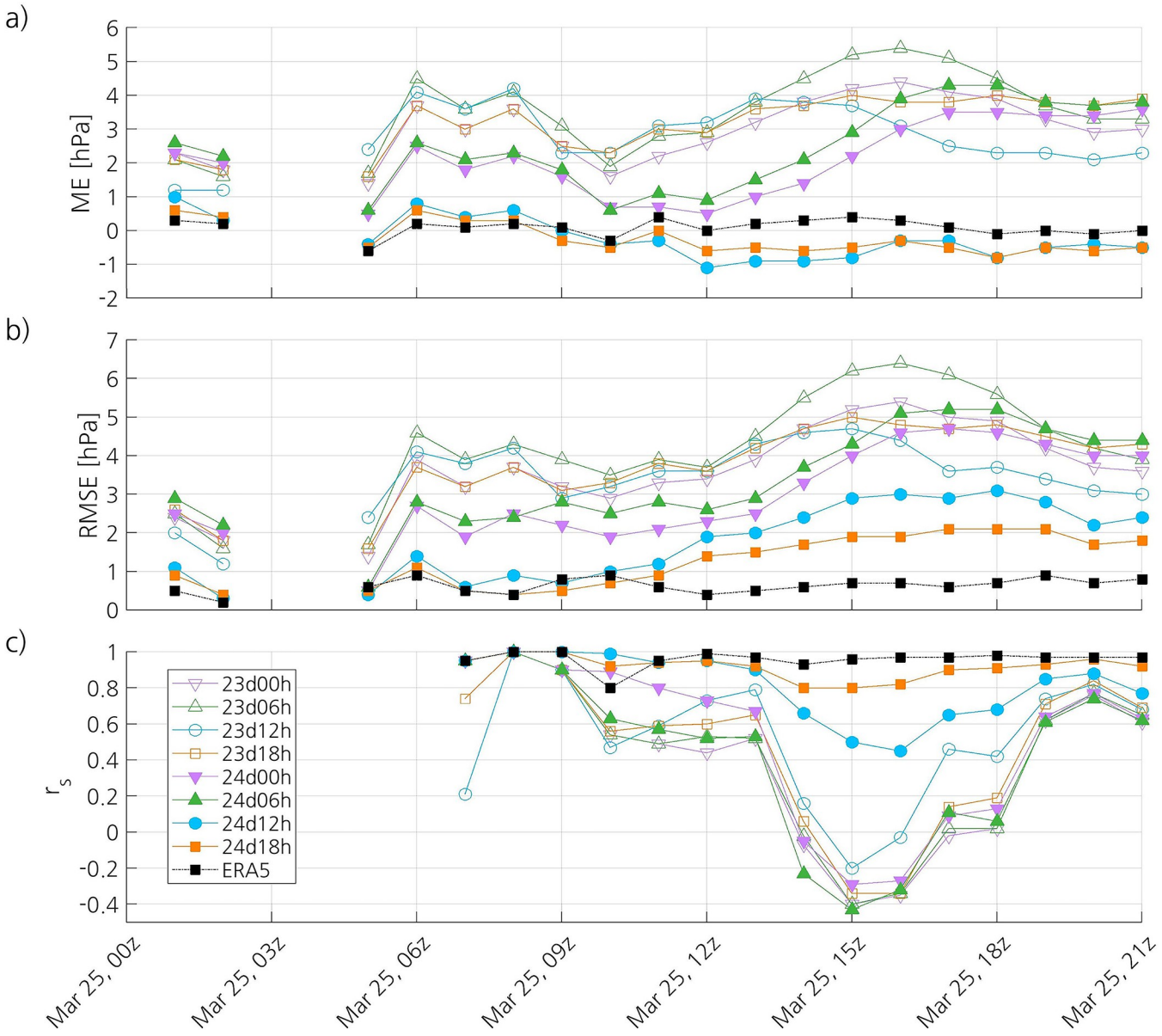

Fig 8. Time series of the (a) ME, (b) RMSE, and (c) Spearman correlation coefficient of the simulated and ERA5 SLP. The dataset used as reference to compute the ME is the SLP measured at surface stations and drifting buoys.

https://doi.org/10.1371/journal.pone.0292250.g008

and the simulations is more important during its dissipation stage (not shown). ERA5 shows a strong correlation with the observations (0.87), which is higher than that of the simulations (Table 3). The time series of the correlation coefficient of ERA5 follows a pattern similar to that of the simulations, but it becomes higher than the correlation coefficients of the simulations during its dissipation stage (not shown).

3.3.3 Dew point temperature at 2 m. The aggregate statistics indicate that the simulations that have captured the PL do not show better skill at representing the dew point temperature than those that have not captured it (Table 4). Most simulations have lower ME than 24d12h and 24d18h (2.2˚C and 2˚C, respectively). All simulations have similar RMSE, ranging from 2.9 to 3.4˚C. Some simulations that have not captured the PL have weak correlation with the

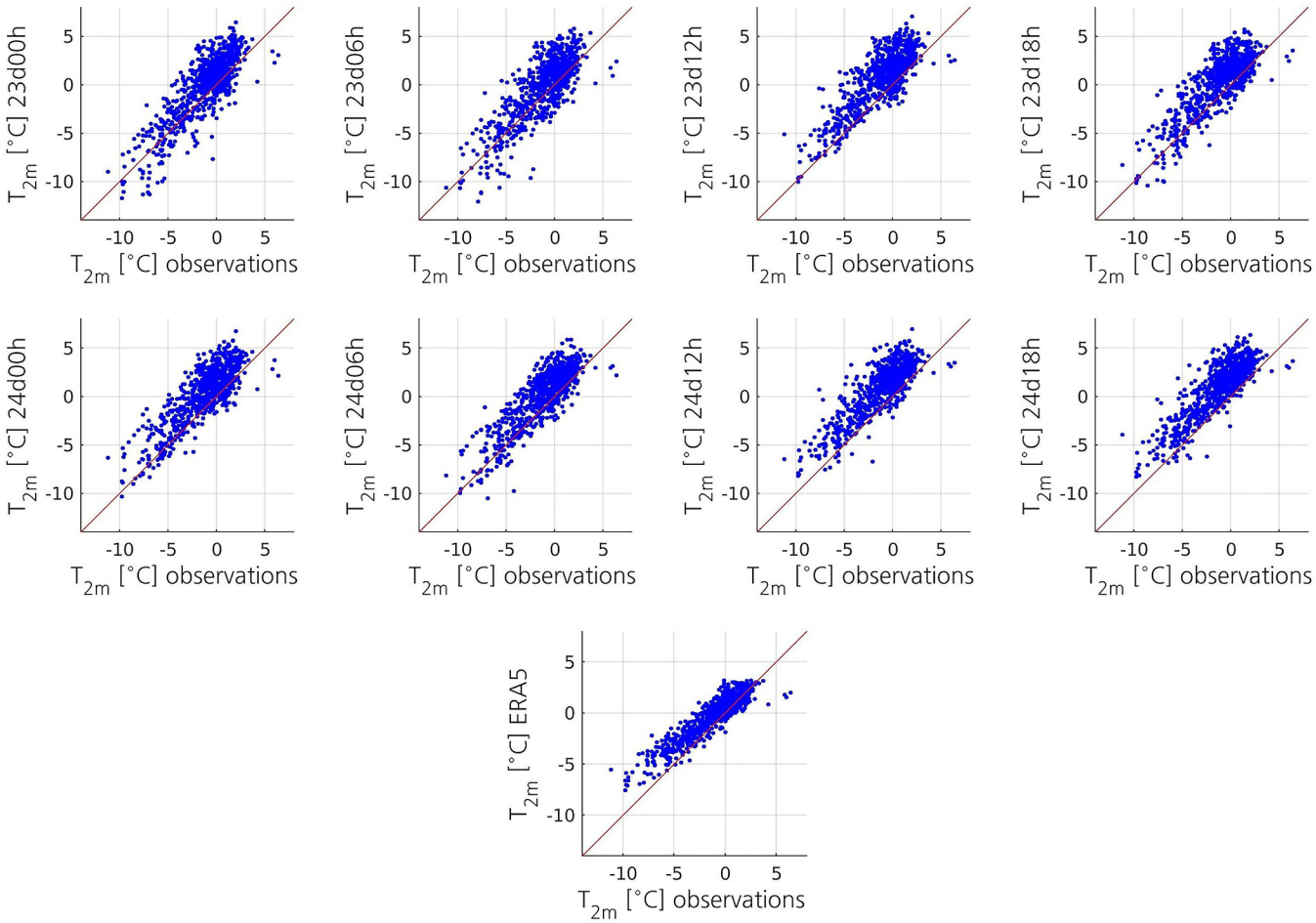

Fig 9. Scatterplots displaying, for each simulation, the relationship between the simulated 2-m temperature and the 2-m temperature measured at the surface stations. The scatterplot on the bottom displays the relationship between the ERA5 2-m temperature and the observed 2-m temperature. The red line represents the regression line that would correspond to a perfect match between the values.

https://doi.org/10.1371/journal.pone.0292250.g009

observations, whereas the other simulations, including those that represent the PL, have modest correlation with the observations. Although the time series of the ME of each simulation is quite different, all the simulations show a positive ME during all or almost all the time

Table 3. Aggregate statistics computed to verify the simulated and ERA5 2-m temperature against the observations from surface stations.

	ME [˚C]	RMSE [˚C]	*r*
23d00h	1	2	0.75
23d06h	0.8	1.9	0.74
23d12h	1.7	2.3	0.74
23d18h	1.2	2	0.73
24d00h	1.3	2.1	0.75
24d06h	1.2	1.9	0.77
24d12h	2	2.4	0.78
24d18h	2	2.4	0.78
ERA5	0.9	1.5	0.87

https://doi.org/10.1371/journal.pone.0292250.t003

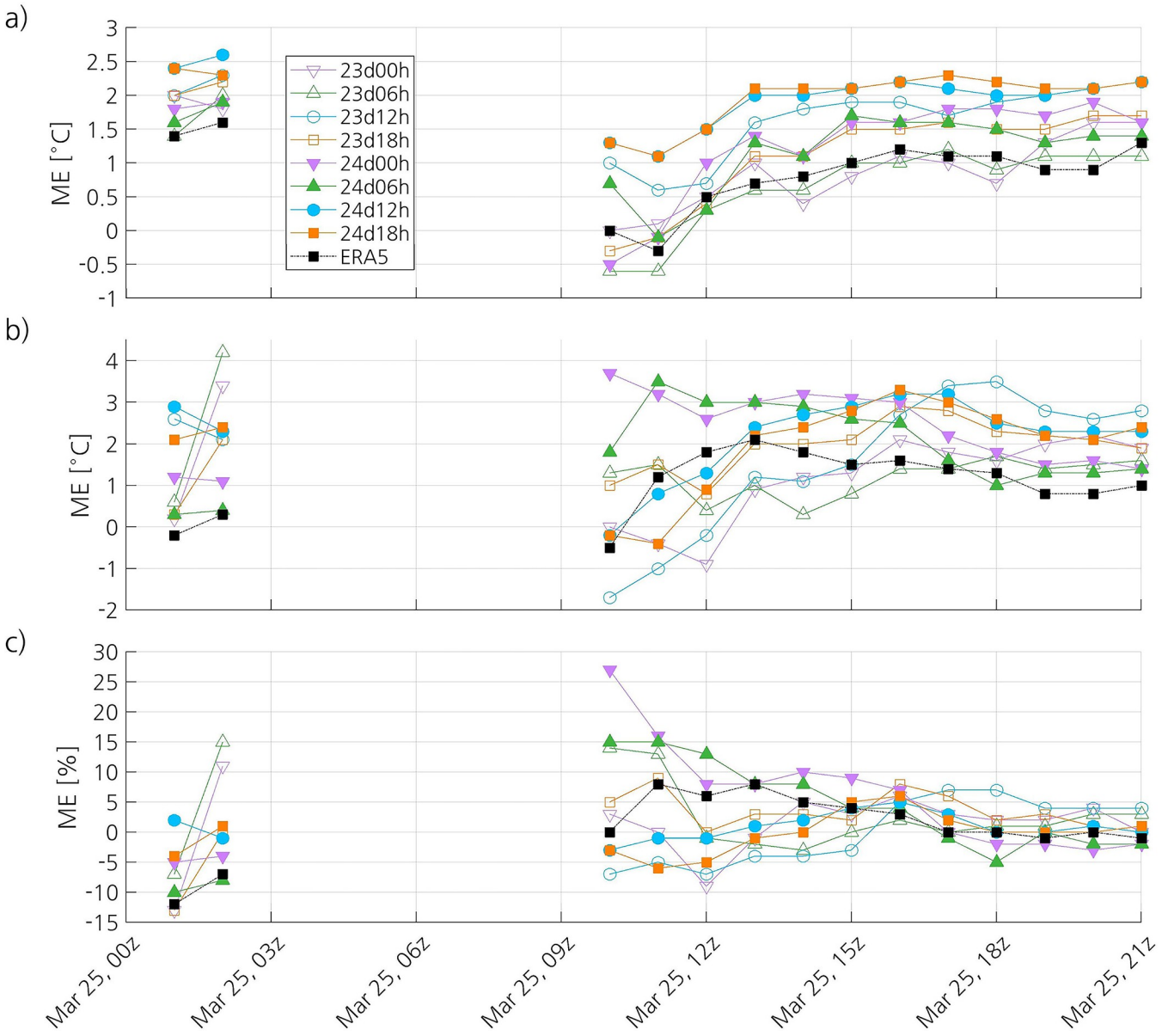

Fig 10. Time series of the ME of the simulated and ERA5 (a) 2-m temperature, (b) 2-m dewpoint temperature and (c) 2-m relative humidity. The datasets used as reference to compute the ME are the observations at surface stations.

https://doi.org/10.1371/journal.pone.0292250.g010

(Fig 10B). In general, the RMSE of the simulations significantly increases from around 1000 UTC until some time between 1400 UTC and 1800 UTC, and then decreases (not shown). The Spearman correlation coefficient varies widely between simulations from 1000 UTC until 1300 UTC, and then it converges to values mostly between 0.4 and 0.6 (not shown).

ERA5 shows better skill at representing the dew point temperature than the simulations. In effect, the reanalysis has the lowest mean error (1.1˚C), the lowest RMSE (2.1˚C), and the highest Spearman correlation coefficient (0.73), indicating quite strong correlation with the observations (Table 4). The ME (Fig 10B) and the RMSE (not shown) of ERA5 decrease from around 1300 UTC until the PL has dissipated. During the last seven hours of the lifetime of the

Table 4. Aggregate statistics computed to verify the simulated and ERA5 2-m dew point temperature against the observations from surface stations.

	ME [˚C]	RMSE [˚C]	*r*
23d00h	1.2	2.9	0.58
23d06h	1.4	3	0.53
23d12h	1.7	3.1	0.55
23d18h	1.9	3.1	0.47
24d00h	2.3	3.4	0.45
24d06h	1.9	3.3	0.44
24d12h	2.2	3.1	0.53
24d18h	2	3	0.56
ERA5	1.1	2.1	0.73

https://doi.org/10.1371/journal.pone.0292250.t004

PL, the accuracy of ERA5 and the correlation coefficient are notably higher than that of the simulations (not shown).

3.3.4 Relative humidity at 2 m. The simulations that have captured the PL show somewhat better skill at representing the relative humidity than those that have not captured it (Table 5). The simulations 23d12h and 24d18h have the lowest mean error (0%), and 24d12h and 24d18h have the lowest RMSE (13%). The simulation 24d18h shows a weak correlation with the observations (0.41), and the other simulations have virtually no correlation with the observations. The time series of the ME (Fig 10C), the RMSE (not shown) and the Spearman correlation coefficient (not shown) differ between simulations, although 24d12h and 24d18h show a quite similar pattern. The ME of the simulations tends to converge with time, and the difference between them remains relatively small from around 1600 UTC on. The time series of the Spearman correlation coefficient shows correlation coefficients ranging from -1 to 1, and even the same simulation shows a wide range of correlation coefficients.

Compared to the simulations, ERA5 has higher accuracy (RMSE of 11%) and notably higher correlation with the observations (*r* of 0.62) (Table 5). However, its ME (1%) is only lower than that of half of the simulations. ERA5 has lower RMSE and higher correlation coefficient than the simulations from 1400 UTC until the PL has dissipated (not shown).

3.3.5 Wind at 10 m. The simulations that have not captured the PL show few values of wind speed over 15 m s^{-1}, whereas 24d12h and 24d18h show several values larger than 15 m s^{-1} (not shown). In general, all simulations show some large overestimations and underestimations of wind speed, but the observed wind speeds over 20 m s^{-1} are better captured by 24d12h and 24d18h. Most of the wind directions of the simulations that did not capture the PL are

Table 5. Aggregate statistics computed to verify the simulated and ERA5 2-m relative humidity against the observations from surface stations.

	ME [%]	RMSE [%]	*r*
23d00h	1	16	0.2
23d06h	3	17	0.23
23d12h	0	14	0.27
23d18h	2	16	0.16
24d00h	5	19	0.03
24d06h	3	17	0.12
24d12h	1	13	0.31
24d18h	0	13	0.41
ERA5	1	11	0.62

https://doi.org/10.1371/journal.pone.0292250.t005

Table 6. Aggregate RMSE-WVD computed to verify the simulated and ERA5 10-m wind against the observations from surface stations.

	RMSE-WVD [m s^{-1}]
23d00h	7.1
23d06h	7.8
23d12h	6.2
23d18h	6.3
24d00h	6.6
24d06h	6.8
24d12h	5.9
24d18h	4.9
ERA5	3.7

https://doi.org/10.1371/journal.pone.0292250.t006

located in the west-north-west/north-west/north-north-west (WNW/NW/NNW) quadrants of the wind rose (not shown), which correspond to the direction of the wind responsible for the MCAO. The main direction of the wind in 24d12h and 24d18h is NW, but these simulations also show winds coming from a wide range of directions, like the observed winds. However, the number of observations of the wind direction in the NW quadrant is much less compared to the simulations and ERA5, which is likely due to the fact that many wind observations are not represented in the wind rose because the recorded wind speed is zero. The simulation with the lowest RMSE-VWD is 24d18h (4.9 m s^{-1}), followed by 24d12h (5.9 m s^{-1}) and 23d12h (6.2 m s^{-1}) (Table 6). Overall, the RMSE-VWD of 24d12h and 24d18h increases from 1100 UTC to 1700 UTC, as the PL deepens (Fig 11A). The RMSE-VWD of 24d18h and 24d12h is lower than that of the other simulations during, respectively, almost all of the time and half of the time.

The wind rose of ERA5 is quite similar to that of 24d12h and 24d18h, the main difference being that ERA5 represents more frequent winds from the north-north-east (NNE) (not shown). ERA5 has the lowest RMSE-VWD (3.7 m s^{-1}), even when compared with the simulations that have captured the PL (Table 6). The time series of the RMSE-VWD of ERA5 is similar to that of 24d12h and 24d18h, with the difference that the RMSE-VWD of ERA5 is lower throughout the whole period (Fig 11A). At the end of the lifetime of the PL, the RMSE-VWD of all the simulations and ERA5 tends to converge to around 5 m s^{-1}.

Given that the simulation and ERA5 capture the observed SLP quite well, it is surprising that the skill of both at capturing the near-surface wind is not as good. This is likely due not only to model error, but also to representativeness error and observational error. In complex terrain, wind observations from weather stations may not be representative of the average wind over a larger area. In addition, measurements by anemometers are affected by topography, surface cover and surrounding obstacles [49]. The differences between the observed and simulated winds may be also due to the different period used to obtain the average wind in the different datasets.

3.3.6 Maximum wind gusts at 10 m. The ME of 24d12h and 24d18h is 1 m s^{-1}, and that of 23d12h is 0.1 m s^{-1}, whereas the ME of the simulations that have not captured the PL is negative or equal to zero (Table 7). The simulation 24d18h shows the lowest RMSE (4 m s^{-1}), followed by 24d12h (4.9 m s^{-1}). The other simulations have lower accuracy, with their RMSE ranging from 5.1 to 7.5 m s^{-1}. The simulations 24d12h and 24d18h have a quite strong correlation and strong correlation, respectively, with the observations, whereas all the others except for 24d00h have modest or virtually no correlation with the observations. The ME of the simulations that have captured the PL remains positive most of the time, whereas the ME of most of

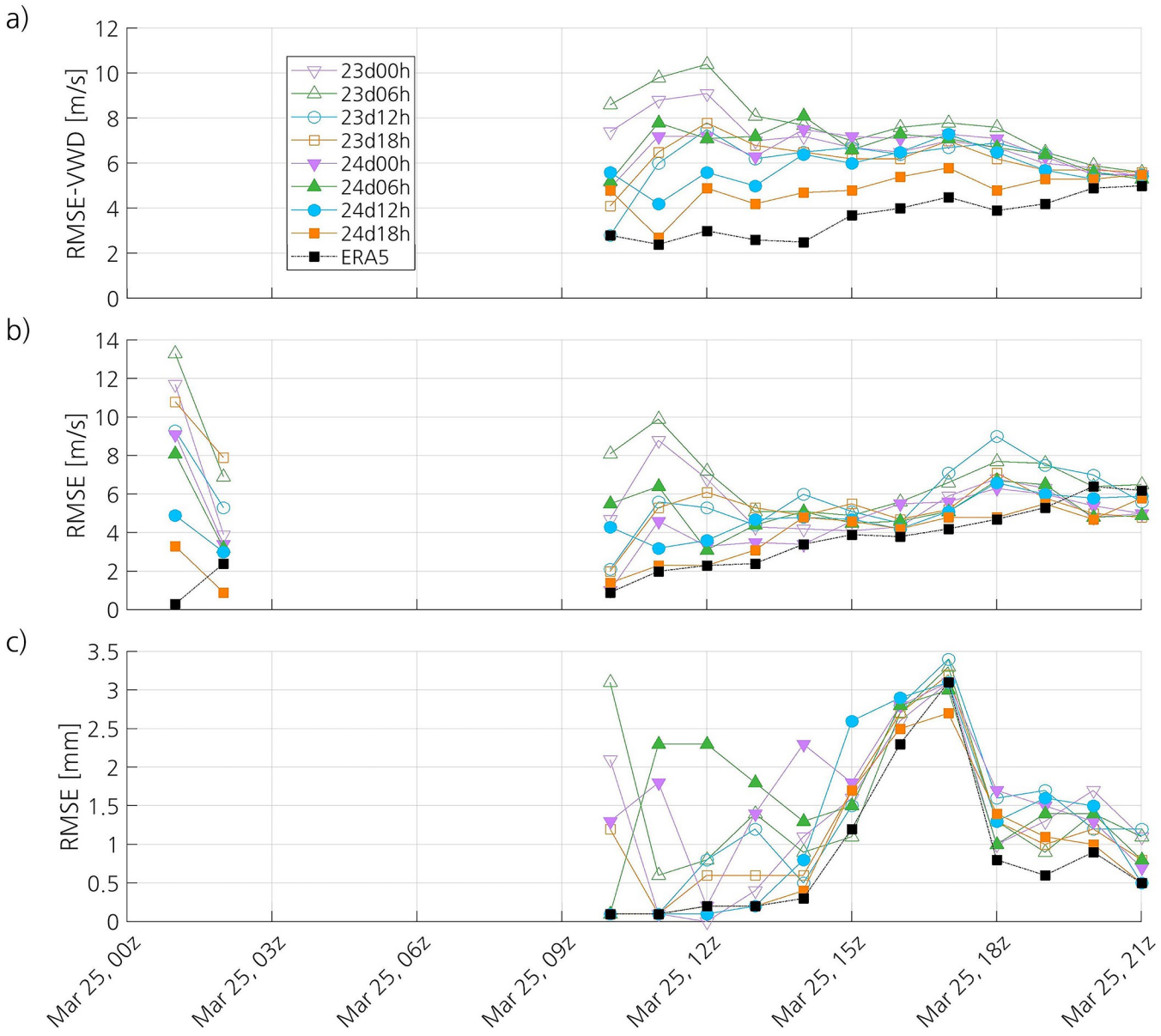

Fig 11. Time series of the (a) RMSE-VWD of the simulated and ERA5 10-m wind, and RMSE of the simulated and ERA5 (b) wind gusts and (c) 1-h accumulated precipitation. The datasets used as reference to compute the RMSE-WVD and RMSE are the observations at surface stations.

https://doi.org/10.1371/journal.pone.0292250.g011

the other simulations is negative from 1600 UTC on (not shown). Overall, the RMSE of 24d12h and 24d18h increases from 1100 UTC on, and the latter has smaller RMSE than the rest of the simulations most of the time (Fig 11B). The time series of the Spearman correlation coefficient varies widely between simulations, with correlation coefficients ranging from -0.19 to 0.85, and even the same simulation shows a wide range of correlation coefficients (not shown).

The aggregate ME of ERA5 (1.9 m s^{-1}) is almost twice as that of the simulations that have captured the PL, but its RMSE (3.9 m s^{-1}) is lower and its correlation coefficient is higher (0.81) (Table 7). However, the difference in the RMSE and the correlation coefficient between ERA5 and 24d18h is very small. Like the simulations that have captured the PL, the ME of

Table 7. Aggregate statistics computed to verify the simulated and ERA5 wind gusts against the observations from surface stations.

	ME [m s^{-1}]	RMSE [m s^{-1}]	*r*
23d00h	-0.8	6.2	0.51
23d06h	-1	7.5	0.37
23d12h	0.1	6.3	0.38
23d18h	-1.2	6.1	0.53
24d00h	-0.1	5.1	0.65
24d06h	0	5.4	0.52
24d12h	1	4.9	0.74
24d18h	1	4	0.8
ERA5	1.9	3.9	0.81

https://doi.org/10.1371/journal.pone.0292250.t007

ERA5 remains positive most of the time (not shown). The time series of the RMSE of ERA5 follows closely that of 24d18h (Fig 11B). The correlation coefficient of ERA5 shows less variability than that of the simulations, remaining between 0.58 and 0.84 (not shown).

3.3.7 1-h accumulated precipitation. The aggregate statistics indicate that 24d18h has the most skill at representing precipitation (Table 8). The ME of the simulations is positive, with 23d12h and 24d18h having the lowest mean bias (0.1 mm). The latter also has the lowest RMSE (1.3 mm) and the highest correlation coefficient (0.53), indicating modest correlation with the observations. The other simulations have virtually no correlation with the observations, except for 24d12h, which shows weak correlation with them. During most of the time, the ME of all the simulations ranges from -1 to 1 mm (not shown). The highest values of RMSE are found at 16:00 and 17:00 UTC, just after the observed SLP minimum is attained (Fig 11C). There is a large spread of the correlation coefficients of the simulations (not shown).

In contrast with the simulations, ERA5 has a negative ME (-0.1 mm) (Table 8). The RMSE of ERA5 (1.2 mm) is lower than that of all the simulations, although it is only slightly lower than that of 24d18h. ERA5 shows modest correlation with the observations (0.62). Most of the time, ERA5 shows a somewhat smaller RMSE compared to the simulations (Fig 11C), and its correlation coefficients are higher than those of most of the simulations (not shown). The ERA5 1-h accumulated precipitation never exceeds 2.5 mm, which is likely due to its relatively low resolution. In contrast, the maximum simulated precipitation is 9.5 mm, corresponding to 24d12h, and the maximum observed precipitation is 20.6 mm. This agrees with the finding of Hu and Franzke [50] that ERA5 underestimates the daily precipitation extremes observed by weather stations in Germany.

Table 8. Aggregate statistics computed to verify the simulated and ERA5 1-h accumulated precipitation against the observations from surface stations.

	ME [mm]	RMSE [mm]	*r*
23d00h	0.2	1.6	0.22
23d06h	0.3	1.8	0.22
23d12h	0.1	1.6	0.35
23d18h	0.2	1.5	0.34
24d00h	0.5	1.8	0.19
24d06h	0.5	1.8	0.23
24d12h	0.2	1.6	0.42
24d18h	0.1	1.3	0.53
ERA5	-0.1	1.2	0.62

https://doi.org/10.1371/journal.pone.0292250.t008

3.4 Final discussion

To understand why only 24d12h and 24d18h correctly capture the development of the PL, it is necessary to analyse the simulated atmospheric fields from a few hours before its formation until its genesis time. It is assumed that, during this period, the synoptic conditions are favourable for PL formation in 24d12h and 24d18h, but not in the other simulations.

Fig 12 shows the SLP, the geopotential height at 500 hPa and the 1000-500 hPa thickness on 25 March at 0000 UTC. There is a 500-hPa through with a northeast-southwest orientation in all simulations. Although its shape is slightly different in the simulations, the through is in the

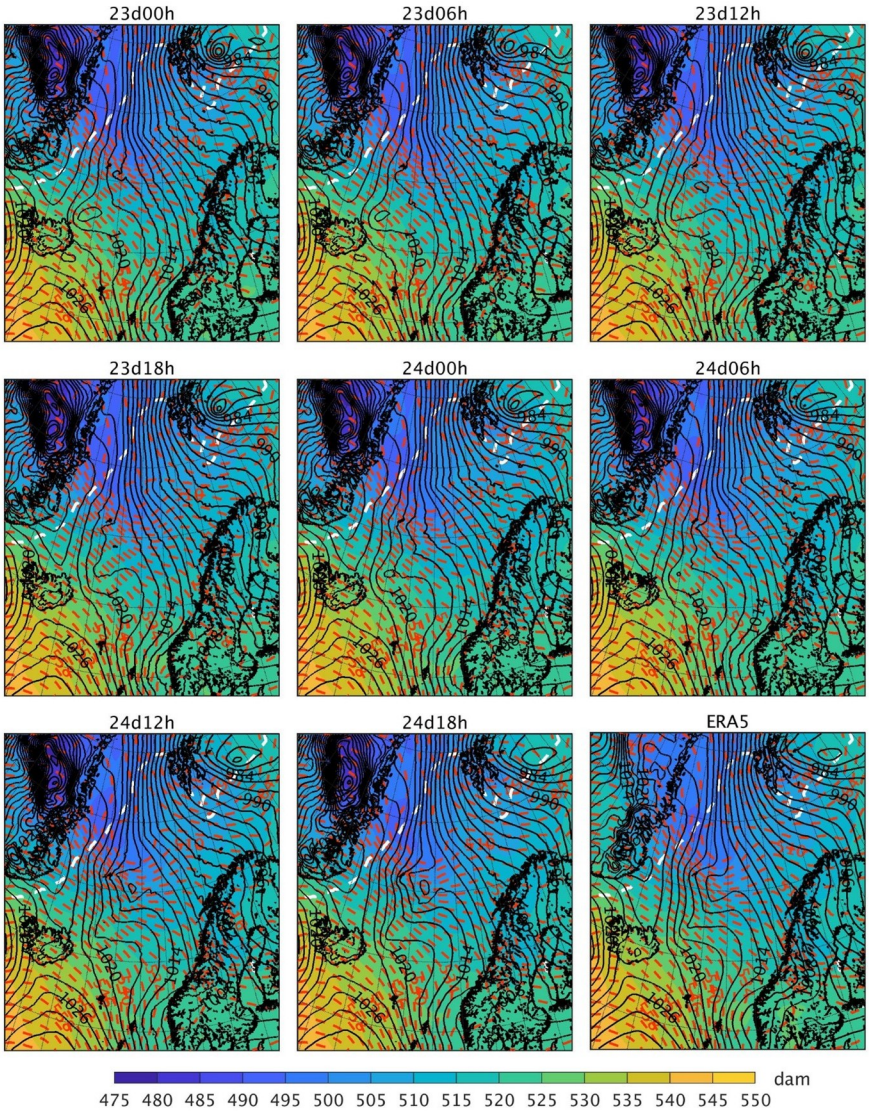

Fig 12. Simulated and ERA5 fields showing the PL on 25 March 2019 at 0000 UTC. The colourmap represents the 1000-500 hPa thickness (dam), the black isobars represent the SLP (hPa, contours every 2 hPa) and the red dashed lines represent the geopotential height at 500 hPa (dam, contours every 2 dam). The black outlining represents the coastline, and the white dashed line represents the sea ice edge, which is defined as the 0.15 contour of the sea ice concentration. ERA5 fields have been interpolated to the grid of the simulation using bicubic interpolation for the SLP, 1000-500 hPa thickness, and geopotential height, and bilinear interpolation for the sea ice concentration. The sea ice edge in ERA5 corresponds to the 25 March 2019 at 1200 UTC. The dataset used to plot the geographic contours has been obtained from the GSHHG [33] under a CC BY license, with permission from Dr. Paul Wessel.

https://doi.org/10.1371/journal.pone.0292250.g012

same region and shows the same depth. The incipient PL in 24d12h and 24d18h with a well defined SLP minimum is located on the right side of this mid-tropospheric through, whereas in the other simulations only a weak (low-level) through within the SLP field in this area is observed. The 1000-500 hPa thickness field shows that the cold air tongue associated with the MCAO has a northwest-southeast orientation in all simulations.

Since the atmospheric conditions aloft are similar in all simulations during the genesis time of the PL, they cannot explain why it has only been correctly captured by 24d12h and 24d18h (with respect to both observations and reanalysis data). Therefore, the difference between the simulations must be in the lower atmosphere. Fig 13 shows the geopotential height, temperature and horizontal wind at 900 hPa on 24 March at 1900 UTC in the region where the low-level through preceding the genesis of the PL started to form (i.e. 5 hours before the PL shown in Fig 12). All simulations show a strong northwest-southeast temperature gradient to the west of Jan Mayen, close to the sea ice edge. In contrast with the other simulations, the northerly cold air advection and winds in 24d12h and 24d18h are more intense and more widely extended; therefore, the cold airmass moves further south in these two simulations. At the same time, on the east side of this cold air, a warm front pushes northward in these two simulations, with a more widely defined and stronger warm air advection in this area than the other simulations. These results indicate that, in the presence of a baroclinic environment, only the low-level atmospheric conditions with a well defined cold/warm air temperature advection present in 24d12h and 24d18h lead to baroclinic instability, which is involved in the genesis of the PL. It is also clear in Fig 13 that the low-level pressure deepens or vorticity (wind rotation) starts to develop in these two simulations, i.e. small scale features corresponding to the PL development phase.

Since 24d12h and 24d18h are the latest initialised simulations, their atmospheric fields during the hours preceding the PL formation are more similar to those of ERA5, the driving data, compared to those of the other simulations. Thus, the fact that the other simulations except for 23d12h do not represent the PL is due to forecast error growth and missing small-scale features during the initial stage of the PL formation. Nevertheless, the question remains about why 23d12h represents a PL at a later moment in time. In 23d12h, a strong low-level baroclinic zone forms a few hours before the PL forms in this simulation (Fig 14), and the PL shows baroclinic development. This PL makes landfall shortly after being formed, thus dissipating before it can reach a larger size. Fig 14 reveals also clearly that stronger winds over both cold (west) and warm (east) near the developed PL induce small scale conditions (i.e., temperature advections) favourable to strengthen low-level baroclinity and cyclogenesis in the latest initialised simulations, not present in the other simulations.

In conclusion, on the 24–25 March, the simulated environmental conditions are favourable for PL development, with a low-level baroclinic environment and an upper-level through, but the different evolution of the low-level circulation and small-scale features explains why a few simulations capture the PL whereas the others do not.

4. Conclusion

Compared to low-resolution models, convection-permitting models provide a better representation of physical processes [20]. Therefore, they are a powerful tool to study mesoscale phenomena, including PLs. This study has focused on a PL that made landfall in Norway in 2019, and the aim was to analyse the impact of the initial conditions on the simulation of the PL, and to analyse the skill of the CRCM6/GEM4 at reproducing it. The main limitations of this study is that the available conventional observations mostly cover the mature and dissipation stages of the PL, and that they are irregularly distributed in space.

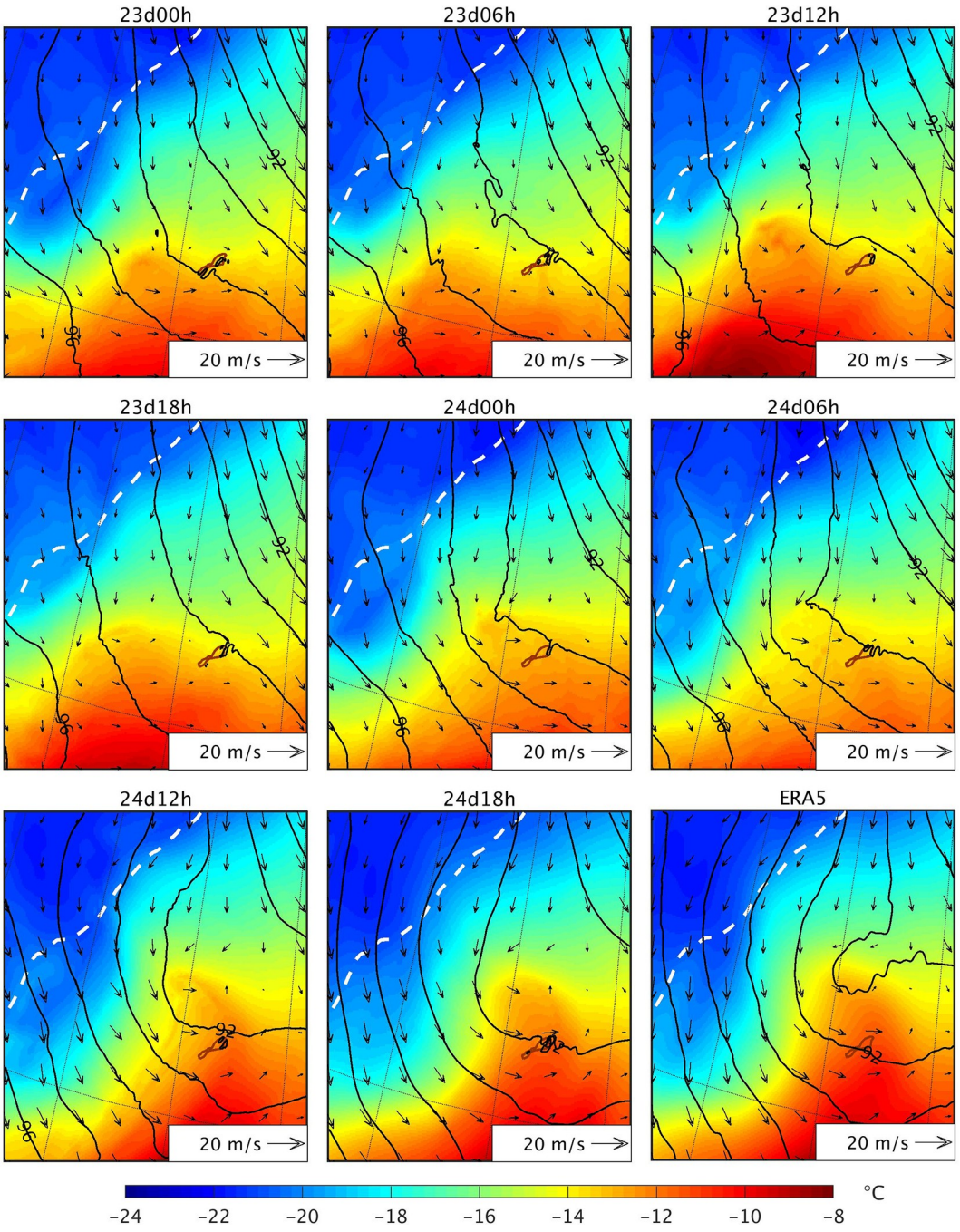

Fig 13. Simulated and ERA5 fields on 24 March 2019 at 1900 UTC over the region around Jan Mayen. The colourmap represents the temperature at 900 hPa (˚C), the black isolines represent the geopotential height at 900 hPa (dam, contours every 1 dam), and the arrows represent the horizontal wind at 900 hPa. The white dashed line represents the sea ice edge, which is defined as the 0.15 contour of the sea ice concentration. ERA5 fields have been interpolated to the grid of the simulation using bicubic interpolation for the temperature and geopotential height, and bilinear interpolation for the horizontal wind and sea ice concentration. The sea ice edge in ERA5 corresponds to the 24 March 2019 at 1200 UTC. The dataset used to plot the geographic contours has been obtained from the GSHHG [33] under a CC BY license, with permission from Dr. Paul Wessel.

https://doi.org/10.1371/journal.pone.0292250.g013

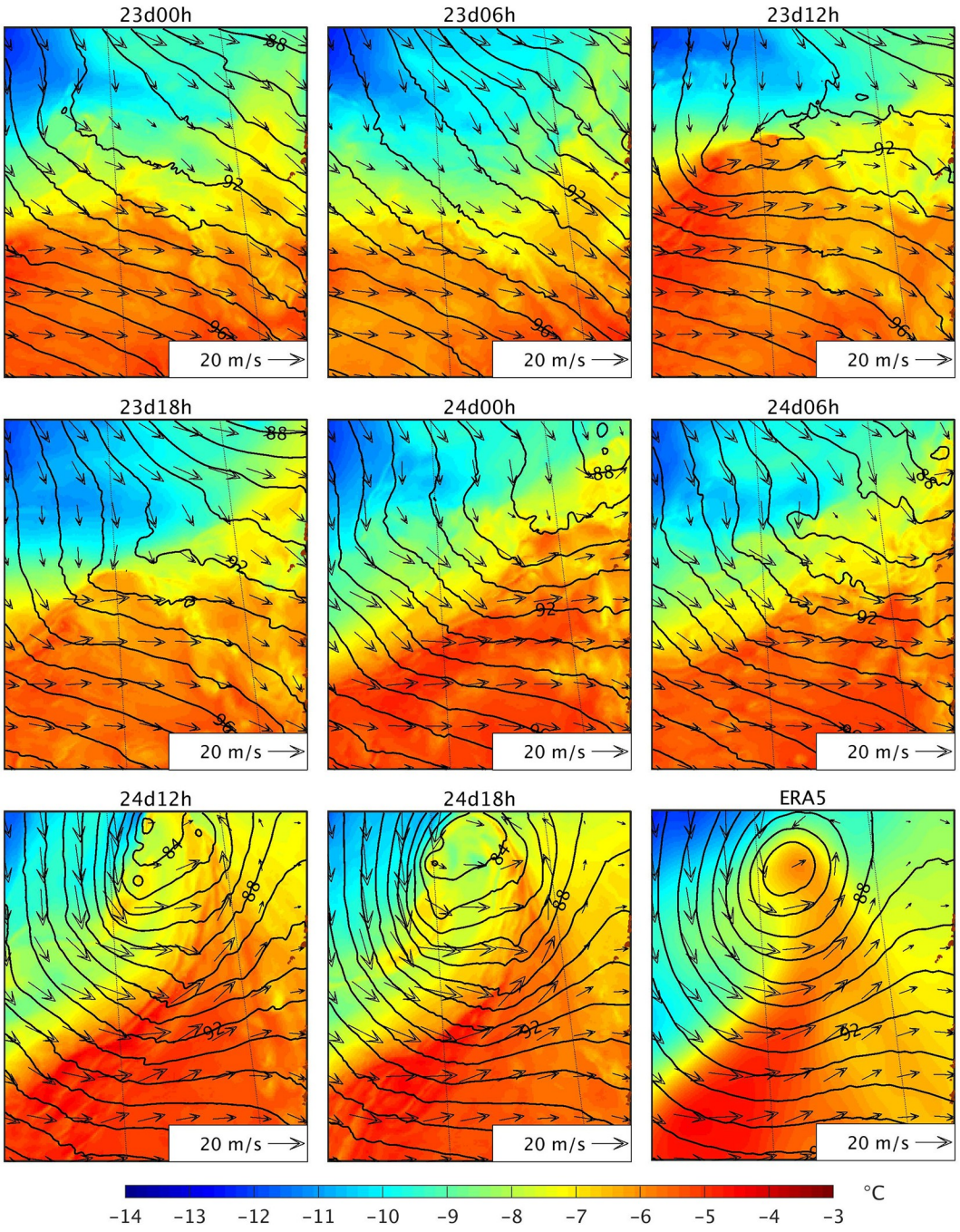

Fig 14. Same as Fig 13, but for 25 March 2019 at 0900 UTC and over the region to the west of the Norwegian coast.

https://doi.org/10.1371/journal.pone.0292250.g014

One of the main findings of this study is that the ability of the CRCM6/GEM4 to capture the PL strongly depends on the initial conditions. In effect, only 23d12h and the latest initialised simulations 24d12h and 24d18h capture the development of the PL. The latter two represent well the lifetime, track and size of the observed PL. In contrast, the PL represented in 23d12h is much smaller than the observed PL, and its lifetime is less than half the lifetime of the observed PL. Further, the verification of the simulations against conventional observations

Table 9. Added value of the CRCM6/GEM4 (simulation 24d18h) compared to ERA5 for the following variables: Sea level pressure (SLP), 2-m temperature (T_{2m}), 2-m dew point temperature ($T_{d,2m}$), 10-m wind (V_{10m}), wind gusts (WG) and 1-h accumulated precipitation (PR). The added value has been computed using the aggregate RMSE (RMSE-WVD for the 10-m wind), based on values presented in Tables 2–8. The added value computation is based on the study of Di Luca et al. [52; Equation 1)].

SLP	T_{2m}	$T_{d,2m}$	RH	V_{10m}	WG	PR
-0.8 hPa	-0.9˚C	-0.9˚C	-2%	-1.2 m s^{-1}	-0.1 m s^{-1}	-0.3 mm

https://doi.org/10.1371/journal.pone.0292250.t009

has shown that 24d18h has more skill than 24d12h at reproducing most of the near-surface variables analysed. These results indicate that the initialisation time has an important impact on whether the model captures or not this PL, and on how well it is represented. The two latest initialized simulations show northerly cold air advection and winds that are more intense than in the other simulations, leading to baroclinic instability and, subsequently, to the genesis of the PL. Nevertheless, since the environmental conditions– strong low-level temperature gradient and an upper-level through –on the 24 and 25 March are favourable for PL development, a PL can form at a later time if the low-level conditions are favourable for baroclinic instability to grow, which is what happens in 23d12h. In view of these results, it is suggested that future studies should investigate the potential to improve PL forecasts by using spectral nudging to maintain the low-level atmospheric fields and small scale features close to the driving data. Sensitivity tests should be conducted with different spectral nudging parameters and nudging horizontal wind, temperature, or both.

Another key finding is that the processes involved in the development of the PL need to be improved in the model in order to decrease the mean bias of the simulations that have captured it. Although all the statistics clearly show the better performance of 24d12h and 24d18h at reproducing SLP compared to the other simulations, it is notable that, for the other variables, these two simulations show similar or higher aggregate absolute mean bias. In particular, the parameterization of the surface heat fluxes in the CRCM6/GEM4 needs to be improved. In effect, the fact that 24d12h and 24d18h represent a PL deeper than the observed one, and show higher temperature mean bias compared to the other simulations and ERA5, seems to indicate that the ocean surface fluxes may be too strong.

Finally, the results have shown that ERA5 has more skill than the simulations, including those that have captured the PL, at reproducing the observed PL during its mature and dissipation stages. Table 9 shows the added value of the CRCM6/GEM4 compared to ERA5 when considering the best simulation (24d18h). For all the near-surface variables analysed here, the model does not provide added value in terms of accuracy (based on the RMSE values shown in Tables 2–8). It is surprising that the CRMC6/GEM4, a high-resolution model, does not provide added value compared to ERA5, the coarser reanalysis that drives it. There are two main reasons that could explain the fact that ERA5 has better skill than CRMC6/GEM4. First, conventional observations are assimilated into ERA5. Second, the verification of high-resolution simulations using standard statistics has some limitations. For instance, when verifying the simulation of a PL using dropsonde observations, Stoll et al. [17] found that a fuzzy verification method showed that the regional model AROME-Arctic had higher skill at capturing extreme values at small scales than the global model ECMWF HRES, whereas standard verification statistics were similar for both models. Finally, note that for this work we used GEM4, but a new version with improved physics parameterizations, GEM5, was recently released [51]. Therefore, an interesting course of research would be to analyse if this new version of GEM provides added value compared to ERA5 and to the current CRCM6/GEM4 simulations.

Acknowledgments

Computations were made on the supercomputer Beluga, managed by Calcul Québec and the Digital Research Alliance of Canada. The authors are deeply indebted to Katja Winger for her essential support in the use of the CRCM6/GEM4, as well as for downloading and preparing available ERA5 reanalyses. The authors would also like to thank François Roberge for his valuable help in the use of the *r.diag* toolkit and the CRCM6/GEM4.

Author Contributions

Conceptualization: Marta Moreno-Ibáñez, René Laprise.

Formal analysis: Marta Moreno-Ibáñez, René Laprise, Philippe Gachon.

Funding acquisition: René Laprise.

Investigation: Marta Moreno-Ibáñez.

Methodology: Marta Moreno-Ibáñez, René Laprise.

Project administration: René Laprise.

Resources: René Laprise.

Software: Marta Moreno-Ibáñez.

Supervision: René Laprise, Philippe Gachon.

Validation: René Laprise, Philippe Gachon.

Visualization: Marta Moreno-Ibáñez.

Writing – original draft: Marta Moreno-Ibáñez.

Writing – review & editing: Marta Moreno-Ibáñez, René Laprise, Philippe Gachon.

References

1. Walsh JE, Ballinger TJ, Euskirchen ES, Hanna E, Mård J, Overland JE, et al. Extreme weather and climate events in northern areas: A review. Earth-Science Reviews. 2020; 209: 103324. https://doi.org/10.1016/j.earscirev.2020.103324
2. Turner J, Rasmussen EA, Carleton AM. Introduction. In: Rasmussen EA, Turner J, editors. Polar Lows: Mesoscale Weather Systems in the Polar Regions. Cambridge: Cambridge University Press; 2003. p. 1–51.
3. Renfrew IA. Polar Lows. In: Holton JR, Curry JA, Pyle JA, editors. Encyclopedia of atmospheric sciences. Amsterdam: Academic Press; 2003. p. 1761–8.
4. Cavaleri L, Barbariol F, Benetazzo A, Bertotti L, Bidlot J-R, Janssen P, et al. The Draupner wave: A fresh look and the emerging view. J Geophys Res Oceans. 2016; 121(8): 6061–75. https://doi.org/10.1002/2016JC011649
5. Yanase W, Niino H, Watanabe SII, Hodges K, Zahn M, Spengler T, et al. Climatology of polar lows over the sea of Japan using the JRA-55 reanalysis. J Clim. 2016; 29(2): 419–37. https://doi.org/10.1175/jcli-d-15-0291.1
6. Casati B, Haiden T, Brown B, Nurmi P, Lemieux J-F. Verification of Environmental Prediction in Polar Regions: Recommendations for the Year of Polar Prediction. Geneva, Switzerland: World Meteorological Organization, 2017 WWRP 2017–1.
7. Jung T, Gordon ND, Bauer P, Bromwich DH, Chevallier M, Day JJ, et al. Advancing Polar Prediction Capabilities on Daily to Seasonal Time Scales. Bull Am Meteorol Soc. 2016; 97(9): 1631–47. https://doi.org/10.1175/BAMS-D-14-00246.1
8. Moreno-Ibáñez M, Laprise R, Gachon P. Recent advances in polar low research: current knowledge, challenges and future perspectives. Tellus A. 2021; 73(1): 1–31. https://doi.org/10.1080/16000870.2021.1890412

9. Dee DP, Uppala SM, Simmons AJ, Berrisford P, Poli P, Kobayashi S, et al. The ERA-Interim reanalysis: configuration and performance of the data assimilation system. Q J Roy Meteorol Soc. 2011; 137(656): 553–97. https://doi.org/10.1002/qj.828

10. Laffineur T, Claud C, Chaboureau J-P, Noer G. Polar Lows over the Nordic Seas: Improved Representation in ERA-Interim Compared to ERA-40 and the Impact on Downscaled Simulations. Mon Weather Rev. 2014; 142(6): 2271–89. https://doi.org/10.1175/mwr-d-13-00171.1

11. Zappa G, Shaffrey L, Hodges K. Can polar lows be objectively identified and tracked in the ECMWF operational analysis and the ERA-Interim reanalysis? Mon Weather Rev. 2014; 142(8): 2596–608. https://doi.org/10.1175/MWR-D-14-00064.1

12. Hersbach H, Bell B, Berrisford P, Hirahara S, Horányi A, Muñoz-Sabater J, et al. The ERA5 global reanalysis. Q J Roy Meteorol Soc. 2020; 146(730): 1999–2049. https://doi.org/10.1002/qj.3803

13. Stoll PJ, Spengler T, Terpstra A, Graversen RG. Polar lows–moist-baroclinic cyclones developing in four different vertical wind shear environments. Weather and Climate Dynamics. 2021; 2(1): 19–36. https://doi.org/10.5194/wcd-2-19-2021

14. Bromwich DH, Wilson AB, Bai L, Liu Z, Barlage M, Shih C-F, et al. The Arctic System Reanalysis, Version 2. Bull Am Meteorol Soc. 2018; 99(4): 805–28. https://doi.org/10.1175/BAMS-D-16-0215.1

15. Smirnova J, Golubkin P. Comparing Polar Lows in Atmospheric Reanalyses: Arctic System Reanalysis versus ERA-Interim. Mon Weather Rev. 2017; 145(6): 2375–83. https://doi.org/10.1175/mwr-d-16-0333.1

16. Prein AF, Langhans W, Fosser G, Ferrone A, Ban N, Goergen K, et al. A review on regional convection-permitting climate modeling: Demonstrations, prospects, and challenges. Rev Geophys. 2015; 53(2): 323–61. https://doi.org/10.1002/2014RG000475 PMID: 27478878

17. Stoll PJ, Valkonen TM, Graversen RG, Noer G. A well-observed polar low analysed with a regional and a global weather-prediction model. Q J Roy Meteorol Soc. 2020; 146(729): 1740–67. https://doi.org/10.1002/qj.3764

18. Bechtold P, Köhler M, Jung T, Leutbecher M, Rodwell M, Vitart F. Advances in simulating atmospheric variability with IFS cycle 32r3. Newsletter No 114 –Winter 2007/08. 2008:29–38.

19. Müller M, Batrak Y, Kristiansen J, Køltzow MAØ, Noer G, Korosov A. Characteristics of a Convective-Scale Weather Forecasting System for the European Arctic. Mon Weather Rev. 2017; 145(12): 4771–87. https://doi.org/10.1175/MWR-D-17-0194.1

20. Prein AF, Rasmussen R, Stephens G. Challenges and advances in convection-permitting climate modeling. Bull Am Meteorol Soc. 2017; 98(5): 1027–30. https://doi.org/10.1175/BAMS-D-16-0263.1

21. Bourassa MA, Gille ST, Bitz C, Carlson D, Cerovecki I, Clayson CA, et al. High-Latitude Ocean and Sea Ice Surface Fluxes: Challenges for Climate Research. Bull Am Meteorol Soc. 2013; 94(3): 403–23. https://doi.org/10.1175/BAMS-D11-00244.1

22. Zhang F, Sun YQ, Magnusson L, Buizza R, Lin S-J, Chen J-H, et al. What Is the Predictability Limit of Midlatitude Weather? J Atmos Sci. 2019; 76(4): 1077–91. https://doi.org/10.1175/jas-d-18-0269.1

23. Spengler T, Renfrew IA, Terpstra A, Tjernström M, Screen J, Brooks IM, et al. High-Latitude Dynamics of Atmosphere–Ice–Ocean Interactions. Bull Am Meteorol Soc. 2016; 97(9): ES179–ES82. https://doi.org/10.1175/BAMS-D-15-00302.1

24. McInnes H, Kristiansen J, Kristjánsson JE, Schyberg H. The role of horizontal resolution for polar low simulations. Q J Roy Meteorol Soc. 2011; 137(660): 1674–87. https://doi.org/10.1002/qj.849

25. Wagner JS, Gohm A, Dörnbrack A, Schäfler A. The mesoscale structure of a polar low: airborne lidar measurements and simulations. Q J Roy Meteorol Soc. 2011; 137(659): 1516–31. https://doi.org/10.1002/qj.857

26. Côté J, Gravel S, Méthot A, Patoine A, Roch M, Staniforth A. The Operational CMC–MRB Global Environmental Multiscale (GEM) Model. Part I: Design Considerations and Formulation. Mon Weather Rev. 1998; 126(6): 1373–95. https://doi.org/10.1175/1520-0493(1998)126<1373:Tocmge>2.0.Co;2

27. Bélair S, Mailhot J, Girard C, Vaillancourt P. Boundary Layer and Shallow Cumulus Clouds in a Medium-Range Forecast of a Large-Scale Weather System. Mon Weather Rev. 2005; 133(7): 1938–60. https://doi.org/10.1175/mwr2958.1

28. Bélair S, Roch M, Leduc A-M, Vaillancourt PA, Laroche S, Mailhot J. Medium-Range Quantitative Precipitation Forecasts from Canada's New 33-km Deterministic Global Operational System. Weather Forecast. 2009; 24(3): 690–708. https://doi.org/10.1175/2008waf2222175.1

29. Girard C, Plante A, Desgagné M, McTaggart-Cowan R, Côté J, Charron M, et al. Staggered Vertical Discretization of the Canadian Environmental Multiscale (GEM) Model Using a Coordinate of the Log-Hydrostatic-Pressure Type. Mon Weather Rev. 2014; 142(3): 1183–96. https://doi.org/10.1175/mwr-d-13-00255.1

30. Zadra A, Caya D, Côté J, Dugas B, Jones C, Laprise R, et al. The next Canadian Regional Climate Model. La Physique au Canada. 2008:75–83.

31. Laprise R. The Euler Equations of Motion with Hydrostatic Pressure as an Independent Variable. Mon Weather Rev. 1992; 120(1): 197–207. https://doi.org/10.1175/1520-0493(1992)120<0197:Teeomw>2.0.Co;2

32. Davies HC. A lateral boundary formulation for multi-level prediction models. Q J Roy Meteorol Soc. 1976; 102(432): 405–18. https://doi.org/10.1002/qj.49710243210

33. Wessel P, Smith WHF. A global, self-consistent, hierarchical, high-resolution shoreline database. Journal of Geophysical Research: Solid Earth. 1996; 101(B4): 8741–3. https://doi.org/10.1029/96JB00104

34. Li J, Barker HW. A Radiation Algorithm with Correlated-k Distribution. Part I: Local Thermal Equilibrium. J Atmos Sci. 2005; 62(2): 286–309. https://doi.org/10.1175/jas-3396.1

35. Mailhot J, Bélair S. An examination of a unified cloudiness-turbulence scheme with various types of cloudy boundary layers. 14th Symposium on Boundary Layer and Turbulence; Wageningen, The Netherlands: Amer. Meteor. Soc.; 2000.

36. Milbrandt JA, Morrison H. Parameterization of Cloud Microphysics Based on the Prediction of Bulk Ice Particle Properties. Part III: Introduction of Multiple Free Categories. J Atmos Sci. 2016; 73(3): 975–95. https://doi.org/10.1175/jas-d-15-0204.1

37. Noilhan J, Mahfouf JF. The ISBA land surface parameterisation scheme. Global Planet Change. 1996; 13(1): 145–59. https://doi.org/10.1016/0921-8181(95)00043-7

38. Brasseur O. and Application of a Physical Approach to Estimating Wind Gusts. Mon Weather Rev. 2001; 129(1): 5–25. https://doi.org/10.1175/1520-0493(2001)129<0005:Daaoap>2.0.Co;2.

39. Centurioni L, Horányi A, Cardinali C, Charpentier E, Lumpkin R. A Global Ocean Observing System for Measuring Sea Level Atmospheric Pressure: Effects and Impacts on Numerical Weather Prediction. Bull Am Meteorol Soc. 2017; 98(2): 231–8. https://doi.org/10.1175/BAMS-D-15-00080.1

40. Bell B, Hersbach H, Simmons A, Berrisford P, Dahlgren P, Horányi A, et al. The ERA5 global reanalysis: Preliminary extension to 1950. Q J Roy Meteorol Soc. 2021; 147(741): 4186–227. https://doi.org/10.1002/qj.4174

41. Graham RM, Hudson SR, Maturilli M. Improved Performance of ERA5 in Arctic Gateway Relative to Four Global Atmospheric Reanalyses. Geophys Res Lett. 2019; 46(11): 6138–47. https://doi.org/10.1029/2019GL082781

42. Mayer M, Tietsche S, Haimberger L, Tsubouchi T, Mayer J, Zuo H. An Improved Estimate of the Coupled Arctic Energy Budget. J Clim. 2019; 32(22): 7915–34. https://doi.org/10.1175/jcli-d-19-0233.1

43. Batrak Y, Müller M. On the warm bias in atmospheric reanalyses induced by the missing snow over Arctic sea-ice. Nature Communications. 2019; 10(1): 1–8. https://doi.org/10.1038/s41467-019-11975-3 PMID: 31519872

44. Wang C, Graham RM, Wang K, Gerland S, Granskog MA. Comparison of ERA5 and ERA-Interim near-surface air temperature, snowfall and precipitation over Arctic sea ice: effects on sea ice thermodynamics and evolution. The Cryosphere. 2019; 13(6): 1661–79. https://doi.org/10.5194/tc-13-1661-2019

45. Wilks DS. Statistical Methods in the Atmospheric Sciences. 4th ed. San Diego, USA: Elsevier; 2019. 842 p.

46. Fast JD. Mesoscale Modeling and Four-Dimensional Data Assimilation in Areas of Highly Complex Terrain. Journal of Applied Meteorology and Climatology. 1995; 34(12): 2762–82. https://doi.org/10.1175/1520-0450(1995)034<2762:Mmafdd>2.0.Co;2

47. Blechschmidt A-M, Bakan S, Graßl H. Large-scale atmospheric circulation patterns during polar low events over the Nordic seas. J Geophys Res Atmos. 2009; 114: D06115. https://doi.org/10.1029/2008JD010865

48. Rojo M, Claud C, Mallet P-E, Noer G, Carleton AM, Vicomte M. Polar low tracks over the Nordic Seas: a 14-winter climatic analysis. Tellus A. 2015; 67(1): 24660. https://doi.org/10.3402/tellusa.v67.24660

49. World Meteorological Organization. Guide to Instruments and Methods of Observation. Volume I–Measurement of Meteorological Variables. 2018 ed. Geneva, Switzerland: World Meteorological Organization; 2018. 573 p.

50. Hu G, Franzke CLE. Evaluation of Daily Precipitation Extremes in Reanalysis and Gridded Observation-Based Data Sets Over Germany. Geophys Res Lett. 2020; 47(18): e2020GL089624. https://doi.org/10.1029/2020GL089624

51. McTaggart-Cowan R, Vaillancourt PA, Zadra A, Chamberland S, Charron M, Corvec S, et al. Modernization of Atmospheric Physics Parameterization in Canadian NWP. J Adv Model Earth Syst. 2019; 11(11): 3593–635. https://doi.org/10.1029/2019MS001781

52. Di Luca A, de Elía R, Laprise R. Potential for small scale added value of RCM's downscaled climate change signal. Clim Dyn. 2013; 40(3): 601–18. https://doi.org/10.1007/s00382-012-1415-z

Published work 5

Analysis of the Development Mechanisms of a Polar Low over the Norwegian Sea Simulated with the Canadian Regional Climate Model

Authors:	Marta Moreno-Ibáñez, René Laprise and Philippe Gachon
Year:	2023
Journal:	*Atmosphere* 14, 998
DOI:	10.3390/atmos14060998

Authorship statement: MMI has contributed 80% (conceptualization, formal analysis, investigation, methodology, software, visualization, writing and editing of the original draft). MMI did the conceptualization, formal analysis and methodology with input from the coauthors, who also reviewed the draft.

atmosphere

MDPI

Article

Analysis of the Development Mechanisms of a Polar Low over the Norwegian Sea Simulated with the Canadian Regional Climate Model

Marta Moreno-Ibáñez [1,2,*], René Laprise [1,2] and Philippe Gachon [1,3]

[1] Centre for the Study and Simulation of Regional-Scale Climate (ESCER), University of Quebec in Montreal (UQAM), Montreal, QC H2X 3Y7, Canada
[2] Department of Earth and Atmospheric Sciences, University of Quebec in Montreal (UQAM), Montreal, QC H2X 3Y7, Canada
[3] Department of Geography, University of Quebec in Montreal (UQAM), Montreal, QC H2X 3Y7, Canada
* Correspondence: moreno_ibanez.marta@courrier.uqam.ca

Abstract: Polar lows (PLs) are maritime mesoscale cyclones associated with severe weather. They develop during marine cold air outbreaks near coastlines and the sea ice edge. Unfortunately, our knowledge about the mechanisms leading to PL development is still incomplete. This study aims to provide a detailed analysis of the development mechanisms of a PL that formed over the Norwegian Sea on 25 March 2019 using the output of a simulation with the sixth version of the Canadian Regional Climate Model (CRCM6/GEM4), a convection-permitting model. First, the life cycle of the PL is described and the vertical wind shear environment is analysed. Then, the horizontal wind divergence and the baroclinic conversion term are computed, and a surface pressure tendency equation is developed. In addition, the roles of atmospheric static stability, latent heat release, and surface heat and moisture fluxes are explored. The results show that the PL developed in a forward-shear environment and that moist baroclinic instability played a major role in its genesis and intensification. Baroclinic instability was initially only present at low levels of the atmosphere, but later extended upward until it reached the mid-troposphere. Whereas the latent heat of condensation and the surface heat fluxes also contributed to the development of the PL, convective available potential energy and barotropic conversion do not seem to have played a major role in its intensification. In conclusion, this study shows that a convection-permitting model simulation is a powerful tool to study the details of the structure of PLs, as well as their development mechanisms.

Keywords: polar low; polar mesoscale cyclone; marine cold air outbreak; convection-permitting model; Canadian Regional Climate Model; baroclinic instability; forward shear; surface pressure tendency

Citation: Moreno-Ibáñez, M.; Laprise, R.; Gachon, P. Analysis of the Development Mechanisms of a Polar Low over the Norwegian Sea Simulated with the Canadian Regional Climate Model. *Atmosphere* **2023**, *14*, 998. https://doi.org/10.3390/atmos14060998

Academic Editors: Gareth Marshall and Anthony R. Lupo

Received: 6 March 2023
Revised: 24 May 2023
Accepted: 3 June 2023
Published: 8 June 2023

1. Introduction

The polar and subpolar regions are extreme environments, where a wide range of atmospheric phenomena with different spatiotemporal scales develop, such as katabatic winds from the Greenland ice sheet (e.g., [1]), mesoscale tip jets and barrier winds (e.g., [2]), polar mesoscale cyclones (PMCs) (e.g., [3]), and Arctic cyclones (e.g., [4]). Interactions between these phenomena can occur; for instance, katabatic winds can trigger PMCs (e.g., [5]).

A specific type of PMC known as polar lows (PLs) are of particular interest, since they are associated with severe weather, and some studies have indicated that they can have an impact on ocean circulation [6,7]. The wider family of PMCs includes cyclones that develop poleward of the main polar front and whose horizontal scale is meso-α or meso-β [8], which correspond to 200–2000 km and 20–200 km, respectively [9]. Whereas PMCs are quite common in both hemispheres, only a small number of PMCs can be considered PLs [10]. What differentiates PLs from the other PMCs is the fact that they are maritime

cyclones with a 200–1000 km horizontal scale and their associated near-surface winds are gale force or stronger [11].

PLs develop during marine cold air outbreaks (MCAOs) [12] near coastlines and the sea ice edge, where strong low-level air temperature gradients are often located during the cold season. MCAOs lead to convergence zones that are favourable for the formation of PLs (e.g., [13]). The shape of the sea ice edge and the coastline has an impact on the generation and intensification of the convergence zones associated with MCAOs, due to the resulting asymmetry in the air mass transformation [14] or due to local discontinuities in surface diabatic fluxes from land or sea ice toward open water areas (e.g., [15]). These convergence zones are more intense the smaller the bend angle (a simple representation of the sea ice edge or coastline consists of two straight lines that meet at a certain angle—the bend angle), the higher the sea surface temperature (SST) and the weaker the stability of the atmosphere. Accordingly, some studies have shown that, compared to a straight sea ice edge, an indented sea ice edge is more favourable for the genesis of PLs [15,16].

In the late 1970s and early 1980s, two alternative hypotheses or theoretical explanations for PL development were suggested [17]. While some researchers concluded that PLs were baroclinic disturbances (e.g., [18]), others argued that PLs were convective systems similar to tropical cyclones (e.g., [19]). Later, several studies indicated that both mechanisms played an important role in PL development (e.g., [20,21]), leading to the idea of a PL spectrum that encompasses not only PLs with baroclinic or a convective origin, but also PLs generated through a combination of different development mechanisms [22]. Recent studies have concluded that moist baroclinic instability plays a major role in PL development [23–25], and the existence of hurricane-like PLs has been questioned [25,26]. Numerous studies have highlighted the contribution of latent heating to PL development (e.g., [27–29]), and several studies have found that surface heat fluxes are important for the maintenance and intensification of PLs (e.g., [29,30]). Upper-level geopotential height anomalies can also contribute to PL development (e.g., [15]). Although all these studies have highlighted the role of different mechanisms in PL genesis and intensification, the relative importance of each one is yet to be determined (for a detailed review of the development mechanisms of PLs see [10]).

The environments where PLs develop can be classified as weak-shear or strong-shear [25]. Most PLs develop in a strong-shear environment, where baroclinic instability plays an important role, and they decay in a weak-shear environment [25]. Strong-shear environments have been traditionally classified into two categories: forward-shear and reverse-shear (e.g., [31]). Recently, Stoll et al. [25] suggested two additional categories, right-shear and left-shear. PLs that develop in right-shear (left-shear) conditions propagate towards colder (warmer) regions. Forward-shear PLs are the most frequent type of PL [32]. The development of forward-shear PLs is similar to the baroclinic development of midlatitude storms, whereas the development of reverse-shear PLs is similar to the secondary development associated with frontal instability [31].

Our knowledge about how polar lows form and intensify is still incomplete because, among other reasons, until relatively recently atmospheric models were too coarse to represent the structure of PLs. In effect, improved predictions of PLs need higher resolution simulations [28]; ideally, a grid mesh of less than 3 km should be used [33]. In the last decade, convection-permitting models have proven to be a useful tool to study PLs (e.g., [26,34]). Nevertheless, the simulation of PLs strongly depends on the initial conditions and on the lead time [33,35].

The main objective of this work was to conduct a detailed analysis of the development mechanisms of an observed PL that is reasonably well represented by the sixth version of the Canadian Regional Climate Model (CRCM6/GEM4) [35]. An older version of the CRCM, with a 30 km grid mesh and 40 vertical levels, was previously used to study a PL that formed over the Hudson Bay in December 1988 [15]. To the best of the authors' knowledge, no study of a PL has been made using the CRCM with high resolution. This study demonstrates that the detailed representation of an observed PL provided by the

CRCM6/GEM4 is invaluable to analyse its development mechanisms. The main conclusion of this analysis is that moist baroclinic instability plays a major role in the genesis and intensification of the observed PL. This article is organised in four sections. Section 2 describes the data and methods used for the analysis of the development mechanisms of this PL. Section 3 presents and discusses the results, and Section 4 provides the main conclusions.

2. Materials and Methods

2.1. Data

The PL studied here developed over the Norwegian Sea on 25 March 2019 (Figure 1). Moreno-Ibáñez et al. [35] conducted an ensemble of eight simulations of this PL with the CRCM6/GEM4 [36–39], with a grid spacing of 0.0225° and a vertical grid with 62 levels. Note that the CRCM6/GEM4 does not include ocean and sea ice simulation components; therefore, high-temporal atmosphere–ocean–sea ice interactions are not explicitly represented, as SSTs and sea ice are prescribed in the CRCM6/GEM4 from daily ERA5 values (see [35]). The authors concluded that the observed PL was quite well represented by the simulation initialised on 24 March at 1800 UTC. In effect, this simulation captured the size, track, and lifetime of this PL. The cloud signature of the simulated PL at its mature stage spanned roughly 600 km, and its lifetime extended from 25 March at 0000 UTC to 25 March at 2100 UTC. The verification of the simulation against conventional surface observations within a 300 km radius from the PL centre showed that the sea level pressure (SLP) field was well represented, although the simulated PL was somewhat deeper than the observed one. The simulation output was available hourly and covered the period from 24 March at 1900 UTC to 26 March at 0600 UTC [40], and the three-dimensional fields were interpolated on 22 pressure levels from 1000 to 10 hPa.

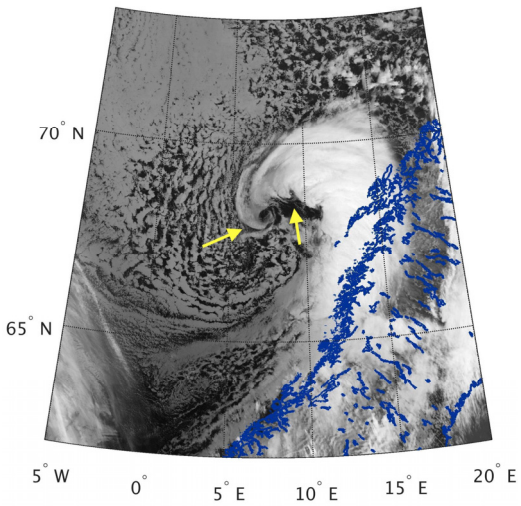

Figure 1. Visible Infrared Imaging Radiometer Suite (VIIRS) [41] channel M15 (10.76 μm) image showing the PL on 25 March, 1248–1254 UTC. The blue outlining represents the coastline. Small meso-vortices are observed along the front of the occluding PL (yellow arrows). The open and closed convective cells are due to mesoscale cellular convection resulting from the MCAO.

2.2. Methods

Life Cycle and Classification of the PL

In order to analyse the life cycle of the PL, horizontal averages of several variables were computed using the values at the grid points within a 300 km radius from the centre of the simulated PL. This radius was selected because it roughly corresponds to the size of the PL at its mature stage [35]. Note that, since the size of the PL increased with time, the average fields computed during the first hours of PL development corresponded not only to the PL itself, but also to its environment. Likewise, maximum and minimum values were

obtained from the values at the grid points within a 300 km radius from the PL centre. Of particular interest was the time evolution of the PL intensity, represented by the minimum SLP at the PL centre and the maximum 10 m wind speed. The time evolution of the average difference between the SST and the temperature at 500 hPa (SST $-$ T_{500}), which has been often used in PL studies as a measure of the atmospheric static stability (e.g., [42]), was also analysed. Note that, in the case of the SST $-$ T_{500}, only the ocean grid points were considered for the computation of the average. In addition, the time series of the average temperature at 2 m, as well as of the average and maximum surface heat fluxes, were examined.

Based on the classification of vertical wind shear environments suggested by Stoll et al. [25], the vertical wind shear category corresponding to each 1 h time step during the lifetime of the PL was determined. The vertical shear strength was computed as follows [25]:

$$\frac{\left|\Delta\langle\vec{V}\rangle\right|}{\Delta\langle Z\rangle} = \frac{\left|\Delta\langle\vec{V}\rangle\right|}{\langle Z_{500}\rangle - \langle Z_{925}\rangle} \tag{1}$$

where $\langle\ \rangle$ is the horizontal averaging operator, $\Delta\vec{V}$ is the differential wind vector, Z_{500} is the geopotential height at 500 hPa, and Z_{925} is the geopotential height at 925 hPa. The horizontal average of the differential wind vector is calculated here as the horizontal average of the horizontal wind vectors at 500 and 925 hPa within a 300 km radius from the PL centre:

$$\Delta\langle\vec{V}\rangle = (\langle u_{500}\rangle - \langle u_{925}\rangle, \langle v_{500}\rangle - \langle v_{925}\rangle) \tag{2}$$

where u is the wind component parallel to the x axis (i.e., east-west component), and v is the wind component parallel to the y axis (i.e., north–south component). The vertical shear vector in the along and across propagation direction is computed as follows [25]:

$$\left(\frac{\left|\Delta\langle\vec{V}\rangle\right|}{\Delta\langle Z\rangle}\right)_p = \frac{\left|\Delta\langle\vec{V}\rangle\right|}{\Delta\langle Z\rangle} \times (\cos\alpha, \sin\alpha) \tag{3}$$

where $\alpha = \alpha_d - \alpha_p$ is the vertical shear angle, with α_d representing the orientation of $\Delta\langle\vec{V}\rangle$, and α_p the propagation direction. The propagation direction is obtained from the PL track points.

2.3. Analysis of the Development Mechanisms of the PL

As when analysing the life cycle of the PL, horizontal averages of different variables were computed using the values at the grid points within a 300 km radius from the PL centre.

Since the presence of the PL is associated with convergence in the planetary boundary layer, due to mass conservation there must be divergence at a higher level of the troposphere. The times series of the vertical profile of the horizontal average of wind divergence $(\vec{\nabla}\cdot\vec{V})$ helps determine the pressure level at which divergence occurs.

The terms that contribute to the atmospheric surface pressure tendency were analysed using the following equation (see Appendix A):

$$\frac{\partial p_s}{\partial t} \approx \frac{p_s}{RT_s}\frac{\partial \Phi_a}{\partial t} + \frac{p_s}{T_s}\int_{p_b}^{p_a}\frac{1}{p}\frac{\partial T}{\partial t}dp \tag{4}$$

where p_s is the atmospheric surface pressure, T_s is the temperature at 2 m, R = 287 J K^{-1} Kg^{-1} is the gas constant for dry air, Φ_a is the geopotential at 500 hPa, p_a is 500 hPa, and $p_b = \min(p_s(x,y))$ is the minimum value of the time series of the surface pressure at each grid point. The time series used for the computation of $p_s(x,y)$ corresponds to the whole

simulation period. The pressure level p_a was selected considering that the PL extends up to ~500 hPa. The first term represents the contribution of the tendency of the geopotential at 500 hPa, and the second term represents the contribution of the warming of the atmospheric column. To analyse the error in the computation of the surface pressure tendency with Equation (4) due to the approximations made, the surface pressure tendency was also computed using the simulated surface pressure field. Time derivatives were calculated with a central-difference scheme, except on the time boundaries where backward-difference and forward-difference schemes were used. The error was then computed as follows:

$$\text{Error} = (\text{Term 1} + \text{Term 2}) - \frac{\partial p_s}{\partial t} \tag{5}$$

where Term 1 $= \frac{p_s}{RT_s}\frac{\partial \Phi_a}{\partial t}$, and Term 2 $= \frac{p_s}{T_s}\int_{p_b}^{p_a}\frac{1}{p}\frac{\partial T}{\partial t}dp$. The mean absolute error over the whole domain and period of the simulation was 0.09 hPa h^{-1}, which is reasonable and quite small on average. However, the maximum and minimum errors were 1.49 hPa h^{-1} and -1.52 hPa h^{-1}, respectively, so the spatial distribution of the error should be considered when interpreting the results.

Computation of the baroclinic conversion term, which represents the conversion from eddy available potential energy to eddy kinetic energy [43,44], helped determine the role of baroclinic instability in the development of this PL. In the scientific literature, the baroclinic conversion term has been computed to analyse the contribution of baroclinic instability to the development of midlatitude storms (e.g., [45]) and PLs [23,46–48]. Since many studies indicated that baroclinic instability plays a major role in PL development (e.g., [49]), it is expected that the baroclinic conversion term was significant during the development of this PL. Given that PLs are mesoscale eddies, we are interested in the deviation of atmospheric variables (ψ') from the time-mean state ($\bar{\psi}$), which is $\psi' = \psi - \bar{\psi}$. Therefore, at each grid point, the baroclinic conversion term was computed as follows:

$$c = -\omega'\alpha' \tag{6}$$

where ω is the vertical velocity in pressure coordinate and α is the specific volume. The period considered for the computation of the time average and deviation corresponds to the lifetime of the simulated PL.

Finally, the atmospheric static stability, and therefore the role of natural convection, was analysed using thermodynamic diagrams. Skew-T log-P diagrams [50] were plotted with the software package MetPy [51]. MetPy computes the convective available potential energy (CAPE) and the convective inhibition (CIN) as follows:

$$CAPE = -R\int_{LFC}^{EL}\int \left(T_{parcel} - T_{env}\right)dlnp \tag{7}$$

$$CIN = -R\int_{SFC}^{LFC}\int \left(T_{parcel} - T_{env}\right)dlnp \tag{8}$$

where R is the gas constant for dry air, T_{parcel} is the parcel temperature, T_{env} is the environmental temperature, EL is the pressure of the equilibrium level, LFC is the pressure of the level of free convection, and SFC is the level of the surface or the beginning of the parcel path.

3. Results and Discussion

3.1. Life Cycle and Classification of the PL

Figure 2 shows time series throughout the life cycle of this PL. The central pressure of the PL dropped from around 1008.3 hPa at 0000 UTC to a minimum of 995.7 hPa at 1500 UTC, which corresponds to an average deepening rate of 0.8 hPa h^{-1} (Figure 2a). Later, the SLP increased to reach 1002.3 hPa at the end of its lifetime. The maximum 10 m

wind speed associated with the PL steadily increased from 18.2 m s^{-1} until it reached a maximum of 29.8 m s^{-1} at 1200 UTC (Figure 2a). The mean SST − T_{500} exceeded 39 °C during the whole lifetime of the PL (Figure 2b). The SST − T_{500} increased from the genesis of the PL, until it reached a maximum of 45 °C at 0600 UTC, and then it decreased. The maximum SST − T_{500} was in the range of values obtained over the Nordic Seas in the recent study of Stoll [32]. During the whole lifetime of the PL, the average surface latent heat flux (LHF) was higher than the average surface sensible heat flux (SHF), especially during the second half of the lifetime of the PL (Figure 2c). The maximum LHF and SHF associated with the PL were 619 W m^{-2} at 1500 UTC and 583 W m^{-2} at 1300 UTC, respectively. The mean 2 m temperature increased from −2.1 °C at 0000 UTC until it reached a maximum of 2.1 °C at 1100 UTC (Figure 2b). The surface diabatic fluxes (SHF and LHF) and the 2 m temperature decreased as the PL moved overland.

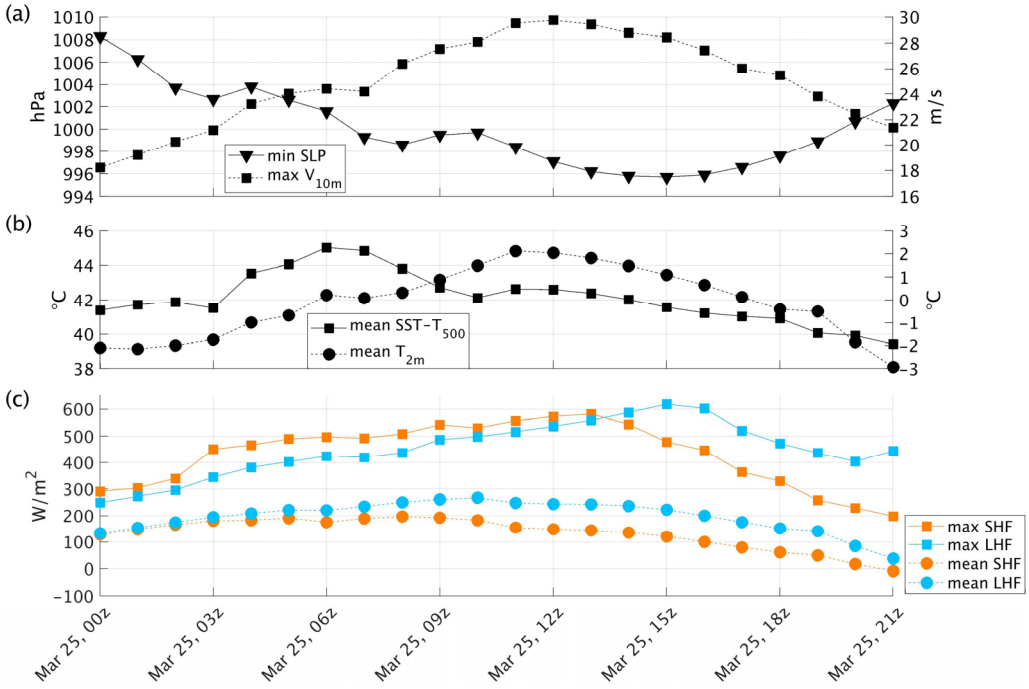

Figure 2. Time series of the (**a**) minimum SLP (hPa) at the centre of the simulated PL, and maximum 10 m wind speed (m s^{-1}), (**b**) mean difference between the SST and the temperature at 500 hPa (°C), and mean 2 m temperature (°C), and (**c**) maximum and mean SHF and LHF (W m^{-2}). The grid points included in the computation of the horizontal average and the maximum are those within a 300 km radius from the PL centre. In the case of the SST − T_{500}, only the ocean grid points have been considered.

The life cycle of the PL can be divided into different stages. The genesis stage includes the first few hours of PL development, from 0000 UTC to around 0300 UTC. The mature stage covers the period around 1200 UTC, which corresponds to the time with the highest maximum 10 m wind speed associated with the PL (Figure 2a). The dissipation stage corresponds to the period after 1500 UTC, i.e., after the central pressure of the PL reached its minimum value (Figure 2a).

Strong vertical wind shear (>1.5 × 10^{-3} s^{-1}) was found during the whole lifetime of the PL, even at the dissipation stage (Table 1). The type of vertical shear dominant during most of the PL lifetime was forward shear (16 h). Forward shear was mainly present when the PL moved eastward or south-eastward. In contrast, right shear (1 h) occurred when the PL moved northward, and left shear (4 h) occurred when the PL moved southward. The fact that the propagation direction changed from eastward to northward and then to southward in a short time was due to the fact that the location of the SLP minimum associated with the PL was somewhat erratic during that time. This is not surprising since,

in general, PL tracks are not smooth (e.g., [25]). The shear strength considerably decreased during the lifetime of the PL, indicating that the environment became less baroclinic. The average SST − T_{500} during the genesis time of this PL, which was almost 42 °C (Figure 2b), is in agreement with Terpstra et al. [31], who found an average SST − T_{500} of 41.0 ± 3.6 °C at the genesis time of forward-shear PLs.

Table 1. Vertical shear strength (10^{-3} s^{-1}), vertical shear vector in the propagation direction (10^{-3} s^{-1}), vertical shear vector across the propagation direction (10^{-3} s^{-1}), and type of shear on 25 March 2019 at different times (UTC) during the lifetime of the PL.

Time	Vertical Shear Strength	Vertical Shear Vector in the Propagation Direction	Vertical Shear Vector across the Propagation Direction	Type of Shear [1]
00:00	4.5	3.8	−2.6	Forward
01:00	4.5	4.5	0	Forward
02:00	4.6	3.6	2.8	Forward
03:00	4.7	4.7	−0.6	Forward
04:00	4.4	4.4	−0.1	Forward
05:00	4.3	4.1	1.2	Forward
06:00	4.1	1.5	−3.9	Right
07:00	3.9	−0.1	3.9	Left
08:00	3.8	1.3	3.5	Left
09:00	3.7	2.5	2.6	Left
10:00	3.5	3.4	0.6	Forward
11:00	3.2	3.2	−0.4	Forward
12:00	3.1	3	0.3	Forward
13:00	3	2.9	0.8	Forward
14:00	2.9	2.7	1.2	Forward
15:00	2.9	2.7	1.1	Forward
16:00	3	2.9	0.7	Forward
17:00	3	3	0	Forward
18:00	2.9	1.7	2.4	Left
19:00	3	3	−0.6	Forward
20:00	2.8	2.7	−0.6	Forward
21:00	2.6	n/a	n/a	n/a

[1] Type of shear according to Stoll et al. [25].

3.2. Development Mechanisms of the PL

The environmental conditions on the 24–25 March were favourable for the formation of the PL [35]. On 24 March at 1900 UTC, a few hours before the PL genesis, there was strong low-level baroclinicity to the west of Jan Mayen, and cold air was being advected by the strong northerly winds, while warm air was being advected northward (see Figure 13 in Moreno-Ibáñez et al. [35]). At 500 hPa, there was a through with its northeast–southwest axis parallel to the sea ice edge (not shown). On the right side of this 500 hPa through, a low-level through, which eventually became a PL, started to form.

Figure 3a shows the horizontal average of the horizontal wind divergence within a 300 km radius from the PL centre. Overall, there was weak convergence in the lower levels of the atmosphere (below 700 hPa) and stronger divergence in the upper levels (more often

above 500 hPa). The level of non-divergence was located at 500 hPa in the beginning of the PL development, and it decreased down to 900 hPa by the time the PL dissipated. In the upper troposphere, there was a notable increase in divergence over time between 500 and 300 hPa. Thus, divergence aloft led to the deepening of the PL. A maximum in divergence was observed at 400 hPa around the time when the central pressure of the PL reached the minimum (Figure 2a). Afterwards, the decrease in divergence aloft was associated with the dissipation of the PL (Figure 3a). In the lower troposphere, the convergence started to decrease halfway through the lifetime of the PL, shortly before hitting Norway (at around 1100 UTC). As the PL moved overland, the low-level divergence field was affected by the complex topography of the Norwegian coast, which resulted in a decrease in convergence. On average, the vertical movement in pressure coordinate (ω) was upward ($-0.53 < \omega < 0$ Pa s^{-1}) between the surface and ~300 hPa during the lifetime of the PL (Figure 3b). The absolute value of the average vertical movement was maximum between 700 and 600 hPa, except for during the first three hours and the last three hours of the PL lifetime, when the maximum was located at 500 and 800 hPa, respectively. The maximum absolute values of the average vertical movement were found between 1000 and 1200 UTC on 25 March.

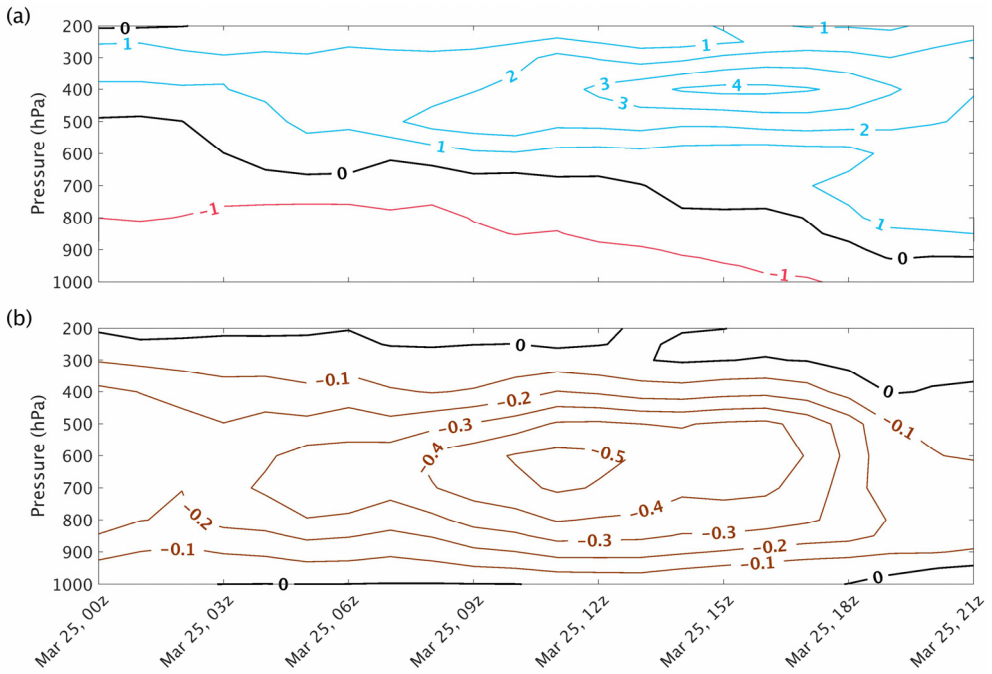

Figure 3. Time series of the vertical profile of the horizontal average of (**a**) the horizontal wind divergence ($\times 10^{-5}$ s^{-1}, contours every 10^{-5} s^{-1}), and (**b**) the vertical motion in pressure coordinate (Pa s^{-1}, contours every 10^{-1} Pa s^{-1}). The grid points included in the computation of the average are those within a 300 km radius from the PL centre.

Figure 4 shows the horizontal wind divergence at 950 hPa and 500 hPa on the 25 March at 0300 UTC and 1200 UTC. During the initial stage of the PL, there was a hook-shaped thin band of very strong convergence at 950 hPa (Figure 4a). This band extended from the west side of the PL to its centre, and from its centre to the southwest. Near the PL centre, on its east and north sides, there was mainly convergence, although the values were much smaller than those of the hook-shaped convergence band. At 500 hPa, there was a comma-shaped area of divergence located above the PL (Figure 4c). This area of divergence was surrounded by a band of convergence that was particularly strong on its north and east sides. The presence of this area of convergence explains why, on average, the horizontal wind divergence was not very strong at 500 hPa (Figure 3a). During the mature stage of the PL, at 950 hPa, there was a strong convergence band that wrapped around the PL, as well as several low-level and alternating strong convergence and divergence bands (Figure 4b).

At 500 hPa, the absolute values of convergence and divergence in the PL region were quite weak, except for a band of strong divergence that extended from the east side of the PL to the south (Figure 4d).

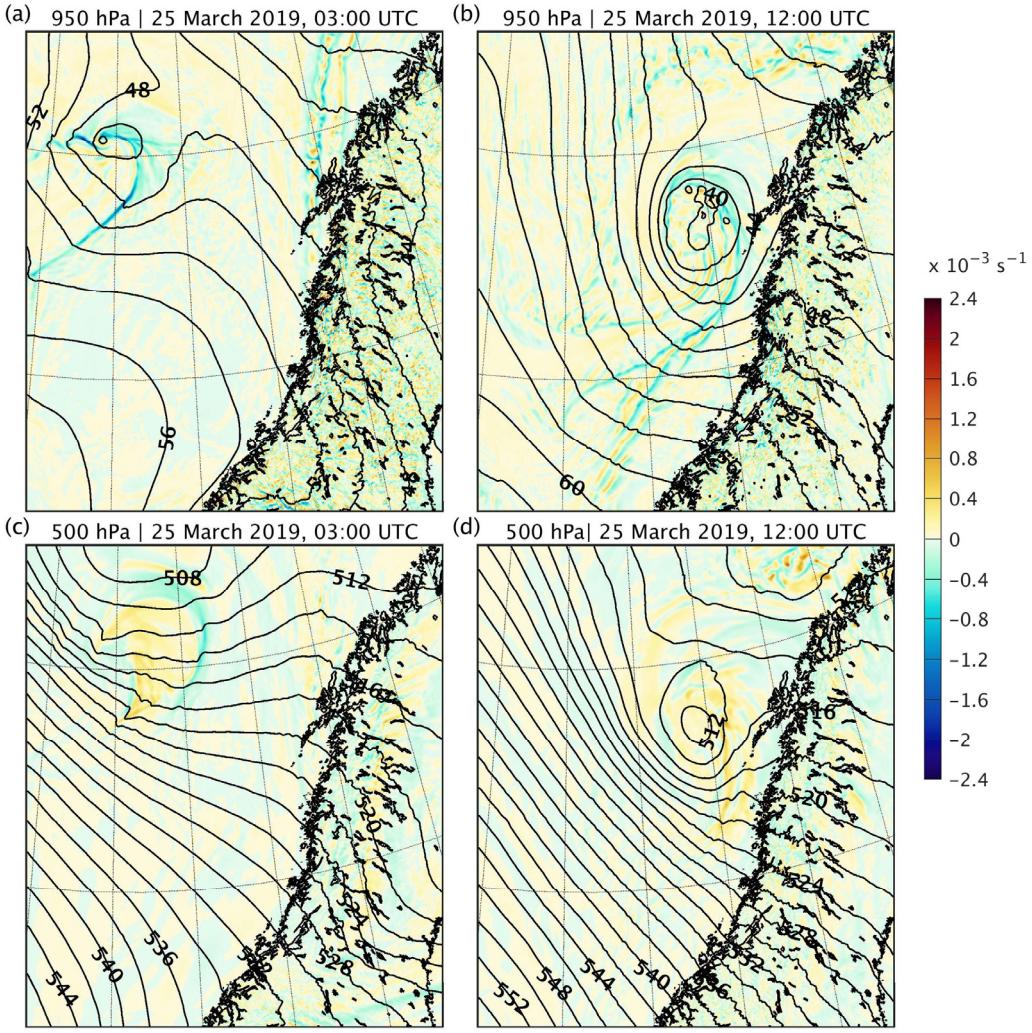

Figure 4. Horizontal wind divergence at (**a**,**b**) 950 hPa and (**c**,**d**) 500 hPa on 25 March 2019 at (**a**,**c**) 0300 UTC and (**b**,**d**) 1200 UTC. The black isolines represent the geopotential height (dam; contours every 2 dam) at (**a**,**b**) 950 hPa and (**c**,**d**) 500 hPa. The black outlining represents the coastline.

The interaction between the low- and mid-troposphere is better understood by looking at the SLP, the geopotential height at 500 hPa, and the 1000–500 hPa thickness, shown in Figure 5. The PL formed downstream of a 500 hPa trough, in a region with a strong 1000–500 hPa thickness gradient, indicating a baroclinic environment (Figure 5a). Thus, the upper-level divergence (Figure 4c) provided a favourable condition for the intensification of the PL. This is in accordance with Stoll et al. [25], who found that PLs that develop in strong-shear environments are associated with an up-shear vertical tilt of the pressure anomaly. At around half its lifetime, the vertical extension of the PL reached 500 hPa (Figure 5c). The 1000–500 hPa thickness field shows that there was southward (northward) cold (warm) air advection to the west (east) of the PL (Figure 5b,c). In other words, the warm (cold) sector was ahead of (behind) the PL with respect to its propagation direction, which is a situation typical of forward shear environments [25]. The PL still had a large vertical extension when it affected the Norwegian coast (Figure 5d), and the upper-level low dissipated at the same time as the low-level one (not shown).

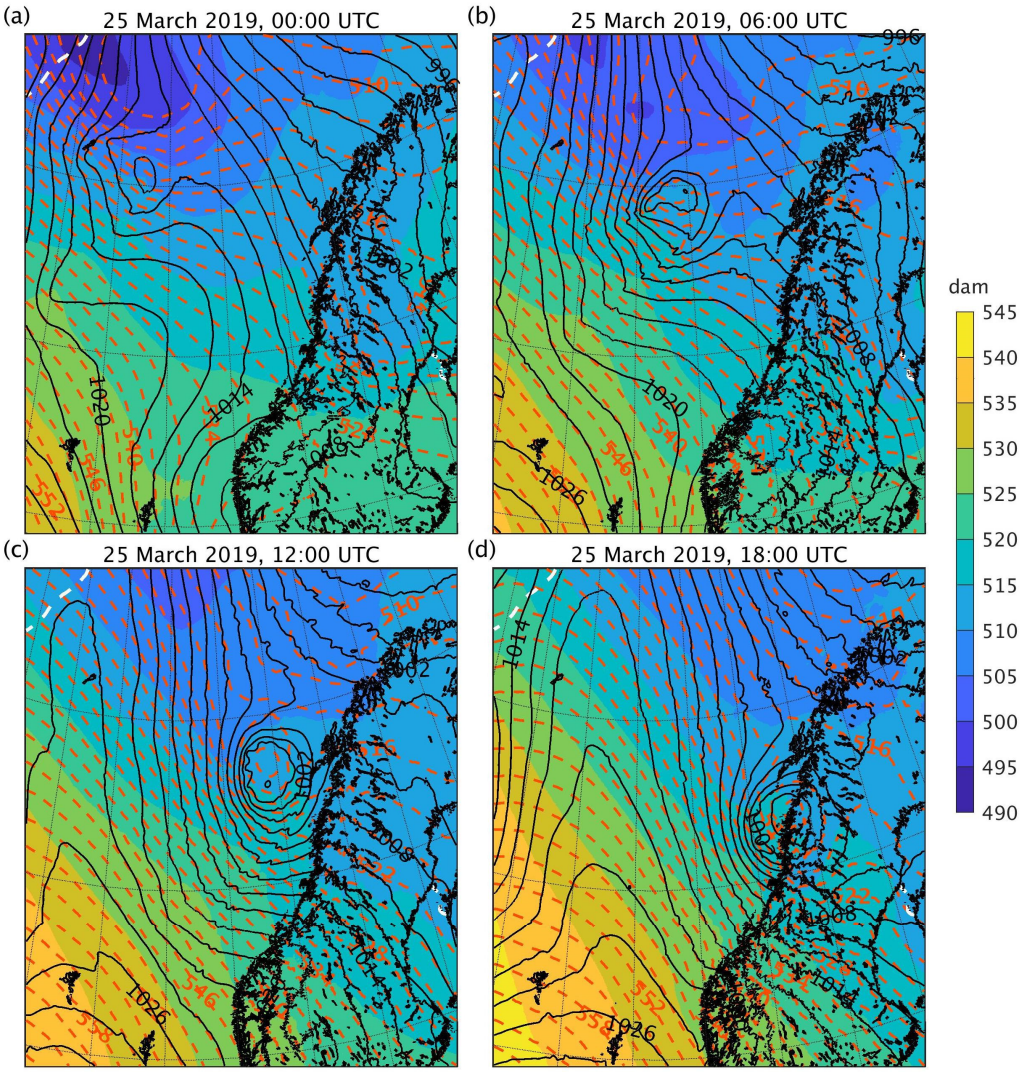

Figure 5. Simulated fields showing the PL on 25 March 2019 at (**a**) 0000 UTC, (**b**) 0600 UTC, (**c**) 1200 UTC, and (**d**) 1800 UTC. The colourmap represents the 1000–500 hPa thickness (dam), the black isobars represent the SLP (hPa, contours every 2 hPa) and the red (dashed lines) isohypses represent the geopotential height at 500 hPa (dam, contours every 2 dam). The black outlining represents the coastline, and the white dashed line represents the sea ice edge, which is defined as the 0.15 contour of the sea ice concentration. Image (**a**) was adapted from Moreno-Ibáñez et al. [35].

Figures 6 and 7 show the terms in Equation (4) contributing to the surface pressure tendency on 25 March at 0000 UTC and 1200 UTC, respectively. Since the PL was moving toward the southeast, the surface pressure tendency was negative (positive) on the south and east (north and west) side of the PL, and the absolute values of the surface pressure tendency were particularly high where the pressure gradients were the strongest (Figures 6a and 7a). The errors in the computation of the surface pressure tendency with Equation (4) were small and of a different sign over the domain shown. At 0000 UTC, the mean absolute error over this domain was 0.07 hPa h^{-1}, and the maximum absolute error was 0.66 hPa h^{-1} (Figure 6b). At 1200 UTC, the mean absolute error over this domain was 0.09 hPa h^{-1}, and the maximum absolute error was 0.85 hPa h^{-1} (Figure 7b). Over the area of the MCAO, the increase in the air temperature of the atmospheric column contributed to a decrease in surface pressure, whereas the increase in geopotential height at 500 hPa contributed to an increase in surface pressure (Figure 7). At 0000 UTC, only term 2 contributed to the decrease in the surface pressure south of the PL (Figure 6). Therefore, the warming of the atmospheric column near the PL centre played an important role in the

deepening of the PL during its genesis. At 1200 UTC, when the PL was well developed, the decrease in geopotential height at 500 hPa was the main driver of the decrease in surface pressure near the PL centre (Figure 7). The contribution of the warming of the atmospheric column to the deepening of the PL was less important at this stage.

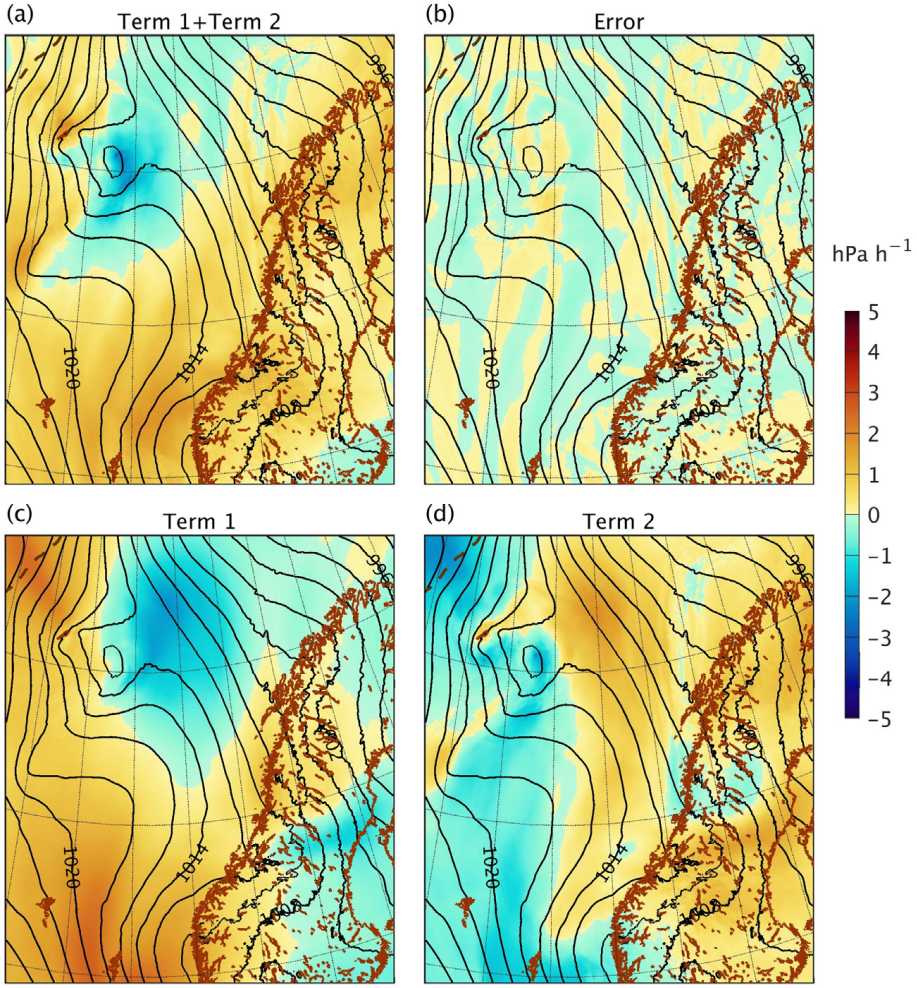

Figure 6. Surface pressure tendency (hPa h^{-1}) on 25 March 2019 at 0000 UTC. (**a**) Surface pressure tendency computed as the sum of term 1 ($\frac{p_s}{RT_s}\frac{\partial \Phi_a}{\partial t}$) and term 2 ($\frac{p_s}{T_s}\int_{p_b}^{p_a}\frac{1}{p}\frac{\partial T}{\partial t}dp$), and (**b**) the error, that is, the sum of term 1 and term 2 minus the surface pressure tendency computed with the simulated surface pressure field. The two terms contributing to the surface pressure tendency are (**c**) term 1 and (**d**) term 2. The black isobars represent the SLP (hPa; contours every 2 hPa). The brown outlining represents the coastline, and the brown dashed line represents the sea ice edge, which is defined as the 0.15 contour of the sea ice concentration.

Figure 8 shows the time average and deviation of SLP, computed considering the period corresponding to the lifetime of the PL. In the region shown in the figure, overall, the average SLP decreased from the southwest to the northeast. The PL formed in an environment with a relatively high SLP (Figure 8a) and moved south-eastward to an environment with lower SLP (Figure 8b). Thus, the propagation of the PL into an environment with lower SLP and strong convergence of northward warm advection at low-levels (see Figure 4a in this article, and Figure 13 in Moreno-Ibáñez et al. [35]) also contributed to the decrease in the central pressure of the PL.

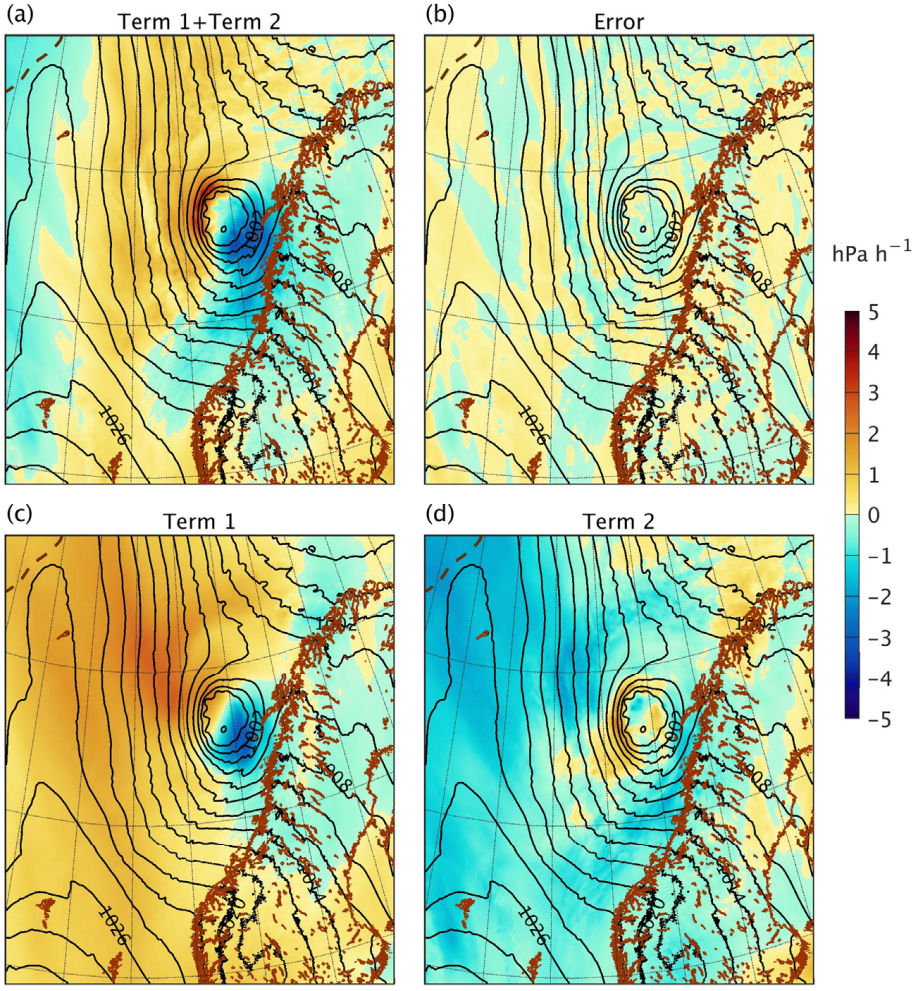

Figure 7. Same as Figure 6, but for 25 March 2019 at 1200 UTC.

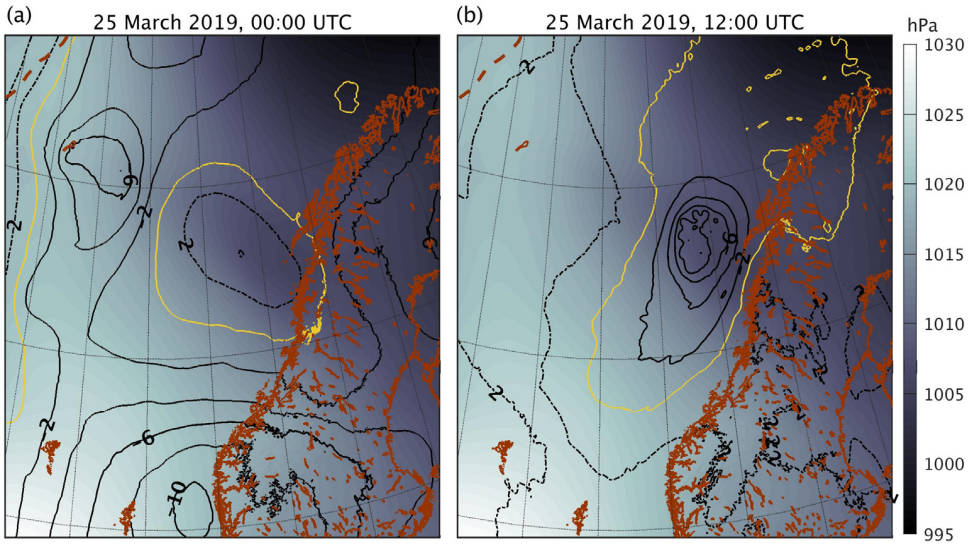

Figure 8. Time average and time deviation of SLP on 25 March 2019 at (**a**) 0000 UTC and (**b**) 1200 UTC. The colour map represents the time average of SLP (hPa) for the period corresponding to the lifetime of the PL. The black continuous (dashed) lines represent the negative (positive) time deviation of SLP (hPa, contours every 2 hPa), and the yellow line represents a zero-time deviation of SLP. The brown outlining represents the coastline, and the brown dashed line represents the sea ice edge, which is defined as the 0.15 contour of the sea ice concentration.

Given that this PL formed in a baroclinic environment downstream of a 500 hPa trough (Figure 5a), baroclinic instability likely played a major role in its genesis, as noted by Moreno-Ibáñez et al. [35]. The time series of the baroclinic conversion term shows that this indeed was the case (Figure 9). We recall that positive $-\omega'\alpha'$ corresponds to rising (sinking) warm (cold) air, resulting in lowering of the centre of mass of the atmospheric column; the decrease of gravitational potential energy is then available for generating kinetic energy. During the whole lifetime of the PL, the horizontal average of $-\omega'\alpha'$ was positive in the lower levels of the troposphere (~1000–700 hPa) and negative in the upper levels (~500–300 hPa). Between 500 and 700 hPa, the term $-\omega'\alpha'$ was initially negative, but it increased as the PL developed, acquiring values close to zero or positive by 1200 UTC. In other words, baroclinic conversion gradually expanded from the lower troposphere to the middle troposphere. The large positive $-\omega'\alpha'$ at low levels contributed to the intensification of the PL, as reflected in the deepening central pressure and increasing surface wind speeds (Figure 2a). The highest values of $-\omega'\alpha'$ were found between 800 and 700 hPa (Figure 9) due to the latent heating of condensation, which increased the air buoyancy (this will be analysed below). The baroclinic term eventually weakened during the second half of the lifetime of the PL, contributing to its dissipation.

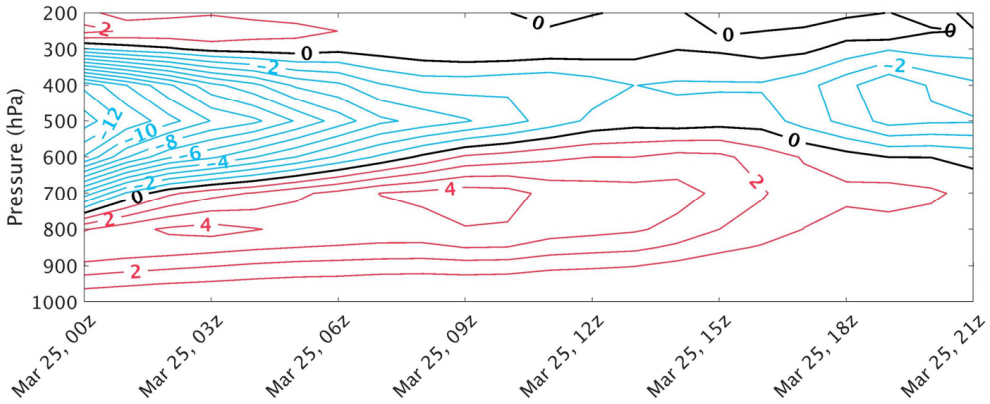

Figure 9. Time series of the vertical profile of the horizontal average of the baroclinic conversion term $-\omega'\alpha'$ ($\times 10^{-3}$ W kg^{-1}, contours every 10^{-3} W kg^{-1}). The grid points included in the computation of the average are those within a 300 km radius from the PL centre.

The spatial distribution of the lower-level (1000–700 hPa) mass-weighted vertical integral of $-\omega'\alpha'$ at the genesis and mature stages of the PL is shown in Figure 10. During the genesis of the PL, a thin band of very high values of $-\omega'\alpha'$ extended from the centre and east side of the PL towards the southwest (Figure 10a). This corresponded to the region where convergence was strongest (Figure 4a). This band is associated with the shape of the SLP gradient as well as the temperature one (Figure 11a), indicating a frontal zone. The values of $-\omega'\alpha'$ in this thin band decreased over time (Figure 10b), and the band disappeared as the PL moved overland (not shown). In summary, these results indicate that low-level baroclinic instability plays an important role in the formation of this PL, and that, during the intensification of this PL, baroclinic instability extended from the low- to the mid-troposphere.

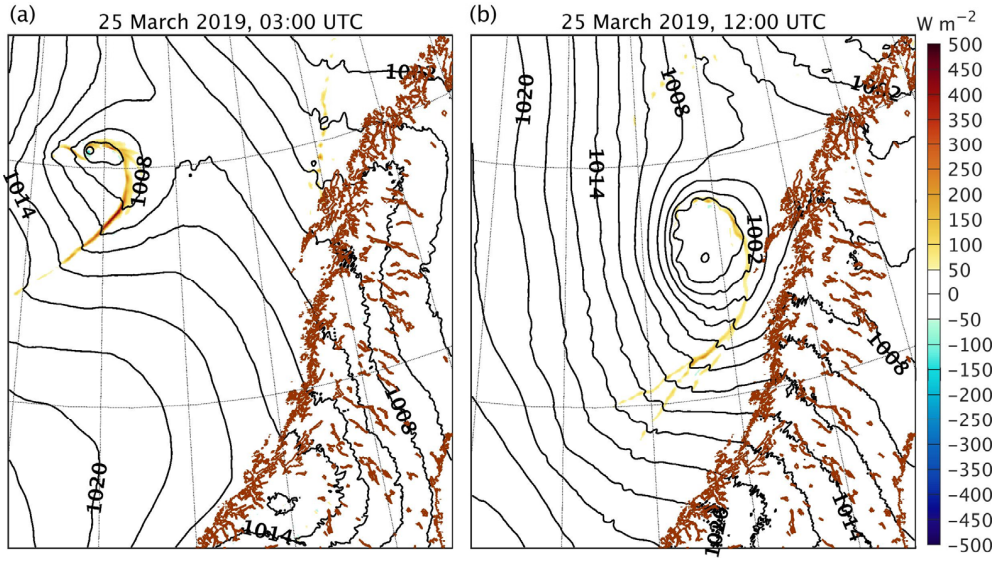

Figure 10. Mass-weighted vertical integral of $-\omega'\alpha'$ (W m^{-2}) at the lower troposphere (1000–700 hPa) on 25 March 2019 at (**a**) 0300 UTC and (**b**) 1200 UTC. The black isolines represent the SLP (hPa; contours every 2 hPa). The brown outlining represents the coastline.

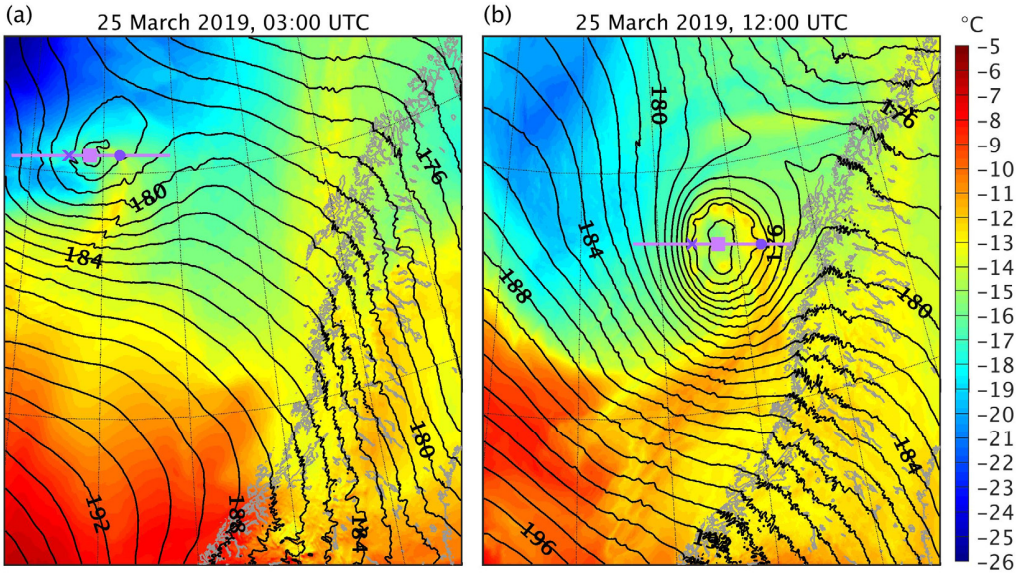

Figure 11. Simulated fields showing the PL on 25 March 2019 at (**a**) 0300 UTC and (**b**) 1200 UTC. The colourmap represents the temperature at 800 hPa (°C), and the black isolines represent the geopotential height at 800 hPa (dam, contours every 1 dam). The grey outlining represents the coastline. The violet line indicates the region whose vertical cross-section is shown in (**a**) Figure 12a and (**b**) Figure 12b. The violet square, cross, and circle indicate the corresponding locations in Figures 12 and 13.

The baroclinic development of this PL is illustrated by a map of the temperature and geopotential height fields at 800 hPa (Figure 11), as well as by a vertical cross-section of the potential temperature and vertical velocity fields (Figure 12) during its genesis and mature stages. During the genesis of the PL, there was low-level southward (northward) cold (warm) air advection on the west (east) side of the PL (Figure 11a). This situation led to the generation of eddy available potential energy, which could then be converted to eddy kinetic energy through baroclinic conversion. There was a very strong updraft on the west side of the PL, where the air was warmer than in the surrounding areas (Figure 12a). The upward vertical movement was particularly strong here because it was a region of strong

low-level convergence (Figure 4a). Moreover, the sensible and latent heat fluxes on the west side of the PL were stronger that on its east side (this will be analysed below), thus increasing the air buoyancy. There was also an upward vertical movement, albeit weaker, at the centre of the PL and on its east side (Figure 12a). This was also a region with high values of low-level convergence (Figure 4a). The contribution to the PL deepening by the warming of the atmospheric column (Figure 6d) was found at approximately the location where baroclinic instability was the most intense (Figure 10a), which was a region with an upward vertical movement (Figure 12a). By 1200 UTC, the PL had occluded (Figure 11b). There was still an upward vertical movement on the west and east sides of the PL (Figure 12b), but the upward movement on the west side was much weaker than during the PL genesis (Figure 12a). This agrees with the lower values of low-level convergence in this region (Figure 4b) compared to the initial stages of PL development (Figure 4a). On the east side, the upward movement extended up to 500 hPa, with the maximum rising motion values mainly between 850 and 650 hPa (Figure 12b). Unlike other PLs (e.g., [52]), this one did not have a warm core (Figures 11 and 12). The formation of the typical comma-shaped cloud (Figure 1), similar to the cloud signature of synoptic-scale cyclones, is explained by the vertical movement (Figure 12) observed in the regions where the baroclinic term was the strongest (Figure 10), which corresponded to the area where the temperature gradient at 800 hPa was highest (Figure 11).

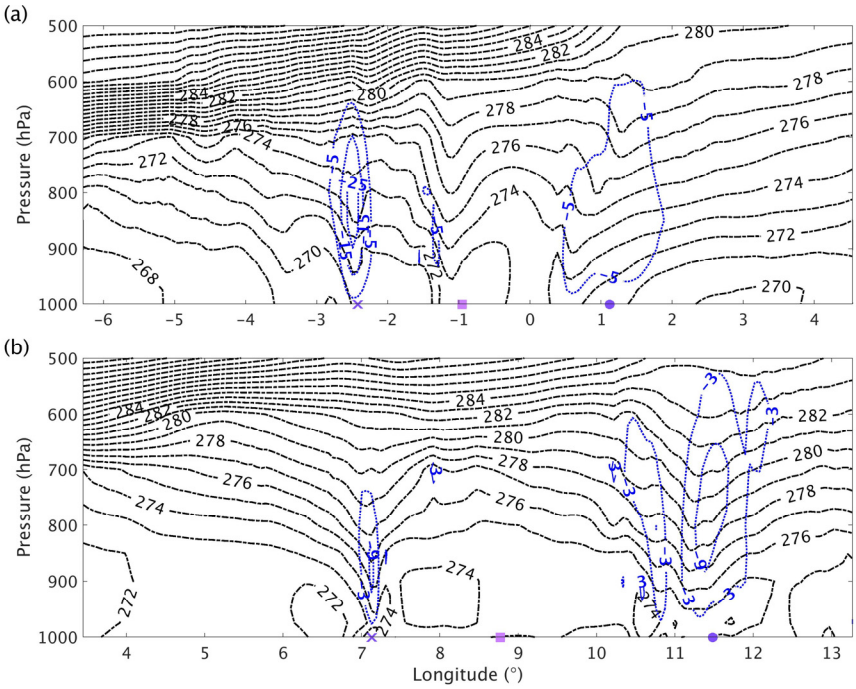

Figure 12. Vertical cross-section of the PL corresponding to the violet lines shown in (**a**) Figure 11a and (**b**) Figure 11b (on 25 March 2019 at 0300 and 1200 UTC, respectively). The black dashed lines represent the potential temperature (K, contours every 1 K). The blue dotted (continuous) lines represent the negative (positive) vertical velocity (Pa s^{-1}, contours every (**a**) 10 Pa s^{-1} and (**b**) 6 Pa s^{-1}). The violet square, cross, and dot correspond to the locations indicated in Figure 11.

An interesting feature of this PL was the formation of a few small and low-level cyclonic mesoscale vortices around the PL centre, embedded in the frontal zone (Figures 1 and 11b). Figure 11b shows that the SLP contour near the PL centre was wavy. The strong positive values of relative vorticity at the location of these wavy patterns indicated that they were mesoscale cyclonic vortices or PL intensification (not shown). Figure 12b shows a strong upward vertical movement around the centre of the mesoscale vortex located at approximately 11° E. These mesoscale vortices had a diameter of up to ~30 km and were warmer than the surrounding area (Figure 11b). This type of vortex typically develops

from a frontal wave formed through barotropic instability, the energy source being the wind shear across the front [53]. The strong horizontal shear near the centre of the PL likely explains the development of barotropic instability and the ensuing frontal wave. Frontal waves are often seen at the centre of synoptic-scale extratropical cyclones [53] and have also been found in some PL studies (e.g., [13]). This is a clear example of the added value of a high-resolution model that can resolve narrow wind shear zones, frontal waves, and small mesoscale vortices.

The role of CAPE in the development of this PL was analysed using a skew-T log-P diagram (Figure 13). On 25 March at 0300 UTC, during the PL genesis, at the locations of rising motion to the west and to the east of the PL centre (Figure 12a), the atmosphere was neutral to moist convection from the surface up to ~700–600 hPa and stable above (Figure 13a,b). At both locations, the CAPE was less than 50 J kg^{-1}, and there was no CIN. The air was saturated in the lower troposphere at both locations; subsequently, latent heat release resulted in diabatically induced upward vertical movement, which reinforced the baroclinically induced rising motion, leading to strong updrafts (Figure 12a). In addition, the release of latent heat in the warm air mass contributed to the maintenance of the horizontal temperature gradient, thus contributing to the baroclinic environment, as found by other authors (e.g., [29]). In the mid-troposphere, the air was quite dry to the west of the PL centre, whereas it was still close to saturation at 500 hPa to the east of the PL centre (Figure 13a,b). As the surface heat fluxes warmed and moistened the atmosphere (Figure 2c), the temperature profile shifted towards higher values in the lowest level of the skew-T log-P diagram (Figure 13c,d). At 1200 UTC, during the mature stage of the PL, at locations of rising motion (Figure 12b), the atmosphere was unstable to moist convection, when considering an air parcel lifted from the surface. The CAPE was 379.39 and 299.69 J kg^{-1} to the west and to the east of the PL centre, respectively, and there was no CIN at any of these locations (Figure 13c,d). At both locations, the air was saturated in the lower troposphere. In the mid-troposphere, the air was quite dry to the west of the PL centre, whereas it was still close to saturation at 500 hPa, to the east of the PL centre.

According to van Delden et al. [17], a moderate amount of CAPE is around 400–600 J kg^{-1}. Hence, the lack of CIN and the negligible (Figure 13a,b) and relatively low (Figure 13c,d) amount of CAPE is in accordance with other studies that found that there is no reservoir of CAPE during PL development, since it is consumed as quickly as it is generated [25,54].

Finally, it is interesting to analyse the role of the surface heat fluxes in the genesis and intensification of this PL. The MCAO led to large surface heat fluxes from the ocean to the atmosphere (Figure 14). However, the surface heat fluxes did not seem to make a significant direct contribution to the PL genesis, since they were not particularly strong in the region where the decrease in the surface pressure was mainly due to the warming of the atmospheric column (Figure 6). Rather, the surface heat fluxes likely had an indirect role in the formation of this PL. By warming the lower atmosphere, the sensible heat flux contributed to the decrease in the static stability of the atmosphere, which favoured the interaction between the low- and high-level anomalies (Figure 5a), contributing to baroclinic development. The latent heat flux provided the cold and dry atmosphere with moisture, thus facilitating the release of latent heat at higher atmospheric levels. When the PL was well developed, both sensible and latent heat surface fluxes were the strongest on the west side of the PL, where the winds were the most intense, as they were reinforced by the winds associated with the MCAO (Figure 15). In the regions where the heat surface fluxes were the strongest, the surface pressure was increasing, and this increase was partly due to the cooling of the atmospheric column (Figure 7). Low-level cold air advection, which contributed to the cooling of the atmospheric column, tended to generate a decrease in cyclogenesis and a downward air motion [15]. Finally, note that an in-depth analysis of the role of surface heat fluxes should be performed to clearly determine the direct and indirect roles of surface heat fluxes in the development of this PL. As Gachon et al. [15] noted in their case study of a PL, sensible heat fluxes can have a direct impact on the low-level

temperature and vorticity advection terms, thus having direct and indirect impacts on the vorticity tendency or cyclogenesis and on the vertical motion near the surface.

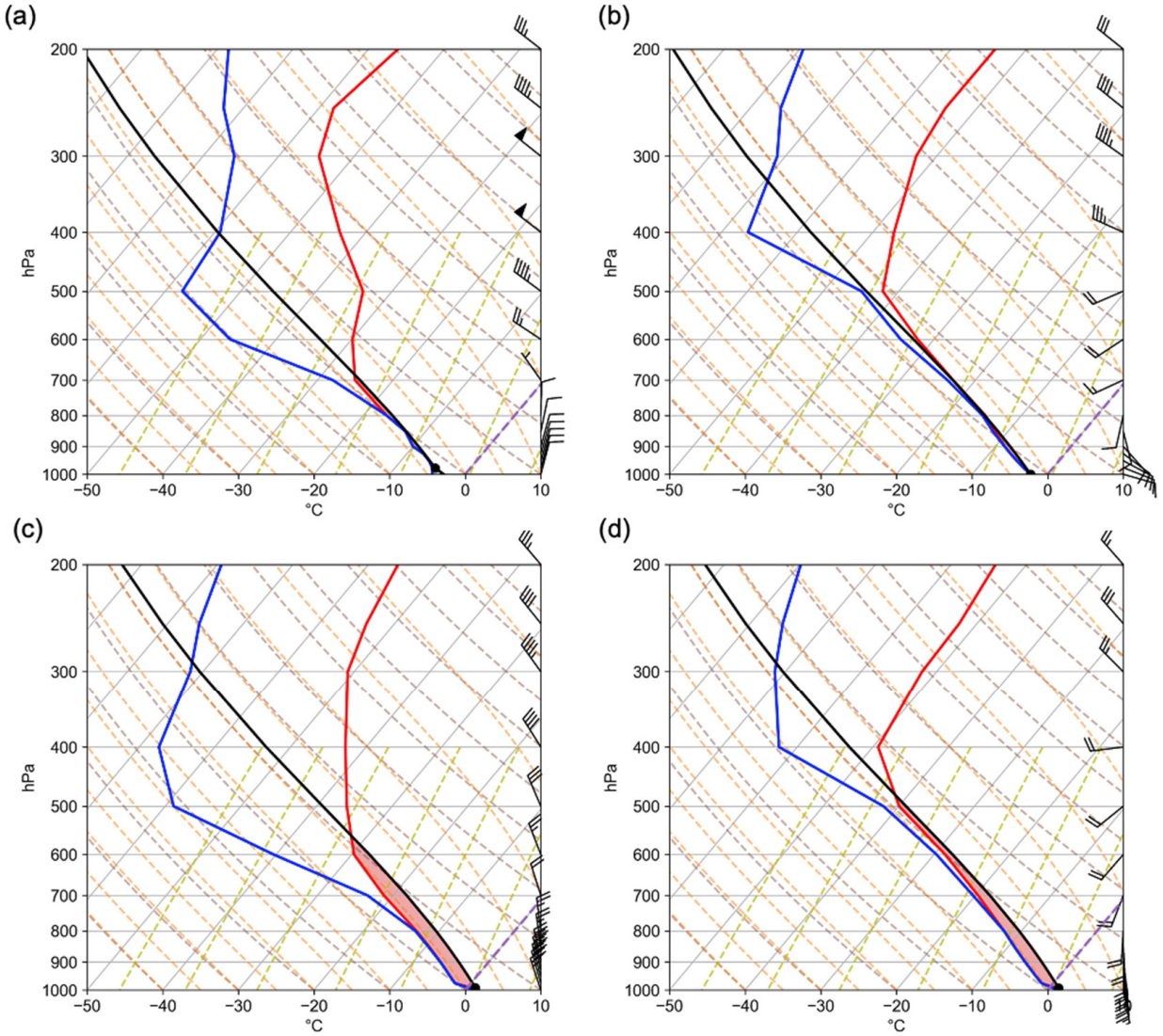

Figure 13. Skew-T log-P diagrams corresponding to 25 March 2019 at 0300 UTC at the location of the (**a**) violet cross and (**b**) violet circle in Figures 11a and 12a, and to 25 March 2019 at 1200 UTC at the location of the (**c**) violet cross and (**d**) violet circle in Figures 11b and 12b. The diagrams show the air temperature (red line, °C), the dew-point temperature (blue line, °C), the parcel profile (black line), the lifting condensation level (black circle), and the wind speed (m s^{-1}) and direction (wind barbs). The violet dashed line is the zero isotherm. The red shading is the convective available potential energy.

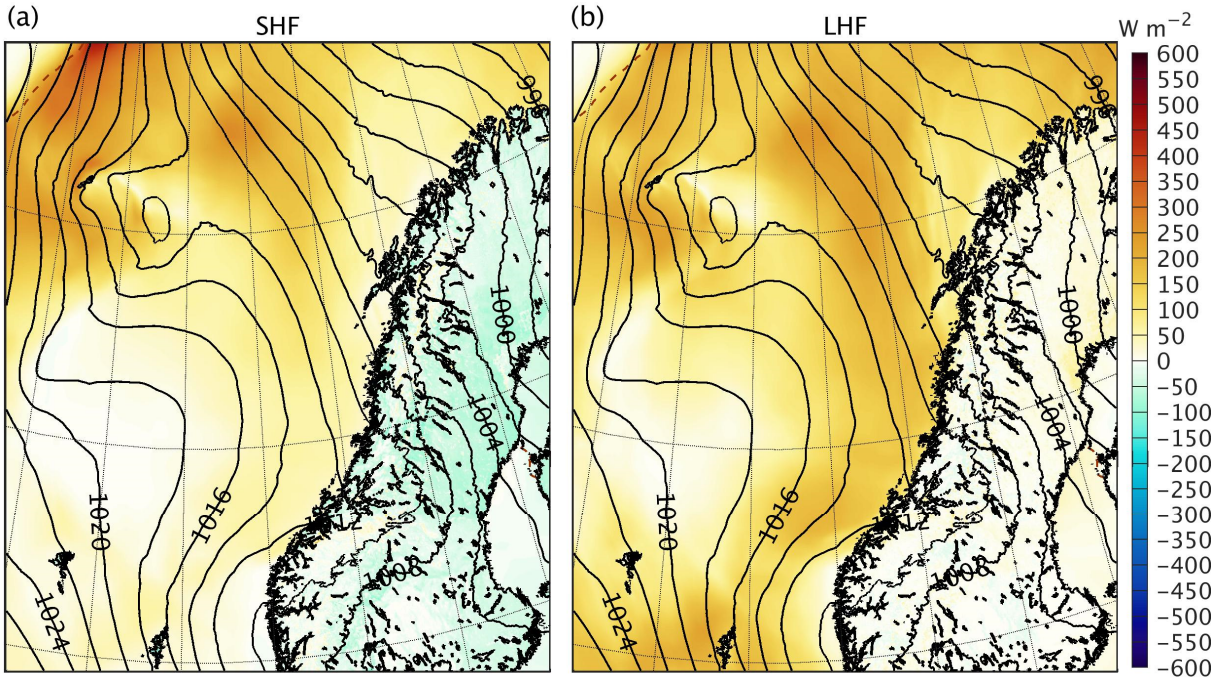

Figure 14. Surface diabatic fluxes (W m^{-2}) on 25 March 2019 at 0000 UTC: (**a**) sensible heat flux, and (**b**) latent heat flux. The black isobars represent the SLP (hPa; contours every 2 hPa). The black outlining represents the coastline, and the brown dashed line represents the sea ice edge, which is defined as the 0.15 contour of the sea ice concentration.

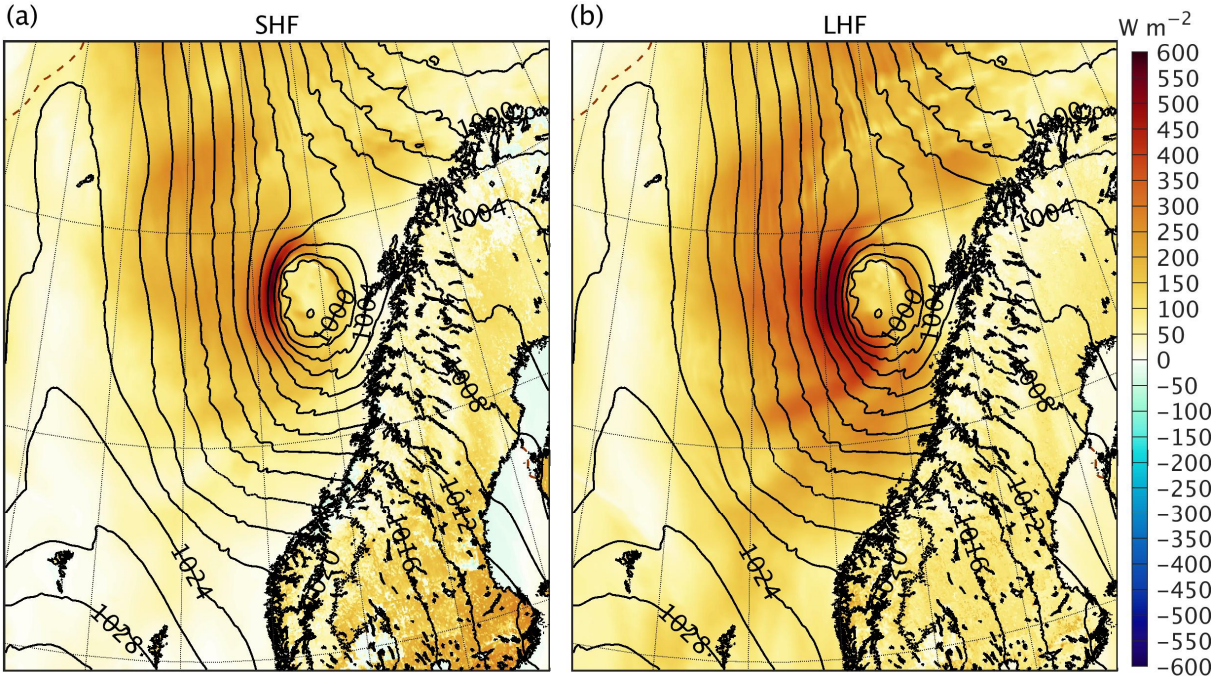

Figure 15. Same as Figure 14, but for 25 March 2019 at 1200 UTC.

4. Conclusions

A case study of the PL that developed over the Norwegian Sea on 25 March 2019 has been presented. The observed PL was simulated reasonably well by the CRCM6/GEM4, a convection-permitting model [35]. The analysis conducted here has allowed gaining an insight into the development mechanisms involved in the genesis and intensification of this PL, showing the potential of convection-permitting models as a tool to study PLs.

The PL developed in a forward-shear environment, and its development resembled that of a typical midlatitude storm. As shown in Stoll et al. [25], forward-shear PLs mainly occur within a MCAO and propagate eastward. Accordingly, the genesis of this PL, which propagated south-eastward, occurred during a MCAO in a region with a high horizontal temperature gradient, near the sea ice edge. The PL formed as a low-level pressure anomaly located downstream (east) of a 500 hPa trough. During the initial stage of the PL, early on 25 March, there was low-level southward (northward) cold (warm) air advection on the west (east) side of the PL. The warming of the atmospheric column near the PL centre contributed to the deepening of the incipient PL. As the PL deepened and its vertical extension increased, reaching the 500 hPa level, the baroclinic instability extended from the low- to the mid-troposphere while weakening. Latent heating of condensation contributed to the intensification of the PL, by reinforcing the upward vertical movement associated with baroclinic conversion. The surface heat fluxes seemed to indirectly contribute to the formation of the PL by decreasing the atmospheric static stability and by providing moisture to the dry atmosphere. By 1200 UTC, the PL had occluded, and it dissipated as the baroclinic conversion term became weaker. In conclusion, moist baroclinic instability was the main driver of the genesis and intensification of this PL, in agreement with recent studies (e.g., [25]).

In addition to baroclinic conversion, other sources of energy, namely barotropic conversion and CAPE, were present during PL development; nonetheless, they do not seem to have played a major role in the intensification of this PL. Barotropic instability led to the formation of a frontal wave that generated small and low-level cyclonic mesoscale vortices around the PL centre. Although some CAPE built up at certain locations, there was no significant reservoir of CAPE during PL development, since the CAPE was consumed as quickly as it was generated.

This study has shown that the CRCM6/GEM4 can represent, among other details, strong temperature gradients, intense and narrow updrafts, narrow wind shear zones, frontal waves, and small low-level mesoscale cyclones. Thus, the CRCM6/GEM4 can provide a detailed representation of the structure of PLs, as well as of the forcing mechanisms involved in the generation and intensification of these mesoscale cyclones. In this case, the baroclinic development was well represented by the CRCM6/GEM4, which captured the evolution of the narrow zones along the front that presented high values of the baroclinic conversion term. To further evaluate the contribution of surface heat fluxes to the PL development, in particular near the sea ice edge, a future study could conduct a more in-depth diagnostic of the direct and indirect effects on both temperature advection and the MCAO features and vorticity maximum location at low levels using the methodology applied by Gachon et al. [15]. An interesting course of research would be to conduct a detailed analysis of a PL that formed under different forcing mechanisms. For instance, it would be very interesting to study the development mechanisms of a PL that formed to the east of Greenland, where topography can play an important role in PL development [55].

The main limitation of this study is that, since the CRCM6/GEM4 does not include either an ocean or a sea ice component, the atmosphere–ocean–sea ice interactions were not explicitly represented, despite the fact that these interactions modulated the PL development during its life cycle. In effect, the shape of the sea ice edge, which is affected by near surface winds and surface oceanic currents, affects the formation of convergence zones within MCAO [14] and influences PL genesis [15]. As suggested in Renfrew et al. [56], coupled interactions between the atmosphere and the oceanic features play a significant role in shaping surface fluxes and impact on the ocean, which in turn modify the low-level atmospheric conditions. PL development can lead to an increase or a decrease in SST [49], which can in turn contribute to the intensification or weakening of the PL. Moreover, the sea ice concentration and SST used as ocean surface boundary conditions in these simulations were obtained from ERA5 [57], which has a grid mesh of 0.25°. Therefore, coupling the atmosphere model with ocean and sea ice models could improve the representation of PLs

by the CRCM6/GEM4, since the interactions between these different components should be represented at high resolution.

Author Contributions: Conceptualization, M.M.-I. and R.L.; methodology, M.M.-I. and R.L.; software, M.M.-I.; validation, R.L. and P.G.; formal analysis, M.M.-I., R.L. and P.G.; investigation, M.M.-I.; resources, R.L.; writing—original draft preparation, M.M.-I.; writing—review and editing, M.M.-I., R.L. and P.G.; visualization, M.M.-I.; supervision, R.L. and P.G.; project administration, R.L.; funding acquisition, R.L. All authors have read and agreed to the published version of the manuscript.

Funding: This work was supported by the Discovery Grant program of the Natural Sciences and Engineering Research Council of Canada (NSERC) under Grant 707337, by the project "Marine Environmental Observation, Prediction and Response" (MEOPAR; http://meopar.ca (accessed on 23 May 2023)) of the Networks of Centres of Excellence (NCE; http://www.nce-rce.gc.ca (accessed on 23 May 2023)) of Canada, and by the excellence scholarship of the Trottier Family Foundation (grant from the UQAM's foundation).

Institutional Review Board Statement: Not applicable.

Informed Consent Statement: Not applicable.

Data Availability Statement: The output of the simulations of this PL and the coordinates of the manually obtained PL track are openly available in Borealis, the Canadian Dataverse Repository at 10.5683/SP3/6E3ITE (accessed on 4 April 2023). VIIRS channel M15 observations are available from NASA (https://ladsweb.modaps.eosdis.nasa.gov/ (accessed on 22 September 2022)). The Global Self-consistent, Hierarchical, High-resolution Geography Database (GSHHG), available at https://www.soest.hawaii.edu/pwessel/gshhg/ (accessed on 7 February 2023), was used to represent the coastlines. The divergent colourmap used in Figure 4, Figure 6, Figure 7, Figure 10, Figure 14, and Figure 15 is provided by the Texas Advanced Computing Center at https://sciviscolor.org/ (accessed on 20 December 2022).

Acknowledgments: Computations were performed on the supercomputer Beluga, managed by Calcul Québec and the Digital Research Alliance of Canada. The operation of this supercomputer is funded by the Canada Foundation for Innovation (CFI), Ministère de l'Économie et de l'Innovation du Québec (MEI) and le Fonds de recherche du Québec (FRQ). The software package MetPy is available at https://unidata.github.io/MetPy/latest/ (accessed on 7 November 2022). The authors would like to thank Katja Winger for her valuable help in the use of the r.diag toolkit, as well as Frédérik Toupin for maintaining an efficient and user-friendly local computing facility.

Conflicts of Interest: The authors declare no conflict of interest. The funders had no role in the design of the study; in the collection, analyses, or interpretation of data; in the writing of the manuscript; or in the decision to publish the results.

Appendix A

An equation to express the surface pressure tendency can be developed using the thermodynamic and hydrostatic equations. When focusing on the PL as a whole, the hydrostatic approximation is adequate [10]. Three vertical levels were considered when developing the equation of the surface pressure tendency: the top level $a = 500$ hPa, the low level $b = \min(p_s(t))$, and the surface level s. The level b is the minimum value of the time series of the surface pressure at each grid point. Therefore, for each grid point, $p_b \leq p_s(t)$.

1. Step 1: Find an expression for $\frac{\partial \Phi_b}{\partial t}$

   Starting from the hydrostatic equation:

$$\frac{\partial \Phi}{\partial p} = -\frac{RT}{p} \tag{A1}$$

We integrate from $a = 500$ hPa to $b = \min(p_s(x,y))$:

$$\int_{\Phi_a}^{\Phi_b} d\Phi = \Phi_b - \Phi_a = -R\int_{lnp_a}^{lnp_b} Tdlnp \tag{A2}$$

We compute the local derivative using Leibniz formula:

$$\frac{\partial \Phi_b}{\partial t} = \frac{\partial \Phi_a}{\partial t} - R\int_{lnp_a}^{lnp_b} \frac{\partial T}{\partial t} dlnp \tag{A3}$$

2. Step 2: Link $\frac{\partial \Phi_b}{\partial t}$ to $\frac{\partial p_s}{\partial t}$

We integrate the hydrostatic equation from b to s:

$$\int_{\Phi_b}^{\Phi_s} d\Phi = \Phi_s - \Phi_b = -R\int_{lnp_b}^{lnp_s} Tdlnp \tag{A4}$$

We compute the local derivative using Leibniz formula:

$$\frac{\partial \Phi_b}{\partial t} = \frac{\partial \Phi_s}{\partial t} + R\frac{\partial}{\partial t}\int_{lnp_b}^{lnp_s} Tdlnp = \frac{\partial \Phi_s}{\partial t} + R\int_{lnp_b}^{lnp_s} \frac{\partial T}{\partial t} dlnp + RT_s\frac{\partial lnp_s}{\partial t} - RT_b\frac{\partial lnp_b}{\partial t} \tag{A5}$$

Since $\frac{\partial \Phi_s}{\partial t} = 0$ and $\frac{\partial lnp_b}{\partial t} = 0$, we obtain:

$$\frac{\partial \Phi_b}{\partial t} = R\int_{lnp_b}^{lnp_s} \frac{\partial T}{\partial t} dlnp + RT_s\frac{\partial lnp_s}{\partial t} \tag{A6}$$

We solve for $\frac{\partial lnp_s}{\partial t}$:

$$\frac{\partial lnp_s}{\partial t} = \frac{1}{RT_s}\left[\frac{\partial \Phi_b}{\partial t} - R\int_{lnp_b}^{lnp_s} \frac{\partial T}{\partial t} dlnp\right] \tag{A7}$$

We assume that term $R\int_{lnp_b}^{lnp_s} \frac{\partial T}{\partial t} dlnp$ will be negligible compared to $\frac{\partial \Phi_b}{\partial t}$ because p_b is close to p_s, so

$$\frac{\partial lnp_s}{\partial t} \approx \frac{1}{RT_s}\frac{\partial \Phi_b}{\partial t} \tag{A8}$$

3. Step 3: The surface pressure tendency equation

Substituting $\frac{\partial \Phi_b}{\partial t}$ by the expression obtained in Step 1, we obtain:

$$\frac{\partial lnp_s}{\partial t} \approx \frac{1}{RT_s}\left[\frac{\partial \Phi_a}{\partial t} - R\int_{lnp_a}^{lnp_b} \frac{\partial T}{\partial t} dlnp\right] \tag{A9}$$

Therefore, the surface pressure tendency is:

$$\frac{\partial p_s}{\partial t} \approx \frac{p_s}{RT_s}\frac{\partial \Phi_a}{\partial t} + \frac{p_s}{T_s}\int_{p_b}^{p_a} \frac{1}{p}\frac{\partial T}{\partial t} dp \tag{A10}$$

References

1. Klein, T.; Heinemann, G. Interaction of katabatic winds and mesocyclones near the eastern coast of Greenland. *Meteorol. Appl.* **2002**, *9*, 407–422. [CrossRef]
2. DuVivier, A.K.; Cassano, J.J.; Craig, A.; Hamman, J.; Maslowski, W.; Nijssen, B.; Osinski, R.; Roberts, A. Winter Atmospheric Buoyancy Forcing and Oceanic Response during Strong Wind Events around Southeastern Greenland in the Regional Arctic System Model (RASM) for 1990–2010. *J. Clim.* **2016**, *29*, 975–994. [CrossRef]
3. Michel, C.; Terpstra, A.; Spengler, T. Polar Mesoscale Cyclone Climatology for the Nordic Seas Based on ERA-Interim. *J. Clim.* **2018**, *31*, 2511–2532. [CrossRef]

4. Valkonen, E.; Cassano, J.; Cassano, E. Arctic Cyclones and Their Interactions with the Declining Sea Ice: A Recent Climatology. *J. Geophys. Res. Atmos.* **2021**, *126*, e2020JD034366. [CrossRef]
5. Gutjahr, O.; Jungclaus, J.H.; Brüggemann, N.; Haak, H.; Marotzke, J. Air-Sea Interactions and Water Mass Transformation During a Katabatic Storm in the Irminger Sea. *J. Geophys. Res. Ocean.* **2022**, *127*, e2021JC018075. [CrossRef]
6. Moore, G.W.K.; York, J.; Sathiyamoorthy, S. Polar lows in the Labrador Sea. *Tellus A* **1996**, *48*, 17–40. [CrossRef]
7. Condron, A.; Renfrew, I.A. The impact of polar mesoscale storms on northeast Atlantic Ocean circulation. *Nat. Geosci.* **2013**, *6*, 34. [CrossRef]
8. Heinemann, G.; Claud, C. Report of a workshop on "theoretical and observational studies of polar lows" of the European Geophysical Society Polar Lows Working Group. *Bull. Am. Meteorol. Soc.* **1997**, *78*, 2643–2658. [CrossRef]
9. Orlanski, I. A Rational Subdivision of Scales for Atmospheric Processes. *Bull. Am. Meteorol. Soc.* **1975**, *56*, 527–530.
10. Moreno-Ibáñez, M.; Laprise, R.; Gachon, P. Recent advances in polar low research: Current knowledge, challenges and future perspectives. *Tellus A* **2021**, *73*, 1890412. [CrossRef]
11. Turner, J.; Rasmussen, E.A.; Carleton, A.M. Introduction. In *Polar Lows: Mesoscale Weather Systems in the Polar Regions*; Rasmussen, E.A., Turner, J., Eds.; Cambridge University Press: Cambridge, UK, 2003; pp. 1–51.
12. Fletcher, J.; Mason, S.; Jakob, C. The Climatology, Meteorology, and Boundary Layer Structure of Marine Cold Air Outbreaks in Both Hemispheres. *J. Clim.* **2016**, *29*, 1999–2014. [CrossRef]
13. Sergeev, D.E.; Renfrew, I.A.; Spengler, T.; Dorling, S.R. Structure of a shear-line polar low. *Q. J. R. Meteorol. Soc.* **2017**, *143*, 12–26. [CrossRef]
14. Watanabe, S.-i.I.; Niino, H.; Spengler, T. Formation of maritime convergence zones within cold air outbreaks due to the shape of the coastline or sea ice edge. *Q. J. R. Meteorol. Soc.* **2022**, *148*, 2546–2562. [CrossRef]
15. Gachon, P.; Laprise, R.; Zwack, P.; Saucier, F.J. The effects of interactions between surface forcings in the development of a model-simulated polar low in Hudson Bay. *Tellus A* **2003**, *55*, 61–87. [CrossRef]
16. Albright, M.D.; Reed, R.J.; Ovens, D.W. Origin and structure of a numerically simulated polar low over Hudson Bay. *Tellus A* **1995**, *47*, 834–848. [CrossRef]
17. van Delden, A.; Rasmussen, E.A.; Turner, J.; Røsting, B. Theoretical investigations. In *Polar Lows: Mesoscale Weather Systems in the Polar Regions*; Rasmussen, E.A., Turner, J., Eds.; Cambridge University Press: Cambridge, UK, 2003; pp. 286–404.
18. Mansfield, D.A. Polar lows: The development of baroclinic disturbances in cold air outbreaks. *Q. J. R. Meteorol. Soc.* **1974**, *100*, 541–554. [CrossRef]
19. Rasmussen, E. The polar low as an extratropical CISK disturbance. *Q. J. R. Meteorol. Soc.* **1979**, *105*, 531–549. [CrossRef]
20. Businger, S. The synoptic climatology of polar low outbreaks. *Tellus A* **1985**, *37*, 419–432. [CrossRef]
21. Sardie, J.M.; Warner, T.T. A numerical study of the development mechanisms of polar lows. *Tellus A* **1985**, *37*, 460–477. [CrossRef]
22. Rasmussen, E.A.; Turner, J.; Ninomiya, K.; Renfrew, I.A. Observational studies. In *Polar Lows: Mesoscale Weather Systems in the Polar Regions*; Rasmussen, E.A., Turner, J., Eds.; Cambridge University Press: Cambridge, UK, 2003; pp. 150–285.
23. Terpstra, A.; Spengler, T.; Moore, R.W. Idealised simulations of polar low development in an Arctic moist-baroclinic environment. *Q. J. R. Meteorol. Soc.* **2015**, *141*, 1987–1996. [CrossRef]
24. Haualand, K.F.; Spengler, T. Direct and Indirect Effects of Surface Fluxes on Moist Baroclinic Development in an Idealized Framework. *J. Atmos. Sci.* **2020**, *77*, 3211–3225. [CrossRef]
25. Stoll, P.J.; Spengler, T.; Terpstra, A.; Graversen, R.G. Polar lows–moist-baroclinic cyclones developing in four different vertical wind shear environments. *Weather Clim. Dyn.* **2021**, *2*, 19–36. [CrossRef]
26. Kolstad, E.W.; Bracegirdle, T.J. Sensitivity of an apparently hurricane-like polar low to sea-surface temperature. *Q. J. R. Meteorol. Soc.* **2017**, *143*, 966–973. [CrossRef]
27. Bracegirdle, T.J.; Gray, S.L. The dynamics of a polar low assessed using potential vorticity inversion. *Q. J. R. Meteorol. Soc.* **2009**, *135*, 880–893. [CrossRef]
28. McInnes, H.; Kristiansen, J.; Kristjánsson, J.E.; Schyberg, H. The role of horizontal resolution for polar low simulations. *Q. J. R. Meteorol. Soc.* **2011**, *137*, 1674–1687. [CrossRef]
29. Føre, I.; Nordeng, T.E. A polar low observed over the Norwegian Sea on 3–4 March 2008: High-resolution numerical experiments. *Q. J. R. Meteorol. Soc.* **2012**, *138*, 1983–1998. [CrossRef]
30. Wagner, J.S.; Gohm, A.; Dörnbrack, A.; Schäfler, A. The mesoscale structure of a polar low: Airborne lidar measurements and simulations. *Q. J. R. Meteorol. Soc.* **2011**, *137*, 1516–1531. [CrossRef]
31. Terpstra, A.; Michel, C.; Spengler, T. Forward and Reverse Shear Environments during Polar Low Genesis over the Northeast Atlantic. *Mon. Weather Rev.* **2016**, *144*, 1341–1354. [CrossRef]
32. Stoll, P.J. A global climatology of polar lows investigated for local differences and wind-shear environments. *Weather Clim. Dyn.* **2022**, *3*, 483–504. [CrossRef]
33. Xue, J.; Bromwich, D.H.; Xiao, Z.; Bai, L. Impacts of initial conditions and model configuration on simulations of polar lows near Svalbard using Polar WRF with 3DVAR. *Q. J. R. Meteorol. Soc.* **2021**, *147*, 3806–3834. [CrossRef]
34. Sergeev, D.; Renfrew, I.A.; Spengler, T. Modification of Polar Low Development by Orography and Sea Ice. *Mon. Weather Rev.* **2018**, *146*, 3325–3341. [CrossRef]
35. Moreno-Ibáñez, M.; Laprise, R.; Gachon, P. Assessment of simulations of a polar low with the Canadian Regional Climate Model. *EarthArXiv* **2023**, Preprint. [CrossRef]

36. Côté, J.; Gravel, S.; Méthot, A.; Patoine, A.; Roch, M.; Staniforth, A. The Operational CMC–MRB Global Environmental Multiscale (GEM) Model. Part I: Design Considerations and Formulation. *Mon. Weather Rev.* **1998**, *126*, 1373–1395. [CrossRef]
37. Bélair, S.; Mailhot, J.; Girard, C.; Vaillancourt, P. Boundary Layer and Shallow Cumulus Clouds in a Medium-Range Forecast of a Large-Scale Weather System. *Mon. Weather Rev.* **2005**, *133*, 1938–1960. [CrossRef]
38. Bélair, S.; Roch, M.; Leduc, A.-M.; Vaillancourt, P.A.; Laroche, S.; Mailhot, J. Medium-Range Quantitative Precipitation Forecasts from Canada's New 33-km Deterministic Global Operational System. *Weather Forecast.* **2009**, *24*, 690–708. [CrossRef]
39. Girard, C.; Plante, A.; Desgagné, M.; McTaggart-Cowan, R.; Côté, J.; Charron, M.; Gravel, S.; Lee, V.; Patoine, A.; Qaddouri, A.; et al. Staggered Vertical Discretization of the Canadian Environmental Multiscale (GEM) Model Using a Coordinate of the Log-Hydrostatic-Pressure Type. *Mon. Weather Rev.* **2014**, *142*, 1183–1196. [CrossRef]
40. Moreno-Ibáñez, M.; Laprise, R.; Gachon, P. Polar low developed in the Norwegian Sea on 25 March 2019–Simulations with the Canadian Regional Climate Model (CRCM6/GEM4) and Manual Track; Borealis; V1; 2023. Available online: https://doi.org/10.5683/SP3/6E3ITE (accessed on 4 April 2023).
41. NASA. *NASA Visible Infrared Imaging Radiometer Suite Level-1B Product User Guide*; NASA Goddard Space Flight Center: Greenbelt, MD, USA, 2019. Available online: https://ladsweb.modaps.eosdis.nasa.gov/api/v2/content/archives/Document%20Archive/Science%20Data%20Product%20Documentation/NASAVIIRSL1BUGAug2019.pdf (accessed on 22 September 2022).
42. Stoll, P.J.; Graversen, R.G.; Noer, G.; Hodges, K. An objective global climatology of polar lows based on reanalysis data. *Q. J. R. Meteorol. Soc.* **2018**, *144*, 2099–2117. [CrossRef]
43. Lorenz, E.N. Available Potential Energy and the Maintenance of the General Circulation. *Tellus* **1955**, *7*, 157–167. [CrossRef]
44. Lorenz, E.N. *The Nature and Theory of the General Circulation of the Atmosphere*; World Meteorological Organization: Geneva, Switerland, 1967.
45. Clément, M.; Nikiéma, O.; Laprise, R. Limited-area atmospheric energetics: Illustration on a simulation of the CRCM5 over eastern North America for December 2004. *Clim. Dyn.* **2017**, *48*, 2797–2818. [CrossRef]
46. Duncan, C.N. A numerical investigation of polar lows. *Q. J. R. Meteorol. Soc.* **1977**, *103*, 255–267. [CrossRef]
47. Yanase, W.; Niino, H. Dependence of Polar Low Development on Baroclinicity and Physical Processes: An Idealized High-Resolution Numerical Experiment. *J. Atmos. Sci.* **2007**, *64*, 3044–3067. [CrossRef]
48. Shimada, U.; Wada, A.; Yamazaki, K.; Kitabatake, N. Roles of an upper-level cold vortex and low-level baroclinicity in the development of polar lows over the Sea of Japan. *Tellus A* **2014**, *66*, 24694. [CrossRef]
49. Wu, L. Effect of atmosphere-wave-ocean/ice interactions on a polar low simulation over the Barents Sea. *Atmos. Res.* **2021**, *248*, 105183. [CrossRef]
50. Wallace, J.M.; Hobbs, P.V. *Atmospheric Science: An Introductory Survey*, 2nd ed.; Elsevier: Amsterdam, The Netherlands, 2006; Volume 92.
51. Unidata. *MetPy Version 1.3.1*; UCAR/Unidata: Boulder, CO, USA, 2022.
52. Føre, I.; Kristjánsson, J.E.; Kolstad, E.W.; Bracegirdle, T.J.; Saetra, Ø.; Røsting, B. A 'hurricane-like' polar low fuelled by sensible heat flux: High-resolution numerical simulations. *Q. J. R. Meteorol. Soc.* **2012**, *138*, 1308–1324. [CrossRef]
53. Leutwyler, D.; Schär, C. Barotropic Instability of a Cyclone Core at Kilometer-Scale Resolution. *J. Adv. Model. Earth Syst.* **2019**, *11*, 3390–3402. [CrossRef]
54. Linders, T.; Saetra, Ø. Can CAPE maintain polar lows? *J. Atmos. Sci.* **2010**, *67*, 2559–2571. [CrossRef]
55. Kristjánsson, J.E.; Thorsteinsson, S.; Kolstad, E.W.; Blechschmidt, A.M. Orographic influence of east Greenland on a polar low over the Denmark Strait. *Q. J. R. Meteorol. Soc.* **2011**, *137*, 1773–1789. [CrossRef]
56. Renfrew, I.A.; Pickart, R.S.; Våge, K.; Moore, G.W.K.; Bracegirdle, T.J.; Elvidge, A.D.; Jeansson, E.; Lachlan-Cope, T.; McRaven, L.T.; Papritz, L.; et al. The Iceland Greenland Seas Project. *Bull. Am. Meteorol. Soc.* **2019**, *100*, 1795–1817. [CrossRef]
57. Hersbach, H.; Bell, B.; Berrisford, P.; Hirahara, S.; Horányi, A.; Muñoz-Sabater, J.; Nicolas, J.; Peubey, C.; Radu, R.; Schepers, D.; et al. The ERA5 global reanalysis. *Q. J. R. Meteorol. Soc.* **2020**, *146*, 1999–2049. [CrossRef]

Datasets

North Atlantic polar low tracks from September 2008 to May 2009 from WRF simulations at 50, 25 and 12.5 km grid spacings

Creator:	Marta Moreno-Ibáñez
Contributors:	John J. Cassano, Suzanne L. Gray and Mark Seefeldt
Year:	2025
Publisher:	University of Reading
DOI:	10.17864/1947.001433
License:	Creative Commons Attribution 4.0 International (CC BY 4.0)
Description:	This dataset contains: 1. The model configuration files of three simulations conducted with the Advanced Research Weather Research and Forecasting (WRF) Model with 50, 25 and 12.5 km grid spacings. The domain is the North Atlantic and the period covered is 2008-09 to 2009-05. 2. The tracks of polar lows in each simulation. 3. Statistics of the characteristics of the polar low tracks and associated fields.
Related publication	Moreno-Ibáñez, M., Cassano, J. J., Gray, S. L. and Seefeldt, M. 2025. Sensitivity of the Representation of Polar Lows to Typical Climate Model Resolutions. *Atmos. Sci. Lett.* **26**, e1319. doi: 10.1002/asl.1319

Polar low developed in the Norwegian Sea on 25 March 2019 – Simulations with the Canadian Regional Climate Model (CRCM6/GEM4) and manual track

Authors:	Marta Moreno-Ibáñez, René Laprise and Philippe Gachon
Year:	2023
Publisher:	Borealis
DOI:	10.5683/SP3/6E3ITE
License:	Creative Commons Attribution-NonCommercial 4.0 International (CC BY-NC 4.0)
Description:	This dataset contains: 1. The output of an ensemble of simulations of a polar low that developed over the Norwegian Sea on 25 March 2019. 2. The manually-obtained tracks of the polar low.
Related publication	Moreno-Ibáñez, M., Laprise, R. and Gachon, P. 2023. Assessment of simulations of a polar low with the Canadian Regional Climate Model. *PLOS ONE* **18**, e0292250. doi: 10.1371/journal.pone.0292250